

A Journey with Dust: From Protoplanetary Disks to Planetary Atmospheres and Outflows

Thesis by
Yayaati Chachan

In Partial Fulfillment of the Requirements for the
Degree of
Doctor of Philosophy

The logo for the California Institute of Technology (Caltech), featuring the word "Caltech" in a bold, orange, sans-serif font.

CALIFORNIA INSTITUTE OF TECHNOLOGY
Pasadena, California

2022
Defended February 24th, 2022

© 2022

Yayaati Chachan

ORCID: 0000-0003-1728-8269

All rights reserved

ACKNOWLEDGEMENTS

I have had the privilege of having Heather Knutson as my mentor and thesis advisor at Caltech. Heather is peerless as a PhD advisor and her dedication, patience, and kindness are inspiring. I hope to emulate her example as a teacher and an advisor. Here, I express my boundless gratitude to her for her guidance and for encouraging me to follow my curiosity and interests.

I am indebted to Dave Stevenson for offering me one of my first planetary science projects, asking questions full of insight, sharing his thoughts on all my papers, and encouraging me to be creative. I am also glad to have had a chance to attend and assist in teaching his class on planetary interiors. I am grateful to Geoff Blake, Yuk Yung, and Konstantin Batygin for agreeing to be on my thesis advisory committee, for their encouraging feedback, and for enriching scientific discussions throughout graduate school.

Numerous collaborators made the work presented in this thesis possible. I am grateful to Eve Lee for her sound theoretical guidance and input, to Daniel Jontof-Hutter for offering me the lead on the Kepler-79d paper, to Paul Dalba for his highly competent data reduction for Kepler-167, and to Peter Gao for teaching me about clouds and hazes. I am especially indebted to Bjorn Benneke and Ian Wong for sharing their Hubble data reduction pipeline with me. Thanks also to Michael Zhang for sharing his masterfully written codes and co-creating PLATON with me.

The staff at the planetary science department and international students program have also enabled me to do my scientific work. My thanks to Margaret Carlos for a smooth-sailing experience in graduate school and to Julie Lee, Ulrika Terrones, Irma Black, and Ruth Loisel for providing timely assistance to me. I am immensely grateful to Daniel Yoder and Laura Flower Kim and ISP staff members for being on top of immigration related requirements and providing timely guidance on international travel rules during the pandemic.

My peers at Caltech made my time here very personally and scientifically fulfilling. I am extremely grateful for the warm camaraderie amongst graduate students that was nourished by our seniors and carried on by us to the best of our ability. I consider myself lucky to have had Ellen Leask, Michael Wong, Pushkar Kopparla, and Tianhao Le as my office mates.

The warmth shared by 2017 GPS graduate student cohort made my time at Caltech especially fulfilling. Special thanks to fellow planetary scientists from my year, Shreyas Vissapragada, Aida Behmard, Qicheng Zhang, and Harriet Brettle for being excellent compatriots during graduate school. My friendship with Madison Douglas and Eva Scheller has been a joyful part of my graduate school experience.

My heartfelt thanks to Nicole Wallack, Cecilia Sanders, and Morgan Hooper for welcoming me to their home for wholesome conversations. I am also grateful to Elizabeth Bailey, Nathan Stein, Nancy Thomas, and Chris Spalding for generously sharing their affirming advice with me. I am thankful to Maria Camarca and Mike Greklek-McKeon for their enjoyable company, great sense of humor, and the warmth they have brought to the planetary science department.

Finally, I am deeply grateful to my family and my partner, Cleo Tay, for providing unwavering support throughout graduate school.

ABSTRACT

Dust in astronomy is often perceived as a hindrance to true characterization of celestial bodies. However, it is the humble dust particles that often run the show in planet formation and evolution. In this thesis, I present four different observationally inspired problems, which span a vast chronological range from core formation to atmospheric escape, and show how dust holds sway over them. In Chapter 2, I demonstrate that protoplanetary disks that are capable of forming giant planets are also capable of hosting close-in super-Earths within the giant planet's orbit, in line with the observed correlation between the occurrence rates of these two sub-populations. In Chapter 3, I show how dust dynamics and differences in grain properties across the water ice line create a region at intermediate distances where gas accretion is rapid. This might explain the preponderance of giant planets at such distances from their host stars, independently or complementarily to prevalent ideas on where massive cores form. Subsequently, since our understanding of the simultaneous accretion of dust and gas during planet formation remains poor, I argue in Chapter 4 that atmospheric characterization of Neptune-class planets is valuable for advances in this area. In particular, I discuss my efforts to characterize one such planet (HAT-P-11b) that, as a low metallicity Neptune, serves as an instructive challenge for formation models. Finally, in Chapter 5, I substantiate the idea that dust in the form of photochemical hazes must be present in outflowing atmospheres of super-puffs (i.e. planets with super-Earth-like masses but giant planet-like radii) by using the transmission spectrum and bulk properties of the canonical super-puff Kepler-79d.

PUBLISHED CONTENT AND CONTRIBUTIONS

- Chachan et al. (2019). “A Hubble PanCET Study of HAT-P-11b: A Cloudy Neptune with a Low Atmospheric Metallicity”. In: *The Astronomical Journal* 158.6, pp. 244–268. DOI: 10.3847/1538-3881/ab4e9a.
Y.C. reduced and analyzed the data, designed the narrative, and wrote the manuscript.
- Chachan et al. (2020). “A Featureless Infrared Transmission Spectrum for the Super-puff Planet Kepler-79d”. In: *The Astronomical Journal* 160.5, pp. 201–219. DOI: 10.3847/1538-3881/abb23a.
Y.C. reduced and analyzed the data, designed the narrative, and wrote the manuscript.
- Chachan et al. (2021). “Radial Gradients in Dust-to-gas Ratio Lead to Preferred Region for Giant Planet Formation”. In: *The Astrophysical Journal* 919.1, pp. 63–80. DOI: 10.3847/1538-4357/ac0bb6.
Y.C. conceived the project, performed the theoretical work, and wrote the manuscript.
- Chachan et al. (2022). “Kepler-167e as a Probe of the Formation Histories of Cold Giants with Inner Super-Earths.”. In: *The Astrophysical Journal* 926.1, pp. 62–77. DOI: 10.3847/1538-4357/ac3ed6.
Y.C. designed the narrative, performed all the theoretical work, and wrote the manuscript.

TABLE OF CONTENTS

Acknowledgements	iii
Abstract	v
Published Content and Contributions	vi
Table of Contents	vi
List of Illustrations	ix
List of Tables	xxi
Chapter I: Introduction	1
Chapter II: Kepler-167e as a Probe of the Formation Histories of Cold Giants with Inner Super-Earths	6
2.1 Introduction	6
2.2 Observations	8
2.3 Model Fitting and Parameter Estimation	11
2.4 A Closer Look at the Kepler-167 Planets	16
2.5 Formation of Inner Super-Earths with Outer Gas Giant Companions	22
2.6 Conclusions	37
Chapter III: Radial Gradients in Dust-to-Gas Ratio Lead to Preferred Region for Giant Planet Formation	40
3.1 Introduction	40
3.2 Models	42
3.3 Dust Opacity in Protoplanetary Disks	50
3.4 Implications for Planet Formation	69
3.5 Discussion and Conclusions	77
Chapter IV: A Hubble PanCET Study of HAT-P-11b: A Cloudy Neptune with a Low Atmospheric Metallicity	80
4.1 Introduction	80
4.2 Observations	83
4.3 Spectral & Photometric Extraction	84
4.4 Systematics and Astrophysical Models	89
4.5 Analysis	97
4.6 Comparison to Forward Models	107
4.7 Atmospheric Retrieval: PLATON	113
4.8 Discussion and Conclusions	124
Chapter V: A Featureless Infrared Transmission Spectrum for the Super-Puff Planet Kepler-79d	128
5.1 Introduction	128
5.2 Observational Data	131
5.3 Light Curve Modelling and Fitting	136
5.4 Results and Discussion	141
5.5 Future Directions and Conclusions	167

Chapter VI: Conclusions	169
Bibliography	172
Appendix A: Pebble accretion efficiency	195
Appendix B: Disk fraction and formation threshold	197
Appendix C: HST spectroscopic light curves for HAT-P-11b	199

LIST OF ILLUSTRATIONS

<i>Number</i>	<i>Page</i>
2.1 Optical <i>Kepler</i> transit photometry of the four Kepler-167 planets folded on their best fit ephemeris along with their best fit models (blue). Note the difference in scale in the panel for Kepler-167e. The data (red) are shown in bins of 10 minutes for the inner planets and 1 hour for the outer planet, although we note that the models were fit to the unbinned data.	13
2.2 Keck-HIRES RV time series data with the median model for Kepler-167e and the corresponding 68% credible interval overplotted.	14
2.3 Planet mass and eccentricity vs semimajor axis for planets more massive than 0.5 M _J in the California Legacy Survey sample (Rosenthal et al., 2021). Giant planets in this sample are shown in two different colors, depending on whether or not they have a detectable inner companion less than 0.1 M _J . We also plot resolved giant planet companions of super-Earths systems studied in Bryan et al. (2019). Kepler-167e is marked in red (3σ upper limit for eccentricity) and has properties that are typical of long period giant planets.	17
2.4 Posterior probability distribution for bulk metallicity and its covariance with the observational priors on planetary mass and age. Kepler-167e’s radius, mass, and age are used to infer its bulk metal content from planetary evolution modeling as described in Thorngren et al. (2016) and Thorngren & Fortney (2019).	19
2.5 Posterior for the total mass contained in the three inner super-Earths obtained using <i>mr-exo</i> (Kanodia et al., 2019), which utilizes the mass-radius relationship from Ning et al. (2018). The median of the distribution is shown with a grey line. We also mark the total mass contained in three planets assuming they are pure rock (MgSiO ₃ , brown), iron (black), or Earth-like (blue) using the median radii of these planets from Table 3 and M-R relations from Zeng et al. (2019).	21

- 2.6 Filled (empty) circles mark disk models for which a $0.01 M_{\oplus}$ seed at 5.6 au does (does not) reach an isolation mass of $15 M_{\oplus}$ core. We show results from models with different initial solid masses M_{dust} (y-axis, product of M_{disk} and Z), disk sizes (x-axis), and three different t_{seed} . The grey shading indicates combinations of solid mass and disk size that are unlikely to exist in nature. For each combination of disk radius and initial solid mass, we use small offsets to show results for different $M_{\text{disk}} \in \{0.05, 0.1, 0.2\} M_*$ and $Z \in \{0.005, 0.01, 0.02\}$, with M_{disk} increasing in the horizontal direction and Z increasing in the vertical direction. 27
- 2.7 The dust mass that filters through to the inner disk between t_{seed} (the time at which a lunar mass seed is introduced) and t_{iso} (when core reaches M_{iso}) for different M_{iso} and a fixed $t_{\text{seed}} = 10^5$ years. All disk models in which a lunar mass seed reaches M_{iso} are shown. The filtered dust mass is primarily a function of M_{iso} and does not depend strongly on the assumed disk properties. 29
- 2.8 Pebble isolation time vs total solid mass available in the inner disk for all disk models in which a $0.01 M_{\oplus}$ seed reaches M_{iso} (i.e., those containing an outer gas giant). In the left panel, we vary t_{seed} and fix M_{iso} to $15 M_{\oplus}$. In the right panel, t_{seed} is fixed to 10^5 yrs and M_{iso} is varied. The initial seeds are placed at 3.2 au, 5.6 au, and 8.2 au to produce cores of $10 M_{\oplus}$, $15 M_{\oplus}$, and $20 M_{\oplus}$, respectively. We mark the estimated dust masses that are required for super-Earth formation in the pebble (Lambrechts et al., 2019) and planetesimal (Drażkowska et al., 2016) accretion paradigms using shaded regions. Models with the same disk size and initial solid mass are connected via dotted lines. 30
- 2.9 The initial solid mass and size of protoplanetary disks that can produce the Kepler-167 planetary system assuming $t_{\text{seed}} = 10^5$ yrs. The color of the points indicates the total amount of solids that is available in the inner disk. We find that $\geq 165 M_{\oplus}$ of solids reach the inner disk for all our models and thus they all exceed the super-Earth formation threshold. We grey out the region corresponding to small disks with very large solid masses, as these disks are unlikely to exist in practice. 34

- 2.10 Disk dust mass and radius estimates for Class 0 and I sources in the Orion cluster that are detected both with ALMA (0.87 mm) and VLA (9 mm) (Tobin et al., 2020). We plot the threshold contour above which disks can form systems like Kepler-167 (corresponding to $M_{\text{iso}} = 15 M_{\oplus}$ and $t_{\text{seed}} = 10^5$ yrs curve in Figure 2.9). Since disks tend to be optically thin in the VLA bandpass, dust mass estimates obtained from these observations are closer to true estimates. However, disk sizes obtained from ALMA are likely to be closer to the characteristic disk size that is used in our modelling. We therefore plot dust mass estimates from VLA against disk radii from ALMA in red. 36
- 3.1 Size distribution and dust-to-gas ratio (ϵ) at time $t = 1$ Myr for a `twopoppy` simulation with variable v_{frag} and $\alpha_t = 10^{-3}$. The size limits imposed by fragmentation and drift are shown with dashed and dotted line in the upper panel. The location of the ice line is marked with blue triangles. 51
- 3.2 Rosseland mean opacity per gram of dust as a function of distance from the star at time $t = 1$ Myr. We adopt $\alpha_t = 10^{-3}$ and a variable v_{frag} that changes across the water ice line for our `twopoppy` model. For the power law distributions, a_{max} is set by the location specific maximum grain size calculated from `twopoppy`, which is given by Equation 3.8 (fragmentation-limited), Equation 3.10 (drift-limited), or the growth-timescale limit. The location of the ice line is marked with blue triangles. 52
- 3.3 Rosseland mean opacity per gram of dust for a power law grain size distribution with $\beta = -3.5$ and -2.5 and three different temperatures. The lowest value of $a_{\text{max}} = 0.25 \mu\text{m}$ on this plot is the commonly adopted value for the ISM size distribution. 53
- 3.4 Rosseland mean opacity per gram of protoplanetary disk material at time $t = 1$ Myr and for a variable v_{frag} and $\alpha_t = 10^{-3}$. This plot is similar to Figure 3.2 except that the opacity per gram of dust is here multiplied by the radially-varying dust-to-gas ratio. For the ISM size distribution, the dust-to-gas ratio is assumed to be 0.01 everywhere. The location of the ice line is marked with blue triangles. 55

- 3.5 The Stokes number of the largest grain size (St_{\max}), dust-to-gas ratio (ϵ), and Rosseland mean opacity per gram of protoplanetary disk material for a range of fragmentation velocities within and beyond the water snow line as well as three different turbulence strengths after 1 Myr of evolution. The fragmentation velocity v_{frag} takes values in the range $0.1 - 10 \text{ m s}^{-1}$ for ice-free grains and $1 - 50 \text{ m s}^{-1}$ for icy grains (Blum & Wurm, 2008; Gundlach & Blum, 2015). The ice line is located at 0.75 au in all of our models. 56
- 3.6 Ratio of the Rosseland mean opacity per gram of protoplanetary disk material at 0.1 au and 5 au after 1 Myr of evolution. The axes labels v_{in} and v_{out} stand for the fragmentation velocity within and beyond the ice line. Our fiducial model is outlined with a black square. . . . 58
- 3.7 The top panel shows the dust-to-gas ratio ϵ as a function of height above the midplane z and distance from the star after 1 Myr of evolution. The white dashed and dotted lines mark the height of the Hill radius R_{Hill} and Bondi radius R_{Bondi} of a $15 M_{\oplus}$ planet, respectively. The bottom panel shows the midplane Stokes number of the largest grains present in the disk at $t = 1 \text{ Myr}$. The water ice line is marked with a blue triangle. Well coupled grains within the ice line lead to efficient vertical mixing of grains and hence a weak dependence of ϵ on z . Beyond the ice line, large grains that dominate the dust mass settle close to the midplane, which leads to a strong decline in ϵ as a function of z 61
- 3.8 Rosseland mean opacity per gram of protoplanetary disk material as a function of height above the midplane z and distance from the star after 1 Myr of evolution. The white dashed and dotted lines mark the height of the Hill radius R_{Hill} and Bondi radius R_{Bondi} of a $15 M_{\oplus}$ planet, respectively. Vertically well mixed dust within the ice line leads to little variation in κ_{R} as a function of z . Grain settling and a strong decline in ϵ with z leads to a gradient in κ_{R} as a function of z beyond the ice line. 62

- 3.9 A comparison of the Rosseland mean opacity per gram of dust, dust-to-gas ratio ϵ , and Rosseland mean opacity per gram of protoplanetary disk material κ_R for our fiducial 2D disk integrated model and our 3D disk model after 1 Myr of evolution. We plot the values of these quantities in the disk midplane ($z = 0$), a single gas scale height above the midplane ($z = H_{\text{gas}}$), and at heights of a $15 M_{\oplus}$ planet's R_{Hill} and $\min(R_{\text{Hill}}, R_{\text{Bondi}})$ above the midplane. The water ice line is marked with blue triangles. 64
- 3.10 Time evolution of the vertically integrated dust-to-gas ratio ϵ and the Rosseland mean opacity per gram of protoplanetary disk material as a function of distance from the star. Although the absolute values of ϵ and κ_R decline over time due to global accretion of dust onto the star, there is little change in their observed profile shapes as a function of time. The minima in ϵ and κ_R profiles move slightly inward with time as a larger fraction of the outer disk becomes drift dominated. The water ice line is marked with blue triangles in the right panel. 66
- 3.11 Post-processed temperature structure of the disk calculated using the method outlined in Birnstiel et al. (2010) with a self-consistent treatment of the opacity calculated using the size distribution and dust-to-gas ratio from our simulations. The disk properties at $t = 1$ Myr are used to calculate the temperature structure and are taken from simulations for which v_{frag} is 1 m/s and 10 m/s for ice-free and icy grains, respectively. The water snow line (150–250 K) is marked with thick lines for each temperature profile. 68
- 3.12 The gas-to-core mass ratio (GCR) at $t = 1$ Myr for a $15 M_{\oplus}$ core as a function of distance from the star, assuming the core starts accreting at $t_0 = 0.1$ Myr. Here, we vary the height z_{ϵ} from which gas is accreted by the planet. A GCR of 0.48 is marked with a dashed grey line, indicating the threshold for the onset of runaway gas accretion (Lee et al., 2014). The water ice line is marked with blue triangles. 72

- 3.13 The gas-to-core mass ratio (GCR) at $t = 10$ Myr for a $15 M_{\oplus}$ core as a function of distance from the star, assuming the core starts accreting at $t_0 = 1$ Myr, for our grid of models. We use a later t_0 here because the dust-to-gas ratio for the $\alpha_t = 10^{-4}$ model varies rapidly at earlier times, and our simple gas accretion model would therefore not be applicable. The dashed grey line indicates the threshold for the onset of runaway gas accretion (GCR of 0.48; Lee et al., 2014). GCRs corresponding to planet masses of $0.3M_J$ and $1M_J$ are marked with black dashes; $0.3M_J$ is commonly used as a lower mass limit when calculating giant planet occurrence rates in RV surveys (e.g. Cumming et al., 2008; Wittenmyer et al., 2020). 73
- 3.14 The gas-to-core mass ratio (GCR) as a function of distance from the star for a $15 M_{\oplus}$ (left panel) and $5 M_{\oplus}$ (right panel) cores for time t in the range 1 – 10 Myr, assuming they start accreting material present at $\min(R_{\text{Hill}}, R_{\text{Bondi}})$ at $t_0 = 0.1$ Myr. GCR of 0.48 (onset of runaway gas accretion Lee et al., 2014) and GCR = 0.1 (for sub-Neptunes and super-puffs) are marked with dashed grey lines in the top and bottom panels, respectively. GCRs corresponding to total planet masses of $0.3M_J$ (left panel) and $10M_{\oplus}$ (right panel) are indicated as well. The locations of solar system giant planets are marked along the abscissa at the top. The water ice line is marked with blue triangles. 75
- 4.1 Observed minus calculated mid-transit times from fits to individual visits, where the color indicates the instrument. Predicted transit times are calculated using the best-fit ephemeris from the global fit, with 1σ uncertainties indicated by the dashed grey lines. Visits with minimal data during ingress or egress have significantly larger uncertainties. 93

4.2 Change in HAT-P-11’s *R* band flux and corresponding spot coverage fraction in 2011 and from late 2015 to early 2017. Points are calculated using photometric monitoring data obtained in the Cousins *R* band pass using the AIT telescope at Fairborn Observatory, in the Johnson *B* and *V* bands using the STELLA telescope at Izaña Observatory, and from the *Kepler* telescope. We assume that the relative flux baseline for all three telescopes corresponds to a spot coverage fraction of 4.4%, and use a photospheric temperature of 4780 K and spot temperature of 4500 K to convert these observations to the equivalent *R* band fluxes. Visit times for *Spitzer* 3.6 μm (black) and 4.5 μm channels (black dashed), *HST* WFC3 G102 (red), STIS G430L (purple), and STIS G750L (blue) observations are indicated by vertical lines. The grey curves are sinusoidal functions that best match the observed variability at different epochs and are used to infer spot coverage fractions for *HST* visits that do not have contemporaneous ground-based monitoring. 94

4.3 We vary star spot temperatures and spot coverage fractions such that they produce the same absolute correction in the *Kepler* bandpass. The spot coverage fractions in the left panel are deduced from *Kepler* long cadence photometry. We fit light curves for these different stellar spot properties and quantify their effect on the retrieved atmospheric metallicity. In the right panel, we show that the posterior for metallicity is relatively insensitive to our choice of spot temperature. We adopt a value of 4500 K in the rest of this study following Morris et al. (2017a). 95

4.4 STIS white light transit light curves before (top) and after (middle) dividing out the best-fit instrumental systematics model. The best-fit transit light curve is shown in blue for comparison, and the fit residuals are shown at the bottom. 98

4.5 WFC3 G102 and G141 white light transit light curves before (top) and after (middle) dividing out the best-fit instrumental systematics model. The best-fit transit light curve is shown in blue for comparison, and the fit residuals are shown at the bottom. 101

- 4.6 *Spitzer* transit light curves before (top) and after (middle) dividing out the best-fit instrumental systematics model. The best-fit transit light curve is shown in blue for comparison, and the fit residuals are shown at the bottom. 102
- 4.7 The transmission spectrum of HAT-P-11b both with and without stellar activity correction. Our transmission spectrum is in good agreement with Fraine et al. (2014)'s published spectrum. In the inset figure, we compare our WFC3 G102 spectrum with a fit to Mansfield et al. (2018)'s light curves, as well as Mansfield et al. (2018)'s published spectra. Our G102 spectrum deviates most significantly from the published spectrum at $0.86 \mu\text{m}$, $1.025 \mu\text{m}$, and $1.095 \mu\text{m}$, which has the effect of washing out the small absorption feature at $0.95 \mu\text{m}$ in the published version. 105
- 4.8 Temperature (left) and vertical mixing parameter K_{zz} (right) profiles as a function of pressure at the orbital phase of the transit (since HAT-P-11b has a significant eccentricity). These profiles are obtained from a SPARC GCM model for HAT-P-11b and are used as inputs in our microphysical cloud models. Transmission spectroscopy probes the atmosphere at pressures roughly between $10^{-1} - 10^{-4}$ bars. 108
- 4.9 Plot windows showing 2D slices of the atmospheric condensate compositions for a $1\times$ solar and $50\times$ solar metallicity atmosphere. The slices sample the atmosphere on the east and west limbs at $\tau \sim 1$ and show the number of condensate particles contained in a $100 \text{ cm} \times 100 \text{ cm} \times 100 \text{ cm}$ volume. Condensates on the two limbs have distinct compositions and increasing the metallicity has a significant effect on condensate number density, especially on the west limb. These plots serve as a visual guide and indicate that the scattering cross-section at the wavelengths of interest is mostly dominated by KCl particles. Mg_2SiO_4 and Al_2O_3 particles also make significant contributions to cloud opacity, especially in the $1\times$ solar metallicity case. 109

- 4.10 Measured transmission spectrum of HAT-P-11b versus transmission spectra generated by averaging CARMA models for the east and west limbs. These model spectra fit the measured spectrum quite well without any fine-tuning or parameter fitting. The *HST* data display a slight preference for the $1\times$ solar metallicity model. However, both the $1\times$ and $50\times$ solar metallicity models are unable to reproduce the *Spitzer* transit depths. 110
- 4.11 Effect of varying σ and refractive index in our Mie scattering model. We assume a particle size $a = 1 \mu\text{m}$, refractive index of 1.5, fractional scale height $f = 1$, particle size distribution width $\sigma = 0.5$, and number density at the base of the atmosphere $n_o = 10^4 \text{cm}^{-3}$ unless specified otherwise. 114
- 4.12 Transmission spectrum in the *HST* WFC3 and STIS bandpasses (black filled circles) with best-fit Mie scattering model spectra from PLATON overplotted along with the 1σ contours. 117
- 4.13 Marginalized posterior probability distributions for the metallicity, C/O ratio, and cloud-top pressure from a fit to the WFC3 data alone and a fit to the WFC3 + STIS dataset. 117
- 4.14 Posterior probability distributions for fits of the *HST* dataset. Median parameter values and 68% confidence intervals for the marginalized 1D posterior probability distributions are indicated with vertical dashed lines. 121
- 4.15 Transmission spectrum for HAT-P-11b including both *HST* and *Spitzer* data (black filled circles) along with the best-fit model from PLATON and corresponding 1σ and 2σ contours (dark blue and light blue, respectively). The best-fit model for *HST* data is also shown for comparison, which predicts a much larger transit depth at $3.6 \mu\text{m}$. The inclusion of the *Spitzer* transit depths shifts the models toward solutions with high atmospheric metallicity, which suppresses the depth of the absorption features in the WFC3 bands and decreases the overall quality of the fit in this region. 122

- 4.16 The left panel (a) shows atmospheric metallicity versus planet mass for planets observed by *HST* and *Spitzer* (Benneke et al., 2019a; Brogi et al., 2017; Kreidberg et al., 2014a; Kreidberg et al., 2015; Morley et al., 2017; Wakeford et al., 2017a; Wakeford et al., 2018). The right panel (b) shows atmospheric metallicity versus bulk metallicity (obtained from Thorngren & Fortney, 2018) for Neptune-class planets. For Neptune, we plot lower and upper limits rather than 1σ error bars (Helled & Guillot, 2018). GJ 3470b is not included on this plot because the assumptions used to derive bulk metallicity constraints in the Thorngren et al. (2016) models may not be appropriate for planets with such low masses. 124
- 4.17 Particle number density as a function of radius from our microphysical cloud models at different pressures/heights in the atmosphere. We overplot a sample of lognormal particle size distributions at 10 mbar from our retrievals for comparison. The best-fit size distribution is highlighted with a dark blue line. All profiles correspond to models with high likelihoods. 125
- 5.1 First exposures of the 2 *HST* visits. The top panel contains the raw images and the bottom panel contains the processed images (after extraction and outlier correction. The region used for sky background calculation is marked out by a white box in the raw images. Kepler-79 has the brightest spectral trace in these images. 132
- 5.2 White light transit light curves before (top) and after (middle) dividing out the best-fit instrumental systematics model. The best-fit transit light curve is shown in blue for comparison, and the fit residuals are shown at the bottom. *Kepler* data has been binned down using a bin width of 200 points. 139
- 5.3 Transit depth measurements for each individual transit of Kepler-79d observed at short cadence. The grey region marks the 1σ limits on the transit depth from our joint fit to the *Kepler* and *HST* data. Black empty circles mark the transits that were significantly affected by correlated noise and red squares show their transit depth measurements obtained using Gaussian Process modelling. 142

- 5.4 Observed and simulated deviations of transit times from a linear fit to the observed *Kepler* data. The colored bands mark the standard deviation of 1000 simulated transit times from the posterior sampling models, with green marking the solutions following *Kepler* only, and magenta marking the dataset including the *HST* times. 144
- 5.5 The transmission spectrum of Kepler-79d measured during 2 visits with the *HST* WFC3 instrument. Black points show the spectrum obtained from a joint fit of the two visits. There is good agreement between the two visits except in two bandpasses centered at 1.135 and 1.495 μm , which show a larger scatter in the measured transit depths. 149
- 5.6 Spectroscopic light curves as well as the best-fit transit models for the 2 *HST* visits (visit 1 in blue and visit 2 in red) and a histogram of the residuals (in parts per thousand). 150
- 5.7 The transmission spectrum of Kepler-79d measured with *Kepler* and *HST* WFC3. The best-fit cloud free models with metal poor composition, 150 \times solar metallicity, and 1000 \times solar metallicity are plotted along with the best-fit constant and linear models. The data are consistent with a constant transit depth model. The Bayesian evidence and the Bayes factor for these models are reported in Table 5.5. . . . 152
- 5.8 Number density of haze particles of different radii at different pressures levels in the atmosphere for $M_{\text{core}} = 5M_{\oplus}$, $T_{\text{int}} = 75$ K, $K_{zz} = 10^7$ cm² s⁻¹, and atmospheric mass fraction of 18%. Haze formation at low pressures and transport due to outflowing wind, vertical mixing, and sedimentation leads to an abundance of sub-micron sized particles at low pressures ($\sim 1 - 10\mu\text{bar}$). 154
- 5.9 Forward CARMA models of the transmission spectrum of Kepler-79d for different optical properties of the aerosols (soots and tholins) and T_{int} values. In the left panel, we compare the models with the transmission spectra. The right panel shows the predicted transmission spectrum out to 30 μm 154

- 5.10 Planet mass vs equilibrium temperature. The contours correspond to planetary radii for which Parker wind mass loss rates would be equal to $M_p \text{ Gyr}^{-1}$. Planets with a mass loss rate smaller (larger) than this value are plotted with filled (empty) circles. Vertical lines originating from the scatter points terminate at the planet mass value for which the mass loss rate would be $M_p \text{ Gyr}^{-1}$ (keeping the planet radius and equilibrium temperature constant). Kepler-79d is plotted at 630 K and $5.3 M_\oplus$ and changes from being an open to a filled circle when the photospheric pressure is changed. 162
- 5.11 Atmospheric lifetime versus planet (stellar) age obtained from Fulton & Petigura (2018). Atmospheric lifetime is calculated by dividing the envelope mass fraction inferred from Lopez & Fortney (2014) with the mass loss rate from either photoevaporation or Parker wind (whichever one is larger, photoevaporation dominated planets circled with black outline). Due to large uncertainties in planetary properties, the uncertainties on the atmospheric lifetime (not shown) are large enough that most planets lie $< 1\sigma$ away from the atmospheric lifetime = age dashed line. 165
- C.1 *HST* STIS G430L wavelength dependent light curves for visits 1 and 2. 199
- C.2 *HST* STIS G750L wavelength dependent light-curves. 200
- C.3 *HST* WFC3 G102 wavelength dependent light curves for visits 1 and 2. 201
- C.4 *HST* WFC3 G102 wavelength dependent light curves for visits 3 and 4. 202
- C.5 *HST* WFC3 G102 wavelength dependent light curves for visit 5. . . . 203
- C.6 *HST* WFC3 G141 wavelength dependent light curves. 204

LIST OF TABLES

<i>Number</i>	<i>Page</i>
2.1 RV measurements of Kepler-167.	10
2.2 Median values and 68% confidence intervals for the stellar parameters for Kepler-167.	12
2.3 Median values and 68% confidence interval of the parameters for each of the Kepler-167 planets.	15
4.1 Observations	85
4.2 Global broadband light curve fit results ^a	99
4.3 Spectroscopic light curve fit results	104
4.4 Median parameters and 68% confidence intervals (CI) from PLATON retrieval	119
4.5 <i>HST</i> retrievals evidence	123
5.1 Global broadband light curve fit results	137
5.2 Transit time variations fit results	146
5.3 Spectroscopic light curve fit results	148
5.4 <i>HST</i> model evidence	148
5.5 <i>Kepler</i> + <i>HST</i> model evidence	152
5.6 Planet properties for our ‘Puffy’ planets sample	161

Chapter 1

INTRODUCTION

Dust plays an important role in astronomy and influences numerous physical processes that affect our big picture understanding of the universe. It controls the cooling of gas, which affects the star formation rate and evolution of galaxies. It acts as a facilitator of chemical reactions in the interstellar medium and protostellar disks around nascent stars. Critically, dust is essential for the formation of planets: smaller planets consist almost entirely of ‘metals’ (elements other than hydrogen and helium) present in the dust and the formation of larger planets is likely contingent on the accumulation of dust in rocky/icy cores. Although dust often hinders our ability to observe celestial bodies, understanding its role in diverse astrophysical processes is of paramount importance. In this thesis, I will focus on dust’s role in planet formation and evolution.

The notion that planets form in disks of dust and gas around nascent stars is at least 250 years old. However, a detailed understanding of the processes by which diffuse dust and gas are transformed into compact planets remains elusive. This challenge is exacerbated for giant planets such as Jupiter that amass hundreds of earth masses of dust and gas. There are two contending ideas for how these planets form: the core accretion theory and gravitational instability. In the core accretion framework (Mizuno, 1980; Pollack et al., 1996), planet formation proceeds in three stages: 1) a planetary core forms from rocky and icy constituents of the protoplanetary disk; 2) if the core becomes massive enough, it starts accreting and holding onto a massive gaseous envelope; and 3) eventually the envelope becomes so massive that it collapses gravitationally and rapid hydrodynamic gas accretion ensues, which leads to the formation of gas giant planets. Gravitational instability proposes a more top down formation pathway in which a clump of disk gas becomes unstable to collapse under self-gravity (akin to how stars form, Boss, 1997). Both formation pathways face fundamental technical challenges and barriers that hinder a detailed understanding of how planets form.

One of the primary challenges faced by the core accretion theory is the formation of massive cores, which requires dust particles the width of a human hair to grow by 12 orders of magnitude into objects that are thousands of km across. Bringing together

small diffuse dust particles into massive gravitating clumps ('planetesimals') is perhaps the biggest theoretical barrier planet formation faces. Dust-gas instabilities that might occur in a protoplanetary disk could lead to the formation of planetesimals. The streaming instability is currently considered the leading contender amongst such mechanisms (Johansen et al., 2007; Youdin & Goodman, 2005). However, planetesimals need to grow further to reach the gigantic masses required to form giant planet cores, either by accreting other planetesimals or by accreting 'pebbles.' Pebbles are dust grains (typically mm-cm sized) that are marginally coupled to the gas, i.e. they are strongly influenced by both gas drag and stellar gravity (Ormel & Klahr, 2010). As a result, they undergo large scale radial drift towards the global pressure maximum (in the absence of local ones) at the center of the disk. Pebble accretion has emerged as a promising mechanism for giant planet core formation due to its rapidity in regions where such cores are expected to form and because it relies on the abundant supply of pebbles that can be sourced from large swaths of the disk (Lambrechts & Johansen, 2012, 2014).

Pebble accretion is thought to be a self-limiting process because when cores become massive enough (i.e. when they reach 'pebble isolation mass'), they create a gas pressure maximum beyond their orbit that traps drifting pebbles and prevents them from reaching the core (Morbidelli & Nesvorný, 2012). If this notion of a pebble isolation mass holds true, it has strong ramifications for the distribution of dust mass available for planet formation, especially in the disk regions interior to the formed core. In Chapter 2 of this thesis, this is precisely what we study to understand why Jupiters at intermediate distances ('cold-Jupiters') are almost always accompanied by inner 'super-Earths' (Bryan et al., 2019; Zhu & Wu, 2018). The correlation between these two planetary populations came as a surprise to the community. The Kepler-167 system serves as a guide in our efforts to understand the coexistence of these planets. By modeling core formation and dust dynamics simultaneously, we show that this correlation is entirely compatible with giant planet core growth by pebble accretion.

In the core accretion framework, the formation of a core is followed by a slow hydrostatic phase of envelope growth during which the core primarily accretes gas from the disk. The accretion rate of the gas is strongly dependent on the mass of the core but has a weak dependence on the local properties of the disk (density and temperature, Lee et al., 2014; Stevenson, 1982a). Importantly, a core's ability to accrete gas is limited by the accreted gas' ability to cool, which

is controlled by the accreted material's opacity (Lee & Chiang, 2015). For the temperatures and densities applicable to planetary envelopes, the opacity of the accreted gas is invariably dominated by its dust content. Dust opacity is determined by grain size distribution, composition, and abundance, i.e. properties that depend on complex physical processes of grain coagulation, fragmentation, and transport. This inevitably appreciates the difficulty of theoretically modeling and predicting gas accretion rates. Nonetheless, advancements that bring our modeling closer to reality are really important to gauge planetary accretion rates and the timescale of planet formation.

The most common methods employed to calculate dust opacity and gas accretion rates in the literature assumed that the dust size distribution as well as the dust-to-gas ratio are akin to that found for dust in the interstellar medium (ISM). This gross simplification significantly eased the calculation and enabled first estimates of planetary envelope accretion rates. However, the deluge of demographic information for exoplanetary systems over the last decade demand a more realistic modeling of the gas accretion process to align observed demographic trends with planet formation models. In Chapter 3, I show that dust dynamics in protoplanetary disks leads to a wide-scale redistribution of dust mass and a radially non-monotonic dust-to-gas ratio. This creates a region at intermediate distances (1-10 au) that is favorable for rapid gas accretion while suppressing gas accretion rates at smaller and larger distances from the star. This remarkable radial variation in gas accretion rates has implications for the observed preponderance of giant planets at intermediate distances (e.g., Fulton et al., 2021) and the envelope mass fractions of sub-Neptunes (e.g., Lopez & Fortney, 2013).

During the gas accretion process, a growing planet may continue to accrete dust in the form of pebbles and planetesimals. Classically, these accreted solids were assumed to travel all the way down to the planetary core and release significant amounts of gravitational potential energy in the process, thereby limiting the gas accretion rate (Pollack et al., 1996). However, recent studies have rightly pointed what was suspected for a long time: incoming solids ablate in the envelope long before they reach the core (Brouwers et al., 2018; Pinhas & Madhusudhan, 2017). This enriches the metal content of the envelope and **if** the envelope is not subsequently mixed up by convective and diffusive processes, the radial metal content of the envelope traces the solid accretion history of a planet (Helled & Guillot, 2018). In general, we expect the solid accretion rate to decline and the gas accretion rate to increase

with time as a planet grows into a gas giant. This would lead to a compositional gradient in the planet's interior, perhaps similar to the ones recently observed in Jupiter's and Saturn's interiors (Mankovich & Fuller, 2021; Wahl et al., 2017).

The solid accretion rate is dependent on the forming planet's location and the solid surface density. Jupiter-like gas giants accumulate such a gargantuan amount of gas that these signatures of solid accretion may get washed out or buried deep in their interiors. However, Neptune-like planets that did not undergo runaway gas accretion are tantalizing targets for studying the effect of their growth environment on their envelope metal content. In Chapter 4, I study the atmospheric composition of the exo-Neptune HAT-P-11b that is a particularly enticing target for atmospheric characterization due to the brightness of its host star and the detection of molecular absorption features in its spectrum. I find that its atmospheric metal content is surprisingly low compared to other exo-Neptunes, which hints at its different formation history and location. The planet's spectrum also contains firm evidence of the presence of aerosols in its atmosphere and I study their likely composition and physical properties to elucidate their nature.

Dust in the form of aerosols has also gained prominence over the last decade due to its ubiquity in planetary atmospheres (Kreidberg et al., 2014b; Sing et al., 2016). The discovery of heavily muted absorption features in atmospheric spectra of numerous planets has led us to suggest the presence of hazes and/or clouds in their atmospheres. In no other type of planet is the case for atmospheric aerosols more compelling than it is for 'super-puffs.' Super-puffs are astrophysical oddities that have super-Earth like masses but giant planet like radii (Jontof-Hutter et al., 2014; Masuda, 2014; Ofir et al., 2014). Their bulk densities (~ 0.1 g/cc) are equivalent to that of cotton candy. Despite such inflated atmospheres, these planets display entirely featureless atmospheric spectra when we would expect them to possess large molecular absorption features (e.g., Libby-Roberts et al., 2020). In addition, the weak gravitational hold of these planets on their envelopes should lead to catastrophic atmospheric mass loss and yet their mature ages defy this expectation (Owen & Wu, 2016; Wang & Dai, 2019).

It seems that aerosols can simultaneously solve both problems by flattening the spectra and making the planet appear less dense than it actually is. This happens because small aerosol particles can get entrained in the planet's outflow and carried to high altitudes (e.g., Gao & Zhang, 2020). In fact, these aerosols probably power the outflow itself by absorbing incoming stellar light and heating up the ambient

gas. In Chapter 5, I discover and study the featureless spectrum of the canonical super-puff Kepler-79d. Furthermore, I show that aerosols can reconcile the ages and mass loss histories of super-puffs as a population. Finally, I conclude in Chapter 6 by tying together dust's role in planet formation and evolution and suggesting promising directions for future research in this area.

KEPLER-167E AS A PROBE OF THE FORMATION HISTORIES OF COLD GIANTS WITH INNER SUPER-EARTHS

2.1 Introduction

The relative rarity of Jupiter analogs around sun-like stars suggests that only $\sim 10\%$ of protoplanetary disks provide the conditions needed for their formation (Cumming et al., 2008; Fulton et al., 2021; Wittenmyer et al., 2016, 2020). In contrast, close-in super-Earths and sub-Neptunes, which are $< 4 R_{\oplus}$ in size, appear to be much more common (30 – 50% occurrence rate for sun-like stars; Batalha et al., 2013; Fressin et al., 2013; Petigura et al., 2018). It was initially thought that distant gas giants and close-in super-Earths were unlikely to occur in the same system, as the growing gas giant planet was expected to prevent the formation of massive inner planets (Izidoro et al., 2015; Ormel et al., 2017). However, there is now growing observational evidence suggesting that cold gas giants are frequently accompanied by inner super-Earths (Bryan et al., 2019; Herman et al., 2019; Zhu & Wu, 2018). This suggests that the same protoplanetary disk properties that allow for the formation of distant giant planets are also compatible with the formation of inner super-Earths, and that the presence of an outer gas giant does not disrupt super-Earth formation. This observed correlation between inner super-Earths and outer giants therefore provides an important constraint on planet formation theories, as they must explain the formation of both types of planets in the same system.

Systems with multiple transiting super-Earths are particularly valuable for testing formation and migration models, as the transit photometry can be used to characterize their mutual inclinations and corresponding dynamical histories (e.g., Masuda et al., 2020). When combined with radial velocity (RV) or transit timing follow up to determine masses, we can additionally measure their average densities and calculate the corresponding masses in solids for these planets (e.g., Dalba et al., 2021; Dubber et al., 2019; Santerne et al., 2019). Transit surveys like *Kepler* (Borucki et al., 2010) and *TESS* (Ricker et al., 2015) are more sensitive than RV surveys (e.g., Howard et al., 2010b; Mayor et al., 2011; Rosenthal et al., 2021) to the presence

of close-in planets in edge-on orbits with masses less than $10 M_{\oplus}$ (Winn, 2018)¹, making it easier to obtain a relatively complete census of the inner regions of these planetary systems. However, the probability of seeing a transit decreases with increasing semi-major axis, and the need to observe multiple transits imposes a hard limit on detectability that is a function of the duration of the survey. To date only the *Kepler* survey has had the sensitivity to detect transiting planets beyond ~ 1 au, and they constitute a tiny fraction of the sample of known transiting planets (Foreman-Mackey et al., 2016; Kawahara & Masuda, 2019; Uehara et al., 2016; Wang et al., 2015). It is therefore quite rare to find transiting outer companions to close-in super-Earths but that may not necessarily indicate that this configuration is rare.

Kepler-167 is unique among the sample of transiting planetary systems detected by Kepler, as it contains three close-in super-Earths accompanied by a confirmed transiting $0.9 R_J$ gas giant planet at 1.9 au (Dalba & Tamburo, 2019; Kipping et al., 2016). However, the measured radius of the outer gas giant is consistent with more than an order of magnitude range in its predicted mass (Stevenson, 1982b), making it difficult to predict its dynamical effect on the inner super-Earths. In §2.2, we present RV observations of the Kepler-167 system collected over 4 years with the HIRES instrument on the Keck telescope. In §2.3, we carry out a joint analysis of the RV and transit data, which we use to place tight constraints on the mass and eccentricity of Kepler-167e. We also derive revised stellar properties using new *Gaia* data and refit the *Kepler* data for the inner super-Earths in order to provide updated radii for these planets. In §2.4, we use Kepler-167e’s measured mass and radius to constrain its bulk metallicity using the methods described in Thorngren & Fortney (2019). Since the super-Earths are not detected in our RV data, we estimate their masses using a non-parametric mass-radius (M-R) relationship (Ning et al., 2018). This allows us to obtain an estimate of the total metal mass contained in the Kepler-167 planets and the corresponding minimum solid mass required to assemble this system.

In §2.5, we examine the implications of these results for the formation history of the Kepler-167 system. We know that the gas giant core must have formed early in order to undergo runaway accretion. In the pebble accretion paradigm, the core grows until it reaches the ‘isolation mass.’ This mass marks the point where the

¹The lower average sensitivity of RV surveys to planets below $10 M_{\oplus}$, which dominate the population of close-in planets, may explain why the correlation between super-Earth and cold Jupiter occurrence rates appears weaker in RV-only samples (Barbato et al., 2018, Rosenthal et al. 2021).

core is massive enough to perturb the gas disk, forming a pressure trap beyond its orbit that effectively halts the accretion of pebbles. This pressure trap also blocks the transport of pebbles to the inner disk (Lambrechts & Johansen, 2014; Morbidelli & Nesvorný, 2012), reducing the reservoir of solids available to form super-Earths (Lambrechts et al., 2019; Ormel et al., 2017). However, pebble accretion is known to be a fairly lossy process (Lin et al., 2018; Ormel, 2017). That is, prior to reaching the isolation mass, a substantial amount of solids can flow past the growing giant planet core.

We use simple dust evolution models (Birnstiel et al., 2010, 2012) to model the growth of the giant planet core in the outer disk and to track the evolution of the solid mass reservoir in the inner disk (Lambrechts & Johansen, 2012; Ormel & Klahr, 2010). We vary the effective pebble flux by changing key disk properties such as initial solid mass and size. This allows us to determine which disks are able to form giant planets, and to quantify the effect that the formation of the outer gas giant has on the amount of dust that reaches the inner disk. We use these models to relate the estimated solid masses of Kepler-167e and the inner super-Earths to the likely properties of its primordial disk. More broadly, we place constraints on the types of disks that can produce systems of inner super-Earths and outer gas giant companions under the pebble accretion paradigm. We summarize our conclusions in §2.6.

2.2 Observations

Archival Photometry

Archival photometry of Kepler-167 exists from the *Kepler* mission (e.g., Borucki et al., 2010), the *Spitzer* spacecraft (Dalba & Tamburo, 2019), and the *Transiting Exoplanet Survey Satellite* mission (*TESS*; Ricker et al., 2015). The transiting planets in this system were initially discovered in the *Kepler* data (Kipping et al., 2016). The *Spitzer* observations specifically targeted a transit of Kepler-167e, but they only spanned part of the transit light curve. While these observations did not improve the precision of Kepler-167e’s transit ephemeris, they did establish that the transit occurred at the expected time. This discovery significantly mitigated some of the uncertainty inherent to long-period exoplanets with only two observed transits, where the existence of transit timing variations (TTVs) can significantly bias initial estimates of the orbital period (e.g., Dalba & Muirhead, 2016; Santerne et al., 2019). Kepler-167 was also observed by *TESS* in Cycle 2 of its primary mission and Cycle 4 of its extended mission.

Our analysis of Kepler-167 archival photometry only uses the *Kepler* data. The *Spitzer* observations mitigate uncertainties in the orbital period due to possible TTVs, but do not improve the precision of the outer planet’s ephemeris when we assume a constant ephemeris. The epochs of the *TESS* photometry span transits of the inner planets but not the outer one. However, *TESS* was designed to survey stars much brighter than Kepler-167 ($V \approx 14$) and the *TESS* observations are too imprecise to improve our constraints on the physical properties of the small inner super-Earths in this system.

The *Kepler* spacecraft observed Kepler-167 during 17 quarters of its primary mission (May 2009 through May 2013). Observations in Quarters 1–8 were long cadence (30 minutes) while those in Quarters 9–17 were short cadence (1 minute). This observation window spanned dozens to hundreds of transits of the three inner planets and two transits of the outer giant planet (Kipping et al., 2016). We accessed the Pre-search Data Conditioning Simple Aperture Photometry (PDCSAP; Jenkins et al., 2010; Smith et al., 2012; Stumpe et al., 2012) through the Mikulski Archive for Space Telescopes² using the `lightkurve`³ package (Lightkurve Collaboration et al., 2018). Although the PDCSAP data are corrected for many sources of systematic noise, we noticed a quasi-periodic variability signal in the corrected photometry for this target that is likely due to stellar rotation. We modeled this signal using Gaussian Process (GP) regression as implemented in the `celerite2`⁴ package built into the `exoplanet`⁵ toolkit (Agol et al., 2020; Foreman-Mackey, 2018; Foreman-Mackey et al., 2017, 2021; Luger et al., 2019). We fit the long and short cadence data with quasi-periodic kernels of different widths but the same period. We determined the *maximum a posteriori* parameters for the GP (see Section 2.5) with a numerical optimization method (Salvatier et al., 2016). Then, we subtracted the GP signal from the long and short cadence data before fitting for the transits.

Keck-HIRES Spectroscopy

We obtained spectroscopic observations of Kepler-167 using the high-resolution echelle spectrometer (HIRES; Vogt et al., 1994) on the Keck I telescope at the W. M. Keck Observatory. We first processed a moderate signal-to-noise (S/N) ratio (40) reconnaissance spectrum with `SpecMatch`⁶ (Petigura, 2015; Petigura et al., 2017b).

²<https://archive.stsci.edu/>

³<https://docs.lightkurve.org/>

⁴<https://celerite2.readthedocs.io/en/latest/>

⁵<https://docs.exoplanet.codes/>

⁶<https://github.com/petigura/specmatch-syn/>

Table 2.1: RV measurements of Kepler-167.

BJD _{TDB}	RV (m s ⁻¹)	S _{HK}
2457988.955812	6.1±7.2	0.195±0.001
2458300.972784	16.1±7.0	0.248±0.001
2458328.854650	22.6±7.0	0.235±0.001
2458363.864254	6.3±7.2	0.267±0.001
2458385.796973	18.1±7.2	0.149±0.001
2458645.987639	-11.8±7.3	0.239±0.001
2458662.992470	-26.3±7.0	0.236±0.001
2458710.986137	-24.2±8.0	0.167±0.001
2458797.818538	-23.2±8.1	0.148±0.001
2459072.003261	5.6±7.3	0.168±0.001
2459101.942839	2.1±7.2	0.166±0.001
2459118.833084	14.4±7.1	0.186±0.001
2459187.714084	29.9±7.3	0.247±0.001

This spectrum was originally acquired for the Kepler-167 discovery effort (Kipping et al., 2016) and processed with the Stellar Parameter Classification pipeline (SPC; Buchhave et al., 2012). The stellar properties that we obtain from SpecMatch are in close agreement with those published by Kipping et al. (2016). Specifically, the stellar metallicity ([Fe/H]), effective temperature (T_{eff}), and projected rotational velocity ($v \sin i$) are -0.02 ± 0.09 dex, 4830 ± 100 K, and 2.0 ± 1.0 km s⁻¹, respectively.

We acquired 13 additional spectra between 2017 August 23 and 2020 December 4 with S/N ranging between 40–52. In these observations, the starlight was passed through a heated iodine cell in order to allow us to obtain a more precise wavelength calibration. Owing to the faintness of Kepler-167 ($V \approx 14$), we did not utilize a high S/N template spectrum for our radial velocity analysis, and instead substituted a best-match template from another star (HD 16160, $T_{\text{eff}} = 4720 \pm 110$ K, $\log g = 4.57 \pm 0.10$, [Fe/H] = -0.02 ± 0.09) in the HIRES spectral library (Dalba et al., 2020; Yee et al., 2017). Aside from the template substitution, the data reduction and Doppler analysis followed the standard procedures of the California Planet Search (Howard & Fulton, 2016; Howard et al., 2010a). This analysis produced RV measurements of Kepler-167 with a median internal precision of 3–5 m s⁻¹. We then added an additional 6.2 m s⁻¹ error in quadrature, which is a conservative estimate of the average uncertainty incurred by the match–template technique (Dalba et al., 2020). The resulting individual RV measurements are listed in Table 2.1. We also include the corresponding S_{HK} activity indicators derived from the Ca II H and K

spectral lines (Isaacson & Fischer, 2010; Wright et al., 2004). We see no evidence for any covariance between the measured radial velocities and this activity indicator.

Constraints on companion properties

High resolution images from UK Infrared Telescope Survey and Keck NIRC2 reveal the presence of a companion 2" to the NE of Kepler-167 (Kipping et al., 2016). This companion is ~ 5 magnitudes fainter than Kepler-167 in the *Kepler* bandpass. Kipping et al. (2016) could not establish whether this companion is bound to Kepler-167. However, the parallax ($\Delta\varpi = 0.15 \pm 0.22$ mas) and proper motion ($\Delta\mu_{ra} = 0.43 \pm 0.27$ mas yr $^{-1}$, $\Delta\mu_{dec} = 1.2 \pm 0.3$ mas yr $^{-1}$) measurements from *Gaia* DR3 for these two sources agree to within the uncertainties (Gaia Collaboration et al., 2021), thus indicating that they are co-moving. The companion has a spectral type of M4V and is $\sim 0.2 M_{\odot}$, which is consistent with the J–K color measured in Kipping et al. (2016). Given the large separation of 2" (~ 700 au, $P > 15,000$ yrs) and the small stellar mass, the companion’s effect on the RVs is negligible. Additionally, although the companion’s light contaminates the *Kepler* light curves, its effect on the measured planetary radii is insignificant. The companion is 100 times fainter than Kepler-167 in the *Kepler* bandpass and thus the true radii of Kepler-167’s planets are only $\sqrt{1.01/1} = 1.005$ larger than our measurements (Ciardi et al., 2015). This effect is an order of magnitude smaller than our uncertainties on the radii.

2.3 Model Fitting and Parameter Estimation

The combined *Kepler* data set for Kepler-167 system contains over 100,000 individual data points measuring signals from four separate transiting planets. When combined with the complexity of a model combining stellar, RV, and transit data, this data volume makes it computationally intractable to fit a single joint model. Instead, we separated the modelling of this system into three parts: the stellar parameters, the long period gas giant Kepler-167e, and the three inner super-Earths.

We first determined the stellar parameters by fitting archival photometry of Kepler-167 from the *Gaia* (Gaia Collaboration et al., 2018), 2MASS (Cutri et al., 2003), and WISE (Cutri et al., 2014) surveys with a model spectral energy distribution to constrain the stellar properties. We employed the EXOFASTv2 modelling suite (Eastman et al., 2013, 2019) to conduct this fit. The fit included the MESA Isochrones and Stellar Tracks (MIST) stellar evolution models (Choi et al., 2016; Dotter, 2016; Paxton et al., 2011, 2013, 2015), which provided constraints on the stellar mass and age. We placed normal priors on [Fe/H] (-0.02 ± 0.09) and T_{eff} (4830 ± 100 K) from

Table 2.2: Median values and 68% confidence intervals for the stellar parameters for Kepler-167.

Parameter	Description	Values
Informative Priors:		
T_{eff}	Effective Temperature (K)	$\mathcal{N}(4830, 100)$
[Fe/H]	Metallicity (dex)	$\mathcal{N}(-0.02, 0.09)$
ϖ	Parallax (mas)	$\mathcal{N}(2.944, 0.018)$
A_V	V-band extinction (mag)	$\mathcal{U}(0, 0.4204)$
Stellar Parameters from SED-only fit:		
M_*	Mass (M_\odot)	$0.777^{+0.034}_{-0.031}$
R_*	Radius (R_\odot)	0.749 ± 0.020
L_*	Luminosity (L_\odot)	$0.289^{+0.017}_{-0.020}$
F_{Bol}	Bolometric Flux (cgs)	$8.02 \times 10^{-11} \begin{matrix} +4.7 \times 10^{-12} \\ -5.7 \times 10^{-12} \end{matrix}$
ρ_*	Density (cgs)	$2.60^{+0.23}_{-0.20}$
$\log g$	Surface gravity (cgs)	$4.579^{+0.027}_{-0.025}$
T_{eff}	Effective Temperature (K)	4884^{+69}_{-75}
[Fe/H]	Metallicity (dex)	0.020 ± 0.067
[Fe/H] ₀	Initial Metallicity ^a	$0.024^{+0.069}_{-0.067}$
Age	Age (Gyr)	$7.1^{+4.4}_{-4.6}$
EEP	Equal Evolutionary Phase ^b	339^{+12}_{-28}
A_V	V-band extinction (mag)	$0.277^{+0.098}_{-0.13}$
σ_{SED}	SED photometry error scaling	$1.23^{+0.48}_{-0.32}$
ϖ	Parallax (mas)	2.945 ± 0.018
d	Distance (pc)	339.6 ± 2.1

Notes.

See Table 3 in Eastman et al. (2019) for a detailed description of all parameters and all default (non-informative) priors beyond those specified here. $\mathcal{N}(a, b)$ denotes a normal distribution with mean a and variance b^2 . $\mathcal{U}(a, b)$ denotes a uniform distribution over the interval $[a, b]$.

^aInitial metallicity is that of the star when it formed.

^bCorresponds to static points in a star’s evolutionary history. See Section 2 of Dotter (2016).

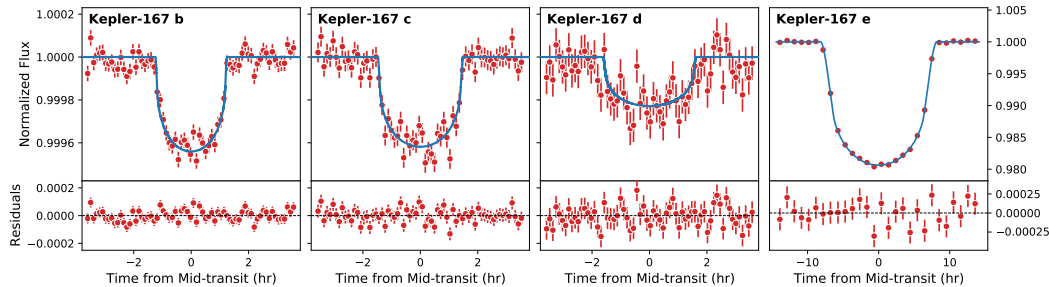


Figure 2.1: Optical *Kepler* transit photometry of the four Kepler-167 planets folded on their best fit ephemeris along with their best fit models (blue). Note the difference in scale in the panel for Kepler-167e. The data (red) are shown in bins of 10 minutes for the inner planets and 1 hour for the outer planet, although we note that the models were fit to the unbinned data.

the SpecMatch analysis of the HIRES iodine-free spectrum (Section 2.2) and an upper limit on the line-of-sight extinction ($A_V < 0.4204$) from galactic reddening maps (Schlafly & Finkbeiner, 2011). The parallax of Kepler-167 as measured by *Gaia* Early Data Release 3 (Gaia Collaboration et al., 2021) and corrected according to Lindegren et al. (2021) is 2.944 ± 0.018 mas, which we applied as a normal prior in the fit. We also enforced a noise floor of 2% on the bolometric flux as suggested by Tayar et al. (2020). We checked that this fit met the default criteria for convergence in EXOFASTv2, which includes at least 1,000 independent draws from the posterior and a Gelman–Rubin statistic below 1.01 for each parameter. The resulting stellar parameters and their corresponding priors are summarized in Table 2.2. All of our stellar parameters are consistent with those derived by Kipping et al. (2016) to the 2σ level. We inflated the widths of the uncertainties on the stellar mass and radius priors to 5% and 4%, respectively, prior to using these values to calculate absolute planetary parameters. This inflation accounts for systematic uncertainty floors set by imperfect models of stellar evolution Tayar et al. (2020).

Second, we conducted a joint fit of the Keck-HIRES RVs and the two *Kepler* transits of Kepler-167e using *exoplanet* (Foreman-Mackey et al., 2021). We allowed for orbital eccentricity and a long-term acceleration (slope) in the RV. For the long-cadence photometry, we numerically integrated the transit model over the appropriate time bin in order to account for the effect of these longer integrations on the shape of the transit light curve. We checked for convergence using both the effective sample size and the Gelman–Rubin statistic, which we required to be greater than 1,000 and less than 1.01 for all parameters, respectively. The resulting parameters and models are provided in Table 2.3 and Figures 2.1 and 2.2.

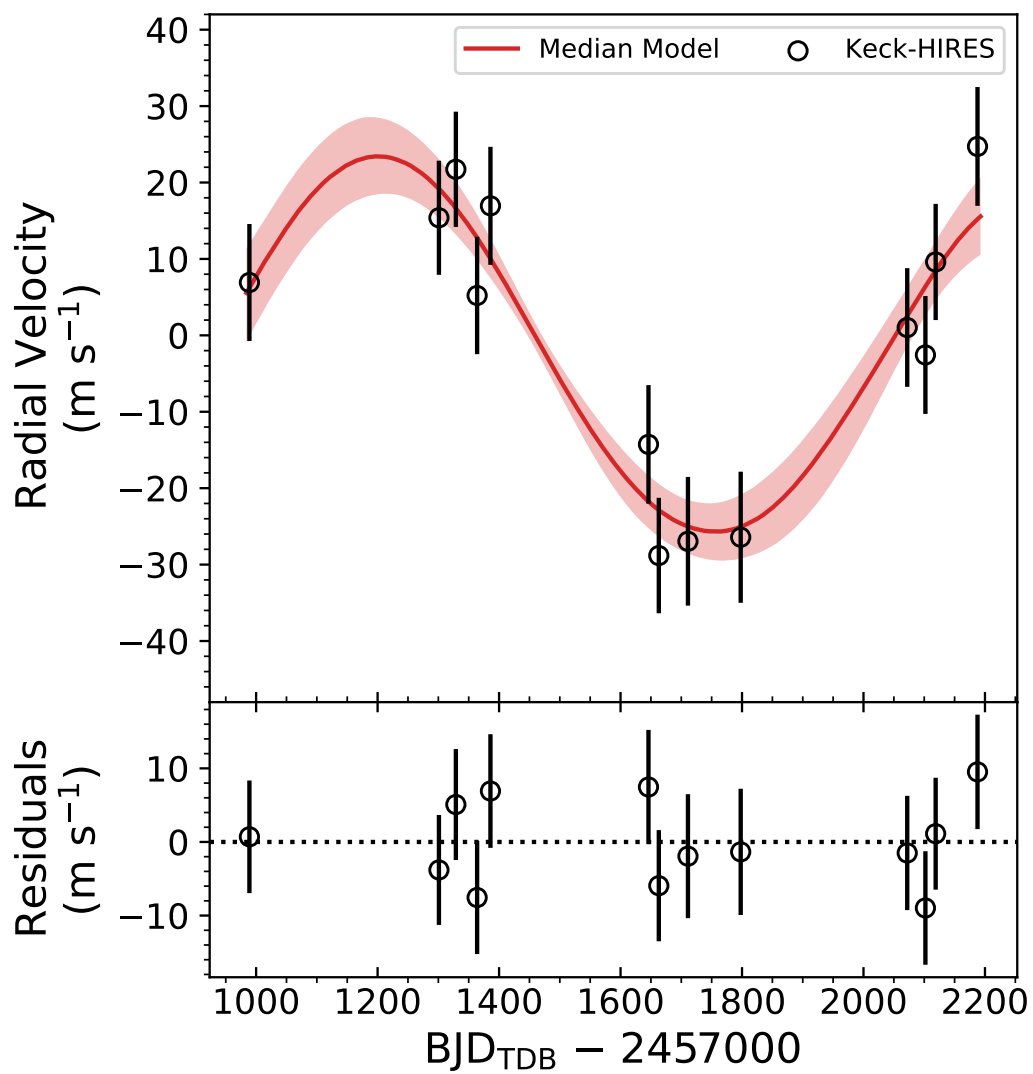


Figure 2.2: Keck-HIRES RV time series data with the median model for Kepler-167e and the corresponding 68% credible interval overplotted.

Table 2.3: Median values and 68% confidence interval of the parameters for each of the Kepler-167 planets.

Parameter	Description	Values
Planetary Parameters:		
P	Period (days)	$1071.23205^{+0.00059}_{-0.00058}$
T_C	Time of conjunction (BJD _{TDB})	$2455253.28756 \pm 0.00039$
R_P	Radius (R_E)	10.16 ± 0.42
a	Semi-major axis (au)	1.883 ± 0.027
i	Inclination (Degrees)	$89.9720^{+0.0069}_{-0.0079}$
b	Transit impact parameter	$0.271^{+0.051}_{-0.073}$
Depth	Transit depth	$0.01540^{+0.00027}_{-0.00032}$
T_{eq}	Equilibrium temperature ^a (K)	134.4 ± 4.0
e	Eccentricity ^b	< 0.29
ω_*	Argument of Periastron (rad)	$-0.4^{+2.0}_{-1.9}$
K	RV semi-amplitude ($m s^{-1}$)	$23.7^{+3.7}_{-3.5}$
M_P	Mass (M_J)	$1.01^{+0.16}_{-0.15}$
ρ_P	Density ($g cm^{-3}$)	$1.68^{+0.34}_{-0.33}$
$\dot{\gamma}$	RV slope ($m s^{-1} day^{-1}$)	$-0.0049^{+0.0068}_{-0.0066}$
Kepler Parameters:		
u_1	Linear limb-darkening coefficient	$0.616^{+0.036}_{-0.034}$
u_2	Quadratic limb-darkening coefficient	0.126 ± 0.096
Keck-HIRES Parameters:		
γ_{rel}	Relative RV Offset ($m s^{-1}$)	$-2.49^{+0.95}_{-0.92}$
σ_J	RV Jitter ($m s^{-1}$)	$3.1^{+2.5}_{-1.6}$
Notes.		
^a Initial metallicity is that of the star when it formed.		
^b Corresponds to static points in a star's evolutionary history. See Section 2 of Dotter (2016).		

Finally, we conducted a separate fit to the transit photometry of the inner three planets in the Kepler-167 system. In order to simplify the fit and reduce the convergence time, we fixed the orbital eccentricity of these planets to zero. This is likely a valid assumption for Kepler-167 b and c, which both orbit within 0.1 au and have either been tidally circularized or have a sufficiently low eccentricity that the effect on the transit shape is negligible (e.g., Mills et al., 2019). However, Kepler-167d is far enough from these two planets to maintain some orbital eccentricity. Using the same *Kepler* data set, Kipping et al. (2016) demonstrated an upper limit on eccentricity of 0.12. This indicates that there is no detectable deviation from the expected transit shape for a circular orbit in the *Kepler* photometry, and we therefore should not introduce any additional error by fixing this planet’s eccentricity to zero in our fits. As in the previous fit, we numerically integrated the model to account for the integration time when fitting the long cadence data.

We applied the priors on limb darkening parameters from our fit to the Kepler-167e photometry, which has a much higher SNR than that of the inner super-Earths. We again gauged convergence with the effective sample size and the Gelman-Rubin statistic, for which we achieved $>1,000$ and <1.01 for all parameters. The best fit models are shown along with the transit and RV data in Figures 2.1 and 2.2, respectively. The resulting planetary parameters are listed in Table 2.3. All of the shared planetary parameters between our work and that of Kipping et al. (2016) are consistent at the 2σ level. We note that the median values of all of the planetary radii are slightly larger than those from Kipping et al. (2016) owing to the increase in stellar radii derived from the updated *Gaia* parallax.

2.4 A Closer Look at the Kepler-167 Planets

Kepler-167e in the context of other cold giants

Our new radial velocity observations allow us to detect the radial velocity signal from Kepler-167e with high statistical significance (6σ). We find a measured mass of $1.01 \pm 0.16 M_J$ and a 3σ upper limit of 0.29 for the orbital eccentricity. This new mass measurement for Kepler-167e allows us to place it in the context of the broader population of long-period gas giant planets ($> 0.5 M_J$) from radial velocity surveys. We focus our comparison on the sample of planets detected in the California Legacy Survey (CLS, Rosenthal et al., 2021), shown in Figure 2.3. Although there have been several other long-term radial velocity surveys capable of detecting Jupiter analogs (e.g., Rowan et al., 2016; Wittenmyer et al., 2016, 2020), the CLS includes data sets for more than seven hundred stars with baselines spanning close to three

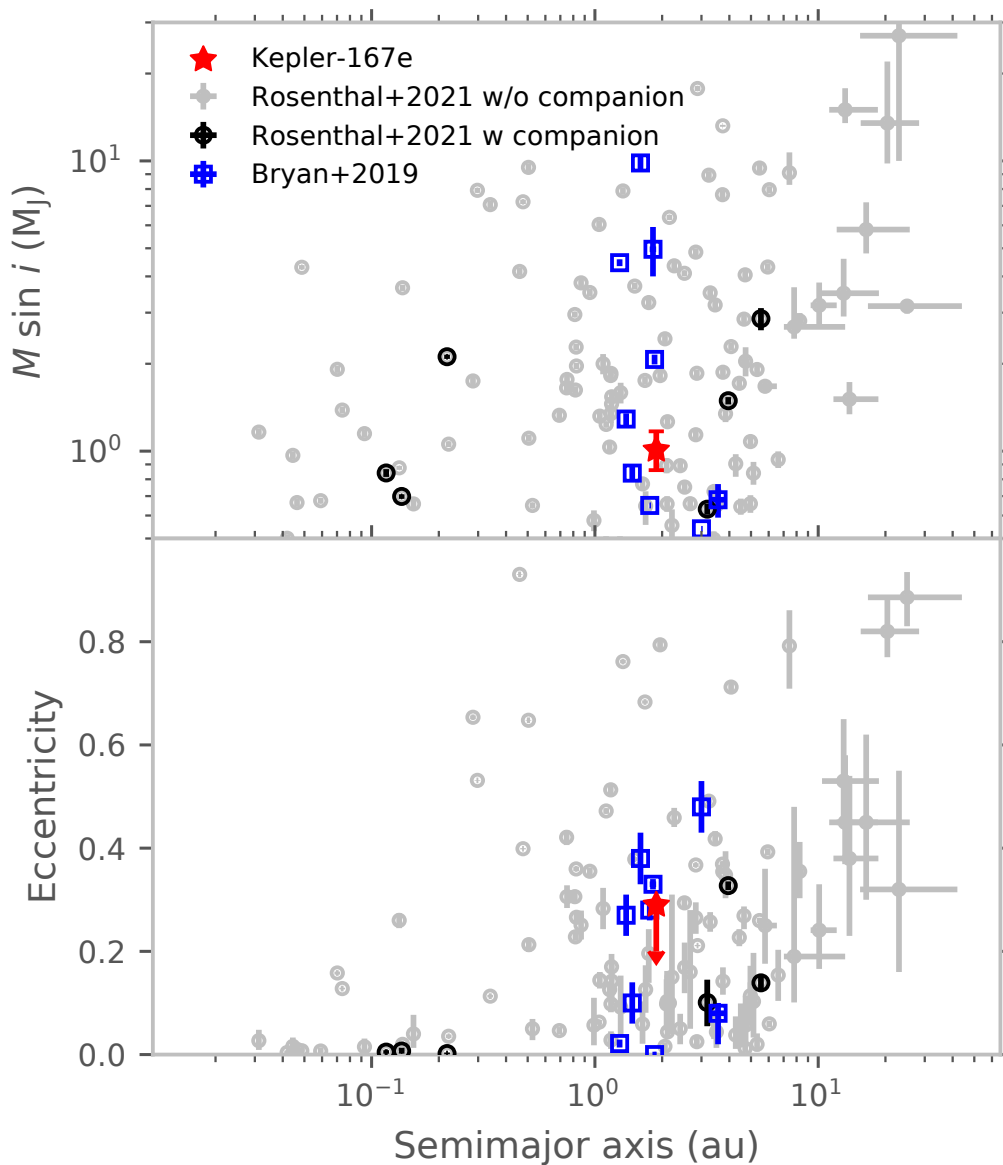


Figure 2.3: Planet mass and eccentricity vs semimajor axis for planets more massive than $0.5 M_J$ in the California Legacy Survey sample (Rosenthal et al., 2021). Giant planets in this sample are shown in two different colors, depending on whether or not they have a detectable inner companion less than $0.1 M_J$. We also plot resolved giant planet companions of super-Earths systems studied in Bryan et al. (2019). Kepler-167e is marked in red (3σ upper limit for eccentricity) and has properties that are typical of long period giant planets.

decades, making it one of the largest and most complete surveys for Jupiter analogs published to date. This allows us to obtain a (relatively) unbiased sample of long period gas giant planets both with and without inner super-Earth companions. We mark giant planets from the Rosenthal et al. (2021) sample that harbor an inner companion ($< 0.1 M_J$) in black. We additionally supplement this sample with the set of (RV) giant planet companions to transiting super-Earths with resolved orbits in Bryan et al. (2019). Although Bryan et al. (2019) had much better sensitivity to small inner companions compared to CLS, the systems in their sample have shorter RV baselines and the companion orbits are therefore biased towards shorter orbital periods than in the CLS sample.

We find that the mass and eccentricity of Kepler-167e are fairly typical of other long period giant planets, both with and without detected inner super-Earths. Despite the faintness of the host star and the relative sparseness of our radial velocity data, our joint fit with transit data results in constraints on mass and eccentricity that are comparable in precision to those of the non-transiting planets detected in these RV surveys. We find that the sample of radial velocity planets span a wide range of masses at Kepler-167e’s location, although these data are relatively insensitive to planets smaller than $\sim 0.5 M_J$ (Rosenthal et al., 2021) at these large separations. While Kepler-167e’s mass may be typical of planets at these separations, it appears to have a relatively low orbital eccentricity. Although it is possible that a higher orbital eccentricity might have destabilized the system of inner super-Earths, we note that there are multiple examples of eccentric gas giants in the Bryan et al. (2019) sample with inner transiting super-Earths.

The fact that Kepler-167e also transits its host star provides us with a unique opportunity to use its measured mass, radius, and age to constrain its bulk metallicity and absolute metal content. Since Kepler-167e has a mass that is indistinguishable from that of Jupiter but is 10% smaller than Jupiter in radius, we can immediately surmise that the planet has a higher bulk metal content. We use the giant planet interior structure and evolution model described in Thorngren et al. (2016) and Thorngren & Fortney (2019) to quantify the corresponding bulk metallicity for Kepler-167e. In this approach, a Bayesian statistical model is used to infer a planet’s bulk metallicity from its mass, age, and radius. The planetary mass and age observations are used as priors and the planetary radius is the independent measurement that yields an estimate of the bulk metallicity. For more details on the giant planet interior structure model and the Bayesian method used to make these inferences, we refer

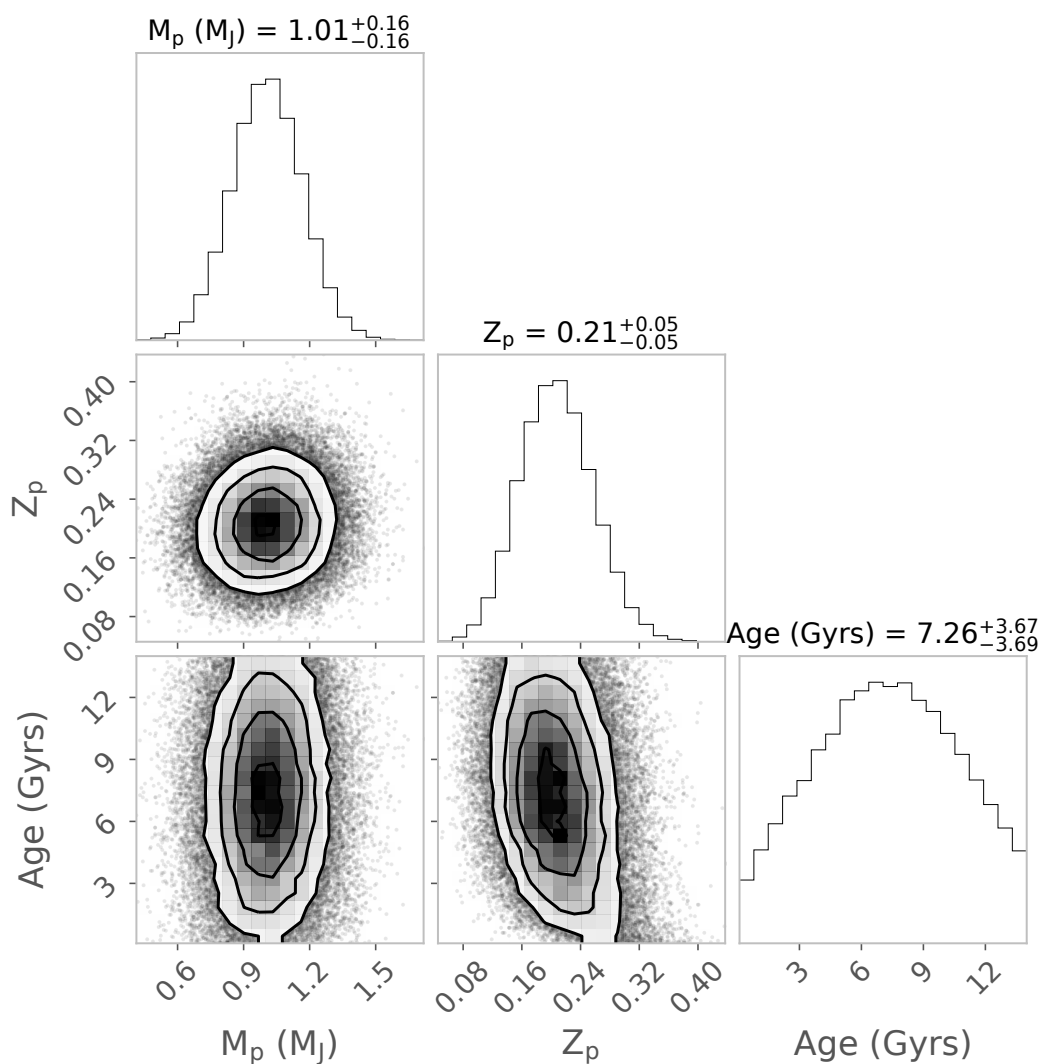


Figure 2.4: Posterior probability distribution for bulk metallicity and its covariance with the observational priors on planetary mass and age. Kepler-167e’s radius, mass, and age are used to infer its bulk metal content from planetary evolution modeling as described in Thorngren et al. (2016) and Thorngren & Fortney (2019).

the reader to Thorngren & Fortney (2019). The only difference between the models described there and the ones used here is that we updated the equation of state for hydrogen and helium to the one given in Chabrier et al. (2019). Figure 2.4 shows the resulting posterior probability distribution for bulk metallicity and its covariance with the observational priors on planetary mass and age.

With a bulk metallicity of 0.21 ± 0.05 , Kepler-167e is significantly enriched in metals relative to its host star, which has a metallicity $[\text{Fe}/\text{H}]$ of 0.02 ± 0.07 (bulk metallicity $Z_* = 0.015 \pm 0.003$ assuming solar $Z = 0.014$, Asplund et al., 2009). A bulk metallicity of 0.21 ± 0.05 and planet mass of $1.01^{+0.16}_{-0.15} M_J$ translates to an absolute metal content of $66^{+20}_{-18} M_\oplus$. Kepler-167e has a bulk metallicity that is fairly typical for gas giants planets in this mass range: transiting planets with measured bulk metallicities in the mass range $0.85 - 1.17 M_J$ have a median bulk metallicity of 0.22 (Thorngren & Fortney, 2019). Although we cannot tell how the metals are partitioned between the core and the envelope, the total metal content of the planet nonetheless provides a useful constraint on the solid inventory of the disk that Kepler-167e formed in. We discuss the implications of this measurement in more detail in §2.5.

To date, only four other transiting giant planets with orbital periods > 200 days have precisely measured masses: the circumbinary planets Kepler-16b (Doyle et al., 2011) and Kepler-34b (Welsh et al., 2012), Kepler-1514b (Dalba et al., 2020), and Kepler-1704b, (Dalba et al., 2021). Amongst the planets around single stars, Kepler-1704b is a massive giant ($4.15 M_J$) on a highly eccentric ($e = 0.92$) orbit and therefore unlikely to harbor any undetected inner companions. Kepler-1514b is also quite massive ($5.3 M_J$) and has a high eccentricity ($e = 0.4$), but it is accompanied by a single transiting inner super-Earth. Kepler-167e is only planet in this sample that has multiple transiting inner super-Earths. Both Kepler-1514b ($1.11 \pm 0.02 R_J$) and Kepler-1704b ($1.07 \pm 0.04 R_J$) are larger than Jupiter in size and therefore their bulk metallicities ($0.06^{+0.03}_{-0.02}$ and 0.12 ± 0.04 , respectively) are lower than Kepler-167e's. However, given their large masses, the bulk metallicities of Kepler-1514b and Kepler-1704b translate to $\sim 100 M_\oplus$ and $\sim 160 M_\oplus$, respectively, in absolute metal content.

How massive are the inner super-Earths?

Our radial velocity data set has relatively sparse sampling, and is therefore not very sensitive to the radial velocity signals of the three inner super-Earths. We quantify

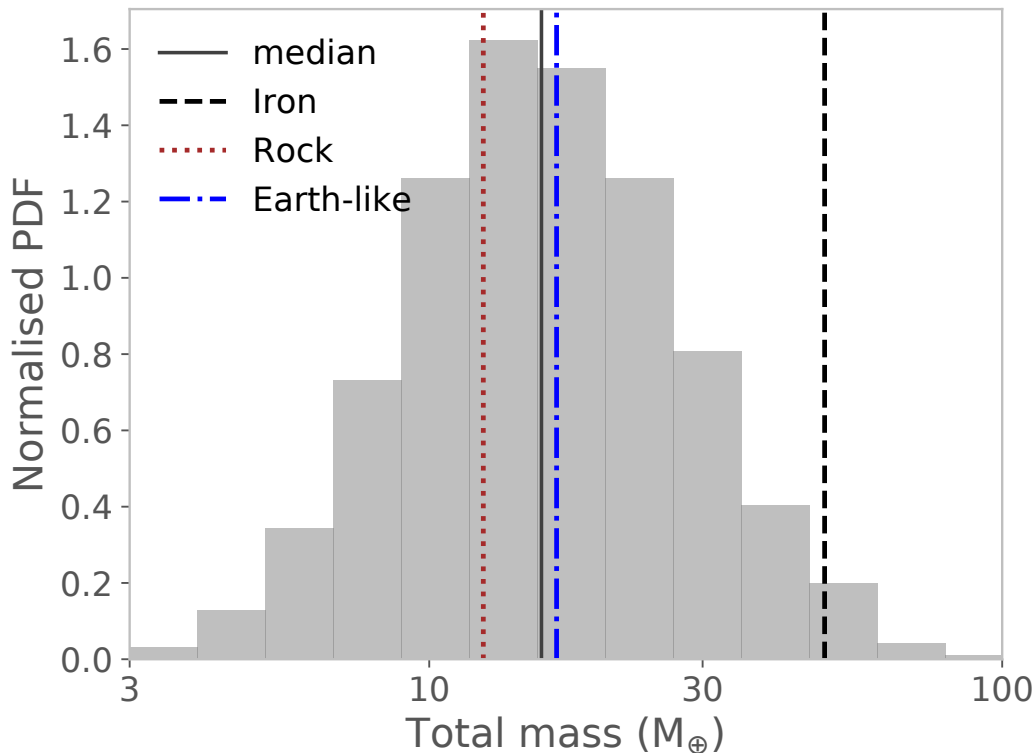


Figure 2.5: Posterior for the total mass contained in the three inner super-Earths obtained using `mr-exo` (Kanodia et al., 2019), which utilizes the mass-radius relationship from Ning et al. (2018). The median of the distribution is shown with a grey line. We also mark the total mass contained in three planets assuming they are pure rock (MgSiO_3 , brown), iron (black), or Earth-like (blue) using the median radii of these planets from Table 3 and M-R relations from Zeng et al. (2019).

the expected RV semi-amplitudes for each planet by using the non-parametric mass-radius (M-R) relationship for *Kepler* planets from Ning et al. (2018) to calculate predicted masses for these planets using their measured radii. We use the `mr-exo` package to obtain posteriors for the masses of the super-Earths using normal distributions for the radii with mean values and distribution widths from Table 2.3 (Kanodia et al., 2019; Ning et al., 2018). The predicted planet masses for Kepler-167 b, c, and d are $4.5^{+6.5}_{-2.6} M_{\oplus}$, $4.4^{+6.3}_{-2.6} M_{\oplus}$, and $3.6^{+5.2}_{-2.1} M_{\oplus}$ respectively. These uncertainties are dominated by the relatively large measurement errors and correspondingly large intrinsic scatter for planets with measured masses in this size range. For median mass estimates of these three planets, we would expect RV semi-amplitudes of 2.1 m s^{-1} , 1.7 m s^{-1} , and 1.0 m s^{-1} , respectively, which are well below the noise floor of our data.

In order to comment on the solid budget required to form the inner super-Earths, we also need to estimate the total amount of solids contained in these planets. In Figure 2.5, we show the posterior for the total mass contained in the three planets ($15.7^{+11.6}_{-6.5} M_{\oplus}$) as well as total mass estimates for median planetary radii assuming they are made of pure rock or pure iron (Zeng et al., 2019). The measured radii and orbital periods of these planets place them at or below the location of the radius valley (Fulton et al., 2017). It is therefore unlikely that they host significant hydrogen-rich envelopes (Ma & Ghosh, 2021; Owen & Wu, 2017; Rogers, 2015). The $15 M_{\oplus}$ peak of the posterior probability distribution is equivalent to the predicted value for Earth-like rock-iron compositions, and we therefore adopt it as our baseline value for all subsequent calculations. How does this mass compare with the solid mass budget in the inner disk? Since disk density profiles are poorly constrained by observations, we use the Minimum Mass Solar Nebula (MMSN) and Minimum Mass Extrasolar Nebula (MMEN) as baselines to estimate the dust content of the inner disk (Chiang & Laughlin, 2013; Chiang & Youdin, 2010; Dai et al., 2020). The MMSN and MMEN predict $7 M_{\oplus}$ and $36 M_{\oplus}$ of solids within the orbit of the giant planet, respectively. Even in the more optimistic MMEN, the formation of Kepler-167’s super-Earths would require dust to be converted to planets with a fairly high efficiency of 40%. The predicted efficiency of converting dust to super-Earths by either pebble accretion or planetesimal accretion is expected to be 10 – 20% instead (Drażkowska et al., 2016; Lenz et al., 2020; Liu & Ormel, 2018; Ormel & Liu, 2018). Moreover, dust in the inner disk is likely to drift into the star on very short timescales. This suggests that the initial solid budget of the inner disk was very likely supplemented by the addition of small solids from regions exterior to Kepler-167e’s orbit, which could have migrated inward via radial drift. We explore this scenario in more detail below.

2.5 Formation of Inner Super-Earths with Outer Gas Giant Companions

We use our observational constraints on the properties of the Kepler-167 planets to explore potential formation scenarios for this system. In particular, we are interested in how the presence of a growing giant planet core affects the dust distribution in the disk, since the dust content of the inner disk determines the potential for close-in super-Earth formation. For the giant planet core, we assume that it grows by accreting the marginally coupled ‘pebbles.’ In the pebble accretion paradigm, the growth of the giant planet core depends on the pebble flux through the disk and a threshold pebble flux is typically required to form a sufficiently large core prior to the

dispersal of the gas disk (e.g., Bitsch et al., 2019). We do not consider planetesimal accretion for the formation of the cold giant planet’s core (e.g., Schlecker et al., 2020) because it is highly inefficient at the relevant orbital distances unless planetesimals are assumed to be small and turbulent stirring is assumed to be very weak (Johansen & Bitsch, 2019). For the inner super-Earths, both pebble and planetesimal accretion appear to be feasible. However, super-Earths progenitors are likely to dynamically evolve and merge after reaching pebble/planetesimal isolation masses (Dawson et al., 2016; Lambrechts et al., 2019), which significantly complicates their formation modeling. We therefore do not model their formation explicitly and instead impose the condition that the amount of solids that reaches the inner disk must be sufficient to form a system of close-in super-Earths (see § 2.5).

In order to understand the formation of the Kepler-167 system, we must therefore first understand the dynamical evolution of solids throughout the disk, which determines the local pebble flux. These pebbles could be directly accreted by the growing protoplanet, or could form planetesimals. The pebble flux is very sensitive to the assumed protoplanetary disk properties such as disk mass, size, metallicity, and turbulence as well as material properties such as the fragmentation velocity of grains (e.g., Drażkowska et al., 2021). Since our knowledge of these properties is incomplete, we explore a broad parameter space of potential disk models. Although these models are motivated by a desire to explain the origin of the Kepler-167 system, we do not make any star-specific assumptions other than the stellar mass. This means that the models presented here are broadly applicable to all sun-like stars.

Protoplanetary disk model

We utilize a simple two-population dust evolution model (Birnstiel et al., 2012) as implemented in the publicly available `twopoppy` code⁷ to determine which disks are most conducive for giant planet core formation and to calculate the amount of solids that reaches the inner disk. This model is described in Birnstiel et al. (2012), which demonstrates that the dust evolution in state of the art numerical simulations is well approximated by splitting the dust population into two groups: one with a spatially and temporally constant size a_0 (assumed monomer size = $0.1 \mu\text{m}$, corresponding to the mass-weighted average of the grains in the interstellar medium, e.g., Laor &

⁷The original code is available at <https://github.com/birnstiel/two-pop-py> and a modified version used in this paper is available at <https://github.com/y-chachan/two-pop-py/tree/kepler-167>.

Draine, 1993) and surface density Σ_0 and the other with size a_1 and surface density Σ_1 . The size of the larger grains (a_1) is set by growth, drift, and fragmentation and varies as a function of time and location in the disk. This approach allows us to model the dust evolution with a simple advection-diffusion equation:

$$\frac{\partial \Sigma_d}{\partial t} + \frac{1}{r} \frac{\partial}{\partial r} \left[r \left(\Sigma_d \bar{u} - D_{\text{gas}} \Sigma_g \frac{\partial}{\partial r} \left(\frac{\Sigma_d}{\Sigma_g} \right) \right) \right] = \dot{\Sigma}_d. \quad (2.1)$$

where r is the cylindrical distance from the star, $\Sigma_d = \Sigma_0 + \Sigma_1$, \bar{u} is the mass weighted velocity of dust grains in the radial direction, Σ_g is the gas density, D_{gas} is the diffusivity of the gas, and $\dot{\Sigma}_d$ is the sink term due to accretion of dust by a growing core. $\dot{\Sigma}_d$ is related to the pebble accretion rate, which is discussed in more detail in § 2.5.

The gas disk is assumed to evolve viscously according to the equations in Lynden-Bell & Pringle (1974) and its initial surface density profile is derived from the self-similar solution to these equations at time $t = 0$. The radial dependence of the density profile is set by the power law exponent p of viscosity ν , which we fix at unity. The viscosity ν is calculated as $\alpha_t c_s H_g$, where α_t is the Shakura-Sunyaev turbulence parameter (Shakura & Sunyaev, 1973), c_s is the sound speed, and H_g is the gas scale height. The turbulence parameter α_t and the fragmentation velocity v_{frag} of the grains determine the Stokes number of the largest grains, which is given by $\text{St}_{\text{frag}} = v_{\text{frag}}^2 / 3\alpha_t c_s^2$, in fragmentation-limited regions of the disk. Since we are primarily interested in understanding the effect of giant planet core formation on the dust flux in the inner disk, we fix $\alpha_t = 10^{-3}$ and $v_{\text{frag}} = 10 \text{ m s}^{-1}$ to reduce the number of free parameters. Although the values of v_{frag} and α_t are both uncertain, these values are reasonably well supported by the literature (e.g., Flaherty et al., 2017; Gundlach & Blum, 2015; Pinte et al., 2016). This combination of values also ensures that giant planet cores can reach the pebble isolation mass prior to the dispersal of the gas disk. If we wished to form cores in disks with lower values of v_{frag} , it would require a correspondingly lower α_t (e.g., Venturini et al., 2020).

We explore models for gas disks with characteristic radii of $R_{\text{disk}} \in \{20, 60, 200\}$ au, masses $M_{\text{disk}} \in \{0.05, 0.1, 0.2\} M_*$, and metallicities $Z \in \{0.005, 0.01, 0.02\}$. This allows us to quantify how the pebble flux and the growth rate of the giant planet core vary as a function of each disk parameter. Although we vary M_{disk} and Z as separate model parameters, our results are primarily presented in terms of $M_{\text{dust}} = Z M_{\text{disk}}$, as this quantity plays an important role in controlling the outcome of our models. We fix the mass of the central star to $0.75 M_\odot$, which is representative

of Kepler-167. We calculate the temperature profile of the disk by assuming that it is passively irradiated (e.g., Chiang & Goldreich, 1997; D’Alessio et al., 1998); this is a reasonable approximation at the location of our giant planet progenitors (see § 2.5):

$$T(r) = \left[\phi T_*^4 \left(\frac{R_*}{r} \right)^2 + T_0^4 \right]^{1/4} \quad (2.2)$$

with a flaring angle $\phi = 0.05$, $T_* = 4180$ K, $R_* = 2.126 R_\odot$, and $T_0 = 7$ K. We obtain the stellar temperature and radius from a MIST model for a $0.75 M_\odot$ star at an age of 1 Myr. Although the inner regions of the disk where super-Earths might form are likely to be viscously heated, this has no effect the *integrated* pebble flux that reaches the inner disk from the outer disk.

Core formation with pebble accretion

To model the formation of a gas giant core, we introduce a seed of mass $0.01 M_\oplus$ at time t_{seed} , which then grows by accreting solids that drift past its location. Although this initial seed mass is somewhat larger than the predicted masses of planetesimals formed by the streaming instability, this choice allows us to circumvent potential complications related to the unknown initial planetesimal distribution and early growth rates of small planetesimals (Johansen et al., 2015; Simon et al., 2016). We vary $t_{\text{seed}} \in \{10^4, 10^5, 10^6\}$ yrs to study the effect of this assumption on the timescale over which the seed reaches the isolation mass. Our chosen t_{seed} values are motivated by a desire to span a wide range for the time at which a lunar mass seed might form in the disk. We model the growth of cores with final masses of $\in \{10, 15, 20\} M_\oplus$. We do not consider more massive cores even though our model fits indicate that Kepler-167e contains $66 \pm 19 M_\oplus$ of metals (see §2.4) because the formation timescales for such cores become prohibitively long unless the disks are extremely massive. We adopt the expression for M_{iso} from Lambrechts et al. (2014):

$$M_{\text{iso}} = 20 \left(\frac{H_g/r}{0.05} \right)^3 \left(\frac{M_*}{M_\odot} \right) M_\oplus. \quad (2.3)$$

Although there are updated expressions for M_{iso} that account for its dependence on other properties of the disk (Ataiee et al., 2018; Bitsch et al., 2018), they are in reasonably good agreement with the simpler expression we adopt and depend on parameters we keep fixed in our work (e.g., turbulence, pressure gradient). We determine the location of our seeds implicitly via this expression for the pebble isolation mass. Our initial seeds are therefore placed at 3.2 au, 5.6 au, and 8.2 au, respectively, in order to produce cores of $10 M_\oplus$, $15 M_\oplus$, and $20 M_\oplus$. Although these

seeds might alternatively have started farther out and then migrated inward as they grew, the predicted migration rates are uncertain and depend sensitively on local disk properties (e.g., Benítez-Llambay et al., 2015; Li et al., 2009; Paardekooper et al., 2010; Rafikov, 2002). We therefore elect to keep the location of each seed fixed in our models. This simplifies our calculations and gives us a conservative lower limit on the dust mass that reaches the inner disk, as an inward-migrating core that starts further out will reach the same isolation mass later, thus increasing the amount of solids that reaches the inner disk. We calculate the growth rate of the core as the accretion rate of dust of size a_1 (larger grain population):

$$\dot{M} = f_{3D} \dot{M}_{2D} \quad (2.4)$$

where \dot{M}_{2D} is the standard 2D pebble accretion rate in the Hill (shear) regime (Lambrechts & Johansen, 2014):

$$\dot{M}_{2D} = 2 \left(\frac{\min(\text{St}_1, 0.1)}{0.1} \right)^{2/3} R_{\text{Hill}}^2 \Omega_K \Sigma_1. \quad (2.5)$$

R_{Hill} is the core's Hill radius, Ω_K is the orbital frequency at the core's location, and St_1 is the Stokes number of grains of size a_1 . Our assumption of accretion in the Hill regime is justified because the transition mass between the Bondi and the Hill regimes (Johansen & Lambrechts, 2017) is smaller than our adopted seed mass ($0.01 M_{\oplus}$) through most of our simulated domain (< 8 au, our outermost seed is located only slightly further out at 8.2 au). The factor f_{3D} in Equation 2.4 accounts for the effect of the relative magnitudes of the dust scale height and the core's R_{Hill} on the accretion rate (Morbidelli et al., 2015):

$$f_{3D} = \min \left(1, \frac{1}{2} \sqrt{\frac{\pi}{2}} \left(\frac{\text{St}_1}{0.1} \right)^{1/3} \frac{R_{\text{Hill}}}{H_{d,1}} \right) \quad (2.6)$$

where $H_{d,1} = H_g \sqrt{\alpha_t / (\alpha_t + \text{St}_1)}$ is the scale height of the large dust grains (Dubrulle et al., 1995). We allow the core to grow until it reaches M_{iso} , and record the corresponding time t_{iso} . We assume that this event effectively truncates the flow of solids to the inner disk.

Model results

Which disks form giant planets?

We determine which of our models are able to successfully form gas giant planets by checking to see which cores reach the isolation mass prior to the dispersal of the

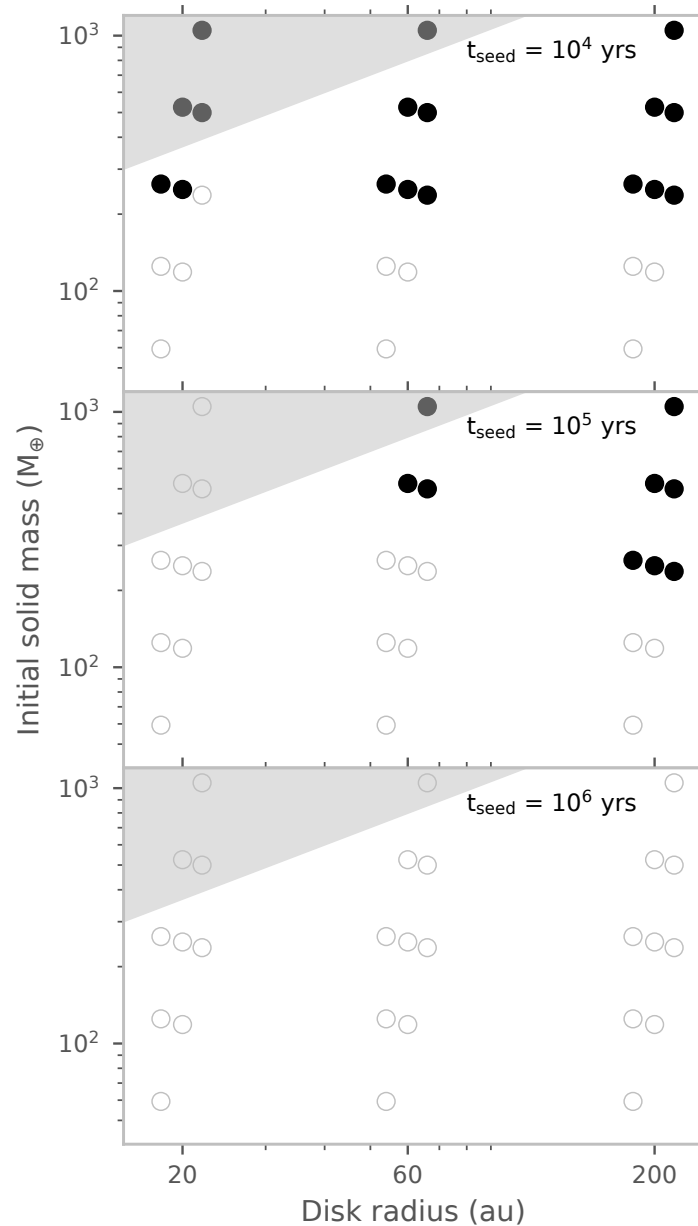


Figure 2.6: Filled (empty) circles mark disk models for which a $0.01 M_{\oplus}$ seed at 5.6 au does (does not) reach an isolation mass of $15 M_{\oplus}$ core. We show results from models with different initial solid masses M_{dust} (y-axis, product of M_{disk} and Z), disk sizes (x-axis), and three different t_{seed} . The grey shading indicates combinations of solid mass and disk size that are unlikely to exist in nature. For each combination of disk radius and initial solid mass, we use small offsets to show results for different $M_{\text{disk}} \in \{0.05, 0.1, 0.2\} M_*$ and $Z \in \{0.005, 0.01, 0.02\}$, with M_{disk} increasing in the horizontal direction and Z increasing in the vertical direction.

gas disk, which we assume occurs at 10 Myr. Figure 2.6 shows results from the full grid of disk models for $M_{\text{iso}} = 15 M_{\oplus}$. Disks where the core reaches the isolation mass are marked with filled circles, while those where it does not are shown as open circles. The importance of the disk’s initial solid reservoir is readily apparent (e.g., Bitsch et al., 2019; Schlecker et al., 2020). If the seed of the giant planet core is introduced early ($t_{\text{seed}} = 10^4$ yrs, top panel), its ability to reach the isolation mass is determined by the initial solid mass for all but the most compact disk models.

If the seed is introduced later ($t_{\text{seed}} = 10^5$ yrs, middle panel), it can only reach the pebble isolation mass if it is located in a relatively large disk. This is because a larger fraction of solids are distributed further out in larger disks, and it takes correspondingly longer for the solids to drain onto the star. This means that seeds that are introduced later can still accrete enough solids to reach the isolation mass (see also Johansen et al., 2019). For a fixed solid mass reservoir and disk size, we find that the influence of the total disk mass and dust-to-gas ratio, which we only vary by a factor of a few in these models, is relatively weak. It is the product of disk gas mass and dust-to-gas ratio that really matters.

When the core seed is introduced very late ($t_{\text{seed}} = 10^6$ yrs, bottom panel), it does not reach the isolation mass in any of the models in our grid. We conclude that $t_{\text{seed}} \lesssim 10^5$ yrs is a requirement for lunar mass seeds to turn into giant planet cores in the framework considered here. We find that seeds introduced at $\lesssim 10^5$ yrs typically reach isolation mass by $\lesssim 1$ Myr (Figure 2.8). This is consistent with the detection of gaps in protoplanetary disks as young as a few Myr old (e.g., Andrews et al., 2018; Long et al., 2018), which are likely opened by planets that are already larger than the pebble isolation mass by this time.

Which systems with outer gas giant planets also form inner super-Earths?

When the giant planet core reaches the pebble isolation mass, the solid reservoir available for planet formation interior to the giant planet’s orbit becomes effectively isolated from the outer disk. Although there may still be a modest inward flux of dust across the gap opened by the planet, it is expected to be a few orders of magnitude smaller than the flux in a smooth disk (e.g., Drażkowska et al., 2019; Lambrechts et al., 2014; Morbidelli & Nesvorny, 2012). This means that the mass budget for planet formation in the inner disk is simply the sum of the initial solid reservoir and the cumulative amount of solids delivered from the outer disk before the gas giant core reaches the isolation mass. The initial solid reservoir in the inner disk is

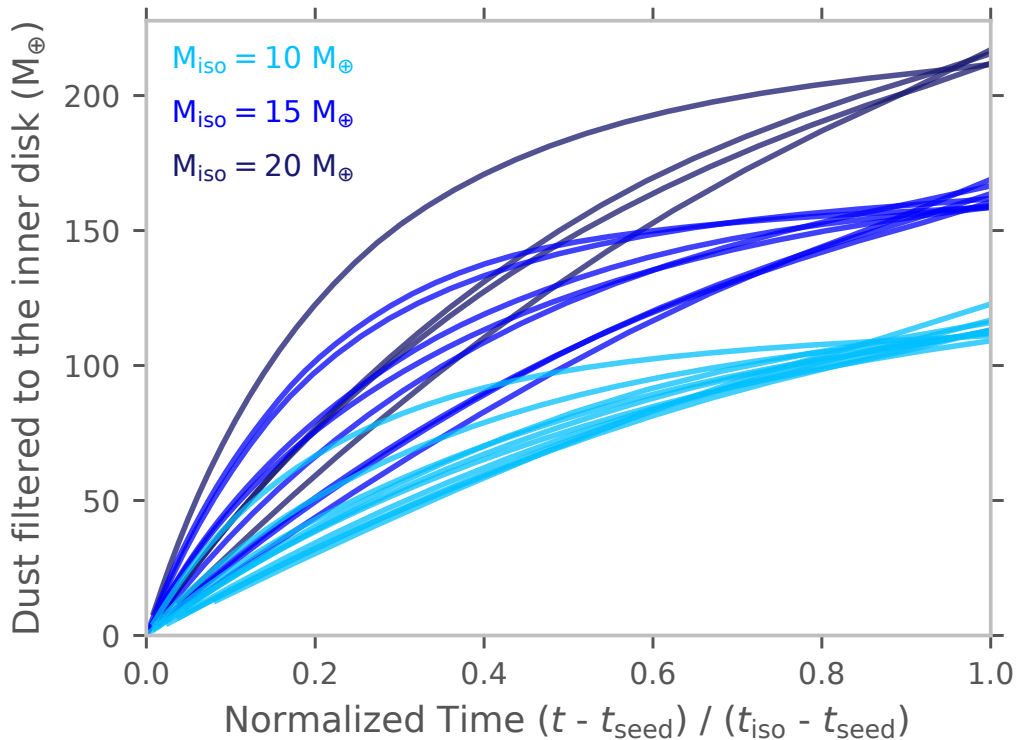


Figure 2.7: The dust mass that filters through to the inner disk between t_{seed} (the time at which a lunar mass seed is introduced) and t_{iso} (when core reaches M_{iso}) for different M_{iso} and a fixed $t_{\text{seed}} = 10^5$ years. All disk models in which a lunar mass seed reaches M_{iso} are shown. The filtered dust mass is primarily a function of M_{iso} and does not depend strongly on the assumed disk properties.

typically negligible compared to the flux from the outer disk for all but the smallest disks.

The next question that arises is: how much solid mass needs to be delivered to the inner disk for close-in super-Earths to form? The required mass depends on how super-Earths are formed and is likely to be model dependent. We adopt two illustrative limits from the pebble and planetesimal accretion paradigms that provide us with useful estimates of the dust mass needed to form super-Earths. Assuming super-Earths form by accretion of ‘dry’ pebbles onto lunar mass seeds, Lambrechts et al. (2019) show that an integrated pebble flux $\gtrsim 190 M_{\oplus}$ is necessary to form systems of super-Earths with masses and orbital architectures comparable to those observed by *Kepler*. In their models, a factor of 2 increase in the pebble flux (from $100 M_{\oplus} \text{ Myr}^{-1}$ to $200 M_{\oplus} \text{ Myr}^{-1}$) changes the final outcome from widely-spaced terrestrial planets to compact systems of close-in super-Earths. Accounting for 50%

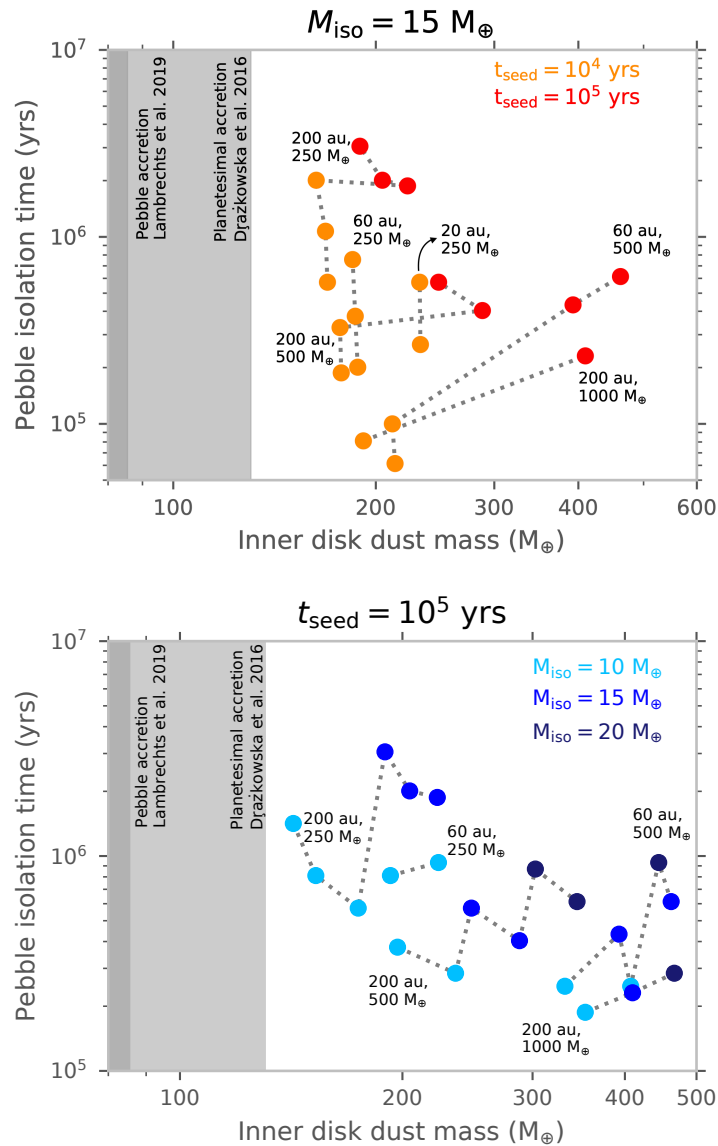


Figure 2.8: Pebble isolation time vs total solid mass available in the inner disk for all disk models in which a $0.01 M_\oplus$ seed reaches M_{iso} (i.e., those containing an outer gas giant). In the left panel, we vary t_{seed} and fix M_{iso} to $15 M_\oplus$. In the right panel, t_{seed} is fixed to 10^5 yrs and M_{iso} is varied. The initial seeds are placed at 3.2 au, 5.6 au, and 8.2 au to produce cores of $10 M_\oplus$, $15 M_\oplus$, and $20 M_\oplus$, respectively. We mark the estimated dust masses that are required for super-Earth formation in the pebble (Lambrechts et al., 2019) and planetesimal (Drażkowska et al., 2016) accretion paradigms using shaded regions. Models with the same disk size and initial solid mass are connected via dotted lines.

mass loss for pebbles across the water snowline, a higher pebble accretion efficiency of our prescription, and the inverse dependence of the accretion efficiency on stellar mass (see Appendix A), we modify this threshold to $190/0.5 \times 3/10 \times 0.75 \sim 86 M_{\oplus}$ ⁸. This modification is likely to be imperfect because the pebble mass threshold is sensitive to various time- and space-dependent quantities. Nonetheless, the key point is to compare the pebble mass threshold for super-Earth formation and the accretion efficiency of a cold giant planet core in the same framework, which we endeavor to do in our study. A less (more) efficient pebble accretion prescription would increase (decrease) the threshold mass for super-Earth formation, but it would also increase (decrease) the pebble mass that filters past the cold giant planet core and reaches the inner disk.

Alternatively, super-Earths might form by planetesimal accretion. To quantify the dust mass needed to form super-Earths in this paradigm, we need to know the efficiencies with which i) dust is converted into planetesimals and ii) planetesimals are converted into super-Earths. Unfortunately, quantifying the efficiency of converting dust into planetesimals is quite challenging and there are few estimates in the literature. Here, we use the results of Drażkowska et al. (2016) who use global dust evolution models coupled with planetesimal formation by the streaming instability to show that $\sim 23\%$ of their dust mass is converted into planetesimals. The planetesimals in Drażkowska et al. (2016) form interior to their location of the water snowline so we additionally account for 50% mass loss of the pebbles that form these planetesimals. Assuming that planetesimals are converted into planets by mutual collision and growth with a 100% efficiency (commonly assumed in this paradigm), the combined mass $\sim 15 M_{\oplus}$ of the Kepler-167 super-Earths translates to $\sim 15/0.23/0.5 \sim 130 M_{\oplus}$ of solids required for formation by planetesimal accretion.

Figure 2.7 shows the dust mass delivered to the inner disk between t_{seed} and t_{iso} , i.e. while the core is growing, for different disks in which the seed reaches M_{iso} . We find that this integrated dust mass is primarily a function of M_{iso} and depends only weakly on disk properties (disk size and dust mass). It also has a weak dependence on t_{seed} itself, i.e. when the seed is introduced (not shown in the plot). This is because the amount of dust mass filtered through to the inner disk while the core is forming depends on the pebble accretion efficiency ϵ (see Appendix A) and most of the parameters that affect ϵ are constant for our disk models (e.g., α_t , temperature

⁸We note that Lambrechts et al. (2019) quantified the pebble mass required to form super-Earths after lunar mass seeds had formed already. This pebble mass threshold does not include the pebble mass required to form the seeds in the first place.

structure). A larger M_{iso} results in the delivery of a larger amount of solids to the inner disk because seeds take longer to reach a larger M_{iso} . This is because the larger M_{iso} places the seed at a larger orbital separation where the disk aspect ratio is higher and pebble accretion efficiency is lower. The amount of dust mass delivered to the inner disk between t_{seed} and t_{iso} is $\sim 10 \times M_{\text{iso}}$, which implies that cumulative $\epsilon \sim 10\%$ for our disk models. With such efficiencies, the dust mass delivered between t_{seed} and t_{iso} alone is enough to form inner super-Earths via planetesimal or pebble accretion for $M_{\text{iso}} \gtrsim 10 M_{\oplus}$. This inflowing material is augmented by the initial dust located interior to the giant planet’s orbit, as well as the dust mass delivered before t_{seed} .

Figure 2.8 shows the pebble isolation time for the outer giant companion and the corresponding total solid mass available in the inner disk for a range of t_{seed} and $M_{\text{iso}} = 15 M_{\oplus}$ (left panel) and for a fixed $t_{\text{seed}} = 10^5$ yrs with varying M_{iso} (right panel). For a fixed M_{iso} (left panel), the amount of solids that reaches the inner disk generally increases with t_{seed} . This is primarily because of the increase in dust mass supplied to the inner disk by radial drift before t_{seed} , and not because of differences in the dust mass delivered between t_{seed} and t_{iso} . We note that for a given t_{seed} , models with different disk gas masses and dust-to-gas ratios but the same total dust mass have fairly different t_{iso} , even though they allow roughly the same mass of solids to reach the inner disk. Although we consider t_{seed} values as low as 10^4 yrs, we find that there are many potential disk models with enough solids to form super-Earths. This implies that no temporal fine-tuning in the giant planet core’s formation is necessary in order to enable the formation of inner super-Earths. For a fixed t_{seed} (10^5 yrs in the right panel of Figure 2.8), a larger M_{iso} results in the availability of a larger amount of solids for super-Earth formation in the inner disk. In this panel, models with the same M_{iso} but different disk properties have different total solid mass available in the inner disk due to the disk dependent contribution of radial drift before t_{seed} .

Variations in disk properties, t_{seed} , and M_{iso} lead to a large range in the dust mass available for planet formation in the inner disk. For the most massive disks, the dust mass supplied to the inner disk can significantly exceed the threshold dust mass required to form super-Earths. This might lead to the formation of inner planets with higher masses. For example, Lambrechts et al. (2019) show that increasing the total available pebble mass from $190 M_{\oplus}$ to $340 M_{\oplus}$ moved the range of planet masses produced from $2 - 20 M_{\oplus}$ to $5 - 30 M_{\oplus}$ and increased the mean mass of

the planets that form by a factor of 2. The most massive disks may therefore also allow for the formation of massive sub-Neptunes and Neptunes interior to a cold giant planet’s orbit. This could possibly explain how planetary systems with such architectures emerge (e.g., HAT-P-11, Yee et al., 2018; HD 47186, Bouchy et al., 2009).

Constraints on Kepler-167’s protoplanetary disk properties

We can use our grid of disk models to constrain the properties of Kepler-167’s protoplanetary disk. We know that: 1) Kepler-167e’s core must reach the isolation mass well before the dissipation of the disk, 2) enough solids must be delivered to the inner disk prior to this point to allow for super-Earth formation, and 3) after Kepler-167e’s core reaches the isolation mass, there must be enough solids still present beyond its orbit to account for its remaining bulk metal content ($\sim 66 M_{\oplus} - M_{\text{iso}}$). By taking these three conditions into account, we can place a lower limit on the initial dust mass of the disk as a function of disk size. For condition 1, we adopt a stricter limit of 1 Myr rather than our prior 10 Myr for t_{iso} as we know that Kepler-167e had enough time to accrete a relatively massive (i.e., Jupiter-like) gaseous envelope. This limit is also in better agreement with observational constraints on average disk lifetimes for isolated sun-like stars, which are around 3 Myr (e.g., Mamajek, 2009; Williams & Cieza, 2011). Our new upper limit on t_{iso} excludes scenarios with t_{seed} of 10^6 , leaving us with a choice between t_{seed} of 10^4 and 10^5 yrs. However, for this exercise we only use $t_{\text{seed}} = 10^5$ yrs as 10^4 yrs is likely too early for a lunar mass seed to form (Johansen & Lambrechts, 2017; Lambrechts & Johansen, 2012; Visser & Ormel, 2016). For condition 2, we adopt the higher limit of $130 M_{\oplus}$ for the dust mass required for super-Earth formation that is imposed by planetesimal accretion (Drażkowska et al., 2016).

Given the sensitivity of gas accretion rates to core mass (e.g., Lee, 2019), we also limit our models to M_{iso} of 15 and $20 M_{\oplus}$, which are more likely to produce a Jovian-mass planet. We note that our results are not qualitatively different for M_{iso} of $10 M_{\oplus}$. Although this requires the giant planet core to accrete additional solids after reaching M_{iso} in order to match the bulk metal content of Kepler-167e ($\sim 66 M_{\oplus}$), this is a more plausible scenario than models in which the pebble isolation mass is set to $66 M_{\oplus}$. Cores of this size can only form in the most massive and largest disk in our grid ($\sim 1000 M_{\oplus}$ solids, disk size of 200 au). Since Kepler-167e’s bulk metal content is typical for planets in its mass range (see § 2.4 and Thorngren

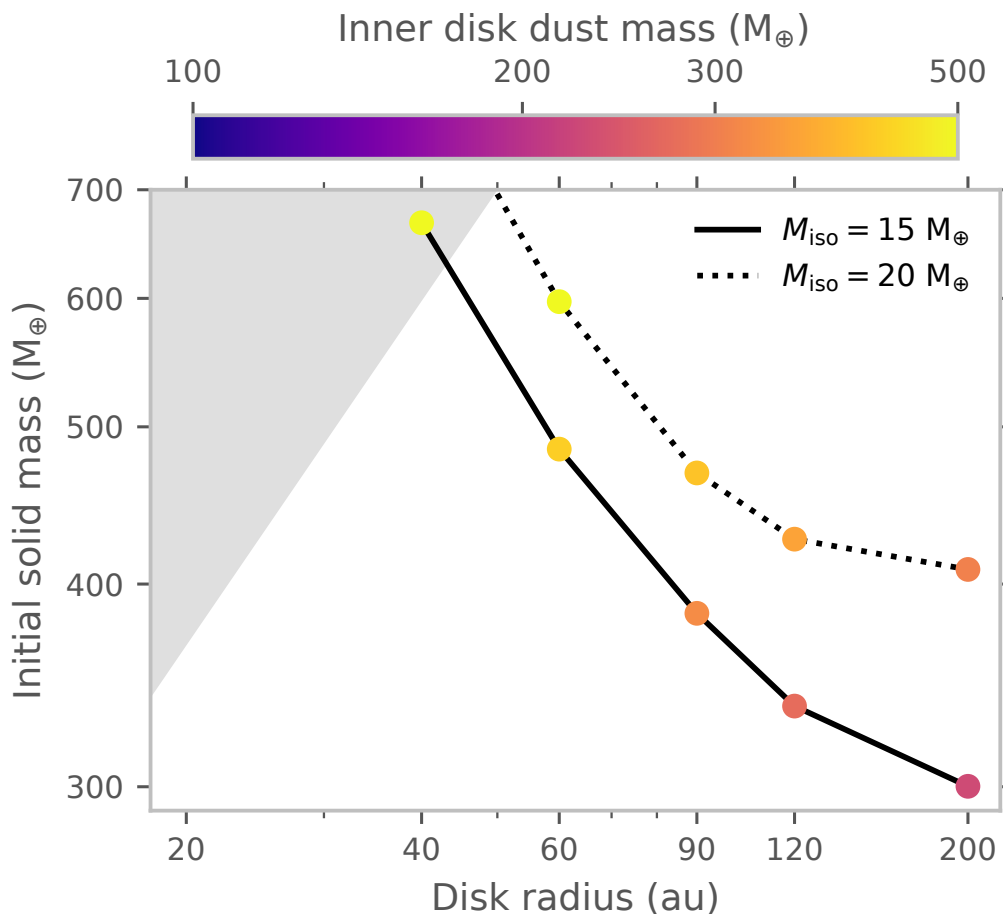


Figure 2.9: The initial solid mass and size of protoplanetary disks that can produce the Kepler-167 planetary system assuming $t_{\text{seed}} = 10^5$ yrs. The color of the points indicates the total amount of solids that is available in the inner disk. We find that $\geq 165 M_{\oplus}$ of solids reach the inner disk for all our models and thus they all exceed the super-Earth formation threshold. We grey out the region corresponding to small disks with very large solid masses, as these disks are unlikely to exist in practice.

& Fortney, 2019), it seems unlikely that all of these giant planets formed with such a large M_{iso} . Planets that have reached the pebble isolation mass may continue to accrete solids in the form of planetesimals (as suggested for Jupiter, Alibert et al., 2018) or they might accrete the pebbles that grow from the dust present the circumplanetary disks (e.g., Drażkowska & Szulágyi, 2018). Indeed, Thorngren et al. (2016) argue that the late stage accretion of planetesimals is needed in order to explain the mass-metallicity relation observed for extrasolar giant planets. We do not model this process explicitly here, but simply require that the remaining solid

content at orbital separations beyond the giant planet’s core is equal to or greater than $66 M_{\oplus} - M_{\text{iso}}$ at the time when the core reaches the isolation mass.

The initial dust mass of the disk is a product of the disk dust-to-gas ratio and disk gas mass. In § 2.5, we showed that varying the disk dust-to-gas ratio and gas mass while keeping the total dust mass constant does not affect the solid mass that reaches the inner disk. We therefore reduce the dimensionality of our original grid by fixing the dust-to-gas ratio to 0.015, taking the median stellar $[\text{Fe}/\text{H}] = 0.02$ and assuming solar $[\text{Fe}/\text{H}] = 0.014$ (Asplund et al., 2009). We are left with a grid in which we vary M_{iso} , t_{seed} , disk size, and disk gas mass. We then identify the subset of models in this grid that fulfill the three conditions listed above. In practice, we find that the second condition ($\gtrsim 130 M_{\oplus}$ supplied to the inner disk) is automatically met when the first and third conditions are satisfied.

Figure 2.9 shows the resulting constraints on the size and initial solid mass of Kepler-167’s protoplanetary disk. We find that we require an initial solid mass larger than $\sim 300 M_{\oplus}$ and a radius larger than 40 au in order to explain this system’s present-day properties. Within this range, disks with a larger M_{iso} require higher initial solid masses in order to form Kepler-167e. For our chosen $t_{\text{seed}} = 10^5$ yrs, the requisite dust mass rises sharply with decreasing disk size. This is primarily driven by the need to have sufficient solid mass beyond the giant planet to explain its bulk metal content (condition 3). Since smaller disks have shorter radial drift timescales and dust rapidly drains out of their outer regions, they need to have larger dust masses to meet this requirement.

We next consider whether or not these constraints are consistent with results from protoplanetary disk surveys. In Figure 2.10, we plot the ALMA and VLA disk radii and dust masses estimated for Class 0 and I sources in the Orion cluster (Tobin et al., 2020) and compare them to the theoretical constraints from our models. Since we are interested in the initial dust mass and size, we exclude Class II disks, which show significant signs of processing, especially for dust mass (e.g., Tychoniec et al., 2020). If we consider the VLA and ALMA measurements in isolation, we find that very few disks lie above the planet formation threshold contours we have for Kepler-167. However, disk radii estimated from VLA and disk dust masses estimated from ALMA tend to be underestimates. This is evident when we instead plot dust masses derived from VLA against disk radii obtained from ALMA for the same disks (shown in red). Doing so moves the ALMA points up in dust mass and the VLA points to larger radii. Dust masses derived from VLA are likely closer

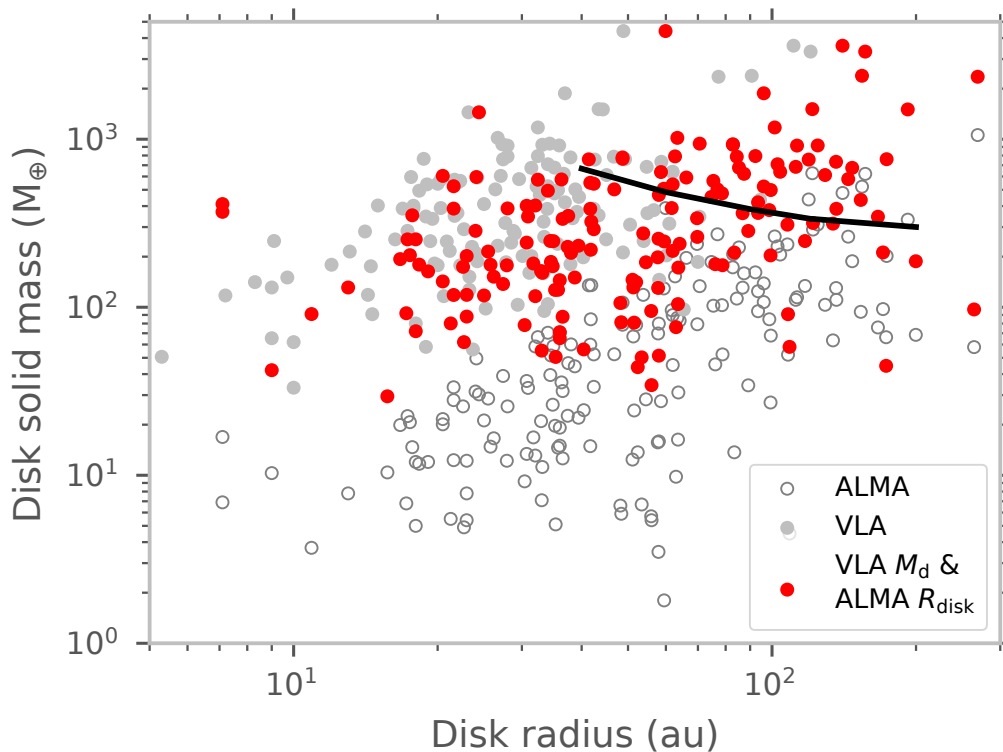


Figure 2.10: Disk dust mass and radius estimates for Class 0 and I sources in the Orion cluster that are detected both with ALMA (0.87 mm) and VLA (9 mm) (Tobin et al., 2020). We plot the threshold contour above which disks can form systems like Kepler-167 (corresponding to $M_{\text{iso}} = 15 M_{\oplus}$ and $t_{\text{seed}} = 10^5$ yrs curve in Figure 2.9). Since disks tend to be optically thin in the VLA bandpass, dust mass estimates obtained from these observations are closer to true estimates. However, disk sizes obtained from ALMA are likely to be closer to the characteristic disk size that is used in our modelling. We therefore plot dust mass estimates from VLA against disk radii from ALMA in red.

to true values as disks are much more likely to be optically thin at 9 mm than at 0.87 mm. Similarly, since disks tend to appear smaller in continuum emission at larger wavelengths, the radii estimated from ALMA are likely to be closer to the characteristic disk radii that we have in our models. When we combine dust masses from VLA with disk radii from ALMA, we find that a substantial fraction of the disks meet the threshold dust mass and disk size necessary for the formation of the Kepler-167 system.

The formation threshold for the Kepler-167 system is primarily driven by the properties of Kepler-167e, in particular its bulk metal content and the need to form it early. Since Kepler-167e is fairly representative of giant planets beyond several au around

FGK stars, we can roughly quantify the fraction of disks around single FGK stars that lie above our formation threshold (f_{disk}) and compare it with the corresponding occurrence rate of giant planets (e.g., Fulton et al., 2021; Wittenmyer et al., 2020). Of the 425 disks targeted by ALMA in Tobin et al. (2020), 45 disks lie above the $M_{\text{iso}} = 15 M_{\oplus}$ threshold. However, this sample is likely to contain both massive and low mass stars that will bias our estimate of f_{disk} . Correcting for this contamination as well as the presence of close companions to FGK stars that likely go undetected in Tobin et al. (2020) (see Appendix B for details of this correction), we find that $f_{\text{disk}} \approx 14\%$.

We conclude that it is reasonably probable that a star with Kepler-167’s mass might host a disk with an initial solid mass and radius that lie above the thresholds indicated by our disk models. If we take the giant planet occurrence rate beyond several au around FGK stars (e.g., Fulton et al., 2021; Wittenmyer et al., 2020) as a proxy for the occurrence rate of Kepler-167-like systems, we find that this value is broadly consistent with our estimated massive disk fraction of 10 – 20%. Our models also suggest that there is likely to be a strong correlation between outer gas giants and inner super-Earths, as most disks that met our conditions for giant planet formation also delivered enough material to the inner disk to form short-period super-Earths. We note that massive metal-rich disks are also more likely to form multiple gas giants, which in turn can pump up the eccentricities of the gas giants and destabilize the system of inner super-Earths. That is, post-formation dynamical evolution might reduce the strength of the correlation between inner super-Earths and outer gas giants for metal-rich stars with massive disks. Nonetheless, our results are consistent with observational studies, which find a strong empirical correlation between these two populations (Bryan et al., 2019; Herman et al., 2019; Zhu & Wu, 2018).

2.6 Conclusions

The fact that close-in super-Earths often accompany cold giant planets provides us with valuable insights into the planet formation process. Systems such as Kepler-167, which can be characterized in detail, serve as an important bridge between observed planetary properties and planet formation models. In this work, we re-fit the *Kepler* photometry in order to derive updated parameters for both the host star and the four transiting planets in the system. We also obtain radial velocity measurements spanning more than three years in order to measure the mass of the outer transiting gas giant, Kepler-167e. We determine that Kepler-167e is a true Jupiter analog with a mass of $1.01_{-0.15}^{+0.16} M_{\text{J}}$. Its mass and semimajor axis are typical

of gas giant planets detected by radial velocity surveys, but it appears to have a relatively low orbital eccentricity (3σ upper limit of 0.29).

We fit Kepler-167e’s measured mass and radius using a giant planet evolution model and find that this planet is more metal-rich than Jupiter, with a bulk metallicity of 0.21 ± 0.05 . This translates to an impressive $66^{+20}_{-18} M_{\oplus}$ of metals in its interior. Although our RV data are not precise enough to place any constraints on the masses of the inner super-Earths, we use the non-parametric M-R relationship from Ning et al. (2018), to estimate that the three planets are predicted to contain $15.7^{+11.6}_{-6.5} M_{\oplus}$ in total. Dust in the inner disk drifts into the star on very short timescales and converting the local dust content into planets requires a rather high formation efficiency. It therefore seems unlikely that these planets could have formed from the material initially located inside Kepler-167e’s orbit, and instead the dust budget must have been supplemented by the migration of solids from the outer disk. Taken together, these two quantities constrain the initial solid budget of Kepler-167’s protoplanetary disk.

We quantify the conditions required to form the Kepler-167 system by exploring a simple grid of protoplanetary disks models spanning a range of initial solid masses and disk radii. We find that giant planets like Kepler-167e preferentially form in fairly massive (in dust content) and large disks, in good agreement with results from previous studies (e.g., Bitsch et al., 2019; Schlecker et al., 2020). Our models assume that once the giant planet reaches the isolation mass, the flow of solids to the inner disk is effectively truncated. Despite this constraint, we find that most disks that form outer gas giants are nonetheless able to supply enough solids to the inner disk to also form super-Earths in both the pebble (Lambrechts et al., 2019) and planetesimal (Drażkowska et al., 2016) accretion paradigms. This remains true regardless of the time at which the giant planet seed is introduced, and we find consistent results across a range of different isolation masses for the giant planet core.

When we incorporate the additional constraint provided by Kepler-167e’s bulk metallicity, we find that we require disks that contains $\gtrsim 300 M_{\oplus}$ of solids and are $\gtrsim 40$ au in size to form this planet. We compare these constraints with the observed properties of Class 0 and I disks in the Orion cluster as measured by ALMA and the VLA (Tobin et al., 2020). We find that 10 – 20% of FGK stars should have disks with masses and radii large enough to form the Kepler-167 system, even after

accounting for contamination from a range of stellar populations. This strengthens the plausibility of our constraints on Kepler-167's protoplanetary disk properties.

Further efforts to characterize the Kepler-167 system will enhance our understanding of the origin of its planetary configuration. In particular, there is a pressing need for mass measurements of the inner planets. Our ignorance of the super-Earth planet masses hinders our ability to estimate the accretion efficiency of pebbles and/or planetesimals. Future observations with next generation instruments such as the Keck Planet Finder (KPF, Gibson et al., 2016) will allow us to measure the masses of the super-Earths and put our formation scenario on a firmer footing. RV semi-amplitudes corresponding to Earth-like planetary composition for Kepler-167 b and c are expected to be accessible with KPF. Additionally, characterization of Kepler-167e's atmospheric composition would be a useful probe of its formation history and location. However, Kepler-167 is a faint star and Kepler-167e has a high surface gravity, a cold atmosphere, and is a good candidate for photochemical hazes. We also cannot stack multiple transits or eclipses because it transits so infrequently. Taken together, these factors mean that it does not appear to be a good target for atmospheric characterization with JWST.

Although it is outside the scope of this study, we note that further characterization of Class 0 and I disks would be particularly valuable for bridging the gap between disk properties and planet formation. It is fortuitous that we can obtain observational constraints on disk dust masses and radii, as these two quantities have a significant impact on planet formation. There is a growing consensus in the field that planet formation starts earlier than the Class II stage (e.g., Segura-Cox et al., 2020; Tychoniec et al., 2020), and it would therefore be particularly useful to carry out additional comprehensive surveys targeting other young star forming regions with a significant population of Class 0 and I disks. This would allow us to more accurately assess the distribution of disk properties at early times, which we can use to make predictions for giant planet occurrence rates. On the modelling end, our Class II disk model is unlikely to be appropriate for the early stages of disk evolution and therefore more accurate models are needed for these initial epochs. A deeper understanding of the connection between the collapse of protostellar cores and the initial properties of protoplanetary disks, such as disk sizes and the timescale over which dust and gas are delivered, would also help to better elucidate the environment in which planets first begin to form (see Lebreuilly et al., 2020, 2021; Lee et al., 2021; Schib et al., 2021, for recent attempts in this direction).

*Chapter 3***RADIAL GRADIENTS IN DUST-TO-GAS RATIO LEAD TO PREFERRED REGION FOR GIANT PLANET FORMATION****3.1 Introduction**

Dust opacity plays an important role in setting the temperatures and vertical structures of protoplanetary disks (e.g., Chiang & Goldreich, 1997; D’Alessio et al., 1998) and determines how rapidly a planet accretes its gaseous envelope (e.g., Ikoma et al., 2000; Pollack et al., 1996; Stevenson, 1982a). The temperature structure of the disk determines where various molecules can condense, resulting in a spatially and temporally varying division of elements between solid and gas phases (e.g. Hayashi, 1981; Oberg et al., 2011). In the core accretion framework, dust opacity regulates the cooling of the envelope accreted by a growing planet (e.g., Lee et al., 2014; Piso & Youdin, 2014; Piso et al., 2015). Because the envelope accretion rate is cooling-limited during the hydrostatic phase of planetary growth, this dust opacity also has a strong influence on the final envelope mass.

In particular, cooling-limited accretion determines which planetary cores reach the threshold for runaway gas accretion within the gas disk lifetime and hence influences the giant planet occurrence rate. Radial velocity surveys indicate that giant planets inside 7 au only occur around 10% of FGK stars and they predominantly orbit their host stars at intermediate distances (3 – 5 au); their occurrence rate declines at both smaller and larger orbital distances (Cumming et al., 2008; Fernandes et al., 2019; Fulton et al., 2021; Howard et al., 2012; Rosenthal et al., 2021; Wittenmyer et al., 2016, 2020; complemented by direct imaging surveys, e.g. Baron et al., 2019; Bowler & Nielsen, 2018). It is unclear why giant planets preferably occur at intermediate distances. The water ice line is typically assumed to play a role in making this region favorable for giant planet formation, primarily by facilitating the formation of massive cores (e.g. Morbidelli et al., 2015). However, the role of gas accretion in shaping the occurrence rate of giant planets remains largely unexplored.

Sub-Neptunes dominate the observed population of exoplanets with orbital periods less than 300 days (e.g., Batalha et al., 2013; Dressing & Charbonneau, 2015; Fressin et al., 2013; Morton & Swift, 2014; Petigura et al., 2018). The measured radii and masses of sub-Neptunes are consistent with hydrogen and helium envelope mass

fractions of a few percent (Ning et al., 2018; Wolfgang & Lopez, 2015), despite the fact that some of these planets have cores massive enough ($\gtrsim 10M_{\oplus}$) to reach the threshold for runaway gas accretion. What regulates the envelope mass fraction at a few percent? It has been suggested that the accretion of material with high dust opacity could prevent these planets from amassing significantly larger envelopes (e.g. Chen et al., 2020; Lee et al., 2014). Here, we revisit this idea and explore why sub-Neptunes might be expected to form close-in whereas gas giants are more common at larger orbital separations.

Determining the dust opacity at a given location in the protoplanetary disk is a non-trivial task as it depends on the poorly known optical properties (composition and structure), size distribution, and dust-to-gas ratio, all three of which are intricately coupled to the protoplanetary disk’s structure and evolution. Previous studies in both the protoplanetary disk and planet formation literature (e.g. Alexander & Ferguson, 1994a; Bell & Lin, 1994) have generally elected to adopt a single global value for the dust-to-gas ratio and a power-law size distribution (both the power-law index and the bounding grain sizes) that is akin to that of dust in the interstellar medium (ISM). However, such a prescription is too simplistic to calculate the mean opacity due to dust grains in a protoplanetary disk. Dust grains in protoplanetary disks grow to sizes that are significantly larger (mm-cm size, e.g. Andrews, 2015; Draine, 2006; Miyake & Nakagawa, 1993; Testi et al., 2003) than the largest sub-micron sized grains in the ISM (Draine & Lee, 1984). A larger maximum grain size redistributes dust mass from smaller grains to larger grains, which significantly alters the short-wavelength and mean opacities of protoplanetary disks (e.g. D’Alessio et al., 2001).

Fortunately, advances in our understanding of grain coagulation and the role of fragmentation and radial drift in limiting grain growth now make it possible to calculate the grain size distribution as a function of location in protoplanetary disks (Birnstiel et al., 2010, 2011; Brauer et al., 2008). In a recent study, Savvidou et al. (2020) assessed the effect of varying grain size distribution from coagulation and fragmentation on the Rosseland mean opacity and the thermal structure of the disk, but without taking dust transport into account. Transport of dust due to radial drift, gas drag, and turbulent diffusion leads to a radially-varying dust-to-gas ratio, which may significantly alter dust opacity. This in turn leads to a location dependence of the gas accretion rates onto planetary cores. The gas accretion rate depends on the envelope’s ability to cool at the innermost radiative-convective boundary (RCB). For envelopes in which dust opacity dominates, the sublimation of dust

leads to the formation of an intermediate radiative zone and the innermost RCB is set by the H_2 dissociation front (Lee et al., 2014). Cooling at the innermost RCB is then controlled by H^- opacity, which depends on the availability of free electrons provided by metals. These metals are mostly present in the dust initially and so the radially-varying dust-to-gas ratio of the accreted material affects the rate at which the envelope can cool.

In this work, we use a published dust evolution model to calculate the spatial and temporal evolution of the dust-to-gas ratio in a protoplanetary disk (Birnstiel et al., 2012) in § 3.2. We then calculate the corresponding Rosseland mean opacity using an approximate size distribution scheme to determine the grain size distribution as a function of distance from the star (Birnstiel et al., 2015). In § 3.3, we compute the disk opacity from dust evolution models as a function of radial distance, height from midplane, and time and show that our results differ starkly from the usual ISM opacity values. We then use our updated opacity values to calculate gas accretion rates onto planetary cores using the analytical scaling laws from Lee & Chiang (2015) and discuss the consequences of our work for the formation of gas giants, sub-Neptunes, and ‘super-puffs’ (low mass planets with sizes beyond $\sim 4 R_\oplus$) in § 3.4. We summarize our results and suggest potential directions for future work in § 3.5.

3.2 Models

ISM size distribution

The ISM size distribution is usually described using a power law distribution:

$$n(a) = A a^\beta, \quad (3.1)$$

where n is the number of particles per unit volume per unit size interval, A is a normalization factor that depends on the assumed dust-to-gas ratio and the minimum and maximum grain sizes, and β is the power law index that characterises how bottom- or top-heavy the size distribution is. The power law index β and minimum and maximum grain sizes (a_{min} and a_{max}) are typically chosen to be -3.5 , $0.005\mu\text{m}$, and $0.25\mu\text{m}$, respectively, which fit the observed extinction law in the diffuse interstellar medium (Alexander & Ferguson, 1994b; Laor & Draine, 1993; Mathis et al., 1977). Although there are small variations in the values used for these parameters in the published literature, especially a_{min} and a_{max} , they do not make an appreciable

difference for the calculated opacity. The value for the normalizing constant A is given by:

$$A = \frac{3\rho_d(\beta + 4)}{4\pi\rho_s(a_{\max}^{\beta+4} - a_{\min}^{\beta+4})}, \quad (3.2)$$

where $\rho_s = 1.675 \text{ g cm}^{-3}$ is the material density of the dust grain, fixed to a value appropriate for the DSHARP mixture (see § 3.2), ρ_d is the density of dust in the disk, ρ_g the density of disk gas, and $\epsilon = \rho_d/\rho_g$ is the dust-to-gas ratio. The ISM dust opacity is typically calculated assuming a global value of $\epsilon = 0.01$ for the entire protoplanetary disk. For ρ_g , we use the gas density in the disk midplane obtained from our protoplanetary disk model, which we describe in the next section.

Protoplanetary disk model

We use the publicly available code `twopoppy` to model the structure of a protoplanetary disk and the dynamics of dust and gas¹. The methods and algorithms used in `twopoppy` are described in Birnstiel et al. (2012) and we will present a brief overview here for completeness. We consider a protoplanetary disk of mass $0.1 M_*$ around a protostar of mass $M_* = 0.7 M_\odot$. The stellar effective temperature (T_*) and radius (R_*) are set to 4010 K and $1.806 R_\odot$, respectively. We assume that the disk is passively heated, and its temperature structure therefore takes the following form (e.g. Chiang & Goldreich, 1997; D’Alessio et al., 1998):

$$T(r) = \left[\phi T_*^4 \left(\frac{R_*}{r} \right)^2 + T_0^4 \right]^{1/4} \quad (3.3)$$

where r is the cylindrical distance from the star, $T_0 = 7 \text{ K}$ is a constant, and $\phi = 0.05$ is the angle between the incident radiation and disk surface (‘flaring’ angle). The sound speed c_s is defined as $\sqrt{k_B T / \mu m_H}$, where k_B is the Boltzmann constant, $\mu = 2.3$ is the mean molecular weight of the gas, and m_H is the mass of hydrogen atom. Our neglect of heating due to viscous dissipation leads to an underestimation of the temperature in the inner regions of the disk, but greatly simplifies the determination of the temperature structure. This choice does not have a significant effect on the position of the water ice line (see § 3.3 for a brief discussion). We note that accounting for the varying opacities that arise from the

¹The original public repository is available at <https://github.com/birnstiel/two-poppy>. A fork of this repository with the changes implemented in our work is available at https://github.com/y-chachan/two-pop-py/tree/rad_grad_d2g.

growth and transport of grains into the temperature profile is outside the scope of this paper (see, e.g. Savvidou et al., 2020, for recent attempts in this direction).

The gas surface density (Σ_g) is evolved following the fluid equations of viscously spreading accretion disk (Lynden-Bell & Pringle, 1974)

$$\frac{\partial \Sigma_g}{\partial t} = \frac{3}{r} \frac{\partial}{\partial r} \left[r^{1/2} \frac{\partial}{\partial r} (\nu \Sigma_g r^{1/2}) \right] \quad (3.4)$$

whose self-similar solution (at time zero) is used to set the initial surface density profile for our calculation:

$$\Sigma_g(r) = C \left(\frac{r}{r_c} \right)^{-p} \exp \left[- \left(\frac{r}{r_c} \right)^{2-p} \right] \quad (3.5)$$

where C is a constant to be normalized by the assumed disk gas mass, ν is the kinematic viscosity with a power law radial profile ($\nu = \nu_c (r/r_c)^p$), and r_c is a characteristic radius of the disk. Following Birnstiel et al. (2012), we set $p = 1$ and $r_c = 200$ au in our work. The viscosity $\nu = \alpha_t c_s H_{\text{gas}}$ is parameterized using the Shakura-Sunyaev turbulence parameter α_t (Shakura & Sunyaev, 1973), the sound speed c_s , and the gas scale height $H_{\text{gas}} = c_s/\Omega$, where Ω is the Keplerian frequency.

The initial dust surface density is set as ϵ times the initial gas surface density given in Equation 3.5, where $\epsilon = 0.01$. The dust surface density evolution and dynamics of dust is modelled using just two representative grain sizes in the disk (hence the name **twopoppy**): the spatially and temporally constant monomer size a_0 and a large grain size a_1 that depends on time and location in the disk. We fix $a_0 = 0.005 \mu\text{m}$ to align this variable with the minimum grain size in the ISM size distribution. These small grains rapidly coagulate to form agglomerates that are many orders of magnitude larger in size. Their growth is limited by processes such as turbulent fragmentation and radial drift. These limiting sizes are what set the value of a_1 as a function of time and r and they are discussed in greater detail later in this section.

Splitting the dust population into two allows us to capture the qualitatively different dynamical behavior of large and small grains. Small grains are well coupled to the gas and are unable to maintain large relative velocities with respect to the gas. On the other hand, large grains are slightly decoupled from the gas and respond to pressure gradients on relatively short timescales. The total surface dust density (Σ_d) is the sum of the surface density of small (Σ_0) and large (Σ_1) grains and can consequently be modelled using a single advection-diffusion equation:

$$\frac{\partial \Sigma_d}{\partial t} + \frac{1}{r} \frac{\partial}{\partial r} \left[r \left(\Sigma_d \bar{u} - D_{\text{gas}} \Sigma_g \frac{\partial}{\partial r} \left(\frac{\Sigma_d}{\Sigma_g} \right) \right) \right] = 0. \quad (3.6)$$

Here, \bar{u} is the mass weighted radial velocity of dust grains and D_{gas} is the gas diffusivity. A derivation of this equation is available in the appendix of Birnstiel et al. (2012).

The Stokes number St is dust grain stopping time under gas aerodynamic drag in units of local orbital time. Dust grains smaller than the gas particle mean free path are in Epstein drag regime and their Stokes numbers follow

$$St = \frac{\pi a \rho_s}{2 \Sigma_g}. \quad (3.7)$$

Detailed dust growth and evolution simulations indicate that grains will continue to grow until they reach a size ($St \sim 0.1 - 1$) where fragmentation due to collisions and/or loss to radial drift become significant (e.g. Birnstiel et al., 2010; Brauer et al., 2008). For grains in this size range, velocity differences between grains due to turbulence become larger ($\Delta u \propto \sqrt{St}$, Ormel & Cuzzi, 2007) and collisions are more likely to lead to fragmentation instead of growth. This limits the maximum Stokes number and corresponding size a_{frag} that the grains can reach:

$$St_{\text{frag}} = \frac{1}{3\alpha_t} \frac{v_{\text{frag}}^2}{c_s^2} \quad (3.8a)$$

$$a_{\text{frag}} = \frac{2}{3\pi} \frac{\Sigma_g}{\rho_s \alpha_t} \frac{v_{\text{frag}}^2}{c_s^2} \quad (3.8b)$$

where v_{frag} is the fragmentation velocity of dust grains.

The rate of radial drift is maximized for particles marginally coupled to gas ($St \sim 1$) (Chiang & Youdin, 2010; Weidenschilling, 1977):

$$u_{\text{drift}} = -\frac{2u_\eta}{St + St^{-1}} \quad (3.9)$$

where $u_\eta = -\gamma c_s^2 / 2v_K$ is the drift velocity, v_K is the Keplerian velocity, and $\gamma = |d \ln P / d \ln r|$ is the power law index characterising the dependence of pressure on distance from the star. In some regions of the disk, particles may drift radially faster than they can grow to the size at which fragmentation dominates. In these regions, the radial drift sets an upper limit on the particle size a_{drift} :

$$a_{\text{drift}} = \frac{2}{\pi} \frac{\Sigma_{\text{d}}}{\rho_{\text{s}} \gamma} \frac{v_{\text{K}}^2}{c_{\text{s}}^2}. \quad (3.10)$$

At early times in the disk evolution, the particle growth rate can also be a limiting factor for grain growth and set the maximum particle size. This can be true even at late times in the outer disk where the growth timescales ($\tau_{\text{grow}} \simeq 1/\epsilon\Omega$) are longer. Relative velocities due to radial drift can also lead to fragmentation, but this effect is only relevant at early times for models with low turbulence ($\alpha_{\text{t}} = 10^{-4}$). As the dust-to-gas ratio in such a region declines due to inward drift, the size limit set by radial drift becomes smaller than the one set by drift-induced fragmentation. In the two population model for dust evolution, the large grain size a_1 is fixed to a fraction of the maximum grain size that is determined by calibrating the `twopoppy` model to the full simulations (Birnstiel et al., 2012). The maximum particle size limit therefore plays an important role in determining the dynamics of the large grains in the disk. Since most of the dust mass tends to be concentrated in the largest grains, which are also the most susceptible to radial drift, the dust-to-gas ratio of the disk can evolve significantly over time.

The turbulence parameter α_{t} and the fragmentation velocity v_{frag} are two of the most important parameters for determining the maximum particle size. The classically quoted range of values for α_{t} is $10^{-4} - 10^{-2}$ (e.g. Turner et al., 2014). However, recent studies of line broadening and dust settling in protoplanetary disks suggest that α_{t} is closer to the lower end of this range (Flaherty et al., 2015, 2018, 2017; Mulders & Dominik, 2012; Pinte et al., 2016). We therefore adopt $\alpha_{\text{t}} = 10^{-3}$ for our baseline model and comment on the consequences of varying α_{t} in § 3.3.²

Both theoretical studies and experiments have long suggested a significant difference between the fragmentation velocities of ice-free and icy dust (Blum & Wurm, 2008; Gundlach & Blum, 2015; Poppe et al., 2000; Wada et al., 2013). Most commonly, ice-free silicate dust is assumed to have a fragmentation velocity of 1 m/s, while icy grains have a fragmentation velocity closer to 10 m/s (e.g. Birnstiel et al., 2010; Drażkowska & Alibert, 2017; Pinilla et al., 2016). Such a difference in fragmentation velocity would lead to an abrupt change in the dust emission spectral index at water ice line (Banzatti et al., 2015) and there is observational evidence to support the occurrence of this phenomenon (Cieza et al., 2016). This increase in fragmentation

²We note that we use the same α_{t} for both the global disk gas evolution and the turbulent stirring of dust. In reality, these two can be different (see, e.g., Carrera et al., 2017; Drażkowska & Alibert, 2017).

velocity for dust exterior to the water ice line has also been invoked to explain the architecture of the solar system and exoplanetary systems (e.g. Morbidelli et al., 2015; Venturini et al., 2020) as well as planetesimal formation (Drażkowska & Alibert, 2017).

Despite this apparent consensus, recent theoretical and laboratory studies have begun to cast doubt on this story. Previous studies attributed the change in v_{frag} to an order of magnitude difference in the surface energies of icy and ice-free dust grains, but recent experimental work now suggests that their surface energies may in fact be quite similar (Gundlach et al., 2018; Steinpilz et al., 2019). Other studies conclude that the fragmentation velocity might exhibit a more complicated and non-monotonic dependence on temperature (e.g. Gundlach et al., 2018; Musiolik & Wurm, 2019), and this topic remains an area of active debate in the community (e.g. Kimura et al., 2020). In this study, we adopt the standard values of 1 m/s for ice-free and 10 m/s for icy grains for our baseline case, as these are close to the values derived from dynamical collision experiments. We assume that the ice line is located where the disk temperature drops below approximately $T = 200$ K, which places the ice line at 0.75 au in all of our models. We use Gaussian convolution to smoothly increase v_{frag} from 1 m/s at 250 K to 10 m/s at 150 K (e.g. Birnstiel et al., 2010). In § 3.3, we also present alternative models where we vary the value of v_{frag} both within and beyond the ice line and show that our results are qualitatively similar for a significant part of the plausible parameter space.

We utilize the approximations from Birnstiel et al. (2015) (Equation 6, 7, and 8 in their paper) that are implemented in `twopoppy` to reconstruct the full grain size distribution in the protoplanetary disk, which we need in order to calculate the corresponding dust opacity. We also modified the `twopoppy` code to include the size limit set by drift-induced fragmentation in the size distribution calculation, which in the default version of the code is approximated by the radial drift-limited grain size instead (see Birnstiel et al., 2012 for a discussion on the validity of this approximation). These approximations match the detailed simulations reasonably well, but can underestimate the number density of small grains. Although this will affect the opacity of the disk at short wavelengths (e.g., $\sim 1 \mu\text{m}$), we find that it only has a modest effect on the Rosseland mean opacity. We quantify this effect by comparing the mean opacity from this approximate method to the more accurate coagulation-fragmentation models from Birnstiel et al. (2011) in the fragmentation dominated region of the protoplanetary disk and find that the opacity from the

approximate method is a factor of two smaller. In regions dominated by radial drift, a change in the assumed power law index for the size distribution can also affect the number of small particles. However, since radial drift tends to dominate in the outer colder parts of the disk, the mean opacity in this region is dominated by slightly larger grains ($\sim 100\mu\text{m}$), which have a more robustly determined number density.

So far, we have discussed grain sizes, distributions, and opacities in the framework of a vertically integrated (2D) disk. If we wish to explore the 3D disk structure, we can extend these 2D models by using some reasonable approximations to calculate the density of dust and gas as a function of height from the midplane. This exercise is particularly valuable for planet formation models because growing protoplanets might not accrete most of their gas from the midplane (see § 3.4). We assume a Gaussian vertical profile with a scale height $H_{\text{gas}}(r) = c_s/\Omega$ for the gas. The midplane gas density is then given by $\rho_{\text{g},0} = \Sigma_{\text{g}}/\sqrt{2\pi}H_{\text{gas}}$ (Equation 3.7, which gives the expression for St in the midplane, also used this assumption). Dust sediments towards the midplane and is carried upward by turbulent diffusion so its vertical density distribution is significantly different from that of the gas. We use the expression for the steady-state vertical distribution of dust derived by Fromang & Nelson (2009):

$$\rho_{\text{d}}(z, a) = \rho_{\text{d},0} \exp\left[-\frac{\text{St}_0}{\alpha_{\text{t}}}\left(\exp\left(\frac{z^2}{2H_{\text{gas}}^2}\right) - 1\right) - \frac{z^2}{2H_{\text{gas}}^2}\right] \quad (3.11)$$

where $\rho_{\text{d},0}(a)$ is the dust density and $\text{St}_0(a)$ is the Stokes number in the midplane for a particular grain size. In reality, the vertical scale height for dust should be set by either turbulent diffusion or the Kelvin-Helmholtz shear instability, depending on which is larger at a given disk location (Rosenthal & Murray-Clay, 2018). We find that for our fiducial model turbulent diffusion sets the dust scale height throughout the disk. The Kelvin-Helmholtz shear instability only comes into play for models with low turbulence strength ($\alpha_{\text{t}} = 10^{-4}$) at large distances (30 – 100 au) and early times (0.1 – 1 Myr). For this subset of models, incorporating its effect on the vertical dust distribution decreases the final gas-to-core mass ratio for a $15 M_{\oplus}$ core by at most 15% if accretion stops at 1 Myr. Continued gas accretion beyond this time wipes out the effect of incorporating Kelvin-Helmholtz instability in our analysis. Since accounting for Kelvin-Helmholtz instability has a negligible impact on our results, we choose to omit it from our work.

Calculation of dust opacity

The composition of dust grains in protoplanetary disks is a topic of active research (see recent review by Oberg & Bergin, 2021). We adopt the grain composition prescribed in the DSHARP survey papers and use the publicly available tools generously provided by the survey team for the calculation of grain properties (Birnstiel et al., 2018). The DSHARP composition mixture consists of water ice (optical properties from Warren & Brandt, 2008), ‘astrosilicates’ (Draine, 2003), and refractory organics and troilite (FeS) (Henning & Stognienko, 1996). The Bruggeman mixing rule is employed to obtain the optical constants for the mixture. We adopt the same grain composition for the entire disk, as removing water from our mixture has only a small effect ($\lesssim 15\%$, accounting for the difference in grain densities and optical properties but keeping the grain size distribution fixed) on the calculated opacity. Our simulations also do not account for the effect of condensation/sublimation on grain size and mass for particles moving across the ice line when calculating the grain size distribution. For the adopted DSHARP mixture, water’s sublimation would reduce dust mass only by 20% within the ice line. Accounting for the reduced mass and increased density of ice free grains would reduce the grain size by $\sim 15\%$, which will have some effect on their dynamics. However, these effects are negligible compared to the other sources of uncertainty in our model.

We use Mie theory to calculate the dust opacity. Our Mie code is publicly available as part of PLATON (Zhang et al., 2019, 2020), which uses the algorithm outlined by Kitzmann & Heng (2018). For particle sizes and wavelengths for which the full Mie treatment is impracticable, we resort to widely used approximations. We use the geometric optics limit to calculate the absorption cross-section of particles for which $|m|x > 1000$ and $|m - 1|x > 0.001$, where m is the complex refractive index of the particle and $x = 2\pi a/\lambda$ is the size parameter (here a being the particle size and λ being the wavelength, van de Hulst, 1957). Specifically, we use the approximation described in Laor & Draine (1993), which uses the extinction coefficient calculated using Rayleigh-Gans approximation (Q_{RG}) to obtain the extinction coefficient in the geometric optics limit (Q_{ext}):

$$Q_{\text{ext}} \approx \frac{Q_{\text{RG}}}{(1 + 0.25Q_{\text{RG}}^2)^{1/2}} \quad (3.12a)$$

$$Q_{\text{RG}} = \frac{32|m - 1|^2 x^4}{27 + 16x^2} + \frac{8}{3} \text{Im}(m)x \quad (3.12b)$$

where $\text{Im}(m)$ is the imaginary part of the refractive index.

Once we have calculated the absorption coefficient for different particle sizes a and wavelength λ , the wavelength dependent opacity $\kappa_{\lambda,a}$ for each particle size per gram of dust is given by:

$$\kappa_{\lambda,a} = \frac{\pi a^2 Q_{\text{ext}}(\lambda, a)}{4\pi \rho_s a^3 / 3}. \quad (3.13)$$

To calculate the opacity per gram of dust in the protoplanetary disk, we need the normalized size distribution of the grains at a specific location. We utilize the mass density distribution of dust $\Sigma_d(r, a)$, calculated in logarithmic bins of grain size using twopoppy. The opacity per gram of dust in the protoplanetary disk is then obtained using:

$$\kappa_\lambda = \frac{\int \kappa_{\lambda,a} \Sigma_d(r, a) \, d \ln a}{\int \Sigma_d(r, a) \, d \ln a}. \quad (3.14)$$

This wavelength dependent opacity is used to calculate the Rosseland mean opacity per gram of dust:

$$\frac{1}{\kappa_R} = \frac{\int_0^\infty (1/\kappa_\lambda) (\partial B_\lambda / \partial T) d\lambda}{\int_0^\infty (\partial B_\lambda / \partial T) d\lambda} \quad (3.15)$$

where B_λ is the Planck function and T is the temperature used in our protoplanetary disk model. To obtain the Rosseland mean opacity per gram of protoplanetary disk material, we multiply the κ_R obtained above by the local dust-to-gas ratio $\epsilon = \Sigma_d(r)/\Sigma_g(r)$ of the disk. We do not include the gas opacity in our calculations, as the dust opacity dominates even in the regions with the lowest dust-to-gas ratio and/or the largest particle sizes (see § 3.4).

3.3 Dust Opacity in Protoplanetary Disks

Opacity from a simulated size distribution

In this section, we focus on quantifying the changes in the dust opacity due to location-dependent variations in the dust size distribution. We show the full radially-varying twopoppy size distribution in the top panel of Figure 3.1 and the resulting Rosseland mean opacity per gram of dust in Figure 3.2. The size distribution in the inner 10 au is dominated by coagulation-fragmentation equilibrium, while the increase in v_{frag} beyond the water ice line at ~ 1 au manifests as an increase in the maximum grain size ($a_{\text{frag}} \propto v_{\text{frag}}^2$ from Equation 3.8). Since larger grains contain more mass and the size distribution is slightly top-heavy, this increase in

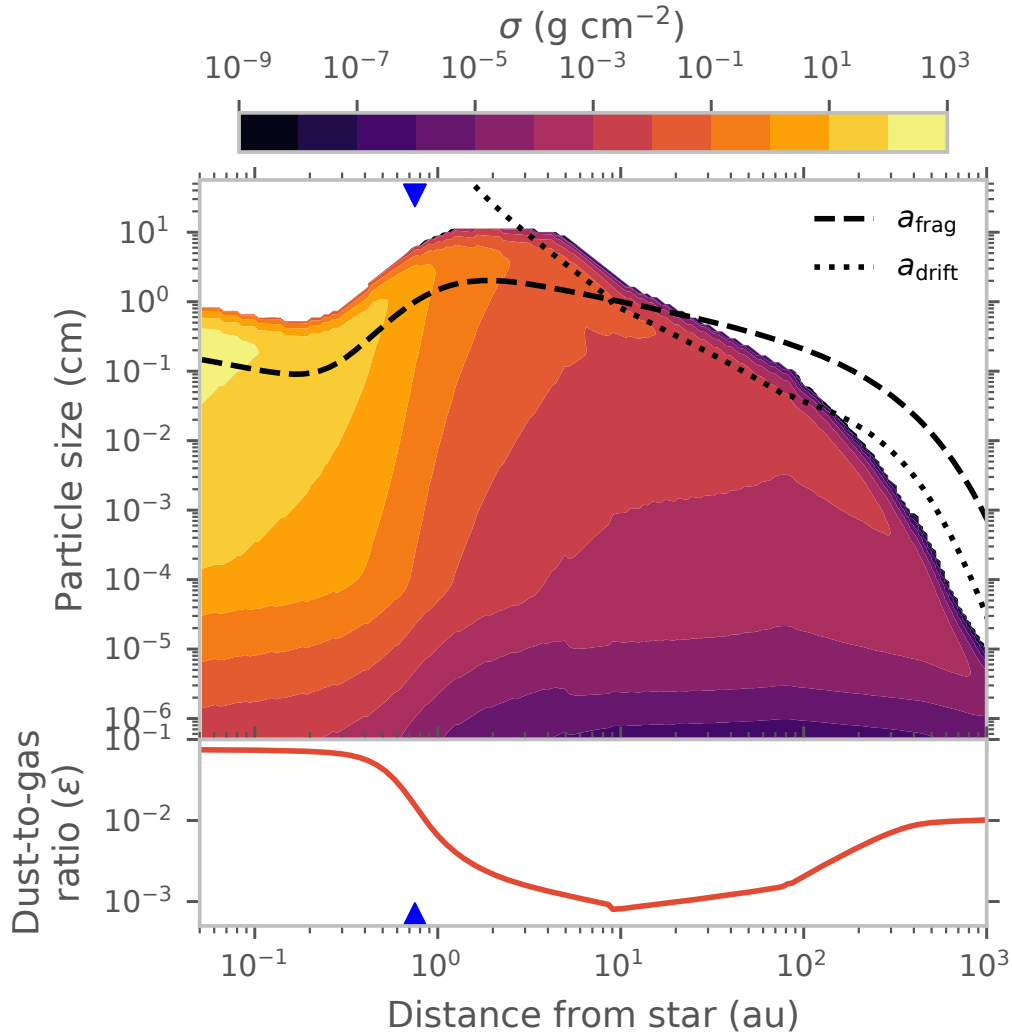


Figure 3.1: Size distribution and dust-to-gas ratio (ϵ) at time $t = 1$ Myr for a twopoppy simulation with variable v_{frag} and $\alpha_t = 10^{-3}$. The size limits imposed by fragmentation and drift are shown with dashed and dotted line in the upper panel. The location of the ice line is marked with blue triangles.

v_{frag} causes the surface density of small grains ($\lesssim 10\mu\text{m}$) to decrease by multiple orders of magnitude. Because these grains contribute significantly to κ_R , this change is responsible for the factor of ~ 5 decrease in the simulated κ_R shown in Figure 3.2. Beyond ~ 10 au, the maximum grain size is set by radial drift of the large grains instead of fragmentation as particles drift inward before they can grow to the fragmentation barrier. Without fragmentation to replenish the supply of small grains, the size distribution in this region becomes more top heavy relative to the distribution produced by the coagulation-fragmentation equilibrium in the inner

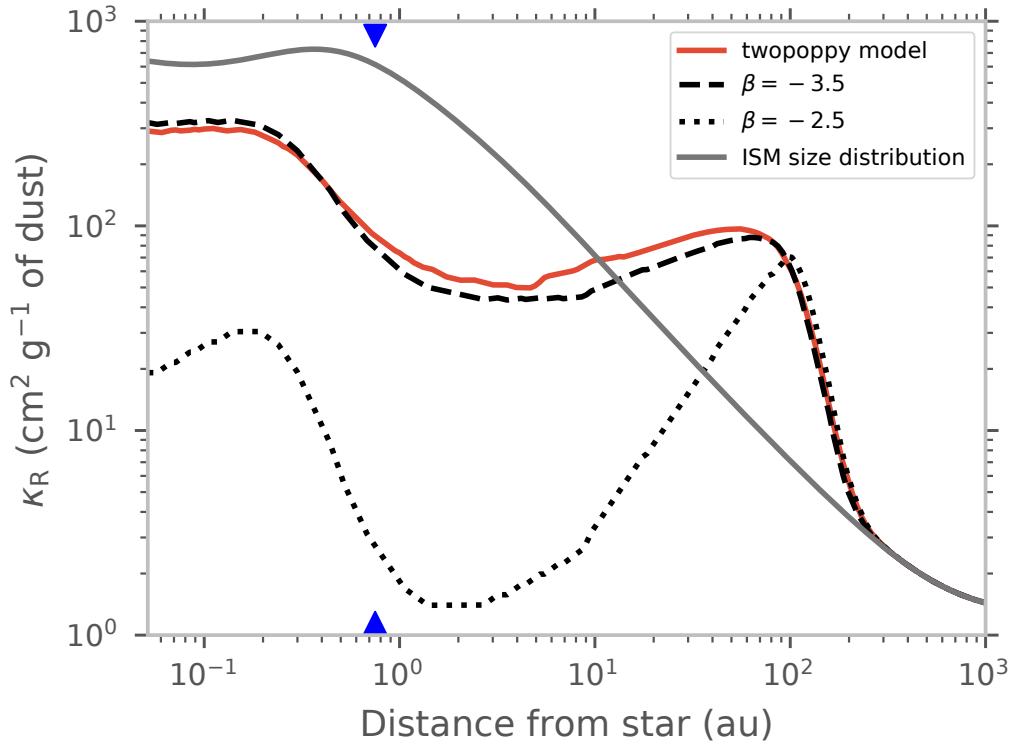


Figure 3.2: Rosseland mean opacity per gram of dust as a function of distance from the star at time $t = 1$ Myr. We adopt $\alpha_t = 10^{-3}$ and a variable v_{frag} that changes across the water ice line for our twopoppy model. For the power law distributions, a_{max} is set by the location specific maximum grain size calculated from twopoppy, which is given by Equation 3.8 (fragmentation-limited), Equation 3.10 (drift-limited), or the growth-timescale limit. The location of the ice line is marked with blue triangles.

disk. κ_R in this cold outer disk region is dominated by larger grains ($\sim 100 \mu\text{m}$) that are relatively abundant, leading to a modest increase in the simulated κ_R as shown in Figure 3.2.

In Figure 3.2, we compare κ_R for size distribution simulated by twopoppy at time $t = 1$ Myr with three different grain size distributions: the ISM size distribution ($\beta = -3.5, a_{\text{max}} = 0.25 \mu\text{m}$) and power law distributions with β of either -2.5 or -3.5 and maximum particle sizes set to the fragmentation (Eq. 3.8), radial drift (Eq. 3.10), or growth-timescale limits, as appropriate. We find that the dust opacity for the simulated size distribution differs significantly from that of the ISM size distribution (see also Savvidou et al., 2020). The opacity of the ISM size distribution only varies as a consequence of the decreasing temperature in the disk. In contrast, opacity from the simulated size distribution reflects radially varying

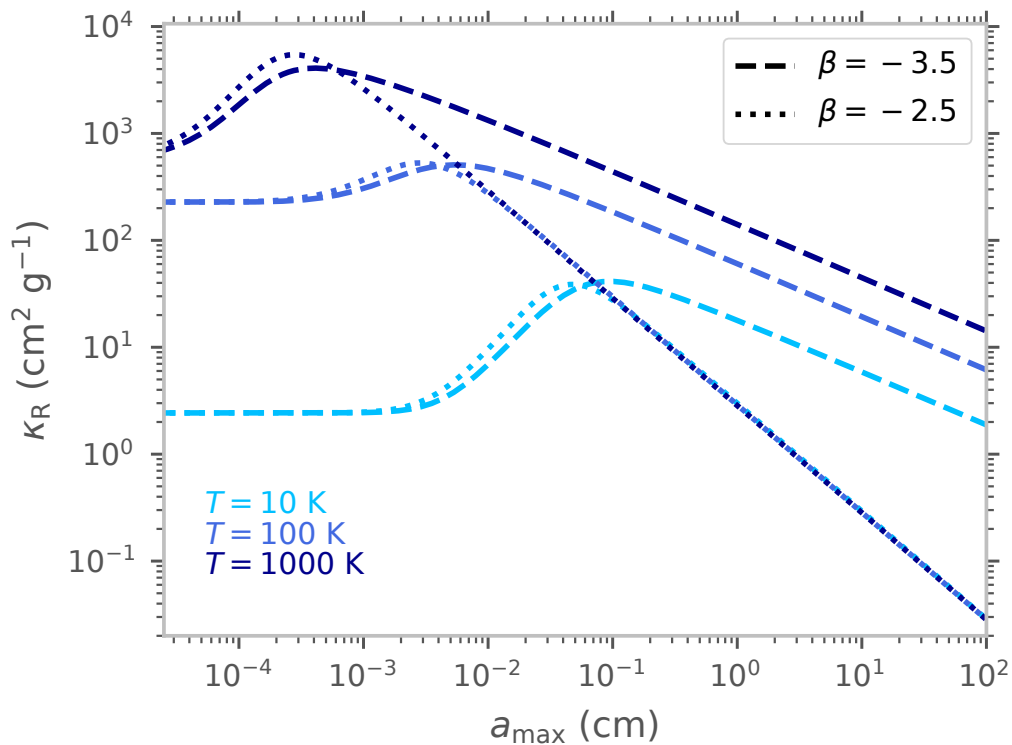


Figure 3.3: Rosseland mean opacity per gram of dust for a power law grain size distribution with $\beta = -3.5$ and -2.5 and three different temperatures. The lowest value of $a_{\max} = 0.25\mu\text{m}$ on this plot is the commonly adopted value for the ISM size distribution.

grain growth and transport processes in the disk (e.g., Akimkin et al., 2020 make the same observation). It is noteworthy that a power law distribution with $\beta = -3.5$ (same as that of the ISM) and a_{\max} set by the relevant physics of fragmentation and radial drift yields a κ_R profile that is in good agreement with the simulated results.

We illustrate the effect of the maximum grain size a_{\max} and the power law index β on κ_R in Figure 3.3. The smallest value of a_{\max} shown on the plot corresponds to the ISM size distribution. For top heavy distributions with $\beta > -4$, most of the mass is concentrated in the larger dust grains. Increasing a_{\max} therefore redistributes dust mass from smaller grains to larger grains, reducing the total number of small grains. This can significantly alter the overall opacity of the dust: if we compare κ_R for $a_{\max} = 0.1$ cm (which is more typical for dust in a disk) and $\beta = -3.5$ with the equivalent ISM value, it is almost 20 times larger at 10 K. Conversely, this same depletion of smaller grains for $a_{\max} = 0.1$ cm means that κ_R is half the corresponding ISM value at 1000 K. Using a realistic a_{\max} for the power law size distribution of dust in a

protoplanetary disk therefore leads to a reduced κ_R in the hotter inner disk and an enhanced κ_R in the colder outer disk.

In contrast to this result, the opacity from a power law size distribution with $\beta = -3.5$ and a_{\max} set by Equations 3.8 and 3.10 and growth timescale τ_{grow} provides a relatively good match to the opacity from the full simulated size distribution. The power law size distribution with $\beta = -2.5$ does not perform as well; this is due to the top heaviness of the $\beta = -2.5$ size distribution, which leads to a dramatic depletion in the number of small grains. Since the small grains that contribute most significantly to κ_R at the protoplanetary disk temperatures are absent, the opacity for $\beta = -2.5$ is $\gtrsim 1$ order of magnitude lower than that for our `twopoppy` simulation. These results for different β values are similar to previous findings for the dust opacity at specific wavelengths (e.g. D’Alessio et al., 2001).

Opacity from a radially varying dust-to-gas ratio

Now that we have explored the effect of a radially varying dust size distribution on the Rosseland mean opacity per gram of dust, we can account for the radially varying dust-to-gas ratio ϵ . As noted earlier, we assume that the contribution of the gas opacity to κ_R is negligible. The dust-to-gas ratio (or metallicity) is typically fixed to a single global value (e.g. Bitsch et al., 2015; Mordasini, 2018). However, this ratio can change radially as dust abundance evolves. Here, we use our simulations to explore how the distribution of dust evolves in time as a function of assumed disk properties such as the turbulence strength α_t and v_{frag} .

We begin our simulation with a globally uniform $\epsilon = 0.01$ and show the resulting vertically integrated dust-to-gas ratio ($\epsilon = \Sigma_d/\Sigma_g$) at time $t = 1$ Myr for our fiducial model in the bottom panel of Figure 3.1. As grains begin to grow and their Stokes number increases, they face a stronger headwind from the gas and start drifting towards the star (see Birnstiel et al., 2012 for a more detailed discussion on how the dust-to-gas ratio evolves in the disk). In the outermost regions of the disk ($\gtrsim 100$ au), the grain growth rate is so slow that particles do not reach the drift barrier, i.e. they do not drift very efficiently. ϵ far out does not evolve significantly and only decreases slowly as one moves closer to 100 au. Between ~ 10 and 100 au, grains drift inward faster than they can grow, causing the dust-to-gas ratio to decrease over time. In the inner disk, orbital timescales are shorter and grain growth is rapid. This means that grains reach the fragmentation barrier before they can drift appreciably. For a fixed v_{frag} and α_t , the Stokes number of the largest grains also decreases as one

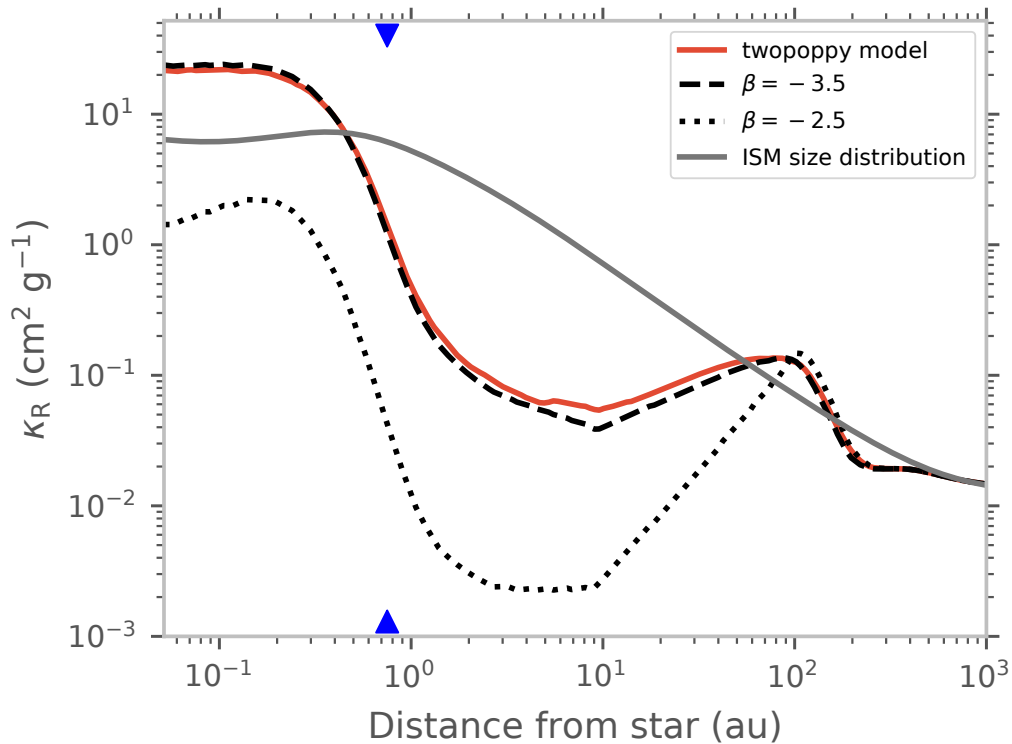


Figure 3.4: Rosseland mean opacity per gram of protoplanetary disk material at time $t = 1$ Myr and for a variable v_{frag} and $\alpha_t = 10^{-3}$. This plot is similar to Figure 3.2 except that the opacity per gram of dust is here multiplied by the radially-varying dust-to-gas ratio. For the ISM size distribution, the dust-to-gas ratio is assumed to be 0.01 everywhere. The location of the ice line is marked with blue triangles.

moves closer to the star (see Eq. 3.8). This means that grains in the fragmentation-dominated inner disk are better coupled to the gas, and the dust-to-gas ratio does not decline as rapidly as in the drift-dominated outer disk region. In fact, the dust-to-gas ratio in the inner disk may even be enhanced by the migration of dust from the outer disk.

Depending on the magnitude of the velocity offset, the change in v_{frag} across the ice line can have a dramatic effect on the dust dynamics. When large grains drifting inward from the outer disk cross the ice line they lose their ice and their fragmentation velocity decreases to the value characteristic of ice-free dust. Post-fragmentation grains are therefore smaller and their St is reduced, slowing their inward drift and causing a pile up of dust inside the ice line. The magnitude of this effect can be quite large: for a factor of 10 decrease in v_{frag} across the ice line, the St of the largest grains decreases by almost two orders of magnitude ($St_{\text{frag}} \propto v_{\text{frag}}^2$). As shown in

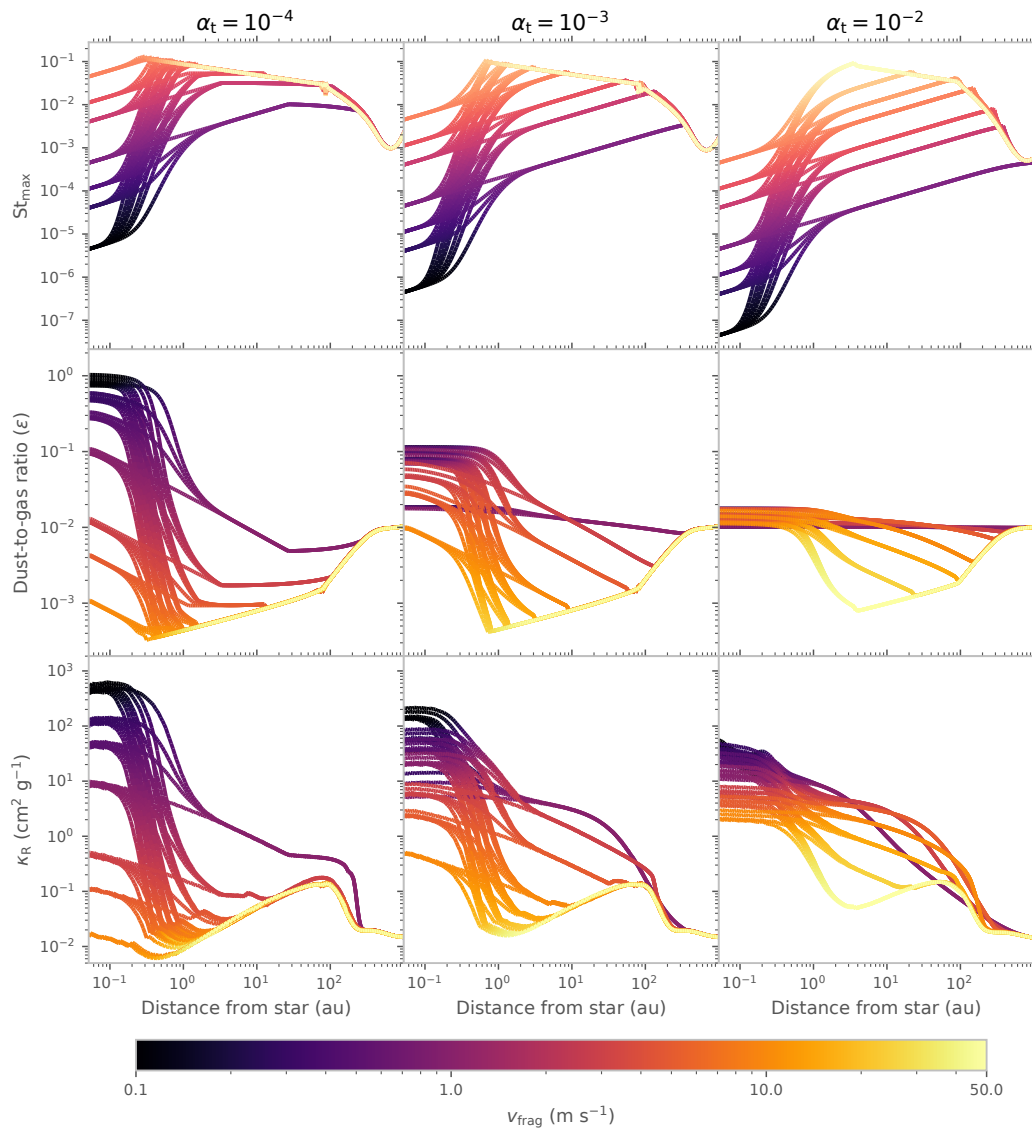


Figure 3.5: The Stokes number of the largest grain size (St_{\max}), dust-to-gas ratio (ϵ), and Rosselland mean opacity per gram of protoplanetary disk material for a range of fragmentation velocities within and beyond the water snow line as well as three different turbulence strengths after 1 Myr of evolution. The fragmentation velocity v_{frag} takes values in the range $0.1 - 10 \text{ m s}^{-1}$ for ice-free grains and $1 - 50 \text{ m s}^{-1}$ for icy grains (Blum & Wurm, 2008; Gundlach & Blum, 2015). The ice line is located at 0.75 au in all of our models.

Figure 3.1 this enhances the dust-to-gas ratio ϵ within ~ 1 au by almost an order of magnitude at $t = 1$ Myr relative to the starting ϵ of 0.01. Conversely, most of the disk beyond 1 au is significantly depleted of dust with $\epsilon \sim 10^{-3}$ for a large part of the outer disk. The effect of radial drift, fragmentation, and a change in v_{frag} across the ice line on dust dynamics have been extensively described in Birnstiel et al. (2010); Pinilla et al. (2017), and we refer the reader to these studies for a comprehensive exploration of this topic.

We can use this radially and temporally varying dust-to-gas ratio to update our calculation of the Rosseland mean opacity of the disk. Figure 3.4 shows κ_{R} per gram of protoplanetary disk material for our simulated size distribution. This plot is the same as Figure 3.2 except that the κ_{R} profiles shown in that figure are now multiplied by the dust-to-gas ratio. We plot the ISM κ_{R} assuming a constant dust-to-gas ratio of 0.01, in order to better illustrate the differences between our model and the widely used ISM opacity model. Within the ice line, the dust-to-gas ratio is enhanced by a factor of ten relative to the ISM model, which partially compensates for the reduction in opacity due to the increased grain sizes (Figure 3.2). As we move beyond the ice line, the decreasing quantity of dust and increasing concentration of dust mass in larger particle sizes lead to a steep decline in the opacity. Our κ_{R} between ~ 1 and ~ 10 au is smaller than the ISM value by more than a factor of ten.

Dependence on the assumed fragmentation velocity and turbulence strength

Our fiducial model predicts that the dust opacity will decrease by more than two orders of magnitude as we move outside the ice line. However, the magnitude of this gradient depends strongly on the absolute and relative efficiency of dust transport in the inner and outer disk. The transition from the fragmentation-dominated to the drift-dominated regime can be expressed as a function of the fragmentation velocity v_{frag} and the turbulence strength α_{t} (e.g. Birnstiel et al., 2015):

$$\frac{v_{\text{frag}}^2}{v_{\text{K}}^2} > \frac{3\alpha_{\text{t}}\epsilon}{\gamma}. \quad (3.16)$$

This transition also depends on the Keplerian velocity v_{K} , the dust-to-gas ratio ϵ , and $\gamma = |\text{dln}P/\text{dln}r|$. All of these quantities can vary as a function of r (although we assume α_{t} is constant in our work) and in regions where this inequality is satisfied, the disk becomes drift-dominated. Since α_{t} and v_{frag} are not known a priori, we run a grid of models over $\alpha_{\text{t}} \in [10^{-4}, 10^{-3}, 10^{-2}]$ where $\alpha_{\text{t}} = 10^{-3}$ is our fiducial, and $v_{\text{frag}} = 0.1 - 10 \text{ m s}^{-1}$ for ice-free grains and $1 - 50 \text{ m s}^{-1}$ for icy grains (e.g. Blum

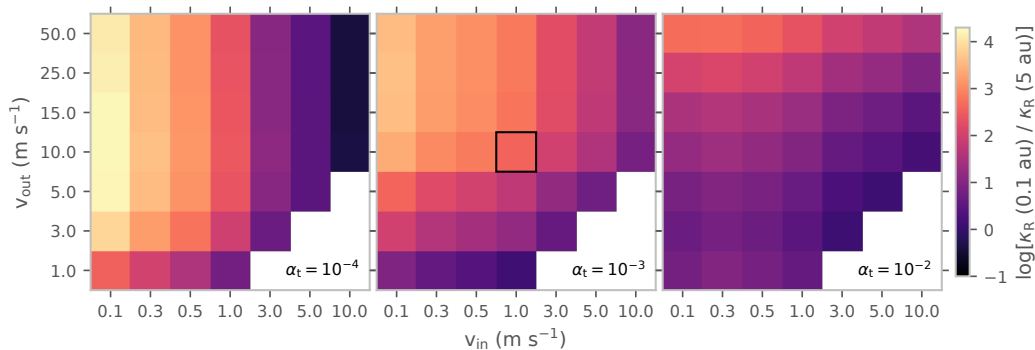


Figure 3.6: Ratio of the Rosseland mean opacity per gram of protoplanetary disk material at 0.1 au and 5 au after 1 Myr of evolution. The axes labels v_{in} and v_{out} stand for the fragmentation velocity within and beyond the ice line. Our fiducial model is outlined with a black square.

& Wurm, 2008; Gundlach & Blum, 2015). We consider all possible combinations of these two fragmentation velocities as long as they meet the requirement that v_{frag} for icy grains is greater than or equal to v_{frag} for ice-free grains³.

Figure 3.5 shows the Stokes number of the largest grains St_{max} , the dust-to-gas ratio ϵ , and the disk’s Rosseland mean opacity κ_{R} for this grid of models. As α_{t} decreases, we find that ϵ varies more strongly with orbital distance: a consequence of the difference in the absolute values of St_{max} for different α_{t} . For $\alpha_{\text{t}} = 10^{-4}$, $St_{\text{max}} \gtrsim 10^{-2}$ between ~ 1 and 100 au. A larger Stokes number beyond the ice line leads to more efficient inward drift of dust from the outer to the inner disk. For lower α_{t} , the transition to the drift-dominated region also happens closer in to the star (see Equation 3.16 above), creating a ‘kink’ in St_{max} and ϵ profiles (e.g. at 10 au in our fiducial model, see bottom panel of Figure 3.1). In the outer disk, all models that transition to the drift-dominated regime converge to similar values for St_{max} and ϵ . For $\alpha_{\text{t}} = 10^{-2}$ this transition moves outside ~ 100 au for most models, causing the disk to be globally fragmentation-dominated. As a result, St_{max} has a lower value throughout the disk and dust migration is suppressed.

The high St in the low α_{t} disk model, which aids the radial transport of dust grains in the outer disk, can also potentially diminish the dust pile-up in the inner disk. Since $St_{\text{frag}} \propto \alpha_{\text{t}}^{-1}$, St_{max} in the inner disk is larger for lower α_{t} . As long as $St_{\text{max}} < 1$, the inward drift velocity will be larger for a larger value of St_{max} . This means that

³We note that the *twopoppy* models are calibrated with the full numerical models for a smaller range of v_{frag} (1 – 10 m/s) than we study here. However, this should not be a major concern as the underlying collisional outcome model is the same.

dust grains in the inner disk will move inward faster when α_t is lower, reducing the timescale over which dust is depleted in the inner disk and preventing a pile-up of dust drifting in from the outer disk. This is evident in the middle panel of Figure 3.5, which shows that when $\alpha_t = 10^{-4}$ the dust-to-gas ratio in the inner disk can be either very high (~ 1 , efficient pile-up, low v_{frag}) or very low ($\sim 10^{-3}$, no pile-up, high v_{frag}) depending on the assumed fragmentation velocities. Maximizing the dust-to-gas ratio and consequently the opacity gradient in the radial direction therefore requires an intermediate value of α_t , which in turn is dependent on v_{frag} .

Larger differences in the v_{frag} values for icy and ice-free grains lead to a larger change in St_{max} across the ice line. This in turn results in a depletion of dust in the outer disk and a pile up of dust in the inner disk, leading to larger opacity contrast between the inner and the outer disk (see Figure 3.6), as long as the value of α_t does not nullify these effects by either producing globally low values of St_{max} (well coupled dust and little dust transport) or large values of St_{max} within the ice line (dust drifts towards the star and does not pile up). However, when v_{frag} is large everywhere in the disk (e.g. 10 m/s for ice-free grains and 50 m/s for icy grains), particles will have large St_{max} and will rapidly drain onto the star.

To simplify comparisons between models, in Figure 3.6 we focus on the ratio of the disk opacity κ_R at 0.1 au and 5 au. These distances are chosen to best capture the opacity contrast for the full set of disk models; they are also approximately where sub-Neptunes and gas giants are most numerous, respectively. We find that there is a large range of choices for v_{frag} and α_t that lead to opacity contrasts that are equal to or larger than the one in our fiducial model. Decreasing α_t enlarges St_{max} and accelerates the grain radial transport, enhancing the contrast in the opacity across the snow line. Larger differences in v_{frag} between icy and ice-free grains also produce greater opacity contrasts as they lead to a strong gradient in dust transport efficiency across the snow line.

The opacity contrast with increasing v_{frag} for icy grains saturates at a value that depends on the v_{frag} for ice-free grains. This is most evident in the lower α_t models and occurs because St_{max} and ϵ converge to similar values in the outer disk (Figure 3.5). Beyond this limit, increasing the v_{frag} for icy grains does not lead to an increase in the Stokes number of the largest grains in the outer disk but instead simply pushes the transition from fragmentation-dominated regime to drift-dominated regime inward. This limits the supply of dust from the outer disk and causes the opacity contrast to saturate at a fixed v_{frag} for ice-free grains.

Recent observations of protoplanetary disks appear to favor values for α_t that are lower than 10^{-2} (e.g. Flaherty et al., 2018; Pinte et al., 2016). As we discussed earlier, it is less clear how large the difference in v_{frag} for icy and ice-free dust grains may be (Gundlach et al., 2018; Kimura et al., 2020; Steinpilz et al., 2019). However, our parameter space exploration suggests that there are a wide range of plausible scenarios that can lead to a large opacity gradient between the inner and outer disk regions.

Dust opacity in a 3D disk

So far, we have only considered vertically integrated disk models. In this section we examine the vertical structure of the dust distribution and its potential importance for planet formation (e.g., polar accretion of gas onto planetary cores; Cimerman et al. 2017; Fung et al. 2015; Lambrechts & Lega 2017; Ormel et al. 2015) and modelling protoplanetary disks. The vertical structure of gas and dust is controlled by a complicated coupling between the disk temperature, opacity, and turbulence. Self-consistently taking these couplings into account is beyond the scope of our study; instead, we utilize a simple vertically isothermal disk model. Even with this simplification, our model produces a non-uniform vertical distribution of dust grains.

We use the prescribed radial temperature structure from Equation 3.3 and assume a vertically isothermal disk structure in order to calculate the vertical structure of the dust and gas. Under this assumption, the gas density $\rho_g \propto e^{-z^2/H_{\text{gas}}^2}$ where z is the height from the midplane and $H_{\text{gas}} = c_s/\Omega$ is the gas disk scale height. For the vertical dust density distribution, we utilize the expression obtained by Fromang & Nelson (2009) for the steady-state distribution of dust (Equation 3.11). We calculate the 3D dust density $\rho_d(z, a)$ for logarithmically binned grain sizes and sum it to obtain the total dust density $\rho_d(z)$. The dust-to-gas ratio ϵ is then simply calculated as ρ_d/ρ_g .

The top panel in Figure 3.7 shows the resulting dust-to-gas ratio ϵ as a function of z and distance from the star for our fiducial model at a disk age of 1 Myr. The differences in ϵ as a function of z within and beyond the ice line can be understood by examining the Stokes number of the largest grains St_{max} present in each region of the disk (bottom panel of Figure 3.7). Within ~ 1 au, St_{max} can fall down to $\sim 10^{-4}$; these particles will be vertically well-mixed with the gas—i.e. the scale height of dust grains is comparable to that of the gas—flattening the vertical gradient in

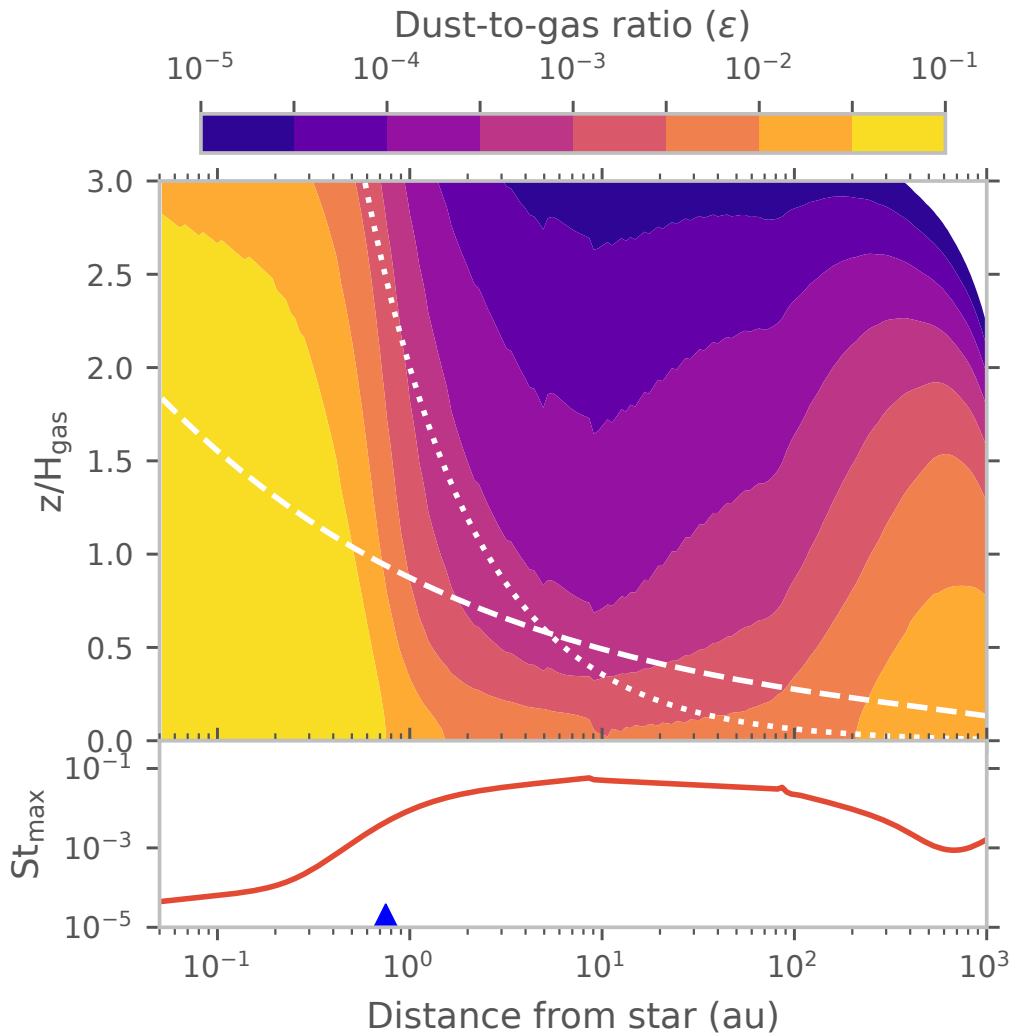


Figure 3.7: The top panel shows the dust-to-gas ratio ϵ as a function of height above the midplane z and distance from the star after 1 Myr of evolution. The white dashed and dotted lines mark the height of the Hill radius R_{Hill} and Bondi radius R_{Bondi} of a $15 M_{\oplus}$ planet, respectively. The bottom panel shows the midplane Stokes number of the largest grains present in the disk at $t = 1$ Myr. The water ice line is marked with a blue triangle. Well coupled grains within the ice line lead to efficient vertical mixing of grains and hence a weak dependence of ϵ on z . Beyond the ice line, large grains that dominate the dust mass settle close to the midplane, which leads to a strong decline in ϵ as a function of z .

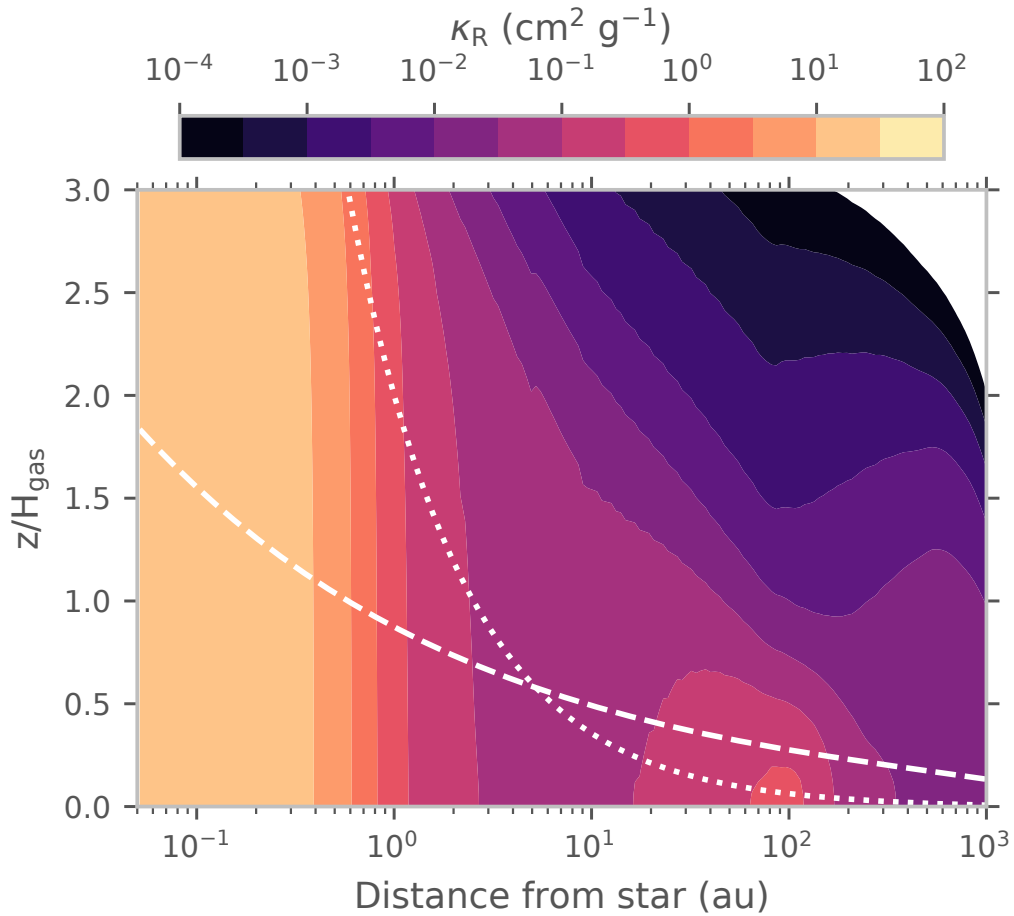


Figure 3.8: Rosseland mean opacity per gram of protoplanetary disk material as a function of height above the midplane z and distance from the star after 1 Myr of evolution. The white dashed and dotted lines mark the height of the Hill radius R_{Hill} and Bondi radius R_{Bondi} of a $15 M_{\oplus}$ planet, respectively. Vertically well mixed dust within the ice line leads to little variation in κ_R as a function of z . Grain settling and a strong decline in ϵ with z leads to a gradient in κ_R as a function of z beyond the ice line.

dust-to-gas ratio. However, outside the ice line, large grains with $St_{\max} \gtrsim 10^{-2}$ are present. These grains are concentrated near the midplane and constitute most of the dust mass budget, resulting in a steep vertical gradient in ϵ . Figure 3.8 shows the Rosseland mean opacity of the disk as a function of height from the midplane and distance from the star. As expected, we find that the disk opacity is essentially independent of z within the ice line. In contrast, the concentration of large grains near the midplane beyond the ice line leads to a decline in disk opacity as a function of z .

We mark the Hill radius $R_{\text{Hill}} = a(M_p/3M_*)^{1/3}$ and Bondi radius $R_{\text{Bondi}} = GM_p/c_s^2$ of a $15 M_\oplus$ core with a dashed and dotted line, respectively, in Figures 3.7 and 3.8. We choose a mass of $15 M_\oplus$ as our fiducial case as it is representative of a giant planet core. Planetary cores close to thermal or superthermal mass (equivalently, $R_{\text{Hill}} \leq R_{\text{Bondi}}$) are expected to accrete gas from heights on the order of the Hill radius (e.g. Lambrechts & Lega, 2017). For subthermal cores (equivalently, $R_{\text{Hill}} > R_{\text{Bondi}}$), on the other hand, the natural length scale is expected to be the Bondi radius (see, e.g., subthermal cases of Ormel et al. 2015 and Fung et al. 2019). The exact origin height of the accretion flow is unclear given how unsteady the flow morphology is in three-dimensional calculations. In this work, we assume that the material accreted by the planet is well represented by the properties of dust and gas present at $\min(R_{\text{Hill}}, R_{\text{Bondi}})$ above the disk midplane. In § 3.4, we show the effect of varying this height on the calculated gas-to-core mass fraction of a planet.

Figure 3.9 highlights how the radial profile of dust-to-gas ratio and dust opacity differ for different heights above the disk midplane: $z = 0$ (disk midplane), $z = H_{\text{gas}}$, and $z = R_{\text{Hill}}$ and $z = \min(R_{\text{Hill}}, R_{\text{Bondi}})$ for a $15 M_\oplus$ core. We also provide a calculation of the vertically integrated disk model for comparison. In the top panel we plot κ_R per gram of dust, which depends only on the local size distribution of the dust. The features present in the κ_R profiles result from changes in the relative abundances of the grain sizes that contribute most to the opacity at the local temperature. In the disk midplane beyond the ice line, most of the opacity contribution comes from grains that are $10 - 100 \mu\text{m}$ in size, but most of the mass (per gram of dust) resides in grains that are larger than this size range. This leads to a substantial decrease in κ_R per gram of dust in the disk midplane in these regions. Conversely, the high relative abundance of small grains at $z = H_{\text{gas}}$ (only small grains can be lifted to this height) leads to a strong enhancement in κ_R per gram of dust at this height. The κ_R

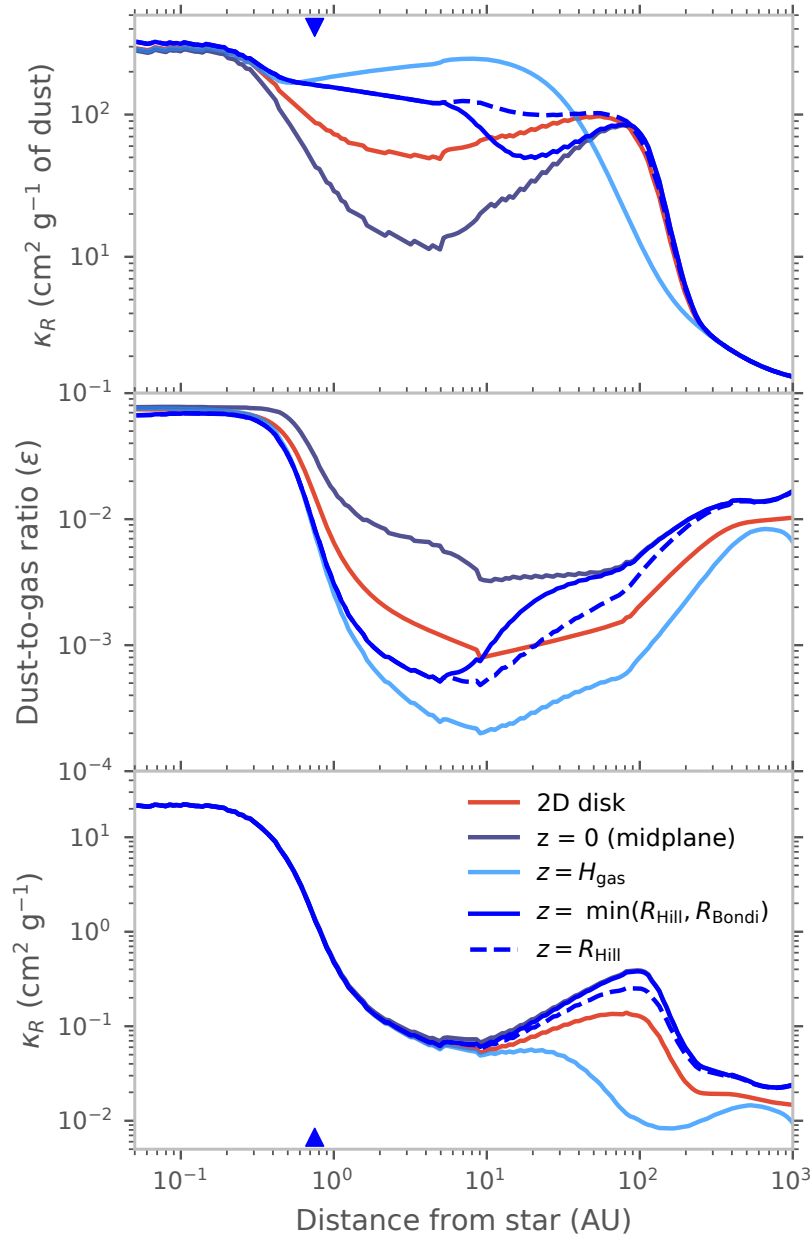


Figure 3.9: A comparison of the Rosseland mean opacity per gram of dust, dust-to-gas ratio ϵ , and Rosseland mean opacity per gram of protoplanetary disk material κ_R for our fiducial 2D disk integrated model and our 3D disk model after 1 Myr of evolution. We plot the values of these quantities in the disk midplane ($z = 0$), a single gas scale height above the midplane ($z = H_{\text{gas}}$), and at heights of a $15 M_{\oplus}$ planet's R_{Hill} and $\min(R_{\text{Hill}}, R_{\text{Bondi}})$ above the midplane. The water ice line is marked with blue triangles.

profile at $z = R_{\text{Hill}}$ and $z = \min(R_{\text{Hill}}, R_{\text{Bondi}})$ in the top panel of Figure 3.9 can be understood using these same principles.

Dust-to-gas ratio increases with higher concentration of large grains for a top heavy size distribution and so we observe a flipped behavior for the ϵ ratio profile (middle panel of Figure 3.9) where it reaches lower values at higher altitudes beyond the ice line. Since larger grains settle close to the midplane, ϵ is highest at the midplane and decreases higher up. The ϵ evaluated at $\min(R_{\text{Hill}}, R_{\text{Bondi}})$ converges to that of the midplane in the innermost and the outermost region. The former arises from efficient vertical mixing whereas the latter materializes from $R_{\text{Hill}}/H_{\text{gas}}$ and $R_{\text{Bondi}}/H_{\text{gas}}$ approaching zero in the outer disk (see R_{Hill} and R_{Bondi} profiles in Figure 3.7).

In the bottom panel of Figure 3.9, we plot the mean opacity per gram of protoplanetary disk material, which is the product of the quantities plotted in the upper two panels. Regardless of our vertical location in the disk, we see the same precipitous decline in disk opacity as in the vertically integrated disk model. Notably, κ_{R} decreases by ~ 2 orders of magnitude between 0.1 au and 5 au at the height of our fiducial planetary core's R_{Hill} . Within ~ 10 au, the κ_{R} profiles for the vertically integrated disk model and the different z values are nearly identical. This happens within the ice line as a result of efficient vertical mixing of grains (i.e. both κ_{R} per gram of dust and ϵ are roughly constant as a function of z). Beyond the ice line and within 10 au, the sharp decline in ϵ with z is counterbalanced by the increase in κ_{R} per gram of dust with z to yield a weakly z dependent κ_{R} (per gram of protoplanetary disk material).

Time evolution of the dust opacity

Up to this point, we have presented results from our models after 1 Myr of disk evolution. In this section, we explore the time-varying grain size distribution and dust-to-gas-ratio from 0.1 to 10 Myrs, where the lower limit is chosen to represent the plausible time at which massive planetary cores emerge. Figure 3.10 demonstrates that the absolute values of the dust-to-gas ratio and mean opacity throughout the disk tend to decline over time. This is due to the global depletion of dust in the disk as it gradually accretes onto the star. Because the timescale over which ϵ and κ_{R} evolve lengthens as time goes on, we present our results as a function of log time. Already by 0.1 Myr, the dust-to-gas ratio and κ_{R} profiles converge to shapes that are qualitatively similar to those of our fiducial 1 Myr model. Although temporal

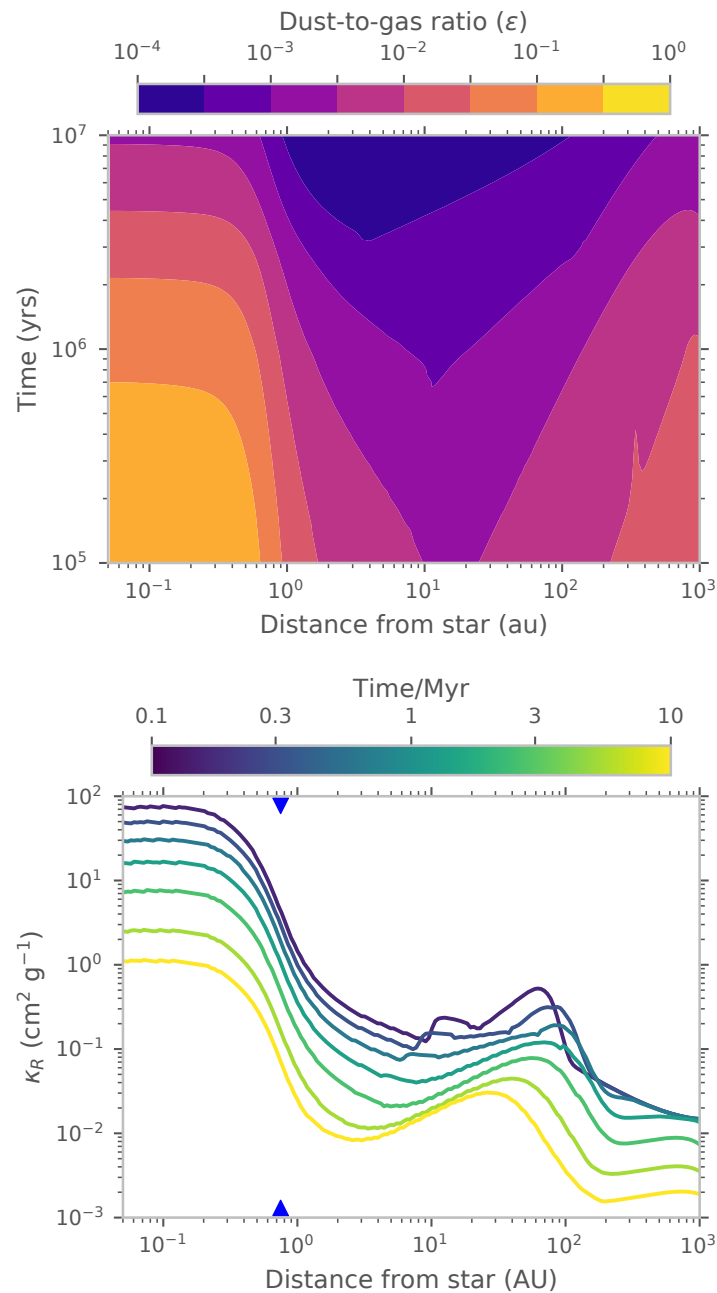


Figure 3.10: Time evolution of the vertically integrated dust-to-gas ratio ϵ and the Rosseland mean opacity per gram of protoplanetary disk material as a function of distance from the star. Although the absolute values of ϵ and κ_R decline over time due to global accretion of dust onto the star, there is little change in their observed profile shapes as a function of time. The minima in ϵ and κ_R profiles move slightly inward with time as a larger fraction of the outer disk becomes drift dominated. The water ice line is marked with blue triangles in the right panel.

evolution of the disk after 0.1 Myr leads to 1 – 2 orders of magnitude decline in the dust-to-gas ratio and opacity, it has a small effect on their radial gradient in the disk. However, there is a noticeable inward movement of the minima in ϵ and κ_R profiles with time. This is because as the dust-to-gas ratio declines in the outer disk, the radius at which the disk transitions from being fragmentation-dominated to drift-dominated moves inwards (Equation 3.16). As we will show in § 3.4, the overall decline in ϵ and κ_R over time leads to the enhancement of gas accretion onto planetary cores.

We note that the assumed disk size also plays an important role in the temporal evolution of the dust-to-gas ratio and consequently dust opacity. Due to radial drift, dust drains onto the star more rapidly in smaller disks and the dust-to-gas ratio in the outer disk can become very small ($\lesssim 10^{-4}$) as early as 1 Myr. Radial drift may be too efficient in disk models and there is some tension with observations (e.g. Brauer et al., 2008; Takeuchi & Lin, 2005), as many disks with ages of a few Myr appear to have mm-sized grains present at large distances ($\gtrsim 100$ of au) (e.g. Andrews et al., 2018; Hendler et al., 2020). Proposed solutions for resolving the radial drift problem include the presence of dust traps (e.g. Kretke & Lin, 2007; Pinilla et al., 2012; Zhu et al., 2014), larger than assumed disk gas density (Powell et al., 2019), and grains with large porosity (Estrada & Cuzzi, 2015; Garcia & Gonzalez, 2020). We circumvent this issue by modeling a relatively large and massive disk, ensuring a reasonable supply of dust throughout the disk lifetime.

Temperature structure of the disk

We have calculated the disk’s temperature profile assuming a passively irradiated disk and thus assumed that it is identical for all of our grid models. However, accretional heating plays a role in setting the temperature structure of the disk, especially in the inner region and in particular for high disk viscosity (high α_t). In addition, dust dynamics and a variable v_{frag} alter the dust-to-gas ratio and the dust size distribution through the disk, leading to a location dependent dust opacity. Ideally, our models would include a self-consistent coupling of the dust and gas dynamics with the disk temperature structure including the effect of heating due to accretion. Although this is beyond the scope of this work, we carry out a preliminary assessment of the effect that accretional heating and enhanced dust-to-gas ratio would have on the temperature profile. In particular, we are interested in whether accretional heating has a significant impact on the location of the water ice line, which marks the transition in v_{frag} values.

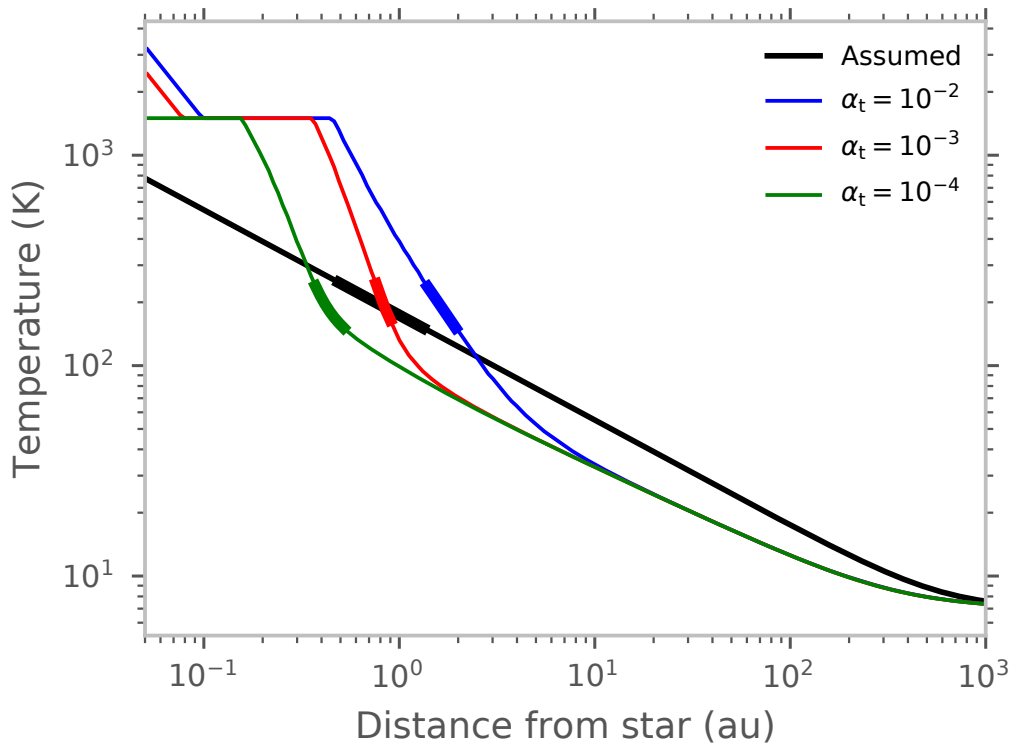


Figure 3.11: Post-processed temperature structure of the disk calculated using the method outlined in Birnstiel et al. (2010) with a self-consistent treatment of the opacity calculated using the size distribution and dust-to-gas ratio from our simulations. The disk properties at $t = 1$ Myr are used to calculate the temperature structure and are taken from simulations for which v_{frag} is 1 m/s and 10 m/s for ice-free and icy grains, respectively. The water snow line (150 – 250 K) is marked with thick lines for each temperature profile.

We post-processed results from our simulations to calculate the temperature structure of the disk using the method outlined in Birnstiel et al. (2010). The only difference in our method is that we self-consistently calculate the Rosseland and Planck mean opacities using the size distribution and dust-to-gas ratio from our simulations. To speed up the calculation of dust opacity, we use a power law size distribution for the dust with the power law index $\beta = -3.5$ and a_{max} set by our *twopoppy* simulations (see § 3.2). We also account for the thermostat effect of dust’s vaporization at high temperatures (Birnstiel et al., 2010). When the temperature reaches 1500 K, any further increase in the temperature leads to the vaporization of dust (and a decrease in opacity) so temperature is kept stabilized at this value. Once the gas opacity alone (assumed to be $0.1 \text{ cm}^2 \text{ g}^{-1}$) is enough to raise the temperature above 1500 K, we assume that all of the dust has evaporated and allow the temperature to rise again.

We find that accounting for the effects of accretional heating and the elevated dust-to-gas ratio significantly increases the temperature of the disk inside ~ 1 au, but it has a negligible impact on the location of the water snow line (Figure 3.11). For our fiducial model with $\alpha_t = 10^{-3}$, the snow line location is essentially identical. For $\alpha_t = 10^{-4}$ and 10^{-2} , the snow line moves from 0.75 au to 0.4 au and 1.6 au, respectively. We speculate that the increased temperature in the inner disk could also have an impact on the dust dynamics as it would lead to a decrease in $St_{\text{frag}} (\propto 1/c_s^2)$. This might further reduce the rate at which dust in the inner disk drains onto the star, thereby resulting in a larger dust pile up. This reinforces our conclusions about the difficulty of accreting gas in this region. However, obtaining a full solution to this problem would require us to couple the dust and gas dynamics with the disk temperature structure, which to the best of our knowledge has only been attempted once in the published literature (Estrada et al., 2016).

3.4 Implications for Planet Formation

Gas accretion mediated by cooling

Our calculated values for the dust opacity as a function of distance from the star show a dramatic decrease as we move beyond the ice line. We now consider what effect this variation in dust opacity and dust-to-gas ratio might have on the ability of planetary cores to accrete hydrogen-rich envelopes. For cores with masses $\lesssim 20 M_\oplus$, the rate of gas accretion onto the planetary core is initially regulated by the envelope's ability to cool and contract (e.g., Lee, 2019). This cooling is controlled by the properties of the gas envelope at the innermost radiative-convective boundary (RCB), as most of the cooling luminosity is generated inside the innermost convective zone (Lee et al., 2014; Piso & Youdin, 2014).

There is a qualitative difference in the radiative-convective structure of planetary envelopes dominated by dust opacity versus gas opacity. For 'dust-free' envelopes with negligible dust opacity, we expect to see a single convective zone that is connected to the disk via a nearly isothermal radiative zone. However, for 'dusty' envelopes where dust opacity dominates over gas opacity, the evaporation of dust grains deep inside the envelope leads to a dramatic drop in the local envelope opacity, which causes an intermediate radiative zone to form. Lee et al. (2014) show that in this case, the innermost RCB appears at the H_2 dissociation front (~ 2500 K) where H^- opacity starts to dominate.

We expect atmospheres to transition to the ‘dust-free’ accretion regime when the dust opacity is comparable to the gas opacity at the relevant temperature. In the inner disk (~ 0.1 au), this transition occurs when the dust opacity approaches $\sim 0.01 \text{ cm}^2 \text{ g}^{-1}$. As we move farther out in the disk, the gas opacity decreases sharply ($\lesssim 10^{-4} \text{ cm}^2 \text{ g}^{-1}$ at the relevant densities; e.g. Freedman et al., 2014) as the number of available molecular line transitions decreases. In our fiducial disk model for a $15 M_{\oplus}$ core, the dust opacity at a height of $\min(R_{\text{Hill}}, R_{\text{Bondi}})$ above the midplane does not go below the gas opacity limit. Our models therefore predict that accretion at all orbital distance occurs in the ‘dusty’ regime, whose RCB opacity—which controls the rate of cooling and therefore accretion—is given by the H^- opacity (Lee & Chiang, 2015):

$$\kappa(\text{H}^-) \sim 3 \times 10^{-2} \text{ cm}^2 \text{ g}^{-1} \left(\frac{\rho}{10^{-4} \text{ g cm}^{-3}} \right)^{0.5} \left(\frac{T}{2500 \text{ K}} \right)^{7.5} \left(\frac{Z}{0.02} \right)^1. \quad (3.17)$$

The only influence dust has on the H^- opacity is via the metallicity dependence Z of the gas. We set Z equal to the local dust-to-gas ratio in our gas accretion calculations as the metals delivered via dust are present in the gas phase at the H_2 dissociation front. Equating Z to the dust-to-gas ratio is justified because the Z dependence of $\kappa(\text{H}^-)$ results from its dependence on the availability of free electrons, most of which are sourced from metallic species. Although some of these metals might be present in the gas, the dust contribution dominates. This is likely to be true even in the most dust depleted regions of the outer disk as CO is predicted to be the dominant gas phase metal in this region. This molecule does not dissociate until much deeper in the planetary atmosphere, and hence it will not contribute free electrons in the region where H^- opacity becomes important.

We use this information to calculate gas accretion rates onto a planetary core as a function of disk location and time using the analytical scaling laws provided by Lee & Chiang (2015), modified for the linear dependence on the bound radius and the weak dependence on nebular density (see Lee & Connors, 2020). The gas-to-core mass ratio (GCR) at time t (with accretion beginning at t_0) in the ‘dusty’ planetary envelope regime is given by:

$$\text{GCR} \sim 0.06 f_{\text{R}} \left(\frac{\Sigma_g}{2000 \text{ g cm}^{-3}} \right)^{0.12} \left(\frac{t - t_0}{1 \text{ Myr}} \right)^{0.4} \left(\frac{\nabla_{\text{ad}}}{0.17} \right)^{3.4} \left(\frac{2500 \text{ K}}{T_{\text{rcb}}} \right)^{4.8} \left(\frac{0.02}{Z} \right)^{0.4} \left(\frac{\mu_{\text{rcb}}}{2.37} \right)^{3.4} \left(\frac{M_{\text{core}}}{5M_{\oplus}} \right)^{1.7}. \quad (3.18)$$

Here, f_{R} is the bounded radius of a planet as a fraction of its $\min(R_{\text{Hill}}, R_{\text{Bondi}})$ and we set it equal to 0.2 (e.g. Fung et al., 2019). The updated scaling law provided by Lee & Connors (2020) also allows us to incorporate the dependence of GCR on the gas surface density Σ_g , which we obtain from our disk model. The normalization factor of 0.06 is valid for $\Sigma_g < 0.1 \times \text{MMEN}$ at 0.1 au. ∇_{ad} , T_{rcb} and μ_{rcb} are the adiabatic gradient, temperature, and the mean molecular weight evaluated at the RCB. We assume a fixed value of $T_{\text{rcb}} = 2500 \text{ K}$ and $\nabla_{\text{ad}} = 0.17$, appropriate for the innermost RCB at the H_2 dissociation front, for all our calculations. We calculate μ_{rcb} assuming a $\mu = 2.3$ for a pure hydrogen-helium mixture (solar abundance ratio) and $\mu = 17$ for a pure metal-rich atmosphere. For the most metal-rich gases ($Z \gtrsim 0.2$; Lee & Chiang, 2016), the strong dependence of GCR on μ_{rcb} dominates over the metallicity-dependent increase in opacity, allowing for rapid accretion (Venturini et al., 2015). Our models predict that the dust-to-gas ratio throughout the disk will remain below this critical value for a majority of the disk lifetime. $Z > 0.2$ in the inner disk only at very early stages ($< 0.1 \text{ Myr}$) when core formation is still likely ongoing.⁴ For the entirety of the duration of gas accretion that we model (0.1–10 Myrs), an increased Z therefore acts to reduce the accretion rate by increasing the gas opacity at the RCB. We incorporate the time dependence of Σ_g , Z , and μ_{rcb} in our calculation of GCR by numerically differentiating Equation 3.18 with respect to time and integrating between $t_0 = 0.1 \text{ Myr}$ (the emergence of the core) and time t (in the range 1 – 10 Myr) at which the planet stops accreting.

If a core reaches the threshold for runaway gas accretion ($\text{GCR} = 0.48$, Lee et al., 2014), we calculate the subsequent gas accretion rate using the minimum of the cooling-limited rate \dot{M}_{cool} , the disk accretion rate \dot{M}_{disk} , and the hydrodynamic accretion rate \dot{M}_{hydro} (see Lee, 2019 for an example):

$$\dot{M}_{\text{cool}} = 0.48 \frac{M_{\text{core}}}{t_{\text{run}}} \exp\left(\frac{t}{t_{\text{run}}}\right), \quad (3.19a)$$

⁴We note that late-stage pollution of an envelope by ambient solids could enhance the interior metallicity beyond $Z \sim 0.2$ and trigger rapid gas accretion (Hori & Ikoma, 2011). The short dynamical timescale in the inner disk suggests that the solids there most likely lock into planetary cores before the late-stage disk gas dispersal, and so such late-stage pollution is more likely to occur in the outer disk.

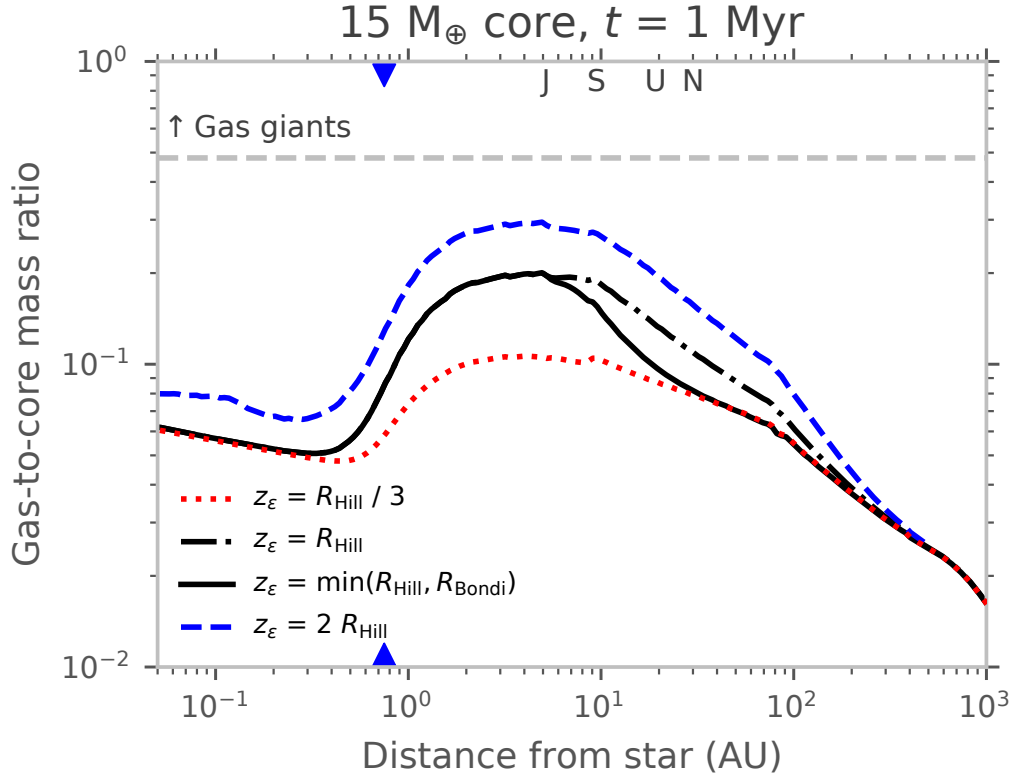


Figure 3.12: The gas-to-core mass ratio (GCR) at $t = 1$ Myr for a $15 M_{\oplus}$ core as a function of distance from the star, assuming the core starts accreting at $t_0 = 0.1$ Myr. Here, we vary the height z_{ϵ} from which gas is accreted by the planet. A GCR of 0.48 is marked with a dashed grey line, indicating the threshold for the onset of runaway gas accretion (Lee et al., 2014). The water ice line is marked with blue triangles.

$$\dot{M}_{\text{disk}} = 3 \pi \nu \Sigma_g, \quad (3.19b)$$

$$\dot{M}_{\text{hydro}} = 0.29 \left(\frac{M_p}{M_*} \right)^{4/3} \frac{\Sigma_g}{1 + 0.034 K} \left(\frac{r}{H_{\text{gas}}} \right)^2 r^2 \Omega_K. \quad (3.19c)$$

Here, t_{run} is the time taken by the core to reach a GCR = 0.48 (t at which GCR = 0.48 minus t_0), $M_p = (\text{GCR} + 1)M_{\text{core}}$ is the total planet mass, and $K = (M_p/M_*)^2 \alpha_t^{-1} (H_{\text{gas}}/r)^{-5}$ accounts for the depletion of gas surface density in the vicinity of the planet due to gap opening. This effect is only included in the gas accretion calculation and not in the evolution of the disk.

Figure 3.12 shows the gas-to-core mass ratio (GCR) calculated for our fiducial core mass of $15 M_{\oplus}$ as a function of distance from the star at $t = 1$ Myr. We vary the height z_{ϵ} from which material is accreted by the planet, which affects the metallicity (dust-to-gas ratio) of the accreted material and therefore the GCR profile. Along

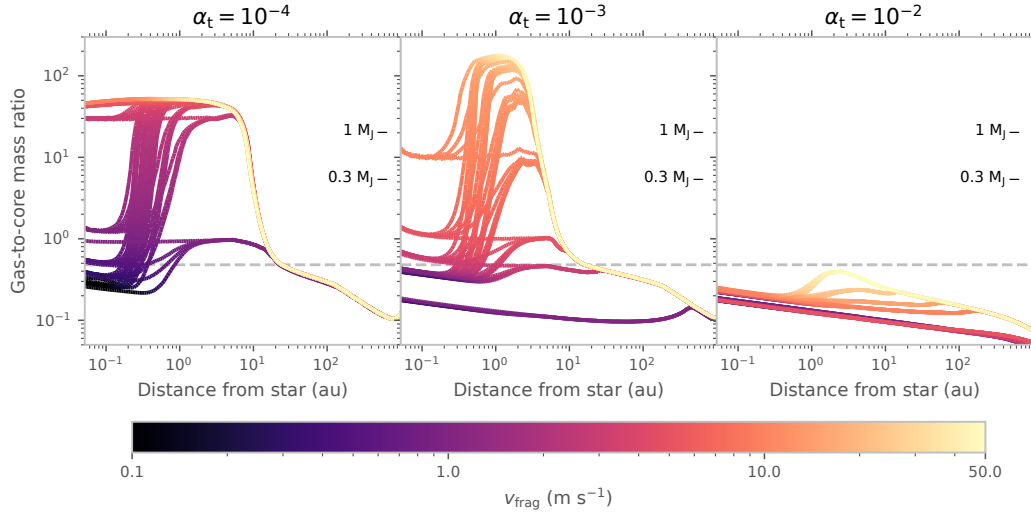


Figure 3.13: The gas-to-core mass ratio (GCR) at $t = 10$ Myr for a $15 M_{\oplus}$ core as a function of distance from the star, assuming the core starts accreting at $t_0 = 1$ Myr, for our grid of models. We use a later t_0 here because the dust-to-gas ratio for the $\alpha_t = 10^{-4}$ model varies rapidly at earlier times, and our simple gas accretion model would therefore not be applicable. The dashed grey line indicates the threshold for the onset of runaway gas accretion (GCR of 0.48; Lee et al., 2014). GCRs corresponding to planet masses of $0.3 M_J$ and $1 M_J$ are marked with black dashes; $0.3 M_J$ is commonly used as a lower mass limit when calculating giant planet occurrence rates in RV surveys (e.g. Cumming et al., 2008; Wittenmyer et al., 2020).

with our default value of $z_{\epsilon} = \min(R_{\text{Hill}}, R_{\text{Bondi}})$, we also show GCR profiles for $z_{\epsilon} = [1/3, 1, 2] \times R_{\text{Hill}}$. Inside ~ 1 au, the relatively high Z (~ 0.1) produces a GCR in the range $0.06 - 0.08$ for a wide range of z_{ϵ} . However, the sharp drop in Z beyond ~ 1 au (see middle panel of Figure 3.9) leads to a rise in the amount of gas accreted by the planetary core, reaching a peak value of ~ 0.2 in the $1 - 10$ au region of the disk for $z_{\epsilon} = \min(R_{\text{Hill}}, R_{\text{Bondi}})$. Beyond ~ 10 au, the metallicity of the gas (i.e. dust-to-gas ratio) at R_{Hill} and R_{Bondi} rises again as the Hill and Bondi radii shrink relative to the disk scale height, which leads to a decline in GCR. The weak dependence of GCR on Σ_g also contributes to a decline in GCR with distance. We note that the peak GCR value in the intermediate $1 - 10$ au region increases with the height above the midplane from which the planet accretes as the dust-to-gas ratio is a strongly decreasing function of z in this region. Overall, Figure 3.12 demonstrates that the amount of gas accreted by a planetary core during the accretion-by-cooling phase, and hence its ability to reach the threshold for runaway growth, varies significantly as a function of its location in the disk.

Figure 3.13 shows how the final GCR for a $15 M_{\oplus}$ core varies as a function of the assumed α_t and v_{frag} values. We calculate the GCR assuming that the core begins accreting at $t_0 = 1$ Myr, as the dust-to-gas ratio at earlier times varies too rapidly for most of the models with $\alpha_t = 10^{-4}$ to allow us to use our simple gas accretion model. We also note that the high dust-to-gas ratio at $t \lesssim 1$ Myr and short orbital timescales in the inner disk for low v_{frag} and $\alpha_t = 10^{-4}$ (Figure 3.5) would probably lead to efficient planetesimal formation, thereby reducing the dust-to-gas ratio of the material that is available for gas accretion. GCR calculations for these models at early times therefore require a more careful study of how the dust-to-gas ratio evolves if planetesimal formation occurs, which is beyond the scope of this work.

We find that for $\alpha_t = 10^{-2}$, the dust-to-gas ratio does not vary significantly with either location or time, and as a result the GCR profiles lie in a relatively narrow range. The declining GCR with increasing distance is primarily due to the decline in gas surface density. In these high viscosity models, a $15 M_{\oplus}$ core is unable to reach the threshold for runaway accretion anywhere in the disk. In contrast, models with $\alpha_t = 10^{-4}$ and 10^{-3} can produce a wide range of GCR values depending on the assumed values of v_{frag} . Models with substantial changes in v_{frag} across the water ice line result in a large radial variation in the GCR, with a sharp rise at ~ 1 au and a sharp fall at ~ 10 au, much more drastic than our fiducial model (Figure 3.12 & 3.14). These models are characterized by a deep minimum in dust-to-gas ratio at ~ 1 – 10 au which accelerates thermodynamic gas accretion, driving planets to runaway whose mass growth is eventually limited by the global disk accretion \dot{M}_{disk} (when $\text{GCR} \gtrsim 10$).

Consequences for giant planet formation and demographics

Our calculations provide a natural explanation for the observed peak in the gas giant planet occurrence rate at ~ 1 – 10 au as measured by radial velocity and direct imaging surveys (e.g. Baron et al., 2019; Fernandes et al., 2019; Fulton et al., 2021; Nielsen et al., 2019; Wittenmyer et al., 2020). Figure 3.14 demonstrates that the location of the most favorable sites for rapid gas accretion is driven by the decrease in dust-to-gas ratio just beyond the ice line where relatively larger grains undergo efficient radial drift and vertical settling. We note that the nucleation of gas giants requires relatively massive cores ($\sim 15 M_{\oplus}$) that assemble early (i.e., accrete gas for at least 3–10 Myrs). Lighter cores and/or those that assemble late (i.e., accrete gas for shorter amount of time) necessarily grow into planets with less massive envelopes. Although it is difficult to obtain good observational constraints on the core masses

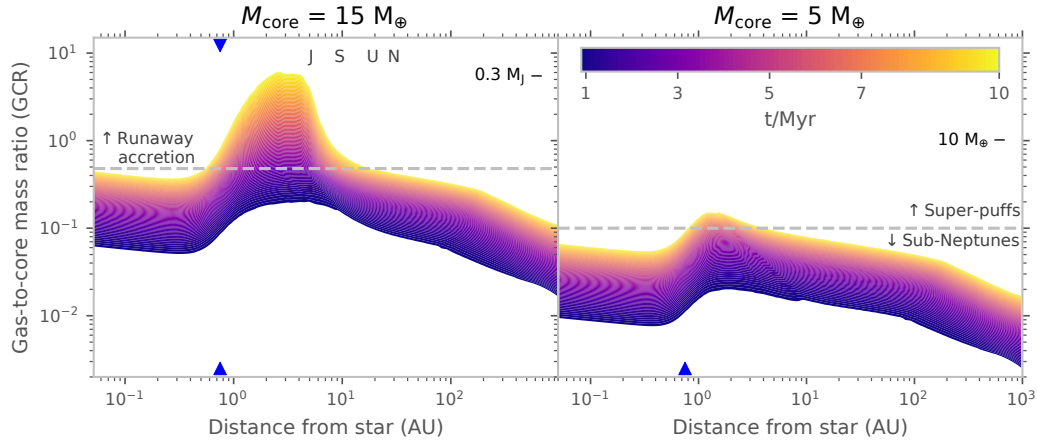


Figure 3.14: The gas-to-core mass ratio (GCR) as a function of distance from the star for a $15 M_{\oplus}$ (left panel) and $5 M_{\oplus}$ (right panel) cores for time t in the range 1 – 10 Myr, assuming they start accreting material present at $\min(R_{\text{Hill}}, R_{\text{Bondi}})$ at $t_0 = 0.1$ Myr. GCR of 0.48 (onset of runaway gas accretion Lee et al., 2014) and GCR = 0.1 (for sub-Neptunes and super-puffs) are marked with dashed grey lines in the top and bottom panels, respectively. GCRs corresponding to total planet masses of $0.3 M_J$ (left panel) and $10 M_{\oplus}$ (right panel) are indicated as well. The locations of solar system giant planets are marked along the abscissa at the top. The water ice line is marked with blue triangles.

of extrasolar Jupiters (Thorngren & Fortney, 2019), we note that the cores of sub-Saturns—planets that were on the verge of runaway, but were halted in growth before they became gas giants—are better-constrained and appear to range between $\sim 15\text{--}20 M_{\oplus}$ in the limiting case where all metals are assumed to be sequestered in the core (Lopez & Fortney, 2014; Petigura et al., 2017a). This range also agrees with core mass estimates derived from fitting mass loss models to sub-Saturn occurrence rate as a function of orbital period (Hallatt & Lee, 2022).

The same change in fragmentation velocity of grains across the ice line that we invoke in our model may also result in the formation of more massive cores outside the ice line (e.g. Morbidelli et al., 2015; Venturini et al., 2020), reinforcing our results that gas giants are more likely to originate farther away from the star. Our work further demonstrates that the dust-to-gas ratio is expected to be radially-variant and that it reaches a local minimum at a specific range of orbital distances (1–10 au), creating a preferred zone of rapid gas accretion. Qualitatively, our solar system also fits into our picture, with gas giants Jupiter and Saturn forming at intermediate distances where the GCR peaks and Uranus and Neptune forming further out where the GCR declines with distance (Batygin & Brown, 2010; Morbidelli et al., 2007).

Formation of sub-Neptunes and super-puffs

Close-in sub-Neptunes appear to possess primordial hydrogen-rich envelopes that are a few percent of the total planet mass (e.g., Lopez & Fortney, 2014; Ning et al., 2018; Wolfgang & Lopez, 2015). Given their estimated core masses of $4 - 8 M_{\oplus}$ (Rogers & Owen, 2020; Wu, 2019), it is difficult to explain why these planets did not undergo runaway gas accretion and turn into gas giants assuming they formed in MMEN and accreted solar metallicity gas. Previous studies have proposed three potential solutions: 1) accretion of metal rich gas, which increases the envelope opacity and slows the gas accretion rate during the cooling growth phase (e.g. Chen et al., 2020; Lee et al., 2014), 2) late-time core assembly, so that there is a very short period for the planet to accrete prior to the dispersal of the gas disk (Lee & Chiang, 2016), and 3) a flow of high entropy gas into the Hill sphere of the growing planet that prevents it from cooling (B ethune & Rafikov, 2019; Ormel et al., 2015, but see Kurokawa & Tanigawa, 2018). Scenario 1 in and of itself applies for either dusty or dust-free accretion, but it is more effective for dusty accretion as its overall higher opacity delays accretion even more. Our work revisits the first scenario in the context of in situ, dusty gas accretion.

Our results suggest that the enhanced dust-to-gas ratio in the inner disk is sufficient to limit the envelope masses/accretion rates of sub-Neptunes forming in this region. We find that for a representative $5 M_{\oplus}$ core, the enhanced dust-to-gas ratio inside the ice line is enough to prevent the accretion of a massive gas envelope (Figure 3.14, right panel). If the metallicity is too high ($Z > 0.2$), the enhancement in the mean molecular weight of the gas can expedite gas accretion (Lee & Chiang, 2015; Venturini et al., 2015). For our fiducial choice of fragmentation velocities and turbulence parameter (as well as for a large swath of the parameter space), Z stays below 0.2 in the inner disk after 0.1 Myrs. As shown in Figure 3.14, a $5 M_{\oplus}$ core inside 1 au attains a few percent by mass envelope, consistent with the measured masses and radii of sub-Neptunes, even if the core assembled early and accreted gas for the full 10 Myrs. We note that this result is not mutually exclusive with late-time core assembly for sub-Neptunes. The late-time, gas-poor environment favors the build-up of $\sim 5 M_{\oplus}$ sub-Neptune cores by a series of collisional mergers. Such mergers are necessary as the isolation masses, either from planetesimal (see Dawson & Johnson, 2018, their Figure 2) or pebble accretion (see, e.g., Bitsch et al., 2018; Fung & Lee, 2018) are on the order an Earth mass or smaller in the inner disk. Furthermore, late-time assembly of sub-Neptunes prevents inward migration of these planets once they assemble (Lee & Chiang, 2016).

Our models also provide support for previously published hypotheses about the origin of ‘super-puffs,’ a rare class of planets with giant planet like radii ($4\text{--}8 R_{\oplus}$) and super-Earth like masses ($2\text{--}5 M_{\oplus}$) (Lee & Chiang, 2016). The low bulk densities of these planets imply that they possess hydrogen-rich envelopes that are tens of % by mass (Jontof-Hutter et al., 2014; Masuda, 2014; Ofir et al., 2014). Although the gas mass fraction of some super-puffs may be overestimated due to the inflation of planetary radii measurements by photochemical hazes lofted by outflowing gas, the majority of super-puffs do appear to have accreted substantially more gas than sub-Neptunes (Chachan et al., 2020; Gao & Zhang, 2020; Libby-Roberts et al., 2020; Wang & Dai, 2019). It is difficult to explain how these planets, which have core masses similar to those of sub-Neptunes, could have accreted an order of magnitude more gas in their present-day locations (Ikoma & Hori, 2012; Lee & Chiang, 2016). Lee & Chiang (2016) proposed that super-puffs might form by accreting ‘dust-free’ gas (dust opacity lower than gas opacity) beyond ~ 1 au. Although the dust opacity in our models is never low enough to qualify as dust-free, we find that this decrease in the dust-to-gas ratio beyond the ice line does indeed lead to significantly higher gas accretion rates and GCRs (Figure 3.14). All of the currently known super-puffs are in or near orbital resonances with other planets⁵, which requires relatively smooth convergent migration (e.g. Cresswell & Nelson, 2006). This is consistent with a scenario in which super-puffs formed beyond ~ 1 au, and then migrated inward via interactions with the protoplanetary gas disk. As Figure 3.14 shows, the creation of super-puffs require their cores to have assembled early so that the total gas accretion time is longer. The requirement for early stage core assembly is also in agreement with the migratory origin of super-puffs as disk-induced migration requires a gas-rich environment.

3.5 Discussion and Conclusions

In this work, we use dust evolution models to demonstrate that the dust opacity and dust-to-gas ratio in protoplanetary disks is expected to be radially and vertically variant, with significant implications for planet formation. This is a result of grain growth and transport, which produce a highly non-uniform dust-to-gas ratio in the disk and generate top heavy size distributions with grains that are orders of magnitude larger than the maximum grain size in the commonly-assumed ISM distribution. We explore the sensitivity of our models to assumptions about the disk

⁵Most super-puffs orbit dim stars, which makes it hard to measure their masses with the radial velocity technique. Their masses have typically been determined by transit timing variations, which by definition require them to be in dynamically interacting multi-planet systems.

turbulence and fragmentation velocities and find that we obtain qualitatively similar results over a wide range of plausible values.

Models with a substantial difference in v_{frag} across the ice line and moderate-to-low turbulence values $\alpha_t \lesssim 10^{-3}$ produce the largest radial variations in dust-to-gas ratio and dust opacity. A large change in v_{frag} across the ice line leads to a large difference in the Stokes number St of the largest grains within and beyond the ice line. In the inner disk with smaller St (well-coupled to gas), dust grains pile up radially and mix well vertically. In the outer disk with larger St (more decoupled from gas), dust grains drift in rapidly and settle to the midplane. As a result, the inner disk is characterized by high dust-to-gas ratio that is near constant with height, whereas the outer disk is characterized by lower dust-to-gas ratio that decreases even further away from the midplane.

We use our location-dependent dust-to-gas ratio to calculate gas accretion rates onto planetary cores as a function of distance from the star. If we assume that the growing planet predominately accretes material present at $\min(R_{\text{Hill}}, R_{\text{Bondi}})$ above the midplane, we find that the gas-to-core mass ratio (GCR) is a strong function of its location in the disk. Within the ice line, gas accretion onto the core is suppressed by the high dust-to-gas ratio. At intermediate distance beyond the ice line (1 – 10 au in our fiducial model), there is a steep decline in the dust-to-gas ratio, causing the GCR to rise and making it easier for cores to reach the threshold for runaway gas accretion. Beyond this point the dust-to-gas ratio increases again as the growing planet accretes from a region closer to the disk midplane ($\min(R_{\text{Hill}}, R_{\text{Bondi}}) / H_{\text{gas}}$ declines with distance). We conclude that dust-gas dynamics favor gas giant planet formation at intermediate distances, potentially explaining the peak in the giant planet occurrence rate vs. orbital distance (e.g. Fulton et al., 2021). Our results also provide support for the hypothesis that super-puffs likely formed beyond the ice line, as the lower dust-to-gas ratio in this region can substantially accelerate their gas accretion rates.

We note that the same models presented in this study could be used to constrain the core mass distribution of gas giant exoplanets by quantifying the fraction of planets that undergo runaway gas accretion as a function of location (e.g. Lee, 2019). Previous studies on core formation have argued that a change in v_{frag} across the ice line could lead to a significant increase in core masses outside the ice line (Morbidelli et al., 2015; Venturini et al., 2020). In a future study we will explore whether the radially-varying dust-to-gas ratio alone is sufficient to reproduce the

observed mass-period distribution of gas giant exoplanets, or whether it is also necessary to invoke a radially varying core mass function or large scale migration. These same models could also be used to explore why outer gas giants are commonly accompanied by inner super-Earths (Bryan et al., 2019; Zhu & Wu, 2018).

In this study we have limited ourselves to a single fiducial disk model to show how dust opacity varies with radial distance. However, observations of protoplanetary disks indicate that there is a large variation in disk properties such as the disk mass, size, lifetime, and metallicity as well as the mass and luminosity of protostars (Andrews et al., 2018; Long et al., 2018; Long et al., 2019). In future studies, we will investigate how dust evolution and gas accretion onto planetary cores depend on these properties and whether the diversity of exoplanets is thus linked to the diversity in disk and stellar properties.

Other potential improvements for these calculations include accounting for the conversion of dust to planetesimals/planetary cores on the dust mass budget (likely to be important in the inner disk for $\alpha_t = 10^{-4}$ and low v_{frag}) and the effect of planet-disk interaction on dust growth and dynamics. In particular, as planetary cores become massive enough to perturb the gas disk, pressure maxima outside the planet's orbit traps some of the dust. This could affect the local size distribution and radial migration of dust as well as the dust-to-gas ratio of the material accreted by the growing planet (Chen et al., 2020). We expect these effects to be perturbative and more localized in nature and the global dust evolution to broadly follow the picture we have painted in this work. Overall, the radial variation of dust-to-gas ratio and dust opacity have a substantial effect on the ability of planetary cores to accrete gas and should be considered in models of planet formation.

*Chapter 4***A HUBBLE PANCET STUDY OF HAT-P-11b: A CLOUDY NEPTUNE WITH A LOW ATMOSPHERIC METALLICITY****4.1 Introduction**

The atmospheric compositions of extrasolar gas giant planets are expected to vary depending on their formation locations and accretion histories. Variation in composition of disk gas and solids as well as the availability of polluting solids at different locations leaves an imprint on a planet’s atmosphere (e.g. Lambrechts & Johansen, 2014; Oberg et al., 2011; Pudritz et al., 2018; Venturini et al., 2016). By measuring the wavelength-dependent transit depth when one of these planets passes in front of its host star (the planet’s “transmission spectrum”), we can detect atmospheric absorption features that directly constrain the mean molecular weight and relative abundances of molecules including water, methane, carbon monoxide, and carbon dioxide. Although some planets with strong and clear absorption features have been thus characterised (e.g. WASP 96b, Nikolov et al., 2018a; WASP 39b, Wakeford et al., 2018; WASP 107b, Kreidberg et al., 2018), large observing campaigns using the *Hubble Space Telescope (HST)* have revealed the presence of high-altitude clouds that attenuate the expected absorption signal in a majority of the close-in gas giant planets observed to date (e.g. Fu et al., 2017; Sing et al., 2016; Tsiaras et al., 2018; Wakeford et al., 2019). This problem is even more acute for the current sample of Neptune-sized planets, whose relatively small radii, high surface gravities, and low temperatures all combine to reduce the expected amplitude of atmospheric absorption as compared to their better-studied Jovian counterparts (e.g. Crossfield & Kreidberg, 2017). This limits our ability to search for trends in atmospheric properties with other parameters of the system, e.g. planet mass, radius, and temperature — all of which are crucial for improving our understanding of planet formation and evolution.

Although the current body of observed transmission spectra clearly require the presence of high altitude scattering particles, there is considerable debate about the nature and origin of these particles. At high temperatures, we expect refractory species such as metal oxides, silicates, and sulphides to condense in exoplanetary atmospheres (e.g. Helling, 2018; Morley et al., 2012; Powell et al., 2018). However,

cloud formation is a complex process that depends on both microphysical processes, such as sedimentation, nucleation, and growth, and the material properties of the condensing species, many of which are highly uncertain or unknown (Helling, 2018). Consequently, the use of different underlying assumptions can lead to significantly different cloud properties, severely limiting the predictive power of these models.

While some of these questions may be resolved by ongoing laboratory experiments (He et al., 2018a,b; Hörst et al., 2018; Johnson et al., 2018, 2017), observational constraints on the properties of clouds in exoplanetary atmospheres provide complementary leverage to further refine and develop microphysical cloud models. The nature of these constraints varies depending on the wavelength of the observations: optical and near-infrared transmission spectroscopy can be used to investigate the sizes, number density, and vertical distribution of cloud particles, while vibrational modes in the mid-infrared can be used to directly determine the compositions of cloud particles (e.g. Kitzmann & Heng, 2018; Pinhas & Madhusudhan, 2017; Wakeford & Sing, 2015).

Although clouds represent a substantial challenge for compositional inferences from transmission spectroscopy, previous *HST* studies have demonstrated that we can nonetheless obtain reasonable constraints on atmospheric composition for planets with detectable near-infrared water features by utilizing information at optical wavelengths to break degeneracies between cloud-top pressure and atmospheric metallicity (e.g. HAT-P-26b, Wakeford et al., 2017a; WASP-39b, Wakeford et al., 2018). Spectroscopic observations in the near infrared have been instrumental in the detection of molecular absorption in exoplanetary atmospheres but they are usually unable to put tight constraints on the composition, i.e. the absolute mixing ratios, of these molecules. This is because the transmission spectra of an atmosphere with a deep cloud and low mixing ratios is statistically indistinguishable (with currently available precision) from an atmosphere with a high cloud and high mixing ratios. These distinct scenarios can be distinguished by their differing spectral behavior in the optical. In this spirit, the Panchromatic Comparative Exoplanet Treasury (PanCET) survey is a multi-cycle *HST* treasury program whose primary goal is to characterize the atmospheres of a sample of 20 transiting gas giant planets at wavelengths ranging from the ultraviolet to the near-infrared (e.g. Alam et al., 2018; Bourrier et al., 2018; Evans et al., 2017; Evans et al., 2018; Nikolov et al., 2018b; Wakeford et al., 2017b). In this study, we present new optical *HST* STIS PanCET observations of HAT-P-11b, a warm Neptune sized planet with a radius of 4.4 Earth

radii and mass of 23 Earth masses on a 4.88 days orbit around a $0.81 M_{\odot}$, $0.68 R_{\odot}$ K4 star ($T_{\text{eff}} = 4780 \pm 50\text{K}$). This planet has a significantly eccentric orbit ($e = 0.218$) and as a result its predicted equilibrium temperature varies between $\sim 600 - 900$ K (Bakos et al., 2010; Deming et al., 2011; Yee et al., 2018). The planet therefore crosses multiple condensation lines, which enhances its potential for cloud formation.

HAT-P-11b has been previously observed with both ground- (e.g. Bakos et al., 2010; Sanchis-Ojeda & Winn, 2011) and space-based telescopes (e.g. Deming et al., 2011; Fraine et al., 2014; Huber et al., 2017) and is one of the most favorable Neptune-sized planets for atmospheric characterization due to its large atmospheric scale height and host star brightness ($V \sim 9$). It is one of the smallest planets with a published detection of water absorption in its $1.1\text{--}1.7 \mu\text{m}$ *HST* WFC3 transmission spectrum (Fraine et al., 2014). Although there is an optical detection of the planet’s secondary eclipse using *Kepler* photometry (Huber et al., 2017), no corresponding infrared detection has been reported to date. Measurements of absorption in the He metastable 10830 \AA line during transit provide complementary constraints on the size of the planet’s exosphere and corresponding mass loss rate (Allart et al., 2018; Mansfield et al., 2018). Although the relatively high activity level of HAT-P-11b’s K dwarf primary can bias the shape of the planet’s measured transmission spectrum (e.g. Rackham et al., 2018; Rackham et al., 2019; Sing et al., 2011), the planet’s nearly polar orbit (Hirano et al., 2011; Winn et al., 2010) has enabled exquisitely detailed studies of the starspot distribution and active latitudes (e.g. Deming et al., 2011; Morris et al., 2017a,b; Sanchis-Ojeda & Winn, 2011) that can be used to effectively correct for these effects.

Here, we combine previously published transit observations from *HST* WFC3 ($0.8 - 1.7 \mu\text{m}$) and *Spitzer* ($3.6, 4.5 \mu\text{m}$) (Fraine et al., 2014; Mansfield et al., 2018) with new optical *HST* STIS observations to obtain the first comprehensive look at HAT-P-11b’s transmission spectrum between $0.35 - 5 \mu\text{m}$. We compare the resulting transmission spectrum to predictions from forward models for cloud condensation and use retrievals to independently constrain the planet’s atmospheric composition and cloud properties. Sections 4.2 and 4.3 describe our spectral and photometric extraction methods, while Section 4.4 discusses instrumental and astrophysical noise sources in our data. Section 4.5 details our fits to these data, and Section 4.6 discusses predictions from forward models for HAT-P-11b’s atmosphere. Adopting some material properties and tools from this section, we then use simple models to directly

fit the observed transmission spectrum in order to derive statistical constraints on atmospheric parameters in Section 4.7, which we compare to the forward models in Section 4.8.

4.2 Observations

A summary of the observations used in our analysis is given in Table 4.1. We analyze 13 transits in total and describe each of them below.

We observed three transits of HAT-P-11b with the Space Telescope Imaging Spectrograph (STIS) on the *Hubble Space Telescope (HST)* (PI Sing & López-Morales, GO 14767). Two observations were conducted using the G430L grism (0.29-0.57 μm) on UT 2017 Feb 22 and UT 2017 May 26, while a third visit on UT 2017 April 12 used the G750L grism (0.524-1.027 μm). All of our observations were obtained using the $52'' \times 2''$ slit. This was done to minimize slit losses and the effect of telescope breathing. Each visit consists of 5 *HST* orbits. Short (1 s) exposures were taken before each orbit to mitigate the severity of the exponential ramp at the beginning of each orbital light curve, but this step did not appear to be effective for these observations. The wavelength calibration and flat field exposures were taken during the occultation of *HST* by Earth during the last orbit. Along with the *HST* STIS data, we independently re-reduce and fit all of the prior data collected with *HST* and *Spitzer* as part of our updated global analysis, which we discuss below in chronological order.

HAT-P-11b was observed with *HST*'s Wide Field Camera 3 (WFC3) instrument in 2012 (PI Deming, GO 12449) using the G141 grism in the 256×256 sub-array mode, which provides a low resolution spectrum in the 1.1 - 1.7 μm wavelength range. The data were collected over 4 *HST* orbits using only forward scans (McCullough & MacKenty, 2012) with a scan rate of $0.3891'' \text{ s}^{-1}$. The second orbit covers part of ingress. A buffer dump occurred during the third orbit, which partially resets the ramp that is used to model the instrumental behaviour (Deming et al., 2013; Knutson et al., 2014b; Kreidberg et al., 2014a); see § 4.4 for more details. These data were originally published in Fraine et al. (2014).

Four transits of HAT-P-11b were observed in 2011 using the Infrared Array Camera (IRAC) mounted on *Spitzer Space Telescope*, with two transits in each of the two warm-*Spitzer* channels (3.6 and 4.5 μm). The observations were taken in the sub-array mode, which yielded 32×32 pixel images with an integration time of 0.4 s.

The *Spitzer* data were published along with the WFC3 G141 data in Fraine et al. (2014).

Finally, five transits of HAT-P-11b were also observed using the WFC3 G102 grism ($0.8 - 1.15 \mu\text{m}$) in the 256×256 subarray mode (PI Bean, GO 14793) on UT 2016 Sep 14, 2016 Oct 13, 2016 Nov 7, 2016 Nov 26, and 2016 Dec 26. This grism is complementary to the G141 observations, as both grisms together span a series of adjacent and overlapping water and methane bands. During each visit, the planet was observed in scan mode over 4 orbits. The use of forward and backward scans and longer exposure times for G102 observations yielded a higher observational efficiency ($\sim 75\%$) than the 2012 G141 observations ($\sim 50\%$). These data were published in Mansfield et al. (2018), which reported a strong helium absorption from escaping gas in the planet’s outer atmosphere but did not see the expected molecular (water) absorption features in this bandpass.

4.3 Spectral & Photometric Extraction

We use the ExoTEP framework (Benneke et al., 2019a) for the extraction and fitting of all datasets. The extraction process for each of the instruments is described below.

HST STIS Spectroscopy

We correct for cosmic ray hits and other transient phenomena by stacking all of the images from a given visit and examining flux as a function of time at each pixel position. Because these data have relatively sparse time sampling (< 100 images per visit) and time-correlated instrumental effects, we find that we obtain optimal results when we flag 4σ outliers in each pixel’s time series and replace them with the median pixel value. We then estimate the background in each image by taking the median pixel value in two rectangular regions located far enough from the spectral trace to avoid contamination. We optimize the aperture width (in the cross-dispersion direction) for extraction of 1-dimension (1D) spectra and decide whether or not to remove the background by minimizing the scatter in the white-light residuals after subtracting the best-fit transit and instrumental noise model for each visit (e.g. Deming et al., 2013). For each visit, we consider aperture sizes of 7, 9, 11, and 13 pixels. In the G750L visit we obtain optimal results when we use a 9 pixel wide aperture centered on the peak of the point spread function and do not subtract the background. For the G430L observations, we prefer to subtract the background and utilize 13 and 11 pixel wide apertures for the first and second visits,

Table 4.1: Observations

Date (UT)	Start Time	Duration	Observatory	Band pass (μm)	Integration Time (s)	Exposures	Reference
2011 Jul 11	23:11:41	7.43 h	Spitzer	3.05 - 3.95	0.4	62592	Fraine et al. (2014)
2011 Aug 5	07:02:48	7.43 h	Spitzer	4.05 - 4.95	0.4	58112	Fraine et al. (2014)
2011 Aug 15	01:49:20	7.43 h	Spitzer	3.05 - 3.95	0.4	52633	Fraine et al. (2014)
2011 Aug 29	17:37:18	7.43 h	Spitzer	4.05 - 4.95	0.4	62592	Fraine et al. (2014)
2012 Oct 18	04:58:38	6.87 h	Hubble	1.1 - 1.70	44.4	113	Fraine et al. (2014)
2016 Sep 14	10:36:07	5.65 h	Hubble	0.8 - 1.15	81.1	99	Mansfield et al. (2018)
2016 Oct 13	18:44:21	5.83 h	Hubble	0.8 - 1.15	81.1	99	Mansfield et al. (2018)
2016 Nov 7	05:12:38	5.88 h	Hubble	0.8 - 1.15	81.1	99	Mansfield et al. (2018)
2016 Nov 26	18:22:55	5.83 h	Hubble	0.8 - 1.15	81.1	99	Mansfield et al. (2018)
2016 Dec 26	02:17:30	5.77 h	Hubble	0.8 - 1.15	81.1	99	Mansfield et al. (2018)
2017 Feb 22	17:04:39	7.17 h	Hubble	0.29 - 0.57	140	82	This work
2017 Apr 12	14:15:13	7.67 h	Hubble	0.524 - 1.027	140	81	This work
2017 May 26	13:50:02	7.28 h	Hubble	0.29 - 0.57	140	81	This work

respectively. We find that in all visits the white-light transit depths and transmission spectral shapes are relatively insensitive to our choice of aperture width.

Data taken with the G750L grism exhibit a fringing effect due to internal reflection within individual pixels. We correct for this effect using a fringe flat field obtained contemporaneously with our data following the methods outlined in Nikolov et al. (2014); Nikolov et al. (2015) and Sing et al. (2016). Using the first frame as a template, we then fit for the shift in position in the dispersion direction and relative amplitude of all subsequent frames in order to align the frames in wavelength. These best-fit relative amplitudes give us the normalised white light curve for each visit. For the wavelength-dependent light curves, we sum the flux within a 200 pixel wide bin for the G750L grism and a 100 pixel wide bin for the G430L grism. We also check for the presence of sodium and potassium absorption in the G750L bandpass by extracting the flux in two narrow bandpasses centered on the corresponding absorption lines (588.7–591.2 and 770.3–772.3 nm, respectively).

HST WFC3 Spectroscopy

We reduce data from both the G102 and G141 grisms following the method outlined in Tsiaras et al. (2016). Unlike that study, we begin with the bias- and dark-corrected `ima` images produced by the standard `calwfc3` pipeline rather than calibrating the raw images ourselves. Each of the exposures consists of 5 non-destructive reads. We create difference sub-exposures by subtracting consecutive reads (e.g. Deming et al., 2013; Evans et al., 2016; Kreidberg et al., 2014a). We determine the extent of the sub-exposure in the scan direction by finding the rows where the median flux profile in the spatial scan direction falls to 20% of the peak flux and add an additional buffer of 15 pixels above and below these rows. The extraction is not very sensitive to the number of pixels used for this buffer and any value between 10 and 20 suffices. We then mask out the rows exterior to this y pixel range and estimate the background using a 20 column wide rectangular region within the sub-exposure spanning columns between the end of the spectral trace and the edge of the array, taking care to avoid any secondary sources in the image. We remove any bad pixels by discarding 3σ outliers from this background region and then subtract the median of the remaining pixels from the unmasked part of the image. We then create a combined full frame image by co-adding all of the background subtracted sub-exposures.

Although the pointing of WFC3 is generally very stable, our scanned observations nonetheless exhibit small image to image variations in the position of the spectral trace in the x (dispersion) direction. By default, we estimate the magnitude of these shifts relative to the first frame by summing each image in the y direction and using this rough 1D-extracted spectrum to calculate the corresponding x offset. We find that the magnitude of this shift is less than 0.1 pixel over the entire duration of the WFC3 G102 visits. The WFC3 G141 data were taken shortly after the spatial scanning mode was first implemented on *HST* and exhibit a larger shift of approximately one pixel over the visit, most likely due to the sub-optimal scanning strategy utilized in these older observations. We find that using the centroid of each exposure and determining the horizontal offset relative to the centroid of the first exposure significantly decreases the scatter in the best-fit residuals for the G141 visit. We then use the wavelength and trace calibration functions provided by STScI (Kuntschner et al., 2009; Kuntschner et al., 2009) for each grism to calculate the full 2D wavelength solution for each image.

We flat-field all frames using the calibration files provided by STScI (Kuntschner et al., 2011) following the method outlined in Wilkins et al. (2014) and identify bad pixels in each individual image using a 6σ moving median filter in both the x and y directions. Although we also consider lower filter thresholds, we find that these result in overly aggressive outlier correction. We replace these outliers with the mean value within the moving filter and repeat the same filtering a second time to ensure that we have identified and removed all outliers.

The width of the spectral trace in the dispersion direction varies with the y -position of the star on the detector. As a result, lines of constant wavelength are slanted relative to the columns of the detector. For the wavelength dependent light curve extraction, we follow the method outlined in Tsiaras et al. (2016) and use the wavelength solution to determine the boundaries of each slanted wavelength bin and sum the flux within each bin. When the bins intersect with pixels, we use a second-order 2D polynomial to interpolate and integrate the flux over each partial-pixel region. This procedure ensures flux conservation and leads to a small reduction in the photometric scatter relative to other commonly employed methods, which usually smooth the data in the dispersion direction before light curve extraction (e.g. Deming et al., 2013; Fraine et al., 2014; Knutson et al., 2014b).

For the wavelength dependent light curves obtained with the G141 grism, we use 30 nm wide bins spanning the wavelength range 1.1-1.7 μm . Fraine et al. (2014)

utilized narrower wavelength bins, but also convolved their 1D spectra with a 4 pixel wide Gaussian filter prior to binning. Since we do not smooth our data, we adopt a lower wavelength resolution. For the G102 data, we utilize bins with a width of ~ 23.3 nm spanning the wavelength range $0.8\text{-}1.15\mu\text{m}$, identical to those adopted by Mansfield et al. (2018). The white light curve is simply obtained by summing the flux from all the spectroscopic light curves.

Spitzer 3.6 and 4.5 μm Photometry

We extract the photometric light curve for each *Spitzer* visit following the method described in Knutson et al. (2012), Wong et al. (2016), and Zhang et al. (2018a). We determine the star’s position in each 32×32 pixel *Spitzer* subarray image by iteratively calculating the flux-weighted centroid within a circular aperture with a radius of 3 pixels. To estimate the sky background, we first mask pixels located within a 12 pixel radius of the star’s position and then iteratively trim 3σ outliers (e.g. Knutson et al., 2012). We calculate the mean value of the remaining background pixels using the biweight location method (Astropy Collaboration et al., 2013, 2018) and subtract it from each image. We then use the `photutils` package (Bradley et al., 2018) to extract the photometry using circular apertures with radii ranging from 1.5 to 3 pixels in 0.1 pixel increments and 3 – 5 pixels in 0.5 pixel increments. We select the optimal aperture for each visit by minimizing the scatter in the best-fit residuals, which are binned in 60 s intervals (see §4.4 for more information). This procedure gives extraction apertures of 2.8 and 2.3 pixels for first and second transit in the 3.6 μm channel, respectively, and 2.3 and 2.6 pixels for the first and second transit in the 4.5 μm channel, respectively.

We iteratively trim outliers in the resulting timeseries using a 50 point moving median filter and discarding photometric points that lie more than 3σ away. We also fit 3rd order polynomials to the star’s x and y positions and discard any photometric points more than 3σ away from the polynomial model position during the observation, as these points are not well-corrected by our instrumental noise model. The number of points removed in each of these steps ranges between 0.09 – 0.97% for each individual visit and is commensurate with expectations for normally distributed data.

4.4 Systematics and Astrophysical Models

HST/STIS Instrumental Model

We remove the first orbit in each of the STIS datasets as the instrumental systematics are notably worse than they are in subsequent orbits. This difference is attributed to the thermal relaxation of *HST* following target acquisition due to the change in incidence angle of solar radiation. In addition, we remove the first exposure within each orbit as it has a much lower flux that is not well-matched by our parametric model. Both of these steps are standard practice for STIS datasets (e.g. Nikolov et al., 2015; Sing et al., 2011; Wakeford et al., 2017a). For the instrumental systematics model, we use a fourth order polynomial in orbital phase and a linear trend in time (Sing et al., 2008). We also fit for a linear trend in the x (dispersion) position of the star on the array for the G750L visit and the first G430L visit as it significantly reduces the Bayesian Information Criterion (BIC: change of 35 and 8, respectively) and lowers the residual scatter in our light curve fits from 1.51 and 1.6 times the photon noise limit to 1.26 and 1.53 times, respectively.

As discussed in Sing et al. (2019), we find that the scatter in our white-light residuals is further reduced if we decorrelate against additional parameters related to variations in telescope pointing. We find that the white-light residuals from our initial fit exhibit a strong correlation with the recorded RA and Dec, V2 and V3 roll, and latitude and longitude from the image file headers. However, these parameters are highly correlated with each other and we therefore use Principal Component Analysis (PCA) to reduce the number of independent fit parameters. We start with 6 principal components and retain those that capture $\geq 95\%$ of the systematic variation in the light curves. Using this criterion, we retain 4 and 3 parameters for the first and second visit in the G430L bandpass, respectively and 3 parameters in the G750L bandpass. We include linear contributions from these PCA parameters as part of our final systematics model. The addition of these linear jitter parameters has a negligible effect on the BIC ($|\text{BIC}| < 2$) for all three visits but it reduces the scatter in our residuals by 5 – 8%. The full systematics model $S(t)$ is given as

$$S(t) = c + vt_v + mx + \sum_i j_i p_{\text{jitter}} + \sum_{k=1}^4 p_k t_{orb}^k, \quad (4.1)$$

where t_v is the time from the beginning of the visit, t_{orb} is the time from the beginning of an orbit, p_{jitter} are the PCA vectors that describe the telescope pointing jitter, and c , v , m , j_i and p_i are free parameters in the fit.

HST/WFC3 Instrumental Model

G141 grism

Fraine et al. (2014) used the spectral template fitting method to derive wavelength-dependent transit depths for the WFC3 data. Here, we fit the timeseries for each individual spectroscopic light curve independently following the method described in Tsiaras et al. (2016). As with the STIS data, we trim the first orbit and the first exposure of each orbit, as they are not well-matched by our instrumental noise model.

Although there is an alternative physically motivated model that would in theory allow us to fit these data (Zhou et al., 2017), we do not expect that this would improve the precision of our transit depth measurement as we already have an out-of-transit baseline that is comparable in duration to our in-transit data. We fit the remaining orbits using a linear function of time and an exponential function of orbital phase, which is needed in order to correct for charge-trapping in the array (e.g. Deming et al., 2013; Zhou et al., 2017).

Our WFC3 systematics model $S(t)$ is

$$S(t) = (c + vt_v) + \left(1 - e^{-at_{orb} - b - D_t}\right), \quad (4.2)$$

where c , v , a , and b are free parameters in the fit, t_v is the time from the beginning of the visit, t_{orb} is the time from the beginning of an orbit, and D_t is a vector (same length as t_v) that is used to add duration-specific non-zero phase offsets. We use it to model the partial reset of the exponential ramp after a mid-orbit buffer dump in the third orbit (free parameter e) and to account for the slightly different ramp amplitude of the first fitted orbit (free parameter d , see Kreidberg et al., 2015). c and v characterize the linear dependence of systematic noise on time. For the exponential dependence, a controls the dependence on t_{orb} , and b sets the overall time-independent amplitude of the exponential term.

G102 grism

Unlike the G141 data, which only scanned in a single direction, the G102 observations were taken with an alternating scan direction. The behavior of the ramp is slightly different for each scan direction, likely due to small offsets in the relative position of the scanned spectrum on the array. We carry out an initial fit in which we allow the full exponential ramp model to vary independently for each of the scan directions and find that all parameters except the constant c in Equation 4.2

are consistent with a single common value. We therefore carry out our final fits assuming the same slope v and exponential ramp coefficients a , b , and D_t for both scan directions, but assign the forward and backward directions separate constant terms c_f and c_b that are allowed to vary independently.

Spitzer Instrumental Model

Spitzer 3.6 and 4.5 μm photometry exhibits a ramp-like behavior (e.g. Lewis et al., 2013; Wong et al., 2016; Zhang et al., 2018a) at the start of each new observation. Rather than fitting this ramp with a model, we simply trim the first 0.5 – 2 hours of data and find that the optimum trim duration for each visit that minimizes the scatter in our binned best-fit residuals is 1 hour. Even after truncation, we find that the second visit in the 3.6 μm bandpass possesses a significant ramp. Fitting this visit with the standard systematics model we adopt (see Equation 4.3 below) yields a much shallower transit depth and larger BIC ($\Delta \text{BIC} \sim 20$) compared to the values we obtain when we fit for this ramp. We do not use the ramp model for the other *Spitzer* visits because it changes the transit depths by $\lesssim 1\sigma$ and increases the BIC. Prior to fitting we bin the data in 60 s intervals. This binning results in a lower level of time-correlated noise in our best-fit residuals while still resolving the transit ingress and egress (for a discussion of binning practices with *Spitzer* data see Deming et al., 2015 and Kammer et al., 2015).

The primary instrumental noise source in the 3.6 and 4.5 μm *Spitzer* arrays is intra-pixel sensitivity variations combined with telescope pointing jitter. We model this behavior using Pixel-Level Decorrelation (PLD) following Deming et al. (2015):

$$S(t) = 1 + vt_v + \sum_{i=1}^9 w_i P_i(t), \quad (4.3)$$

where t_v is the time from the beginning of the visit, P_i is the normalized pixel count in the 3×3 array around the source, and w_i are the weights assigned to each of these arrays, which are determined using linear regression after dividing out the transit light curve at each step in the fit. The slope parameter v is left to vary as a free parameter. For the second visit in the 3.6 μm bandpass, we have an additional ramp term in the model with an amplitude A and decay timescale τ : $Ae^{-t_v/\tau}$.

Transit Model

We use the BATMAN package (Kreidberg, 2015) to model the transit light curve. The astrophysical model depends on the planet-star radius ratio R_p/R_* , planet semi-

major axis to stellar radius ratio a/R_* , impact parameter b , period P , and transit center time T_c . We fit for all of these parameters in our global fit, but use fixed values for P , a/R_* , and b when fitting individual transits. We fix the orbital eccentricity $e = 0.218$ and longitude of periastron $w = 199^\circ$ to the best-fit values from Yee et al. (2018). We validate our assumption of a linear ephemeris by comparing the best-fit mid-transit times from individual visits with the best-fit ephemeris from our global fit in Figure 4.1. The best-fit mid-transit times for all visits are consistent with a linear ephemeris at the 2σ level or better.

Our updated ephemeris is consistent with the values reported in Deming et al. (2011) and Southworth (2011) to within 0.2σ . However, there is only moderate agreement with the values reported in Sanchis-Ojeda & Winn (2011) and Huber et al. (2017). Curiously enough, the values reported by Huber et al. (2017), Sanchis-Ojeda & Winn (2011), and Southworth (2011) are for the same epoch and they disagree at the 10σ level. We suspect this is due to errors in reporting of the mid-transit time in the stated time convention. For example, Southworth (2011) and Sanchis-Ojeda & Winn (2011) report almost identical values for the mid transit time but the former report it in BJD UTC while the latter do so in BJD TDB. These two time conventions differ by 66.184 s (an additional leap second was added in the first month of *Kepler*'s quarter 14). Similarly, the value reported by Huber et al. (2017), supposedly in BJD UTC, match that of Southworth (2011) converted to BJD TDB. Careful accounting of these errors might resolve the paradoxes posed by these differing mid-transit times.

As part of ExoTEP, we employ the Python package LDTk (Parviainen & Aigrain, 2015) to calculate limb darkening coefficients for all of our observations except the *Spitzer* transits. LDTk queries spectral intensity profiles from the PHOENIX library (Husser et al., 2013) and computes a mean limb darkening profile for a star given its effective temperature, surface gravity, and metallicity (and associated uncertainties). We then fit this profile with a 4-parameter non-linear limb darkening model, and we fix the limb darkening coefficients to the model values in our light curve fits. PHOENIX profiles extend from 50 nm to 2600 nm in wavelength space and can therefore only supply limb darkening coefficients for the *HST* bandpasses. For the *Spitzer* bandpasses, we use the (4-parameter non-linear) limb darkening coefficients tabulated by (Sing, 2010, assuming $T_{\text{eff}} = 4750$ K, $\log g = 4.5$, $[\text{Fe}/\text{H}] = 0.3$), which are calculated from ATLAS models. We investigate the importance of our choice of limb-darkening models in the *Spitzer* bands by re-fitting the *Spitzer*

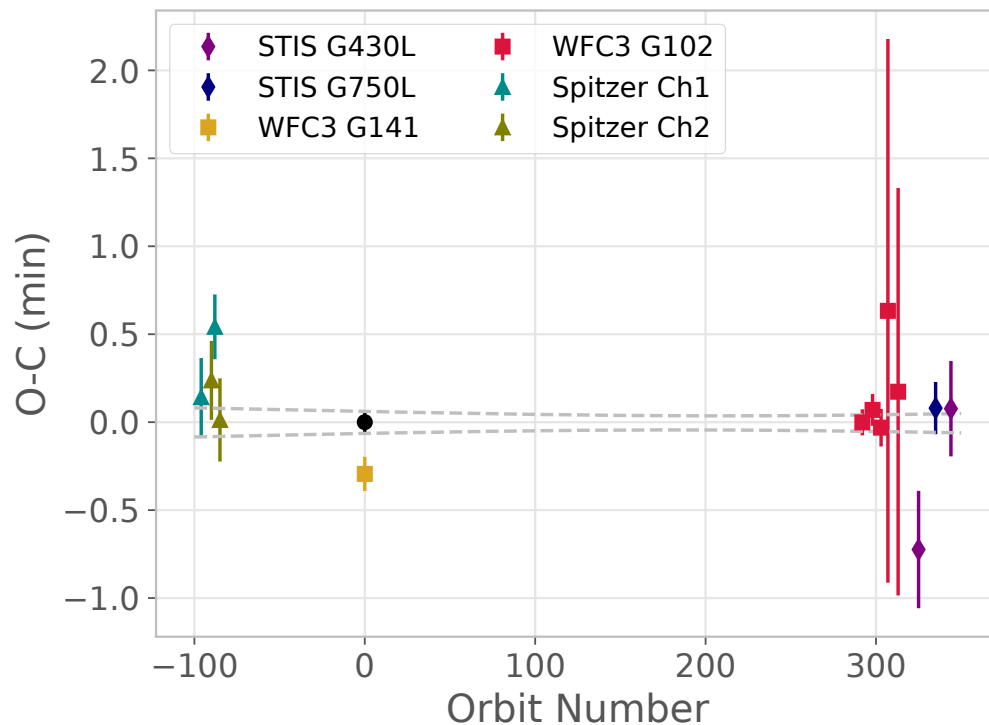


Figure 4.1: Observed minus calculated mid-transit times from fits to individual visits, where the color indicates the instrument. Predicted transit times are calculated using the best-fit ephemeris from the global fit, with 1σ uncertainties indicated by the dashed grey lines. Visits with minimal data during ingress or egress have significantly larger uncertainties.

light curves with quadratic limb darkening coefficients as free parameters. We obtain transit depths that agree to within 0.5σ with those obtained with ATLAS limb darkening coefficients. We therefore conclude that our use of ATLAS models instead of PHOENIX models at 3.6 and $4.5 \mu\text{m}$ has a negligible effect on our results.

Stellar Activity

HAT-P-11 is a relatively active K dwarf with a Ca II H & K emission line strength of $\log(R'_{\text{HK}}) = -4.57$ (Knutson et al., 2010), and it is therefore important to address the impact of its activity on the transmission spectrum (McCullough et al., 2014; Morris et al., 2017a,b). Both occulted and unocculted spots introduce wavelength dependent biases in the transmission spectrum (e.g. Pont et al., 2008; Rackham et al., 2018; Sing et al., 2011). These biases must be corrected to combine transit depth measurements from different epochs and different wavelength bandpasses.

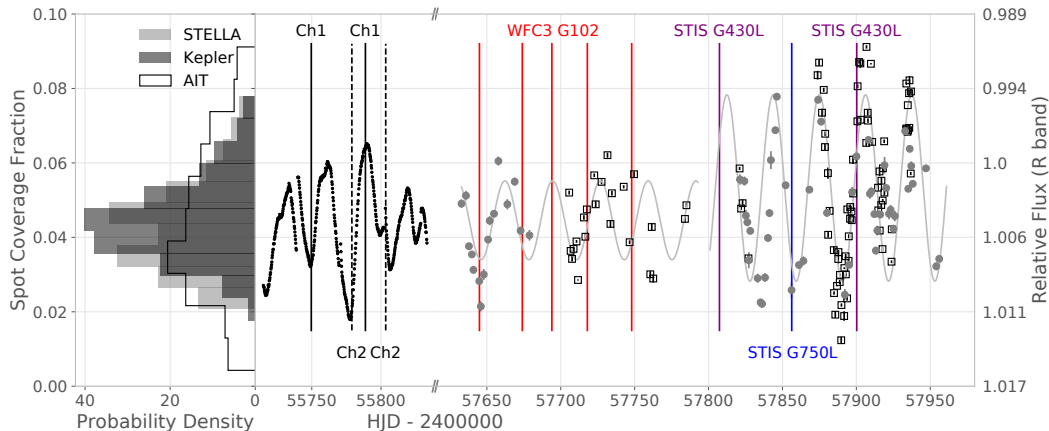


Figure 4.2: Change in HAT-P-11’s R band flux and corresponding spot coverage fraction in 2011 and from late 2015 to early 2017. Points are calculated using photometric monitoring data obtained in the Cousins R band pass using the AIT telescope at Fairborn Observatory, in the Johnson B and V bands using the STELLA telescope at Izaña Observatory, and from the *Kepler* telescope. We assume that the relative flux baseline for all three telescopes corresponds to a spot coverage fraction of 4.4%, and use a photospheric temperature of 4780 K and spot temperature of 4500 K to convert these observations to the equivalent R band fluxes. Visit times for *Spitzer* 3.6 μm (black) and 4.5 μm channels (black dashed), *HST* WFC3 G102 (red), STIS G430L (purple), and STIS G750L (blue) observations are indicated by vertical lines. The grey curves are sinusoidal functions that best match the observed variability at different epochs and are used to infer spot coverage fractions for *HST* visits that do not have contemporaneous ground-based monitoring.

We find no evidence for any spot crossings during the *HST* observations included in this analysis, with the exception of two G102 visits. Following Mansfield et al. (2018), we simply trim the data associated with the spot occultation rather than including this effect in our models. While two of the four *Spitzer* transits with contemporaneous *Kepler* transit photometry included a spot occultation, this occultation was evident only in the *Kepler* light curve. Given the relatively small chromatic effect of spot crossing at infrared wavelengths, Fraine et al. (2014) concluded that these spots would have had a negligible effect on the measured *Spitzer* transit depths.

Unocculted spots are usually much harder to correct for as accounting for their effect requires knowledge of the fractional surface area of the star that is covered by the spots as well as the average spot temperature. Fortunately, HAT-P-11 has some of the best constraints on spot properties amongst all stars that host transiting planets. This is because HAT-P-11b orbits its star from pole to pole (its orbit is misaligned

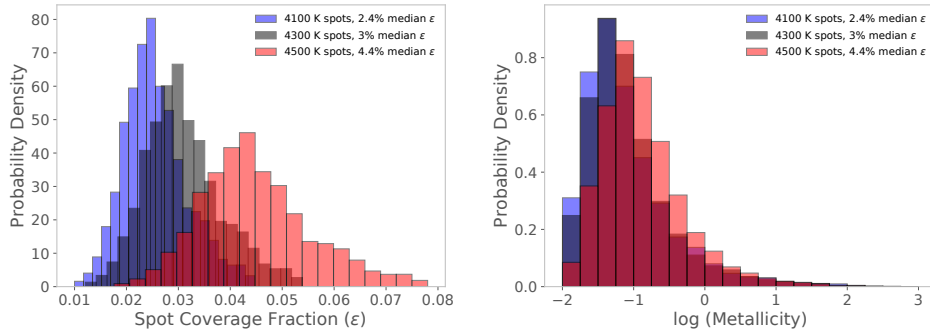


Figure 4.3: We vary star spot temperatures and spot coverage fractions such that they produce the same absolute correction in the *Kepler* bandpass. The spot coverage fractions in the left panel are deduced from *Kepler* long cadence photometry. We fit light curves for these different stellar spot properties and quantify their effect on the retrieved atmospheric metallicity. In the right panel, we show that the posterior for metallicity is relatively insensitive to our choice of spot temperature. We adopt a value of 4500 K in the rest of this study following Morris et al. (2017a).

with the stellar spin axis by 106 degrees; Deming et al., 2011; Sanchis-Ojeda & Winn, 2011) and the star was monitored by *Kepler* in a broad optical bandpass from 2009 – 2012, allowing us to observe more than 200 transits of the planet. This essentially provides us with a latitude-longitude map of the entire stellar surface and constrains the spot covering fraction of the stellar surface to be $3_{-1}^{+6}\%$ (Morris et al., 2017a,b).

The *Kepler* data span the epoch of the *Spitzer* transit observations and although the G141 observations were taken in 2012, they unfortunately coincided with a gap in the *Kepler* coverage (Fraine et al., 2014). We also obtained photometric monitoring data in the Cousins R band pass with the Celestron 14-inch (C14) Automated Imaging Telescope (AIT) at Fairborn Observatory (Sing et al., 2015) and in the Johnson B and V filters from the 1.2 m robotic STELLA telescope at Izaña Observatory (Strassmeier et al., 2004; data taken from Mansfield et al. (2018)). These data were obtained between 2015 – 2017, covering the epochs of the WFC3 G102 and STIS observations but not the 2012 WFC3 G141 observations. This introduces a source of uncertainty, as there is no uniform source of monitoring data spanning the epochs of all of the datasets included in our global analysis.

We use the *Kepler* and ground-based photometric monitoring data to estimate the spot coverage fraction during the *Spitzer*, *HST* WFC3 G102, and *HST* STIS observation epochs. We assume that the baseline of the relative flux from each telescope

corresponds to a median spot coverage fraction $\bar{\epsilon}$ and calculate the absolute values of ϵ for all the other relative flux values. We account for the difference in the telescope bandpasses while calculating the spot coverage fraction. In Figure 4.2, we show the photometric data, relative flux in R band, and the corresponding spot coverage fraction from *Kepler*, STELLA, and the AIT for a median spot coverage fraction $\bar{\epsilon}$ of 4.4% and average spot temperature of 4500 K. Histograms for the inferred spot coverage fraction from the photometric data are consistent with each other and with the $3_{-1}^{+6}\%$ estimate obtained by Morris et al. (2017a). We find that during the STIS observations, the stellar variability is best matched by a sine curve with a period of 30 days and peak-to-peak relative flux of about 1.5%. The star appears to have been somewhat less active and variable during the epoch of the WFC3 G102 observations with peak-to-peak relative flux of 0.7% and a period of 33 days. These observations imply that there is almost a 1 – 2% difference in the relative transit depth between epochs due to changes in stellar brightness. These periods and variability are also in good agreement with inferences from *Kepler*.

The spot coverage fraction ϵ , stellar photospheric temperature, and spot temperature determine the ratio of the observed ($D_{\lambda,obs}$) to true (D_{λ}) transit depths (Rackham et al., 2018):

$$D_{\lambda,obs} = \frac{D_{\lambda}}{1 - \epsilon (1 - F_{\lambda,spots}/F_{\lambda,star})}, \quad (4.4)$$

where $F_{\lambda,spots}$ and $F_{\lambda,star}$ are the stellar intensity profiles corresponding to the temperature of the spots and the unspotted stellar photosphere, respectively. We apply this correction by re-scaling the model transit light curves at each step in our fits by the denominator in Equation 4.4. We do not include faculae in our model because they produce a distinct spectral signature in the optical region of the transmission spectrum (e.g. Zhang et al., 2018b), and we observe no such effect in our three *HST* STIS visits (see § 4.5).

To model the star spots and the surface fluxes, we use BT-NextGen (AGSS2009) stellar models (Allard et al., 2012) and fix the photospheric temperature to 4780 K. The brightness contrasts estimated from spot crossings in the *Kepler* light curves give a range for spot temperatures. We explore the effect of changing median spot coverage fraction $\bar{\epsilon}$ and spot temperature on the retrieved atmospheric metallicity of the planet. We choose combinations of spot temperatures and $\bar{\epsilon}$ such that the absolute corrections to the transit depths in the *Kepler* bandpass are identical. Spot temperatures of 4100 K, 4300 K, and 4500 K are thus combined with $\bar{\epsilon}$ of

2.4%, 3%, and 4.4%, respectively. Figure 4.3 shows histograms for spot coverage fractions for the range of variability observed in the *Kepler* light curves and the corresponding atmospheric metallicity constraints for HAT-P-11b obtained from retrievals. We find that the metallicity posterior is relatively insensitive to our choice of spot temperature. Following the more detailed stellar activity study of HAT-P-11 conducted by Morris et al. (2017a) and spot temperature characterization by Mansfield et al. (2018), we choose to adopt a spot temperature of 4500 K in the rest of this study.

For the *HST* WFC3 G141 data, we assume a fixed spot coverage fraction of 4.4% as this visit is not covered by any photometric observation. For the *Spitzer*, WFC3 G102, and STIS visits, we apply a visit-specific correction. We fit periodic curves to the spot coverage fraction to determine its value for the third G102 visit and the first G430L visit as ground based data at these epochs are scarce. For the other WFC3 G102 and STIS visits, we use the closest observation to obtain an estimate of the spot coverage fraction, if the next closest observation is more than 0.5 days away (i.e., on a different night). Otherwise, we use the average of the two nearest observations.

4.5 Analysis

The log-likelihood \mathcal{L} (logarithm of the posterior probability) of our astrophysical transit model M and systematics model S given data D with uncertainty σ is

$$\mathcal{L} = \sum_{i=1}^n \left[\left(\frac{D_i - (M_i \times S_i)}{2\sigma_i} \right)^2 + \ln(\sqrt{2\pi}\sigma_i) \right]. \quad (4.5)$$

We use the Markov Chain Monte Carlo (MCMC) method to fit the white-light timeseries for each visit individually and then carry out a joint fit where the same transit shape and ephemeris parameters are used for all datasets, while the planet-star radius ratio is allowed to vary across different bandpasses. In all cases we fit an independent instrumental systematics model for each individual transit. We carry out our fits using the *emcee* package, which is an affine-invariant ensemble sampler (Foreman-Mackey et al., 2013).

We first fit each dataset individually to obtain an initial set of best-fit parameters. For these individual fits, in addition to fitting for astrophysical and systematics model parameters, we allow the measurement error σ to vary as a free parameter to ensure we obtain a reduced χ^2 of unity and to accurately model uncertainties in the

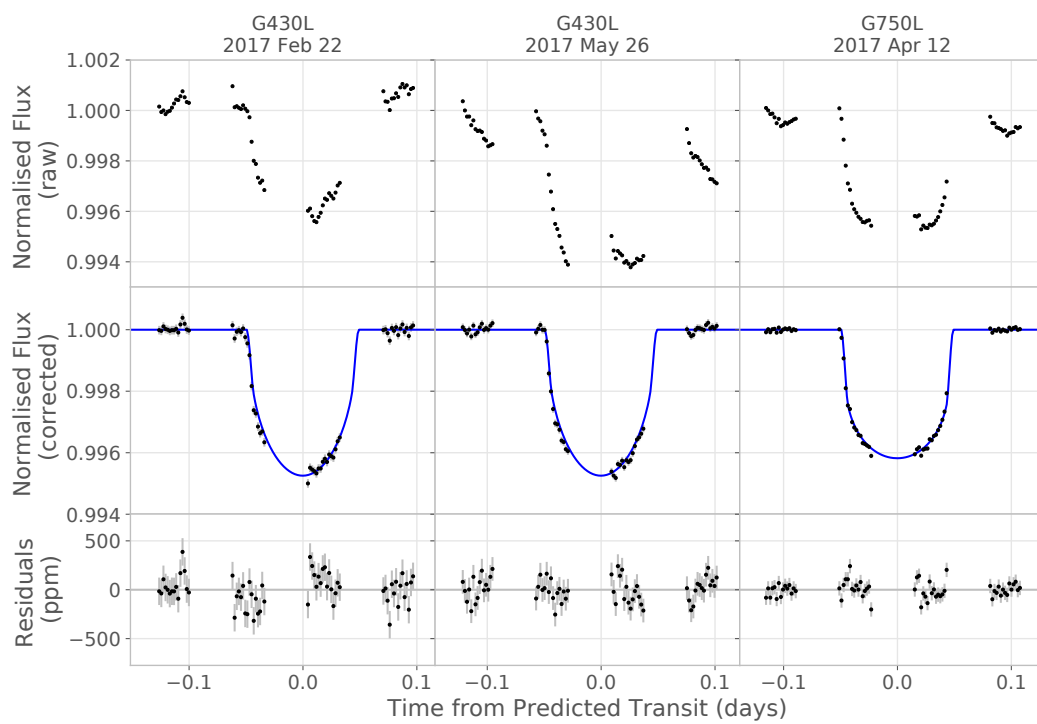


Figure 4.4: STIS white light transit light curves before (top) and after (middle) dividing out the best-fit instrumental systematics model. The best-fit transit light curve is shown in blue for comparison, and the fit residuals are shown at the bottom.

Table 4.2: Global broadband light curve fit results^a

Parameter	Instrument	Band pass (μm)	Value
Planet radius, R_p/R_*	STIS G430L	0.29 - 0.57	$0.05806^{+0.00036}_{-0.00028}$
Planet radius, R_p/R_*	STIS G750L	0.524 - 1.027	$0.05783^{+0.00034}_{-0.00035}$
Planet radius, R_p/R_*	WFC3 G102	0.8 - 1.15	$0.05788^{+0.00016}_{-0.00011}$
Planet radius, R_p/R_*	WFC3 G141	1.1 - 1.7	$0.05847^{+0.00016}_{-0.00015}$
Planet radius, R_p/R_*	IRAC Channel 1	3.16 - 3.93	$0.05778^{+0.00024}_{-0.00026}$
Planet radius, R_p/R_*	IRAC Channel 2	3.97 - 5.02	$0.05811^{+0.00028}_{-0.00027}$
Transit center time T_c (BJD _{TDB})	—	—	$2456218.866182^{+0.000042}_{-0.000044}$
Period P (days)	—	—	$4.88780228^{+0.00000016}_{-0.00000018}$
Impact parameter b	—	—	$0.135^{+0.064}_{-0.078}$
Relative semi-major axis a/R_*	—	—	$17.46^{+0.14}_{-0.20}$
Inclination ^b i	—	—	$89.56^{+0.26}_{-0.22}$

Notes.

^aThe R_p/R_* values reported here have been corrected for unocculted spots assuming a photosphere temperature of 4780 K, spot temperature of 4500 K, and spot covering fraction of 4.4%.

^bCalculated from posteriors for b and a/R_* .

parameters due to the intrinsic scatter in the light curves. We then use the results of these individual fits as initial guesses in the joint fit and fix the measurement error σ for each visit to the best-fit value obtained from its corresponding individual fit. We run an initial burn-in phase with 2000 steps for individual datasets and 40,000 steps for the global fit. We identify and discard walkers that become trapped in local minima by removing any chain whose maximum likelihood value is lower than median likelihood value of any of the other chains. We set the initial number of walkers to four times the number of free parameters and typically reject $\lesssim 10\%$ of these walkers. Whenever an odd number of walkers remain, we randomly remove a walker from the remaining set. After burn-in, the fit is continued with the remaining walkers for another 3000 steps for individual fits and 60,000 steps for the global fit. We assume flat priors within a suitable range for each parameter. We check for convergence by inspecting the chain plots and running these fits with long chains three times. We find that the parameter estimates are consistent at the 0.5σ level or better and the transmission spectrum is consistent to within 0.5σ .

We fit a total of thirteen individual transits in our global analysis, each with their own instrumental systematics model. This corresponds to a total of 93 free parameters, which is too large to reliably explore with MCMC. We therefore utilize linear optimization to reduce the number of free parameters in our MCMC fit. At each step in the fit, we calculate new best-fit values for all linear parameters in the global systematics model using linear regression while keeping all other model parameters fixed to their values at that step in the MCMC. This reduces the number of free parameters in the MCMC fit to 48. We additionally fix the σ parameters for all visits in our global fit to the values obtained in our individual fits, which reduces the number of free parameters to 35. This is small enough to ensure reliable convergence within a reasonable number of steps. We acknowledge that in principle this approach might cause us to underestimate the uncertainties in our astrophysical model parameters, as we are optimizing rather than marginalizing over the linear instrumental model parameters (see e.g. Benneke et al., 2019a). However, we find that in practice these linear instrumental model parameters contribute negligibly to the uncertainties in our astrophysical model parameters. Optimizing the linear instrumental parameters in a global fit to the data excluding G102 light curves reduces the uncertainties in R_p/R_* by less than 5%.

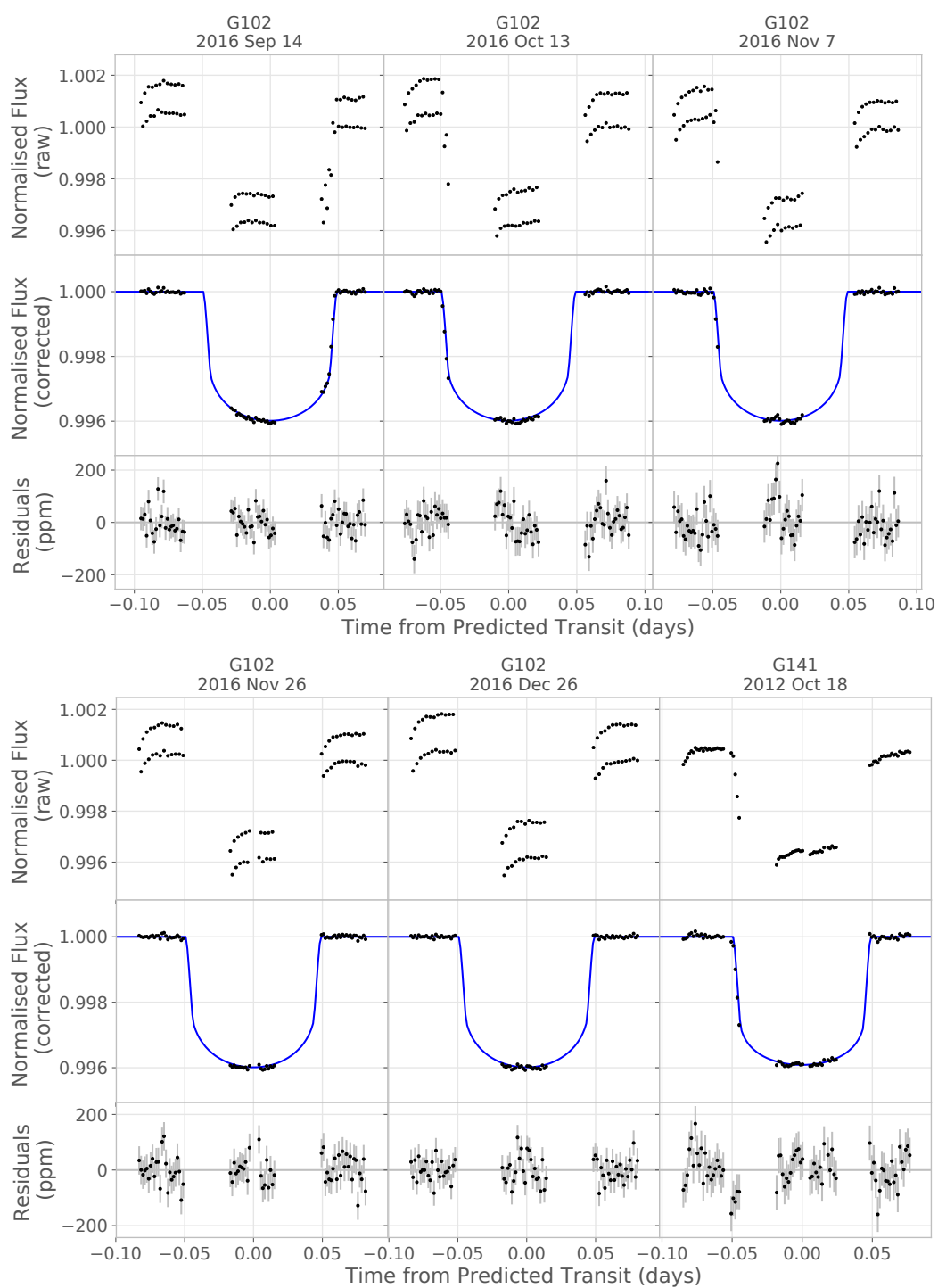


Figure 4.5: WFC3 G102 and G141 white light transit light curves before (top) and after (middle) dividing out the best-fit instrumental systematics model. The best-fit transit light curve is shown in blue for comparison, and the fit residuals are shown at the bottom.

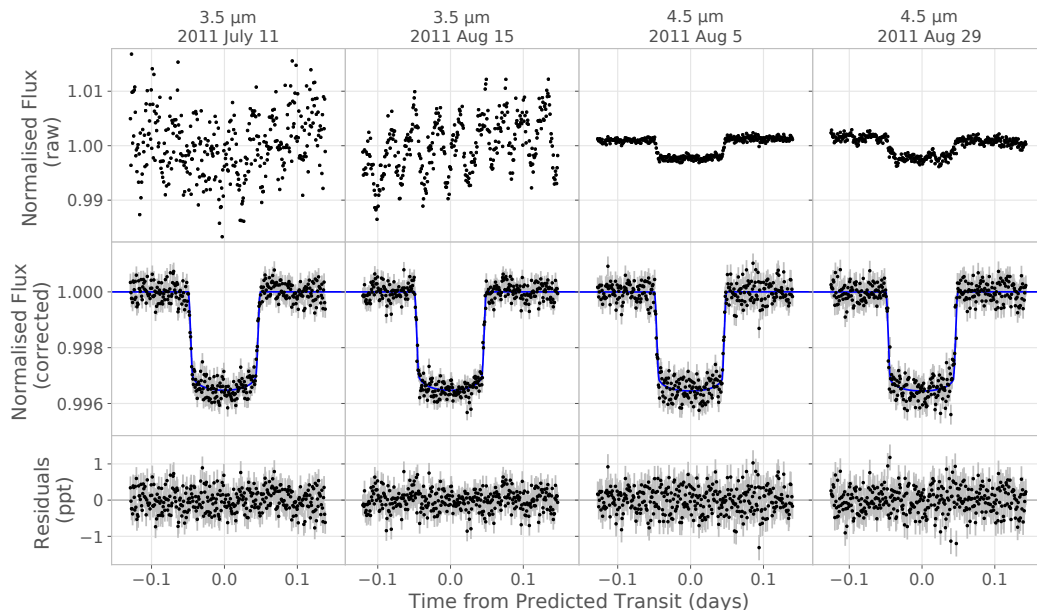


Figure 4.6: *Spitzer* transit light curves before (top) and after (middle) dividing out the best-fit instrumental systematics model. The best-fit transit light curve is shown in blue for comparison, and the fit residuals are shown at the bottom.

White Light Curve Fits

We confirm that the individual transit depths in bandpasses with multiple visits agree to within 2σ after correcting for the effects of unocculted star spots, as discussed in § 4.4. We therefore report the global best-fit transit depths for each band in Table 4.2. The best-fit transit light curves and their residuals are shown in Figures 4.4-4.6. The white light curve depths for the WFC3 G141 visit and G102 visits agree with the values reported by Fraine et al. (2014) and Mansfield et al. (2018) at the 1.5σ and 0.6σ level, respectively. Our visit-averaged 3.6 and 4.5 μm *Spitzer* transit depths are in good agreement (1.5σ lower and 0.5σ higher, respectively) with the values obtained by Fraine et al. (2014). The residuals from our *Spitzer* fits display the predicted root- n scaling expected for Gaussian noise.

We find that both our 3.6 and 4.5 μm *Spitzer* transit depths are somewhat lower than our WFC3 G141 white light transit depth. The difference in white light curve depths between the WFC3 G141 observations and the *Spitzer* observations is consistent with the results reported by Fraine et al. (2014). Fraine et al. (2014) attributed this difference to stellar activity and used an offset of 93 ppm for the WFC3 spectrum to obtain their best-fit model. However, this difference cannot be explained by stellar activity for plausible star spot properties. For the *Spitzer* transit depths to be $\gtrsim 100$

ppm higher than the *HST* measurements, HAT-P-11 would need to be 3% brighter during the *Spitzer* epochs than the *HST* ones, which is larger than the observed peak-to-peak variability of the star. For representative spot temperatures of 4500 K and 4300 K, the spot coverage fraction would need to be different by >10% and ~5%, respectively, to obtain such a large relative correction to the transit depths. Finally, such a large correction to the *HST* measurements would strongly distort the transmission spectrum from 0.3 μm – 1.7 μm and impart an almost unphysical upward slope (with increasing wavelength) to it. We discuss this difference in the *HST* and *Spitzer* transit depths and our efforts to interpret it in § 4.7.

Wavelength-Dependent Light Curves

When fitting for the wavelength-dependent radius ratio R_p/R_* within each *HST* STIS and WFC3 bandpass, we fix the orbital parameters P , T_c , a/R_* and b to the best-fit values from the global fit. We re-fit the full systematics model in each individual bandpass without recourse to values obtained from the white-light fit. We found that fitting the individual spectroscopic light curves with the full systematics model significantly improved the quality of the fit as compared to using the (scaled) systematics models from the global fit. For the *HST* STIS data, all parameters in the full systematics model are obtained by linear optimization and we simply use this model for the spectroscopic light curves as well. We find that fitting the individual spectroscopic light curves with the full systematics model as compared to using the (scaled) systematics models from the global fit significantly improves the quality of the fit for the WFC3 G102 data ($\Delta\text{BIC} > 10$ for 8 out of 12 wavelength bins) but not for the WFC3 G141 data. Applying a common-mode correction to the spectroscopic light curves obtained by dividing the white light curve flux with the best-fit transit model (e.g. Deming et al., 2013) and employing a simpler model for the residual systematics in the spectroscopic light curves is strongly favored ($\Delta\text{BIC} > 10$ for 16 out of 19 wavelength bins). Our simple model for the WFC3 G141 spectroscopic light curves is a linear function of the measured shift $(x - x_o)$ in the dispersion direction relative to the first exposure with offset c and slope v :

$$S(t) = c + v(x - x_o). \quad (4.6)$$

We present R_p/R_* and associated errors for each bandpass in Table 4.3, the transmission spectrum in Figure 4.7, and show the corresponding wavelength-dependent light curves in Figures C.1–C.6 in Appendix C.

Table 4.3: Spectroscopic light curve fit results

Wavelength (μm)	R_p/R_*	$\pm 1\sigma$	Wavelength (μm)	R_p/R_*	$\pm 1\sigma$
<u>STIS G430L</u>			<u>WFC3 G141</u>		
0.346-0.401	0.05788	0.00117	1.120-1.150	0.05899	0.00044
0.401-0.456	0.05821	0.00045	1.150-1.180	0.05896	0.00041
0.456-0.511	0.05828	0.00031	1.180-1.210	0.05825	0.00028
0.511-0.566	0.05812	0.00029	1.210-1.240	0.05740	0.00033
<u>STIS G750L</u>			1.240-1.270	0.05726	0.00031
0.528-0.577	0.05903	0.00086	1.270-1.300	0.05842	0.00023
0.577-0.626	0.05719	0.00068	1.300-1.330	0.05803	0.00023
0.626-0.674	0.05787	0.00070	1.330-1.360	0.05914	0.00030
0.674-0.723	0.05766	0.00073	1.360-1.390	0.05867	0.00031
0.723-0.772	0.05587	0.00109	1.390-1.420	0.05909	0.00030
0.772-0.821	0.05763	0.00084	1.420-1.450	0.05941	0.00031
0.821-0.870	0.05789	0.00116	1.450-1.480	0.05933	0.00030
0.870-0.919	0.05732	0.00129	1.480-1.510	0.05751	0.00029
0.919-0.967	0.05597	0.00159	1.510-1.540	0.05878	0.00027
0.967-1.016	0.05687	0.00210	1.540-1.570	0.05846	0.00030
0.589-0.591*	0.06244	0.00361	1.570-1.600	0.05827	0.00036
0.766-0.773*	0.05689	0.00192	1.600-1.630	0.05889	0.00030
<u>WFC3 G102</u>			1.630-1.660	0.05950	0.00037
0.850-0.873	0.05812	0.00019	1.660-1.690	0.05823	0.00102
0.873-0.897	0.05778	0.00016			
0.897-0.920	0.05782	0.00015			
0.920-0.943	0.05795	0.00014			
0.943-0.967	0.05807	0.00013			
0.967-0.990	0.05810	0.00013			
0.990-1.013	0.05805	0.00013			
1.013-1.037	0.05784	0.00011			
1.037-1.060	0.05811	0.00013			
1.060-1.083	0.05787	0.00012			
1.083-1.107	0.05811	0.00012			
1.107-1.130	0.05831	0.00012			

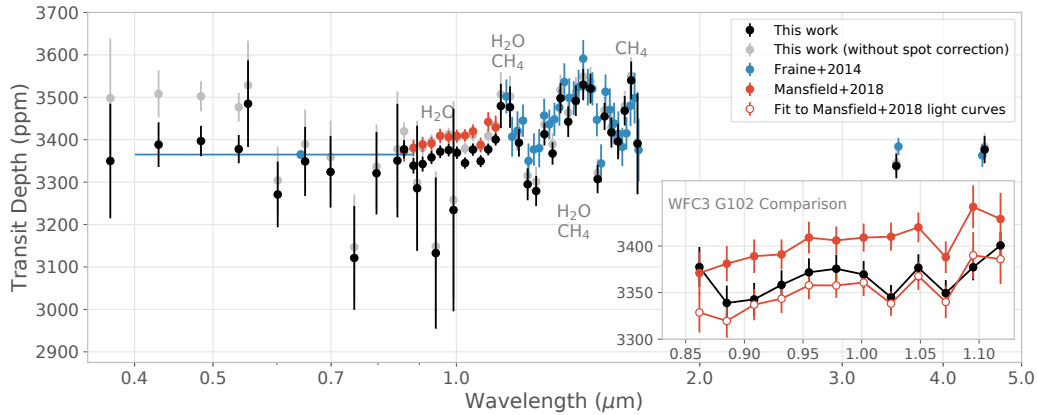


Figure 4.7: The transmission spectrum of HAT-P-11b both with and without stellar activity correction. Our transmission spectrum is in good agreement with Fraine et al. (2014)’s published spectrum. In the inset figure, we compare our WFC3 G102 spectrum with a fit to Mansfield et al. (2018)’s light curves, as well as Mansfield et al. (2018)’s published spectra. Our G102 spectrum deviates most significantly from the published spectrum at $0.86 \mu\text{m}$, $1.025 \mu\text{m}$, and $1.095 \mu\text{m}$, which has the effect of washing out the small absorption feature at $0.95 \mu\text{m}$ in the published version.

In Figure 4.7, we show both stellar activity corrected and uncorrected transit depths. We obtain the uncorrected depths by fixing the orbital parameters b and a/R_* to values obtained from the global white light curve fit (shown in Table 4.2) and fitting the light curves without any wavelength or epoch dependent correction. This allows us to isolate the effect of activity correction on the transit depths. We note that activity correction is crucial for obtaining correct inferences from the optical data. The uncorrected upward slope in the STIS G430L bandpass would dramatically affect our interpretation of the planet’s atmospheric properties. In addition, the magnitude of the correction is commensurate with values necessary to produce a consistent and connected spectrum across multiple bandpasses. For example, the uncorrected STIS G750L depths are fairly low compared to the STIS G430L measurements, but STIS G750L observations are taken at a time when spot coverage of the star is at a minimum and the STIS G430L measurements are obtained when the star is fairly spotted (see Figure 4.2). This produces a small correction for the STIS G750L measurements and a large one for the STIS G430L depths, as one would expect.

We see evidence for molecular absorption in the WFC3 G141 bandpass, in good agreement with the results from Fraine et al. (2014). Our spectrum is not as smooth as that of Fraine et al. (2014), but this is likely due to their use of a 4-pixel

wide smoothing kernel (Figure 4.7). Our spectrum agrees within $\sim 1\sigma$ with the previously published spectrum in almost all the wavelength bins. Stellar activity correction introduces a slightly different slope than that of Fraine et al. (2014), with shallower transit depths at short wavelengths and larger transit depths at longer wavelengths. Notably, our updated spectrum (both with and without correction) possesses a steeper rise longward of $1.5 \mu\text{m}$ compared with Fraine et al. (2014)'s, suggesting the presence of methane in the planet's atmosphere (see § 4.7).

Our WFC3 G102 spectrum differs from the version published by Mansfield et al. (2018) in subtle but significant ways (see inset, Figure 4.7). We diagnose the reason for this discrepancy by carrying out an additional set of fits using our models applied to the light curves from Mansfield et al. (2018). We find that a majority of the observed vertical offset between the spectrum published in Mansfield et al. (2018) and our fit to Mansfield et al. (2018)'s light curves is due to differences in the assumed values for the orbital parameters. We fit for period, while fixing impact parameter and a/R_* to the best-fit values from our global fit, and eccentricity and argument of pericenter values to the values obtained from Yee et al. (2018). In contrast, Mansfield et al. (2018) fix the period and eccentricity to values from Huber et al. (2017) and use impact parameter and a/R_* values from Fraine et al. (2014) with Gaussian priors. Small differences in the stellar activity correction were found to be insignificant. Our spectrum is not a perfect match for the one we derive using Mansfield et al. (2018)'s light curves. The spectral shape of our fit to Mansfield et al. (2018)'s light curves is intermediate to that of our spectrum and the published spectrum. This implies that although our choice of systematics model (especially the use of an additional ramp delay parameter d for the first fitted orbit) and global fitting of orbital parameters improves the agreement between our spectra, some differences must partly arise due to choices made in the light curve extraction. In particular, there are significant differences in our light curves for the first visit, which arise due to Mansfield et al. (2018)'s decision to exclude the last non-destructive read (for forward scan, first read for backward) of the scan. These differences are important, as the absorption features at $1.15 \mu\text{m}$ and $0.95 \mu\text{m}$ are barely discernible in the spectrum published by Mansfield et al. (2018). In our updated spectrum, the combination of WFC3 G102 and G141 data reveals three molecular absorption features: two strong features centered at $1.15 \mu\text{m}$ and $1.4 \mu\text{m}$ and a weak feature at $0.95 \mu\text{m}$ (Figure 4.7). This allows us to infer the presence of water and/or methane with a combined significance of 4.4σ (see § 4.7).

Our new STIS observations indicate that HAT-P-11b has a relatively featureless transmission spectrum at optical wavelengths with a hint of increasing transit depth with decreasing wavelength (scattering slope). This is in agreement with recently reported measurements obtained from ground-based observations (Murgas et al., 2019). As mentioned above, a careful accounting for the effects of unocculted spots produces a much flatter optical transmission spectrum than the uncorrected version. This plays an important role in constraining atmospheric metallicity and places constraints on the effective size and number density of the particles responsible for scattering in the atmosphere. We see no evidence for narrow-band sodium or potassium absorption, although these features are expected to form at relatively low pressures where cloud opacity should be less important. This is not surprising, as HAT-P-11b’s atmosphere is predicted to be too cold for these elements to remain in vapour form (e.g. Lodders, 1999). Additionally, we do not see the jump in transit depth at $0.8 \mu\text{m}$ that Lothringer et al. (2018) report for GJ 436b and note for HAT-P-26b.

4.6 Comparison to Forward Models

We next compare HAT-P-11b’s observed transmission spectrum to predictions from a 1D microphysical cloud model originally developed for use with solar system planets (e.g. Colaprete et al., 1999; Gao et al., 2017; James et al., 1997; Toon et al., 1992, 1979). These cloud models require a temperature-pressure profile and a prescription for the vertical mixing in the atmosphere as inputs. We draw both of these profiles from results of a 3D general circulation model (GCM) for HAT-P-11b. We discuss the details of both models in the following two sub-sections.

General Circulation Model

We use a GCM to put constraints on the extent of (1D) mixing in the atmosphere. This allows us to take into account the effect of three-dimensional (3D) dynamics on the 1D atmospheric profiles used in transmission spectroscopy studies. This is particularly important for eccentric short-period planets like HAT-P-11b, which are presumed to be tidally locked and therefore may have a pressure and temperature structure that varies significantly with longitude. The appreciable eccentricity of HAT-P-11b also leads to the convolution of latitudinal structure and orbital phase of the planet. We take the planet’s eccentricity into account in our GCM and use atmospheric profiles (for temperature, pressure, eddy diffusion coefficient) from the planet’s transit. In this case, we utilize the Substellar and Planetary Radiation

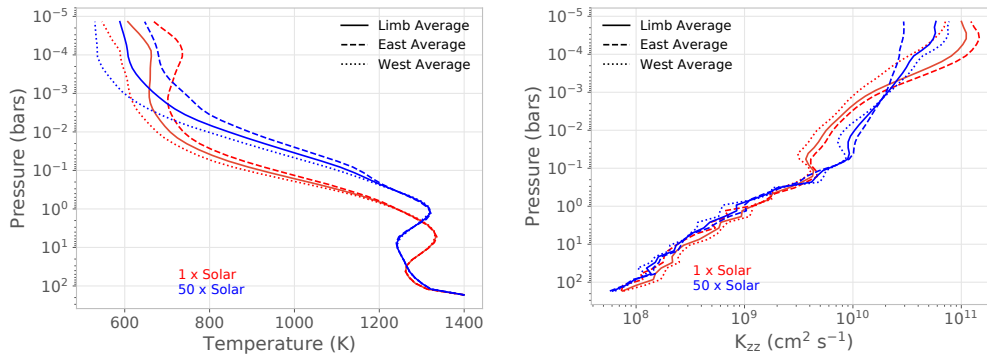


Figure 4.8: Temperature (left) and vertical mixing parameter K_{zz} (right) profiles as a function of pressure at the orbital phase of the transit (since HAT-P-11b has a significant eccentricity). These profiles are obtained from a SPARC GCM model for HAT-P-11b and are used as inputs in our microphysical cloud models. Transmission spectroscopy probes the atmosphere at pressures roughly between $10^{-1} - 10^{-4}$ bars.

and Circulation (SPARC) model (Kataria et al., 2016; Showman et al., 2009), which couples the MITgcm dynamical core (Adcroft et al., 2004) with a plane-parallel, two-stream version of the multi-stream radiation code developed by Marley & McKay (1999). As we will discuss in §4.7, our retrievals using the *HST* data prefer relatively low metallicity values, so we choose models with atmospheric metallicities of $1\times$ and $50\times$ solar (we multiply relative abundances of elements heavier than hydrogen and helium by this metallicity value and renormalize the sum of relative abundances to 1); this range is therefore a good match for the posterior probability distribution for this parameter.

We model vertical mixing as a diffusive process with an effective eddy diffusion coefficient K_{zz} . Deviations from this diffusive approximation are almost guaranteed for tidally locked planets, which are expected to also have vigorous horizontal transport between the day and night sides (e.g. Zhang & Showman, 2018a,b). However, it is non-trivial to accurately capture this horizontal transport, and we therefore neglect it for the moment in order to explore the effects of vertical mixing, which is key for cloud formation. This mixing is typically parameterized as a constant value with or without an inverse dependence on square root of pressure (e.g. Parmentier et al., 2013). We depart from this formalism and instead use the temperature, pressure, and K_{zz} profiles from the GCM, which should be more representative of the relevant conditions in HAT-P-11b’s atmosphere. We use the GCM results to calculate 1D pressure-temperature profiles that are spatially averaged over the east and west limbs

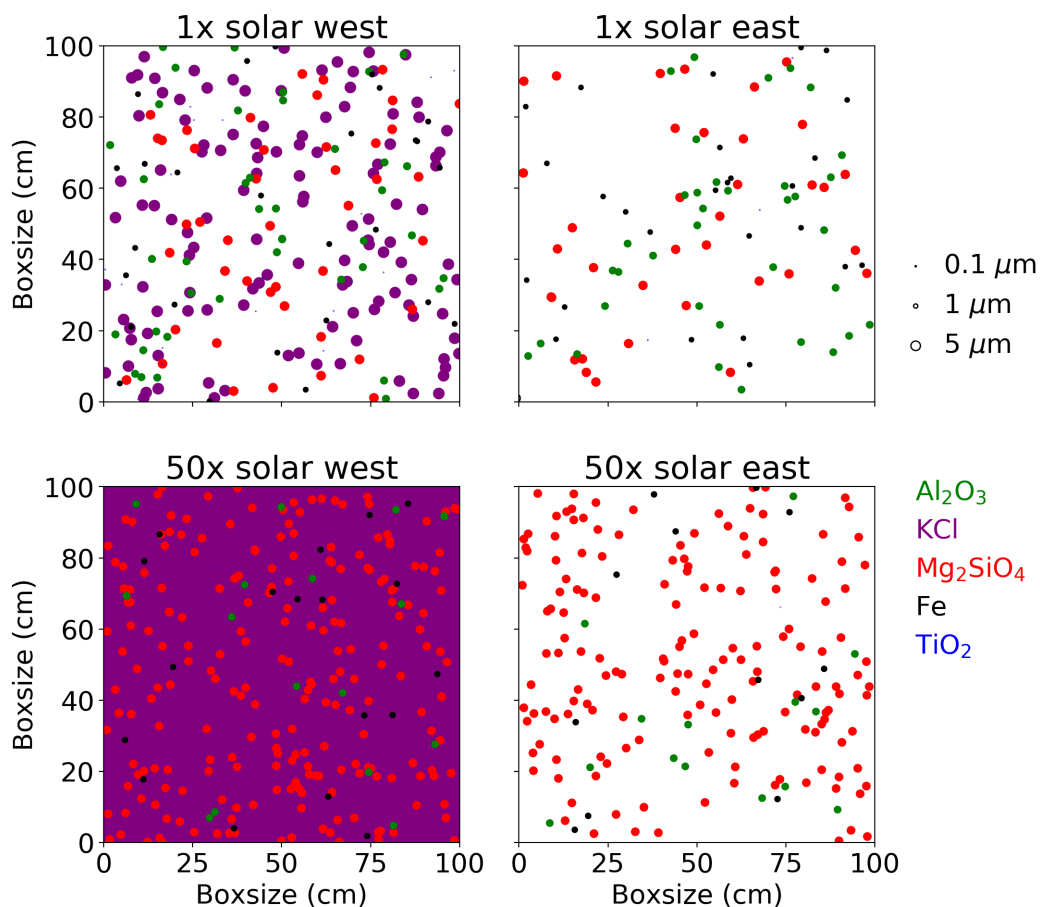


Figure 4.9: Plot windows showing 2D slices of the atmospheric condensate compositions for a $1\times$ solar and $50\times$ solar metallicity atmosphere. The slices sample the atmosphere on the east and west limbs at $\tau \sim 1$ and show the number of condensate particles contained in a $100\text{ cm} \times 100\text{ cm} \times 100\text{ cm}$ volume. Condensates on the two limbs have distinct compositions and increasing the metallicity has a significant effect on condensate number density, especially on the west limb. These plots serve as a visual guide and indicate that the scattering cross-section at the wavelengths of interest is mostly dominated by KCl particles. Mg_2SiO_4 and Al_2O_3 particles also make significant contributions to cloud opacity, especially in the $1\times$ solar metallicity case.

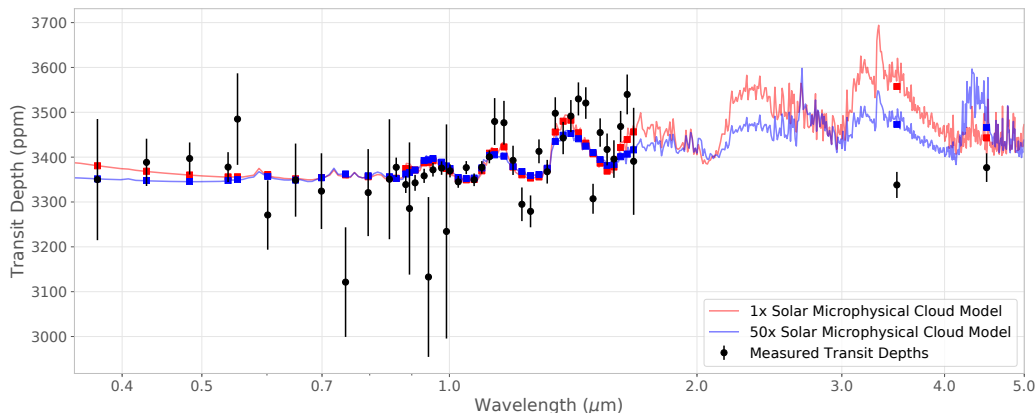


Figure 4.10: Measured transmission spectrum of HAT-P-11b versus transmission spectra generated by averaging CARMA models for the east and west limbs. These model spectra fit the measured spectrum quite well without any fine-tuning or parameter fitting. The *HST* data display a slight preference for the $1\times$ solar metallicity model. However, both the $1\times$ and $50\times$ solar metallicity models are unable to reproduce the *Spitzer* transit depths.

of the planet. We estimate the corresponding pressure/height dependent K_{zz} values for these locations using mixing length theory:

$$K_{zz} = w(z)L(z) = \frac{\omega H^2}{P} \quad (4.7)$$

where $w(z)$ is the vertical velocity in m/s and $L(z)$ is a characteristic length scale, in this case the atmospheric pressure scale height. This commonly adopted method (e.g. Moses et al., 2011) gives us a height dependent K_{zz} value which we then use in our microphysical cloud models. We show the resulting K_{zz} and temperature profiles as a function of pressure for the limb average, eastern limb average, and western limb average in Figure 4.8. As shown in previous GCM studies exploring the effect of atmospheric metallicity (e.g. Kataria et al., 2014; Lewis et al., 2010), the higher metallicity profile of HAT-11b has a higher photosphere due to the higher opacity, which produces a K_{zz} profile that rises more rapidly with height than the lower metallicity model.

Microphysical Cloud Model

We use the Community Aerosol and Radiation Model for Atmospheres (CARMA) to determine which species are expected to condense in HAT-P-11b's atmosphere and the corresponding particle size distribution and abundance. CARMA is a bin-

scheme cloud microphysics model that considers microphysical processes such as nucleation, evaporation, condensation, sedimentation, and diffusion. The strength of bin-scheme microphysics is that it uses discrete bins for particle sizes and makes no prior assumption regarding the size distribution, instead allowing the different bins to ‘interact’ (i.e. exchange mass) via the aforementioned microphysical processes. For a thorough exposition of the model, we direct the reader to Gao et al. (2018) and Powell et al. (2018).

We include the following condensible species in our model: Cr, KCl, Al₂O₃, Mg₂SiO₄, Fe, and TiO₂. We also consider condensation of metal sulphides but find it to be unimportant. Na₂S, MnS, and ZnS have high nucleation energy barriers that inhibit the formation of these cloud species (Gao et al. 2019, submitted). Another reason ZnS clouds can be neglected is the low abundance of Zn. We assume that KCl, Cr, TiO₂ and Al₂O₃ can nucleate homogeneously, meaning that they can condense into stable clusters directly from the gas phase and subsequently grow to larger sizes. In contrast, heterogeneous nucleation requires a foreign surface or ‘seed’ onto which vapor can condense. Though the majority of Al₂O₃ condensates likely form via heterogeneous surface reactions (e.g. Helling, 2018), assuming homogeneous nucleation is unlikely to greatly affect our results, as Al₂O₃ condenses at much higher temperatures (~2000 K) than considered here. Al₂O₃ is present in small concentrations at the high altitudes that we probe (Figure 4.9), but its distribution in this region is primarily controlled by transport processes rather than condensation and nucleation (Gao & Benneke, 2018). We assume that Fe and Mg₂SiO₄ nucleate heterogeneously on TiO₂ particles, similar to the treatment of Helling (2018) and related works. Although Fe can nucleate homogeneously as well, we do not consider it as this process may not be efficient (Lee et al., 2018).

We model the east and west limbs separately, as well as a limb averaged profile, (T and K_{zz}) for both solar and 50× solar metallicity atmospheres. We neglect the effect of radiative feedback from condensation and cloud formation on the atmosphere’s T-P profile. The resulting particle sizes and number densities of the dominant condensate species are shown in Figure 4.9 as a 2D visualization of a slice of the atmosphere at a pressure of ~2 mbar ($\tau \sim 1$ for transmission spectroscopy) with a path length of 100 cm through the atmosphere. In addition, the area covered by the different condensate species is proportional to the geometric cross-section due to each species, thereby visually indicating which species dominate the cloud opacity.

It is immediately evident that for both metallicity cases, the east and west limb-averaged profiles display distinct cloud properties and are dominated by different condensate species. This is primarily due to the temperature difference between the two limbs, which can be as large as 100-200 K (see Figure 4.8). Most notably, the west limb is cool enough for KCl to condense and contribute dominantly to the opacity whereas the east limb is completely devoid of condensed KCl. The lower temperature of the west limb also causes more nucleation sites to form, additionally increasing the cloud opacity in this region. The east limb has a significantly lower condensate number density ($< 100 \text{ m}^{-3}$) and consists of species that have cloud bases deep in the atmosphere but are carried to pressures probed by transmission spectroscopy by strong vertical mixing (Figure 4.8). These differences result in distinct predictions for the mid-IR spectra of the two limbs, and suggest that cloud models utilizing the limb averaged pressure-temperature profile may not produce accurate predictions (e.g. Kempton et al., 2017). Using the average of the transmission spectra rather than the average of the pressure-temperature profile for the two limbs should allow a better comparison of the models with the data. We therefore compare our retrieval results with model transmission spectra generated by averaging the spectra from the east and west limbs.

Increasing the metallicity from $1\times$ solar to $50\times$ solar increases the abundance of condensates by 1 – 2 orders of magnitude. Although the rate of homogeneous nucleation increases when the metallicity increases, the particle sizes tend to be somewhat smaller because there is less gas (per nucleated site) to provide additional condensible material for the growing particle. KCl overwhelms the absorption cross-section on the west limb while the east limb is much clearer.

Figure 4.10 shows transmission spectra generated using CARMA models. The models provide a good match to the observed absorption features at 0.95, 1.15, and $1.4 \mu\text{m}$ while maintaining a relatively flat optical spectrum without any fine-tuning or fitting. We find that the $1\times$ solar metallicity atmosphere is a slightly better match for the observed amplitude of the molecular absorption bands and optical scattering between $0.3 - 1.7 \mu\text{m}$ than the $50\times$ solar metallicity model (reduced χ^2 of 1.8 and 2.1, respectively). However, both of these models predict strong methane absorption in the $3.6 \mu\text{m}$ *Spitzer* band, making them a relatively poor match to the observed transit depth in this band.

4.7 Atmospheric Retrieval: PLATON

We use a simple and highly customisable atmospheric retrieval model, PLATON¹ (Zhang et al., 2019) to constrain HAT-P-11b’s atmospheric properties using its transmission spectrum. PLATON is based on ExoTransmit (M-R Kempton et al., 2017) and uses a fast Python based algorithm to compute forward models for planetary atmospheres, which are then compared with the data in a retrieval framework. PLATON includes opacities for 30 different molecular and atomic species (Zhang et al., 2020), the majority of which are calculated using line lists from ExoMol (Tennyson et al., 2018) and HITRAN (Gordon et al., 2017). We use nested sampling for our retrievals to accurately capture the posteriors of atmospheric model parameters that may display multi-modality. More importantly, using nested sampling allows us to compare the Bayesian evidence for different retrievals and rigorously quantify the significance of molecular absorption detection.

We fit for HAT-P-11b’s atmospheric properties assuming an isothermal atmosphere in chemical equilibrium. We allow the planet radius R_p , temperature T , atmospheric metallicity $\log(Z)$, and the carbon-to-oxygen ratio C/O to vary as free parameters in our fit. We also include scattering from high-altitude clouds, which we discuss in the following section. All of these parameters have flat priors. For R_p and T we choose physically motivated lower and upper bounds, while our prior range for metallicity and C/O ratio is dictated by limitations in our model’s pre-computed equilibrium chemistry grid (see Table 4.4). Our grid limits us to $\log(Z) \geq -1$, but we linearly (in Z) extrapolate abundances of atoms and molecules containing elements heavier than hydrogen and helium to lower metallicities (down to $\log(Z) = -2$) to resolve the posterior distribution on the lower metallicity end. We verify that linear extrapolation in Z captures the atmospheric composition reasonably well by comparing transmission spectra obtained for atmospheric metallicities between $0.1 \times -1 \times$ solar from extrapolation and from the pre-computed abundance grid. We include the stellar radius ($0.683 \pm 0.009 R_\odot$; Deming et al., 2011) and planetary mass ($23.4 \pm 1.5 M_\oplus$; Yee et al., 2018) as free parameters in our model with Gaussian priors set to the published values. This ensures that we correctly account for the effects of these uncertainties in our model fits. We also include an additional parameter (“Error Multiple” σ_{mult} , same for all instruments) that multiplies the errors on the data with a constant factor to account for the errors’ under- or over-estimation.

¹Planetary-Transmission-Atmosphere-Tool-for-Observer-Noobs:
<https://github.com/ideasrule/platon>

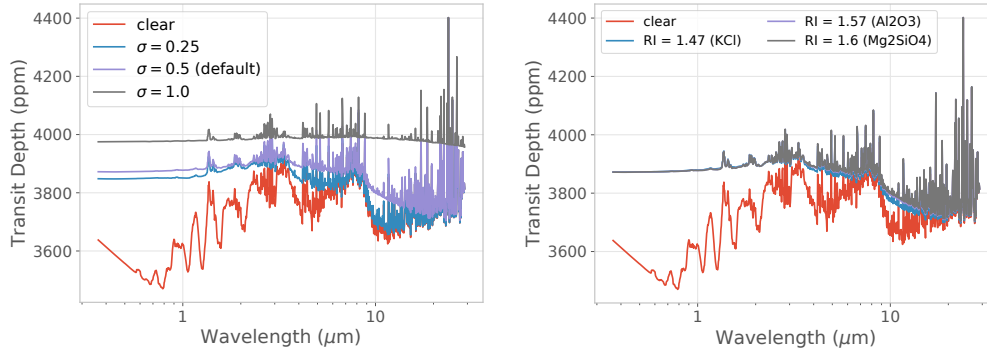


Figure 4.11: Effect of varying σ and refractive index in our Mie scattering model. We assume a particle size $a = 1 \mu\text{m}$, refractive index of 1.5, fractional scale height $f = 1$, particle size distribution width $\sigma = 0.5$, and number density at the base of the atmosphere $n_0 = 10^4 \text{cm}^{-3}$ unless specified otherwise.

Scattering from Clouds

We model scattering particles with five parameters: a cloud-top pressure (P_{cloud}) below which the atmosphere is opaque at all wavelengths (top of a grey cloud), particle number density n_0 at P_{cloud} , a lognormal distribution of particle sizes centered on an effective particle size a with distribution width σ , and the scale height for particle number density as a fraction f of the gas scale height H_{gas} . This allows for a deep grey cloud that begins to thin as the pressure decreases. Alternatively, it can be interpreted as a haze layer lying on top of a grey cloud. The particle size distribution $p(r)$ and number density as a function of height $n(z)$ are given by:

$$p(r) = \frac{1}{\sqrt{2\pi}\sigma r} \exp\left[-\frac{(\ln r - \ln a)^2}{2\sigma^2}\right], \quad (4.8)$$

$$n(z) = n_0 \exp[-z/(fH_{\text{gas}})]. \quad (4.9)$$

The extinction cross-section, σ_{ext} , from condensate particles is then given as:

$$\sigma_{\text{ext}}(\lambda, z) = n_0 e^{-z/fH_{\text{gas}}} \int p(r) Q_{\text{ext}}(\lambda, r) \pi r^2 dr. \quad (4.10)$$

We calculate Q_{ext} , which depends on the refractive index, using the Mie scattering formalism. The effective particle size a , number density n_0 , and relative scale height f play a decisive role in shaping the planetary transmission spectrum. The

effective particle size a determines the wavelength where the Rayleigh slope begins ($\lambda \sim 2\pi a$). The number density n_0 and fractional scale height f set the overall scale of the opacity contribution from scattering (relative to molecular absorption opacity) and are partially degenerate with each other. We find that f is almost entirely unconstrained by our data and allowing it to vary in our retrievals does not have any significant effect on the posteriors for the other parameters in our model. We therefore turn to our microphysical cloud models for HAT-P-11b, which indicate the effective particle size is roughly constant in the pressure range 0.1 mbar - 100 mbar and that the effective number density falls off with the pressure scale height H_{gas} . We fix $f = 1$ unless otherwise specified in order to reduce the number of free parameters and to allow for a more direct comparison with predictions from our microphysical models.

We also keep the value of the refractive index fixed to a single, wavelength-independent value in our fits. Our microphysical cloud models predict that condensate clouds in HAT-P-11b's atmosphere will include multiple distinct species. However, the refractive indices for all these species apart from Fe have a very weak dependence on wavelength and negligible imaginary parts in the $0.1 - 5 \mu\text{m}$ region spanned by our data (e.g. see Kitzmann & Heng, 2018). Adopting a wavelength independent real value for the refractive index also speeds up our model computations enormously, which is a necessary requirement for retrieval codes. Figure 4.11 shows that the shape of the predicted transmission spectrum is relatively insensitive to the exact value we assume for the refractive index in our wavelength range of interest. We set this parameter equal to 1.5, as this is fairly representative of the dominant cloud species (KCl) predicted by our forward models.

Although the particle size distribution can take an arbitrary functional form, the distribution of large particles that are abundant enough to contribute most significantly to scattering may be captured by a lognormal distribution. We keep the width of the lognormal distribution fixed in our fits. Varying this parameter mimics the effect of increasing particle size as a broader distribution shifts the effective size of the particles to larger values and large particles tend to dominate the cloud opacity (e.g. Wakeford & Sing, 2015). Therefore, variations in the distribution width are degenerate with changes in particle size distributions. Increasing the distribution width makes the spectrum flatter in a given wavelength range, as does increasing the effective particle size (see Figure 4.11). We fix $\sigma = 0.5$, which agrees well with typical values for aerosols in the Earth's atmosphere (e.g. Ackerman & Marley,

2001; Elias et al., 2009; Pinnick et al., 1978; Shen et al., 2015) and produces a scattering behavior that is roughly compatible with that produced by the CARMA model with its non-parameterized particle size distribution.

Retrieval Results

HST WFC3

We begin by fitting the molecular absorption features in the WFC3 G102 and G141 bandpasses, as these features provide the strongest constraints on the planet’s atmospheric composition. Because these data span a relatively limited wavelength range, a simplified cloud model with a single opaque cloud deck is adequate. Nonetheless, we ‘fit’ for Mie scattering parameters for later comparison of best-fit models with models that match the entire *HST* transmission spectrum. We fit for temperature, atmospheric metallicity, and C/O ratio as well, assuming chemical equilibrium. The resulting best-fit model is shown in Figure 4.12 and the corresponding constraints on the model parameters are given in Table 4.4. The steep rise in transit depth longward of $1.5 \mu\text{m}$ hints at the presence of methane in the atmosphere. We verify this by confirming that this upward rise disappears if methane is removed from our atmospheric models.

We find that HAT-P-11b’s atmospheric parameters, in particular its metallicity, are poorly constrained in these fits (see Figure 4.13 and Table 4.4). The limited wavelength range of the WFC3 data limits our ability to uniquely infer the metallicity and cloud top pressure. As for the C/O ratio, the presence of absorption features due to water does not automatically imply a C/O ratio < 0.9 for planets with equilibrium temperatures $\lesssim 800\text{-}1000 \text{ K}$ as it does for hot Jupiters² (Heng, 2018; Kreidberg et al., 2015; Madhusudhan, 2012). Below $\sim 800 \text{ K}$, methane is the thermodynamically favored carbon-bearing species in hot Neptunes, except at very high atmospheric metallicities (Moses et al., 2013). Adding more carbon relative to oxygen does not therefore increase the abundance of CO at the expense of water. Our models indicate that increasing the C/O ratio (even to values greater than one) at temperatures below 800 K has a negligible effect on the water abundance and the methane abundance simply increases linearly with C/O.

The results from this retrieval differ significantly from those presented in Fraine et al. (2014) primarily for three reasons. Firstly, we include WFC3 G102 data here

²The exact transition temperature depends on other properties such as atmospheric metallicity and surface gravity.

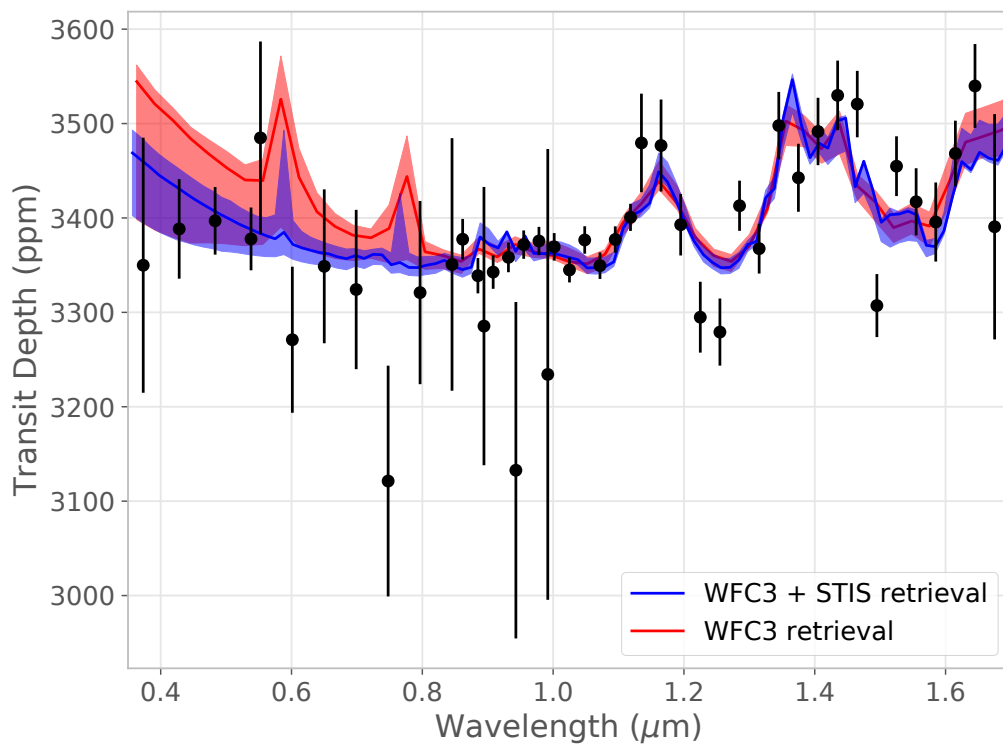


Figure 4.12: Transmission spectrum in the *HST* WFC3 and STIS bandpasses (black filled circles) with best-fit Mie scattering model spectra from PLATON overplotted along with the 1σ contours.

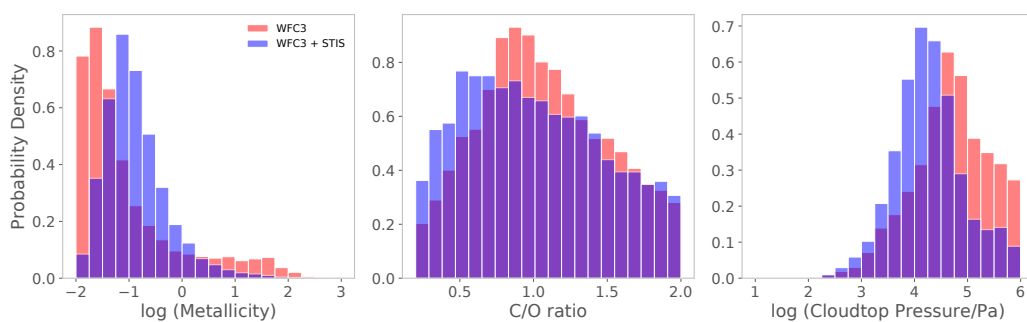


Figure 4.13: Marginalized posterior probability distributions for the metallicity, C/O ratio, and cloud-top pressure from a fit to the WFC3 data alone and a fit to the WFC3 + STIS dataset.

that have small uncertainties and consequently a strong influence on the retrieved posteriors. The addition of WFC3 G102 data shifts the peak of the metallicity posteriors to lower values. When we utilize only the WFC3 G141 data (or WFC3 G141 + *Spitzer* data with an offset for the *Spitzer* data), our retrieved results agree with Fraine et al. (2014)'s. Secondly, we apply a wavelength dependent stellar activity correction that changes the spectrum in such a way that a low metallicity - deep cloud solution fits the data. To test whether this shift to low metallicity is due to our stellar activity correction, we combined the WFC3 G141 spectrum from Fraine et al. (2014) and our WFC3 G102 spectrum and performed retrieval analysis on the corrected and uncorrected version of the combined spectrum. We found that applying the stellar activity correction shifts the posteriors to low metallicity. Thirdly, we choose a different prior for atmospheric metallicity and extend it to $0.01\times$ solar so as to resolve the posterior for the retrieved metallicity. Fraine et al. (2014) only explored atmospheric metallicities $\geq 1\times$ solar in their retrievals and we find that restricting our prior space to match theirs results in significantly better agreement. Additionally, our models do not favor atmospheric metallicities $\gtrsim 100\times$ solar primarily because our spectrum, unlike the one published in Fraine et al. (2014), favors the presence of methane in the atmosphere (see § 4.7 for more details).

HST WFC3 + STIS

Next, we see how the inclusion of STIS data alters the posteriors for these parameters. Because our data now span a much larger wavelength range, we must include wavelength-dependent scattering in our model (§ 4.7). The best-fit model is shown in Figure 4.12, parameter constraints are tabulated in Table 4.4, and the full posteriors for key atmospheric parameters are shown in Figure 4.14. The data place relatively tight constraints on the cloud-top pressure, indicating that we are probing down to ~ 100 mbar. This is in rough agreement with the inferred (grey) cloud top pressures of 10 – 50 mbar for CARMA models. The constraints on atmospheric metallicity are significantly tighter than those provided by WFC3 data alone, with a 2σ confidence interval of $0.02 - 4.6 \times$ solar. The posterior for atmospheric metallicity has a skewed shape with a long tail towards high metallicities. We find that the 3σ upper limit for metallicity is $86 \times$ solar, indicating that enhanced metallicities are still consistent with our data. Unlike Fraine et al. (2014), our fits prefer lower atmospheric metallicities. Nonetheless, for metallicities greater than the lower prior bound in Fraine et al. (2014) ($1\times$ solar), our metallicity posteriors are

Table 4.4: Median parameters and 68% confidence intervals (CI) from PLATON retrieval

Parameter	Prior	HST WFC3		HST WFC3 + STIS ³		HST + Spitzer	
		Median	68% CI	Median	68% CI	Median	68% CI
Isothermal Temperature (K)	[500, 1200]	941	[726, 1114]	740	[635, 876]	736	[540, 1026]
log (Metallicity/ Z_{\odot})	[-2, 3]	-1.39	[-1.79, -0.16]	-0.98	[-1.40, -0.36]	2.04	[0.12, 2.75]
C/O	[0.2, 2]	1.03	[0.62, 1.56]	0.97	[0.51, 1.56]	0.63	[0.30, 1.49]
log (Cloudtop Pressure/Pa)	[1, 6]	4.71	[3.96, 5.46]	4.25	[3.67, 4.88]	2.94	[2.02, 4.77]
log (Particle Size/m)	[-8, -5]	-6.69	[-7.61, -5.62]	-6.67	[-7.59, -5.65]	-6.60	[-7.58, -5.60]
log (Number Density/ m^{-3})	[-10, 15]	-1.70	[-7.11, 3.92]	-1.70	[-7.09, 3.67]	-0.59	[-6.65, 5.42]
Error Multiple (σ_{mult})	[0, 4]	1.46	[1.29, 1.69]	1.32	[1.19, 1.48]	1.67	[1.51, 1.87]

in qualitative agreement with the ones published in Fraine et al. (2014). The addition of the STIS data to WFC3 data limits the degeneracy between cloudtop pressure and atmospheric metallicity (see Figure 4.14) encountered by Fraine et al. (2014), resulting in correspondingly narrower constraints on these properties (Benneke & Seager, 2012).

We show the marginalized posterior probability distributions for metallicity, C/O, and cloudtop pressure in Figure 4.13. The *HST* STIS data provide additional constraints on atmospheric properties by disfavoring models with very low metallicity ($\log(Z) \lesssim -1.5$, and correspondingly high cloud top pressure P_{cloud}) and high metallicity ($\log(Z) \gtrsim 1$). This is apparent in Figure 4.12 where we see that the STIS data narrow the range of model transmission spectra that agree within $\pm 1\sigma$.

HST + Spitzer data

We carry out a final set of fits including both the *HST* STIS + WFC3 and *Spitzer* transit depths. The full transmission spectrum with the best-fit model from PLATON is shown in Figure 4.15 and the median and confidence intervals for retrieved parameters are given in Table 4.4. Our $3.6 \mu\text{m}$ *Spitzer* transit depth is low relative to the *HST* data and discrepant with the depth predicted by the best-fit model to the *HST* data. We are unable to find a single model that can simultaneously match the observed strength of the WFC3 absorption features while fitting the noticeably shallower *Spitzer* transit depths.

The inclusion of *Spitzer* data worsens the constraints on most atmospheric parameters (Table 4.4). The acceptable temperature and cloudtop pressure ranges now span the entire prior range. The constraints on metallicity from this fit are inconsistent with results from the *HST*-only fits. The preferred metallicity rises to a few $100\times$ solar, which allows the models to fit the flat baseline of the data by reducing the scale height while still maintaining some molecular absorption and reducing the relative abundance of methane in the atmosphere. We find that the particle size and number density are relatively unconstrained in both the *HST*-only and *HST* + *Spitzer* fits. The upper limit on the number density varies as a function of particle size (as expected) and is marginally higher for the *HST* + *Spitzer* fit. The error multiple (σ_{mult}) parameter, which is a measure of how underestimated the errors in the data are, jumps to ~ 1.7 , i.e. $> 20\%$ larger than the value obtained with *HST* data alone. In addition, the reduced χ^2 value (calculated using the errors on the transit depth measurements) increases from 1.9 for the *HST*-only fit to 2.8 for the full dataset

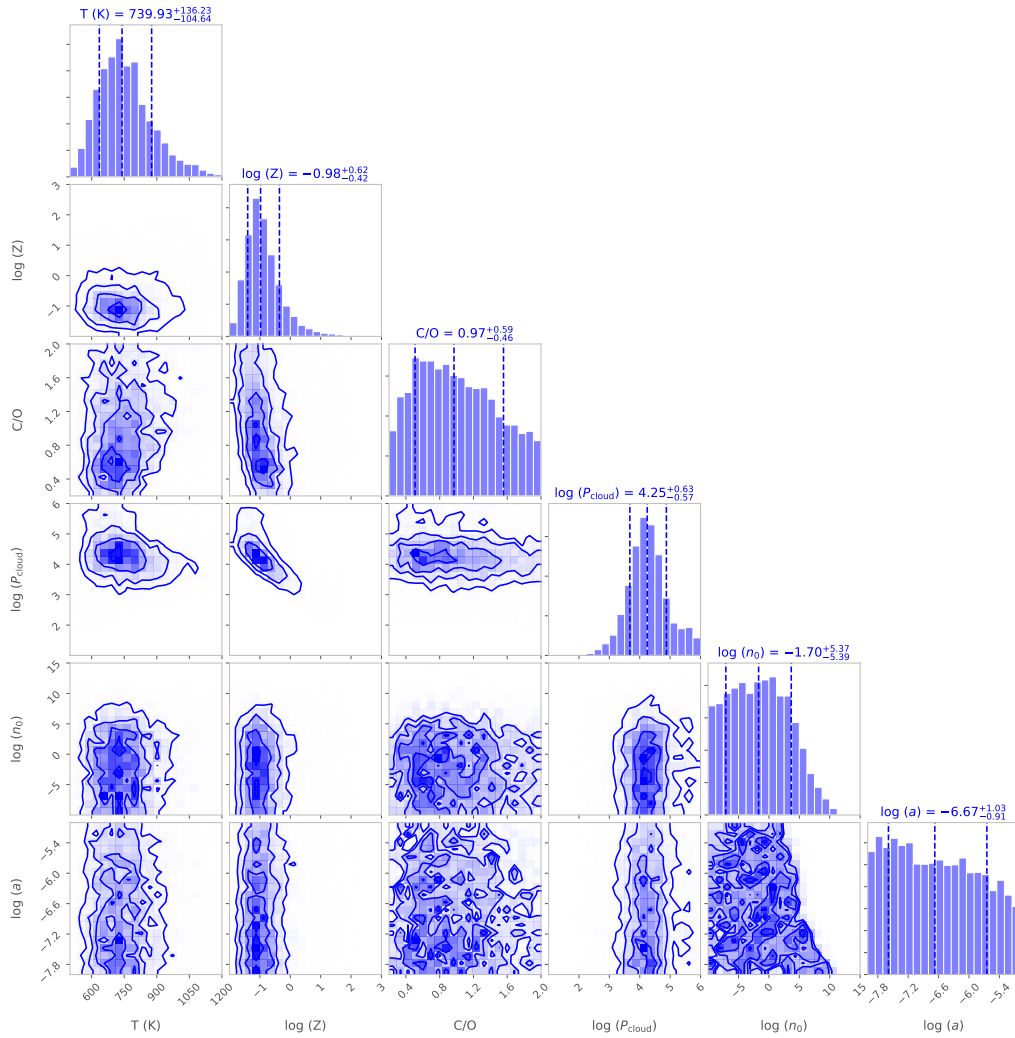


Figure 4.14: Posterior probability distributions for fits of the *HST* dataset. Median parameter values and 68% confidence intervals for the marginalized 1D posterior probability distributions are indicated with vertical dashed lines.

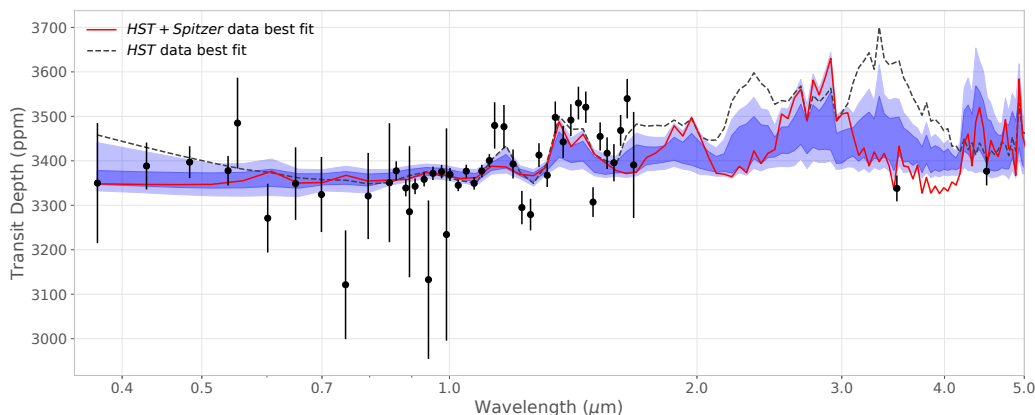


Figure 4.15: Transmission spectrum for HAT-P-11b including both *HST* and *Spitzer* data (black filled circles) along with the best-fit model from PLATON and corresponding 1σ and 2σ contours (dark blue and light blue, respectively). The best-fit model for *HST* data is also shown for comparison, which predicts a much larger transit depth at $3.6\ \mu\text{m}$. The inclusion of the *Spitzer* transit depths shifts the models toward solutions with high atmospheric metallicity, which suppresses the depth of the absorption features in the WFC3 bands and decreases the overall quality of the fit in this region.

fit. We therefore conclude that our models are unable to provide a satisfactory fit to the full dataset. Including an offset of $\sim 100\text{--}150$ ppm could reconcile the *Spitzer* depths with the models that fit the *HST* data. Fitting for this offset in a retrieval framework also yields similar estimates for its magnitude. However, as emphasized in § 4.4 and 4.5, such a large stellar activity correction is incommensurate with the observed stellar variability.

Retrievals without methane and/or water opacity

We quantify the significance of observed molecular absorption features by using the evidence obtained from nested sampling to compute Bayes factor for model comparisons. To test for the presence of a certain molecule (and the associated confidence/significance), we remove opacity contributions from the molecule and refit the transmission spectrum while keeping the priors unchanged. The ratio of the Bayesian evidence for fits with and without the molecular opacity yields the Bayes factor and allows us to quantify the data’s preference for one model over the other (e.g. Benneke & Seager, 2013). There is significant overlap between methane and water features in the near-infrared region ($0.8\text{--}1.7\ \mu\text{m}$), and we therefore perform three additional retrievals for the *HST* data along with the nominal case described

Table 4.5: *HST* retrievals evidence

Model	log (Evidence)	Bayes factor	σ
Nominal	368.9 ± 0.1	–	
Without CH ₄ and H ₂ O	361.0 ± 0.1	1:2812	4.4
Without CH ₄	364.8 ± 0.1	1:64	3.4
Without H ₂ O	366.1 ± 0.1	1:17	2.9

above. In these three retrievals, we remove both water and methane opacity, just water opacity, and just methane opacity.

The evidence, Bayes factor (relative to the nominal model that includes both methane and water opacity), and equivalent σ significance for each of the three cases are shown in Table 4.5. The combined significance for the presence of water and methane is 4.4σ . The Bayes factor for the two molecules individually is lower than the reported combined significance. The detection significance for each molecule is sensitive to relatively subtle features of the spectrum and may change due to small differences in the shape of the absorption features. Notably, the inclusion of *HST* STIS data makes the case for the presence of water and/or methane stronger. With WFC3 data alone, a similar comparison gives lower values for the Bayes factor for all three retrievals. This is primarily because the relatively flat optical spectrum excludes very low atmospheric metallicity models ($\log Z \lesssim -1.5$), which possess somewhat higher evidence values (in *HST* WFC3 only retrievals) and therefore weaken the case for the presence of these molecules.

This exercise also allows us to investigate whether the disagreement between inferences made from *HST* and *Spitzer* data arises simply due to the absence of methane from the atmosphere. Vertical mixing and quenching could lower the methane abundance by orders of magnitude relative to the equilibrium values (Moses et al., 2011; Moses et al., 2013). However, quantifying this effect for HAT-P-11b requires a more careful analysis as its temperature-pressure profile overlaps with the equal abundance curve of CH₄-CO. This picture is further complicated by the planet’s orbital eccentricity (see Visscher, 2012). We test whether our fit to the *HST* data without CH₄ opacity fits the *Spitzer* data any better. We find that removing methane’s opacity requires a larger abundance of water to match the strength of the spectral features in the WFC3 bandpass. This pushes the best-fit models to higher metallicities (lower abundances/metallicities are ruled out by the STIS data). The best-fit models thus obtained match the $3.6 \mu\text{m}$ depth quite well but the higher atmospheric

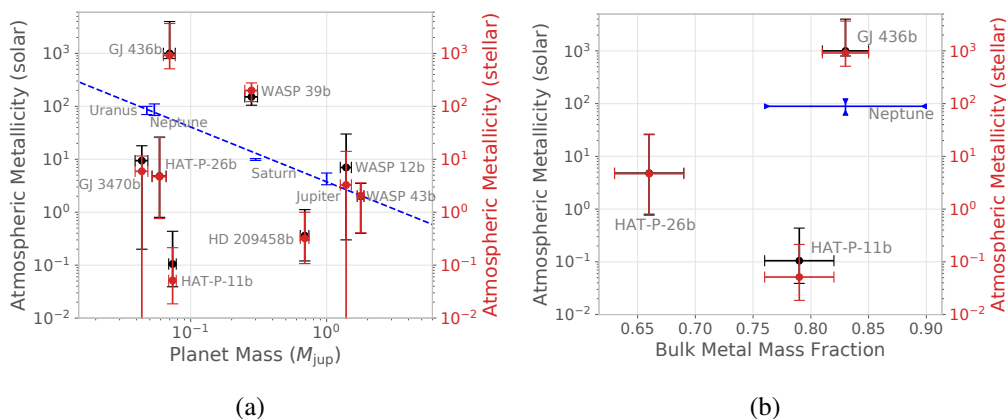


Figure 4.16: The left panel (a) shows atmospheric metallicity versus planet mass for planets observed by *HST* and *Spitzer* (Benneke et al., 2019a; Brogi et al., 2017; Kreidberg et al., 2014a; Kreidberg et al., 2015; Morley et al., 2017; Wakeford et al., 2017a; Wakeford et al., 2018). The right panel (b) shows atmospheric metallicity versus bulk metallicity (obtained from Thorngren & Fortney, 2018) for Neptune-class planets. For Neptune, we plot lower and upper limits rather than 1σ error bars (Helled & Guillot, 2018). GJ 3470b is not included on this plot because the assumptions used to derive bulk metallicity constraints in the Thorngren et al. (2016) models may not be appropriate for planets with such low masses.

metallicities imply the presence of a substantial amount of CO and CO₂ as well, which increases the $4.5 \mu\text{m}$ model depth and make it as discrepant with the data as the $3.6 \mu\text{m}$ depth is in our nominal model, which includes methane opacity.

4.8 Discussion and Conclusions

Our picture of HAT-P-11b’s atmosphere is primarily driven by the *HST* observations, which provide a self-consistent, spectrally resolved picture of the planet’s atmosphere over nine separate transit observations. The fact that we see clear evidence for molecular absorption across multiple visits and multiple bands leads us to conclude that any plausible model for this planet’s atmosphere must be able to reproduce the observed shape of these absorption (water + methane) bands. These models all overestimate the observed transit depth in the $3.6 \mu\text{m}$ *Spitzer* band; this may indicate that methane is under-abundant in HAT-P-11b’s atmosphere as compared to the predictions of our equilibrium chemistry models. However, comparison of Bayesian evidence for *HST* retrievals suggests that methane is indeed present. We are unable to resolve these apparent contradictions with the current dataset, but future spectroscopic observations of this planet with the *James Webb Space Tele-*

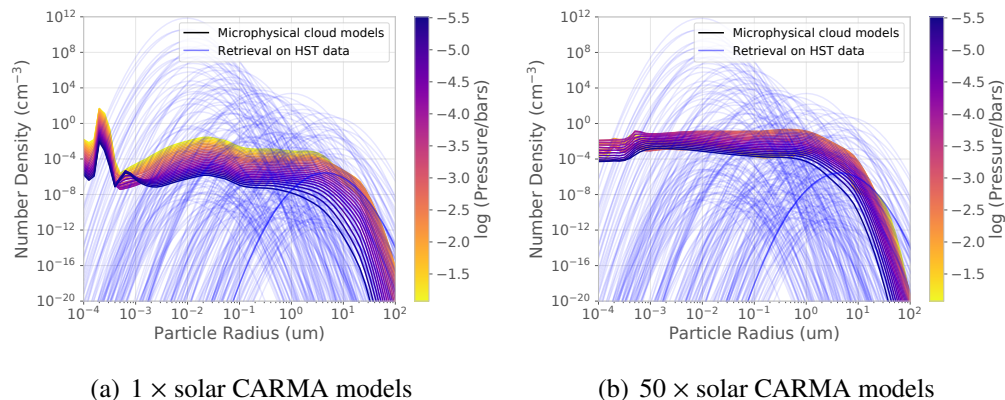


Figure 4.17: Particle number density as a function of radius from our microphysical cloud models at different pressures/heights in the atmosphere. We overplot a sample of lognormal particle size distributions at 10 mbar from our retrievals for comparison. The best-fit size distribution is highlighted with a dark blue line. All profiles correspond to models with high likelihoods.

scope (JWST) should provide a much clearer picture of its transmission spectrum in the mid-infrared wavelengths probed by the *Spitzer* photometry.

If we focus our attention for now on the *HST*-only fits, our updated results point to a significantly lower value for the planet’s atmospheric metallicity than that reported by Fraine et al. (2014). This runs counter to the trend observed in the solar system (Figure 4.16 (a)): Uranus and Neptune have atmospheric C/H ratios between 70 – 100 \times that of the Sun, while Jupiter’s C/H ratio is just a few times solar (Fletcher et al., 2009; Karkoschka & Tomasko, 2011; Sromovsky et al., 2011; Wong et al., 2004, see also e.g. Kreidberg et al., 2014a). Although there are relatively few published constraints on the atmospheric metallicities of Neptune-mass planets around other stars, GJ 436b appears to have an atmospheric metallicity of at least 200 \times solar (Madhusudhan & Seager, 2011; Morley et al., 2017; Moses et al., 2013). However, HAT-P-26b (Wakeford et al., 2017a) provides a counter-example of an extrasolar Neptune with a relatively low atmospheric metallicity ($4.8^{+21.5}_{-4.0} \times$ solar). Our new observations suggest that HAT-P-11b is more similar to HAT-P-26b than it is to either Neptune or GJ 436b. The low atmospheric metallicity of HAT-P-11b is all the more striking because it orbits a metal rich star ($[\text{Fe}/\text{H}] = +0.3$). The composition of the planet’s atmosphere therefore verges on being almost identical to that of the primordial gas that formed the star. This diversity in atmospheric composition of Neptune-mass planets suggests that they may not be a homogeneous planet population.

Comparison of atmospheric metallicity with bulk metallicities (mass fraction) calculated by Thorngren & Fortney (2018) indicates that Neptune class planets may possess low metallicity envelopes despite having a high bulk metal fraction (Figure 4.16 (b)). This implies that most of the solids, which have the potential to enrich the envelope, ought to have finished accreting before the initiation of substantial gas accretion from the disk. It also requires mixing in the interior to not be strong enough to significantly enrich the envelope. We expect that the sample of Neptune-mass planets with well-measured atmospheric metallicities will be significantly expanded by *JWST*, providing a much clearer view of the statistical properties of this population of planets.

In addition to providing improved constraints on HAT-P-11b's atmospheric metallicity, our updated transmission spectrum provides us with an opportunity to explore the properties of the scattering particles in this planet's atmosphere. We find that transmission spectra for our microphysical cloud models agree quite well with the observed *HST* spectrum (Figure 4.10). In Figure 4.17, we compare our retrieved cloud properties to those predicted by the models. The data do not put narrow constraints on these retrieved cloud properties and there is a degeneracy between mean particle size and number density (as evident in Figure 4.14). Regardless, the upper limit on mean particle size and its corresponding number density is roughly commensurate with predictions from the microphysical cloud models. Improved constraints provided by new data in the future should enable us to compare the predictions of the forward model and the retrieved parameters more rigorously. Moreover, the good agreement between the CARMA models and the retrieved models from PLATON (which uses local condensation from GG-chem⁴ to deplete the gas phase) is reassuring because it is usually unclear if the amount of retrieved cloud opacity is realistic or not compared to the gas phase chemistry and condensation.

In the future, more accurate microphysical cloud models will be crucial for improving our understanding of the properties of these atmospheres. Better a priori predictions for cloud formation could allow future *JWST* observers to identify and prioritize observations of planets with relatively cloud-free terminators, while model-based constraints on cloud properties would help to limit degeneracies between cloud properties and atmospheric metallicity for planets with cloudy atmospheres. Our observations of HAT-P-11b serve as a useful illustration of both the limitations

⁴GG-chem is an open source thermo-chemical equilibrium code that calculates abundances of different molecular and atomic species given gas elemental composition, temperature, and pressure (Woitke et al., 2018, <https://github.com/pw31/GGchem>).

of our current understanding of cloud formation in these atmospheres, and also the power of spectrally resolved data with broad wavelength coverage to provide useful constraints on atmospheric composition despite our limited understanding of relevant cloud formation processes.

A FEATURELESS INFRARED TRANSMISSION SPECTRUM FOR THE SUPER-PUFF PLANET KEPLER-79D

5.1 Introduction

The *Kepler* telescope was the first observatory with both the sensitivity and temporal baseline to detect small transiting planets at Earth-like distances around Sun-like stars. Amongst the most valuable contributions of the telescope is the discovery of dynamically interacting multi-planet systems spanning a broad range of orbital periods. *Kepler*'s long 4-year baseline allowed us to observe multiple transits of such systems, to record the variations in the planets' orbital period (Transit Timing Variations a.k.a TTVs), and to obtain dynamical mass measurements for planets that were otherwise inaccessible to the radial velocity (RV) technique due to the host stars' dimness. This technique also led to the discovery of an intriguing new class of extremely low density planets (dubbed 'super-puffs') that have super-Earth like masses ($\lesssim 10M_{\oplus}$) and gas-giant like radii ($\gtrsim 5R_{\oplus}$; Jontof-Hutter et al., 2014; Masuda, 2014; Mills et al., 2016; Ofir et al., 2014; Orosz et al., 2019; Vissapragada et al., 2020; Xie, 2014). Their low implied bulk densities (typically ~ 0.1 g/cc) require the possession of a hydrogen-helium envelope that is tens of percent by mass, quite unlike the typical $\sim 1\%$ that most super-Earths are inferred to possess (Lopez & Fortney, 2014). This makes super-puffs particularly interesting from a planet formation perspective, as it is unclear how they were able to acquire such large H/He envelopes. Lee & Chiang (2016) were the first to point out that super-Earth cores could only accrete such large gas envelopes if the gas had a relatively low opacity (i.e., was effectively dust-free) and the planet was located in a cool, low-density region of the disk. Protoplanetary disk models indicate that these conditions were not likely met at the present-day locations of these super-puffs (e.g. Chiang & Laughlin, 2013; Ikoma & Hori, 2012; Inamdar & Schlichting, 2015) and so it is hypothesized that these planets could have formed at a more distant location and then migrated inward. If dust opacity somehow becomes negligible, disk conditions (temperature and hence opacity) beyond the ice line could be favorable for formation of super-puffs, possibly enriching them in water relative to super-Earths that formed in situ.

The relatively low densities of super-puffs also make them highly vulnerable to atmospheric mass loss, either due to photoevaporation or Parker wind-like outflow (Cubillos et al., 2017; Gao & Zhang, 2020; Lopez & Fortney, 2014; Owen & Wu, 2016; Wang & Dai, 2019). The latter mechanism is important for super-puffs because their low gravities result in non-negligible densities at the Bondi radius. This is especially true if the atmospheric pressure corresponding to the observed transit radius (slant optical depth $\tau \sim 1$ surface) is equal to tens or hundreds of mbar, similar to the values inferred for other exoplanets via transmission spectroscopy (e.g. Sing et al., 2016). In this scenario, the implied mass loss rates for some super-puffs should already have caused them to lose their entire envelope. The fact that super-puffs have managed to retain their large envelopes over billions of years suggests that our knowledge of mass loss processes in these atmospheres is incomplete (Cubillos et al., 2017; Fossati et al., 2017; Owen & Wu, 2016; Wang & Dai, 2019).

Transmission spectroscopy is a powerful tool that can provide us with new insights into both the compositions of super-puff atmospheres and their corresponding mass loss rates. Super-puffs are favorable targets for transmission spectroscopy: they have relatively low gravity and their low bulk densities suggest that they are unlikely to have atmospheric metallicities higher than a few $100\times$ solar (e.g. Lopez & Fortney, 2014; Thorngren & Fortney, 2019); as such, their atmospheric scale heights are comparable to or greater than those of hot-Jupiters despite their relatively cool equilibrium temperatures (~ 500 K). However, the first two super-puffs observed by the *Hubble Space Telescope* (*HST*) appear to have featureless $1.1 - 1.7\mu\text{m}$ transmission spectra (Libby-Roberts et al., 2020). Although Libby-Roberts et al. (2020) could not entirely rule out atmospheric metallicities above $300\times$ solar for Kepler-51b and d, they argue that high-altitude aerosols provides a more plausible explanation.

In principle these aerosols could be either condensate clouds or photochemical hazes, but the temperature-pressure profiles for most super-puffs are not expected to cross condensation curves in the upper region ($P < 1$ bar) of the atmosphere (e.g. Crossfield & Kreidberg, 2017; Gao & Zhang, 2020; Morley et al., 2015). On the other hand, the relatively low (~ 500 K) temperatures of these hydrogen-rich atmospheres make them favorable sites for photochemical haze production, which occurs at relatively low pressures (1-10 μbar) (e.g., Adams et al., 2019; He et al., 2018a,b; Hörst et al., 2018; Kawashima & Ikoma, 2018, 2019). Aerosols entrained in an outflowing atmospheric wind could be carried to even lower pressures ($\lesssim 1$

μbar), significantly reducing the gas density at the $\tau \sim 1$ surface and thus the Bondi radius, leading to a reduction in the mass loss rate (Gao & Zhang, 2020; Wang & Dai, 2019). This offers an explanation for how these planets have managed to retain their hydrogen-rich envelopes to the present day.

Alternative theories that attempt to explain the large radii and correspondingly low densities of super-puffs have also been proposed. Pu & Valencia (2017) and Millholland (2019) argue that larger internal heat fluxes, due to Ohmic dissipation and obliquity tides, respectively, could inflate planetary radii to produce super-puffs. This would reduce the amount of hydrogen-helium required to match the planet’s mass and radius. However, it is unclear if this reduction is sufficient to make the super-puffs’ hydrogen-helium repository more commensurate with the wider sub-Neptune population. These models also do not satisfactorily resolve the tension between mass loss rates, atmospheric lifetimes, and planetary ages; regardless of the inflation mechanism, puffy planets are still vulnerable to rapid atmospheric mass loss. Although the Millholland (2019) models (based on Chen & Rogers, 2016 models) include photoevaporative mass loss, they do not include Parker wind mass loss, which tends to be more important for the most vulnerable super-puffs. Moreover, Ohmic dissipation is unlikely to be as important at equilibrium temperatures of $\sim 500 - 700$ K that are typical for super-puffs (Pu & Valencia, 2017). It has also been suggested that super-puffs may not be puffy planets at all but planets with face-on rings (Piro & Vissapragada, 2020). However, this idea has trouble providing a unifying explanation for all super-puffs and is difficult to verify observationally. In this work, we assume that super-puffs do possess large hydrogen-helium envelopes and will comment on these alternative explanations when the need arises.

In this paper, we examine the super-puff Kepler-79d, a planet on a 52 day orbit around an F-type star (Jontof-Hutter et al., 2014). Kepler-79 has four dynamically interacting planets with periods that are near a 1:2:4:6 chain of commensurability, which allows us to derive planet masses from transit timing variations. All planets in this system have masses in the super-Earth regime ($\lesssim 10M_{\oplus}$) and relatively large radii (varying from $3.5 - 7R_{\oplus}$), implying low bulk densities and a significant volatile envelope. In particular, Kepler-79d has a mass of $5.3 M_{\oplus}$ and a radius of $7 R_{\oplus}$, with corresponding bulk density of 0.08 g/cc , placing it firmly in the super-puff regime. Kepler-79, with an estimated age of $1.3_{-0.4}^{+1.0}$ Gyrs (Fulton & Petigura, 2018), is most likely older than Kepler-51 (0.5 ± 0.25 Gyrs, Libby-Roberts et al., 2020). As a result,

we expect that the planets in the Kepler-79 system are less likely to be appreciably inflated by residual heat from their formation than those in the Kepler-51 system. This is because most of the contraction happens in the first few 100 Myrs (e.g., Libby-Roberts et al., 2020; Lopez & Fortney, 2014). This means that Kepler-79d’s anomalously large radius and low density can only be matched with a high gas-to-core mass fraction ($\sim 36\%$, Lopez & Fortney, 2014). Kepler-79 also appears to be less active than Kepler-51, with a low variability amplitude in the *Kepler* bandpass ($< 0.2\%$ compared to $\sim 1.2\%$ for Kepler-51; McQuillan et al., 2014; see § 5.4) and no evidence for spot crossings in the *Kepler* transit light curves of Kepler-79d (as opposed to Kepler-51b and d: 17% of their *Kepler* transits show spot crossings by eye; Libby-Roberts et al., 2020). This makes it less likely (relative to Kepler-51) that the planet’s transmission spectrum will be significantly affected by stellar activity.

Here, we present new *HST* WFC3 transit spectroscopy for Kepler-79d spanning the 1.1 – 1.7 μm wavelength range and combine our analysis with previously published *Kepler* data in a self-consistent framework. We describe our data reduction and light curve fitting routines in §5.2 and 5.3. The resulting white light curve depths and updated mass estimates from a transit timing variation (TTV) analysis are presented in §5.4 and §5.4. In §5.4, we use the shape of the observed transmission spectrum to place constraints on Kepler-79d’s atmospheric composition and aerosol properties. We also present models for Kepler-79d generated using a modified version of the Community Aerosol and Radiation Model for Atmospheres (CARMA) to study haze formation and entrainment in the outflowing atmospheric wind. In §5.4, we examine the mass loss rates for the super-puff population as a whole and discuss the implications in light of the host stars’ ages. Finally, in §5.5 we present our conclusions and discuss potential future observations.

5.2 Observational Data

HST WFC3 Observations and Spectral Extraction

We observed transits of Kepler-79d with *HST*’s Wide Field Camera 3 (WFC3) instrument on UT 2018 April 12 and UT 2018 November 6 (PI Jontof-Hutter, GO 15138). This relatively long period (52 days) planet has an approximately eight hour transit duration, and each visit therefore consisted of 13 *HST* orbits in order to ensure that that our out-of-transit baseline was comparable to the time in transit. The long duration of these observations meant that *HST* inevitably crossed the South Atlantic Anomaly (SAA) during a few orbits in each visit, however its impact on our data appears to be minimal as we discuss below.

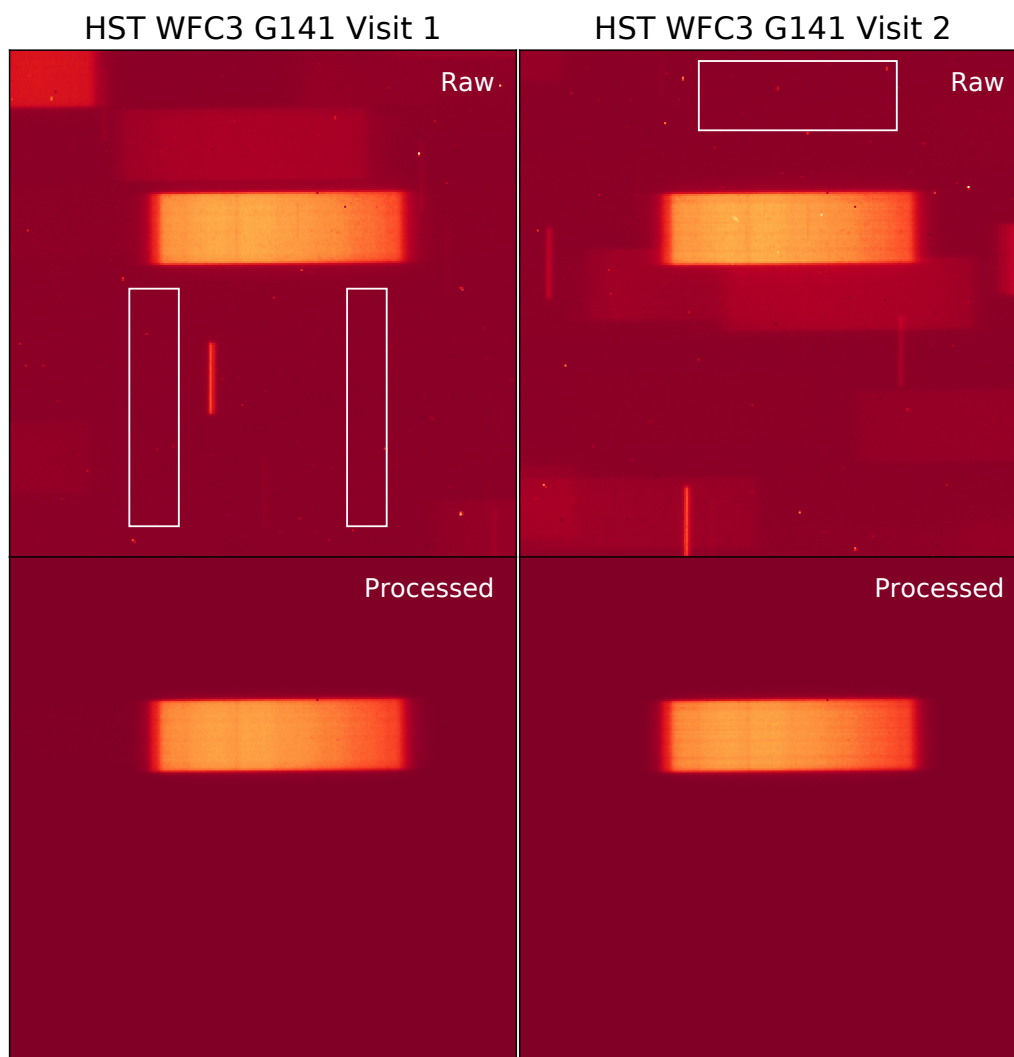


Figure 5.1: First exposures of the 2 *HST* visits. The top panel contains the raw images and the bottom panel contains the processed images (after extraction and outlier correction). The region used for sky background calculation is marked out by a white box in the raw images. Kepler-79 has the brightest spectral trace in these images.

The data were taken with the G141 grism in the 256×256 sub-array mode. We utilized the unidirectional (forward scan only) spatial scan mode in order to increase the duty cycle for these observations relative to the more conventional staring mode (Deming et al., 2013; McCullough & MacKenty, 2012). Although observations of the brightest ($J \lesssim 10$) stars typically alternate forward and reverse scans (e.g., Knutson et al., 2014b; Mansfield et al., 2018; Stevenson et al., 2014), this would have required us to fit two independent instrumental noise models, one for each scan direction. For Kepler-79 ($J = 12.9$), the difference in duty cycle for forward-only versus forward and reverse scans was negligible, and we therefore opted for the simpler unidirectional scan mode. The orientation of the spacecraft during data collection and the scan length ($4.46''$ with a scan rate of $0''.015 \text{ s}^{-1}$) were set to ensure that the spectrum of Kepler-79 did not overlap with those of any neighbouring stars (Figure 5.1). For this relatively faint star each exposure lasted 290.8 seconds, yielding 7 exposures per *HST* orbit. Kepler-79 is only visible for approximately half of *HST*'s 96 minute orbit, leading to gaps in our observations. During the first visit, one orbit covered part of ingress, but none of the orbits in the second visit covered ingress or egress. As a result, the transit time for the first visit from our white-light fits is much better constrained than the transit time for the second visit.

We use the ExoTEP suite for our data reduction, which is described in detail in Benneke et al. (2019a) and follows the methods previously adopted in Berta et al. (2012), Deming et al. (2013), and Knutson et al. (2014a) for WFC3 data. We use bias- and dark-corrected ima images produced by the standard *calwfc3* pipeline. Each exposure consists of 14 non-destructive reads and we subtract consecutive reads to create difference sub-exposures (e.g. Deming et al., 2013; Evans et al., 2016; Kreidberg et al., 2014a). The rows where the median flux profile falls to 20% of the peak flux value in the cross-dispersion direction delineate the vertical extent of the sub-exposure. We find that including the flux from an additional buffer of pixels above and below these rows reduces the correlated noise in the white light curves. We optimize this buffer by picking the values (9 pixels and 10 pixels for the first and second visit respectively) that minimize the scatter in the residuals in our light curve fits and ensure by visual inspection that secondary sources are not included.

We estimate the sky background using two 120×20 pixel boxes below the spectral trace in the first visit and one 35×100 pixel box above the trace in the second visit (Figure 5.1). We ensure that these regions do not contain secondary sources and

remove 3σ outliers before subtracting the median of the remaining pixels from the sub-exposure. These background subtracted sub-exposures are then combined to form full frame images. We flat-field all frames using the calibration files provided by STScI (Kuntschner et al., 2011) following the method outlined in Wilkins et al. (2014). We quantify image-to-image variations in the position of the spectral trace in the x (dispersion) direction by summing each image in the y direction and using the first summed image as a 1D spectral template to calculate the x offset of all the subsequent images. The 2D wavelength solution is then calculated for each image with the method outlined in Tsiaras et al. (2016) and Benneke et al. (2019a) using the wavelength and trace calibration functions provided by STScI (Kuntschner et al., 2009).

Because Kepler-79 is fainter and our exposure times are longer than in previous studies utilizing the ExoTEP pipeline (Benneke et al., 2019a,b; Chachan et al., 2019; Wong et al., 2020), we find that we require a more robust outlier recognition and replacement method to correct for cosmic rays and bad pixels. We do a first pass filtering step to flag obvious outliers using the same spatial outlier correction used in previous studies. In this case, we make two passes with a moving median filter (11 pixels by 11 pixels) where we flag 6σ outliers and replace them by the median value in each image. Although we experimented with lower σ thresholds, we found that they led to overly aggressive spatial outlier correction.

We identify and correct any remaining outliers using the spatio-temporal filtering method outlined in Nikolov et al. (2014) and Nikolov et al. (2018b). In this step, we subtract the two preceding and two succeeding images from the current exposure to construct four difference images. We then take the median of these four difference images and flag 5σ outliers in this median difference image using the same 2D moving median filter as before. For each outlier, we then construct a median ‘PSF’ profile in the cross-dispersion (scan) direction from the five preceding and succeeding columns in the image. This median ‘PSF’ profile is scaled to match the median flux level in the column with the outlier. The outlier is then replaced with the corresponding flux value at that pixel location in the scaled median ‘PSF’ profile. This method results in more accurate replacement flux values than a simple spatial median because it is better able to account for variations in the scan rate of the telescope as it moves across the detector. We find that two iterations with this filter are enough to remove visible outliers from all of our exposures.

We use the 2D wavelength solution to determine the boundaries of 30 nm wide bins and sum the flux from both fully and partially included pixels to obtain a 1D spectrum. For the partial pixels, we use a flux-conserving second order 2D polynomial to calculate the contribution of flux to that particular bin (see Tsiaras et al., 2016 for more details). The white light curve is obtained by summing the flux from all the spectroscopic light curves (1.12 – 1.66 μ m).

Kepler Light Curves

The *Kepler Space Telescope* observed 28 transits of Kepler-79d between 2009 and 2013. Most of these data were obtained in short cadence (1 min integrations) mode, but during the first, second, and seventeenth quarters, only long cadence (30 min integrations) data were collected. In this study, we utilize the short cadence simple aperture photometry (SAP) light curves (24 transits in total), as these data provide better information about the transit shape than the long cadence observations. The 10th, 16th, and 17th transit data contain significant correlated noise with an estimated magnitude larger than 100 ppm (see § 5.4) and we therefore exclude them when we create our phased *Kepler* light curve. Since the ephemeris for Kepler-79d is not linear, we utilize individual mid-transit times from Jontof-Hutter et al. (2014) to extract sections of the light curve centered around each transit event with a length of three times the transit duration. We then fit for a quadratic trend in the out of transit baseline and remove it from each transit before combining all the transits to form a single light curve centered on the mid-transit phase.

We find that linear detrending is inadequate to fit the out-of-transit baseline; this is unsurprising given the relatively long duration (~ 24 hours) of our extraction window. When we compare quadratic and linear detrending, we find that quadratic detrending is highly favored by the Bayesian information criterion ($\Delta \text{BIC} = 74$) and reduces the scatter in the residuals by 1σ . After creating our phased transit light curve, we perform outlier correction on it by using a moving median filter in two steps. First, we perform three iterations of outlier rejection using a moving median filter with a width of 20 exposures and a relatively high 5σ threshold. We then repeat this outlier rejection using a filter with a 50 exposure width and trim any points that deviate from this moving median by more than 3σ . This second step flags just 0.06% of all the short cadence data points, and therefore has a negligible effect on the best-fit transit shape.

5.3 Light Curve Modelling and Fitting

Astrophysical Model

We use the BATMAN package (Kreidberg, 2015) to model transit light curves and fit for the planet-star radius ratio R_p/R_* , mid-transit time T_c , impact parameter b , and semi-major axis to stellar radius ratio a/R_* . We calculate custom stellar limb darkening coefficients for the *HST* WFC3 bandpass using the package LDTk (Parviainen & Aigrain, 2015), which uses the PHOENIX stellar spectra models (Husser et al., 2013). LDTk generates radial stellar brightness profiles and then fits these profiles with a fourth order non-linear limb darkening model. The stellar properties are taken from Petigura et al. (2017c) and Fulton & Petigura (2018), and are derived using *Gaia* parallaxes, *Kepler* photometry, and spectroscopic temperatures from Keck/HIRES. For *Kepler*-79, this study finds $T_{\text{eff}} = 6389 \pm 60$ K, $[\text{Fe}/\text{H}] = 0.06 \pm 0.04$, and $\log g = 4.33 \pm 0.10$. Since the *Kepler* light curve contains dense sampling of the transit shape, we fit for quadratic limb darkening coefficients instead of fixing them to the model values from LDTk (also recommended in the literature, e.g. Espinoza & Jordán, 2015). ExoTEP allows for a quadratic and a four parameter limb darkening law and we verified that using the latter does not improve the fit. Our fitted quadratic limb darkening coefficients (listed in Table 5.1) are consistent within 1σ with those obtained from ATLAS models in J-band (Claret & Bloemen, 2011; Kurucz, 1979). Although the two limb darkening coefficients obtained from LTDk (which uses PHOENIX models that are more suitable to cooler stars) are 3σ and 1σ off from our fitted values, this does not introduce any wavelength dependent bias in our analysis as the difference in the limb darkening between ATLAS and PHOENIX models in the *HST* WFC3's infrared bandpass is negligible compared to the uncertainties in the measured flux.

HST/WFC3 Systematics Model

We fit the white-light curve for each *HST* visit using a linear plus exponential function of the orbital phase (t_{orb}) and the x position of the spectral trace on the detector (relative to the first exposure's position x_o). We also include an exponential function of time since beginning of visit (t_v). These exponential terms are needed in order to correct for charge-trapping in the array (e.g. Deming et al., 2013; Zhou et al., 2017). Our WFC3 systematics model $S(t)$ is then:

$$S(t) = (c + p t_{orb} + m (x - x_o)) \left(1 - e^{-at_{orb} - b - dt_v} \right) \quad (5.1)$$

Table 5.1: Global broadband light curve fit results

Parameter	Instrument	Band pass (μm)	Value
Planet radius, R_p/R_*	<i>Kepler</i>	0.42 - 0.9	$0.04979^{+0.00027}_{-0.00021}$
Transit depth, $(R_p/R_*)^2$ (ppm)	<i>Kepler</i>	0.42 - 0.9	$2478.9^{+27.0}_{-20.9}$
Planet radius, R_p/R_*	WFC3 G141	1.1 - 1.7	0.04876 ± 0.00046
Transit depth, $(R_p/R_*)^2$ (ppm)	WFC3 G141	1.1 - 1.7	$2377.7^{+45.0}_{-44.3}$
Transit center time T_c (BJD _{TDB}) ^a	WFC3 G141 (Visit 1)	1.1 - 1.7	$2458221.38634^{+0.00093}_{-0.00092}$
Transit center time T_c (BJD _{TDB}) ^a	WFC3 G141 (Visit 2)	1.1 - 1.7	$2458429.7253^{+0.0074}_{-0.0066}$
Impact parameter b	—	—	$0.16^{+0.12}_{-0.11}$
Relative semi-major axis a/R_*	—	—	$47.04^{+0.51}_{-1.23}$
Inclination ^b i	—	—	$89.81^{+0.13}_{-0.16}$
Limb darkening coefficient u_1	<i>Kepler</i>	0.42-0.9	0.25 ± 0.06
Limb darkening coefficient u_2	<i>Kepler</i>	0.42-0.9	0.33 ± 0.11

Notes.^aSubtract 69.184 seconds to convert to BJD_{UTC} (see Eastman et al., 2010).^bCalculated from posteriors for b and a/R_* .

where c , p , m , a , b , and d are free parameters in the fit. The parameters c , p and m characterize the linear dependence of systematic noise on t_{orb} and the x position of the spectral trace. For the exponential ramp, b sets the overall time-independent amplitude of the exponential term, and a and d control the dependence on t_{orb} and t_v , respectively (e.g. Berta et al., 2012; Knutson et al., 2014a). We find that including a visit-long ramp (exponential term in t_v) along with the classic orbit-long ramp significantly improves our fit to the systematics in the data (Δ BIC = 160 and 277 for the first and second visit, respectively). In addition, this exponential term in t_v is preferred over the more typically utilized polynomial functions of t_v (e.g. Δ BIC = 145 and 261 for the first and second visit, respectively, for a linear t_v function as opposed to the exponential ramp we use). Although *HST* WFC3 phase curve observations (e.g., Kreidberg et al., 2018; Stevenson et al., 2014) often have observational baselines with a length comparable to that of our Kepler-79 observations, they typically observe stars much brighter than Kepler-79. Because the timescale for charge-trapping increases for faint stars, it is unsurprising that the initial exponential ramp would persist across multiple orbits, whereas for bright stars it is typically converged by the end of the first orbit. We also consider fits with an additional linear trend in t_v , but found that this does not improve the fit and is disfavoured by BIC.

It is common practice to discard the first exposure in each orbit and the first orbit in each visit in *HST* transit observations, as the very steep rise in flux during these sections of the light curve is typically not well matched by the simple polynomial and/or exponential functions used to approximate trends due to charge-trapping and other spacecraft systematics (e.g., Deming et al., 2013; Sing et al., 2016; Tsiaras et al., 2018). For this reason, we also discard the first exposure of each orbit for both of our visits and the first orbit of the first visit. For the second visit, we find that the first orbit is well-matched by our exponential model and its inclusion or exclusion does not bias our estimates of the astrophysical parameters, and we therefore include it in our fits.

For the wavelength-dependent light curves, we consider two different instrumental noise models. The first model involves fitting the full systematics model (Equation 5.1) to each spectroscopic light curve. In the second model, we apply a common-mode correction to the light curve before fitting a linear function of the x (dispersion direction) position of the each exposure. For the common mode correction, we divide each spectroscopic time series by the ratio of the uncorrected white

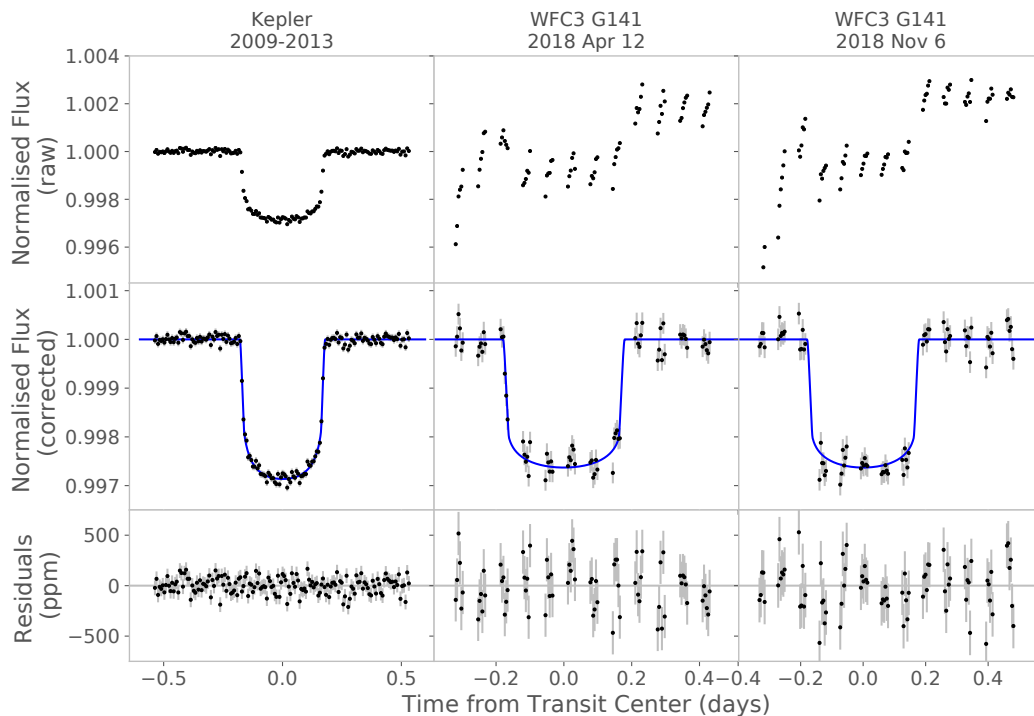


Figure 5.2: White light transit light curves before (top) and after (middle) dividing out the best-fit instrumental systematics model. The best-fit transit light curve is shown in blue for comparison, and the fit residuals are shown at the bottom. *Kepler* data has been binned down using a bin width of 200 points.

light curve and the best-fit white light curve transit model (e.g. Deming et al., 2013). The resultant spectroscopic time series is fit with a systematics model that depends on just two parameters, an offset f and a slope v for the detrending parameter x :

$$S(t) = f + v (x - x_o). \quad (5.2)$$

We find that the second instrumental noise model is strongly favored by BIC (Δ BIC in the range 14 – 73 for the 18 spectroscopic light curves), and therefore use it for our final analysis of the spectroscopic light curves.

Light Curve Fits

We initially fit the phased TTV-removed *Kepler* transit light curve (extraction described in § 5.2) and each individual *HST* transit light curve separately and use the best-fit values obtained from these fits as our initial guesses for the joint fit. For the processed *Kepler* light curve, only the astrophysical model is used to fit the data as the systematic trends have already been removed. For the joint fit, we assume that b and a/R_* are the same for all light curves, but allow the mid-transit times

for the two *HST* visits to vary independently. Assuming the same b and a/R_* for all visits allows a robust comparison of the transit depths in different bandpasses. We fit for two separate R_p/R_* values, corresponding to the measured transit depths in the *Kepler* and *HST* WFC3 bandpasses. We do not fit for the orbital period, eccentricity, or the argument of periastron in our default fit and instead fix these parameters to the values reported in Jontof-Hutter et al. (2014). We fit a total of 23 parameters in our joint fit using the affine-invariant ensemble sampler `emcee` package (v2.2.1, Foreman-Mackey et al., 2013). The number of walkers is set equal to $4 \times$ the number of parameters (e.g., 92 walkers for our joint fit).

For the individual fits of the light curves, we run a 4,000 step burn-in chain followed by a 6,000 step chain that is used to obtain initial guesses for the joint fit of the light curves. Using the burn-in chain, we identify and discard any walkers that get trapped in local minima: if any walker’s maximum likelihood is less than the median likelihood of any of the other walkers, we discard it. For the joint fit, we perform two independent fits to the light curves. In the first fit, we run a 40,000 step burn-in chain and an additional 60,000 step chain thereafter to obtain parameter estimates. We then initiate a second fit to the light curves by setting the initial positions of the walkers to within 1σ of the best-fit solution from the first fit. For this second fit, we again run a 40,000 step chain for burn-in to ensure that the spread in the walkers’ positions equilibrates. After the burn-in, we run a 400,000 step chain to obtain our posteriors and parameter estimates.

To check for convergence in our joint fit, we plot a histogram of likelihoods for individual walkers and find that they all have similar peaks, i.e., all walkers have found the correct global maximum likelihood by the end of burn-in. The parameter estimates we obtain from our two independent joint fits agree at better than the 0.05σ level. We also calculate the autocorrelation length (ξ) for each walker and variable from our 400,000 step chain using the autocorrelation calculator provided in v3.0.2 of `emcee`. On average, ξ for a given walker is a factor of 400 – 500 times smaller than the chain length for all but three parameters. The strong degeneracy between a/R_* and b leads to longer ξ for these parameters such that the chain length is $\sim 130 - 150$ times their ξ on average. This degeneracy also lengthens ξ for R_p/R_* in the *Kepler* bandpass, but with a chain length equal to 167ξ on average, our estimate is reliable at the requisite confidence level.

5.4 Results and Discussion

White Light Curve Fits

Results from our global fit to the *Kepler* and *HST* WFC3 white light curves are tabulated in Table 5.1 and the raw and fitted light curves are shown in Figure 5.2. Our best-fit orbital parameters and *Kepler* planet-star radius ratio agree with those published in Jontof-Hutter et al. (2014) at the $\sim 1\sigma$ and $\sim 2\sigma$ level, respectively. Our measured radius ratio in the *Kepler* band is approximately 4% (2.2σ) larger than the corresponding radius ratio in the *HST* WFC3 band. This allows us to place constraints on the magnitude of potential signatures from scattering (§ 5.4) and stellar activity (§ 5.4).

We test for the presence of time variability in the transit shape by re-fitting individual *Kepler* and *HST* transits with orbital parameters and limb darkening coefficients (for the *Kepler* transits) fixed to the best-fit values from the global fit. Light curves for individual transits in the *Kepler* bandpass are extracted using mid-transit times from (Jontof-Hutter et al., 2014) and are subject to the same outlier correction method that is used for the phase folded light curve (see § 5.2 for more details). Unlike in the global fit, we do not detrend the *Kepler* data prior to fitting the transit. Instead we simultaneously fit a quadratic function of time along with the transit light curve. We find that this simultaneous baseline and transit fit increases the average uncertainty on individual transit depths by approximately 40% as compared to fits where we detrend the data first and fit the transit afterward.

We fit all 24 *Kepler* transits using the method described above and find that there is one transit (the 10th) that appears to be significantly deeper than the other transits. We investigate whether or not this could be due to time-correlated noise in the transit light curve as follows. First, we estimate the magnitude of the correlated noise in each individual transit light curve by fitting the standard deviation of the residuals (σ) as a function of bin size (N) with a two component model: $\sigma = \sqrt{\sigma_w^2/N + \sigma_r^2}$. Here, σ_w and σ_r are the white (Gaussian) and correlated noise components, respectively (e.g., Pont et al., 2006). Our transit light curves have $\sigma \sim 1000$ ppm at 1 min cadence, and we set a threshold of $\sigma_r > 100$ ppm (10% excess) for flagging transits with significant correlated noise. When we bin the data on 30 min timescales (comparable to the timescale of ingress or egress), this means that the red noise is a significant fraction ($\geq 50\%$) of the white noise component.

We find that 10th, 16th, and 17th transits all have red noise levels that exceed this threshold, and we therefore exclude these transits from our phased *Kepler*

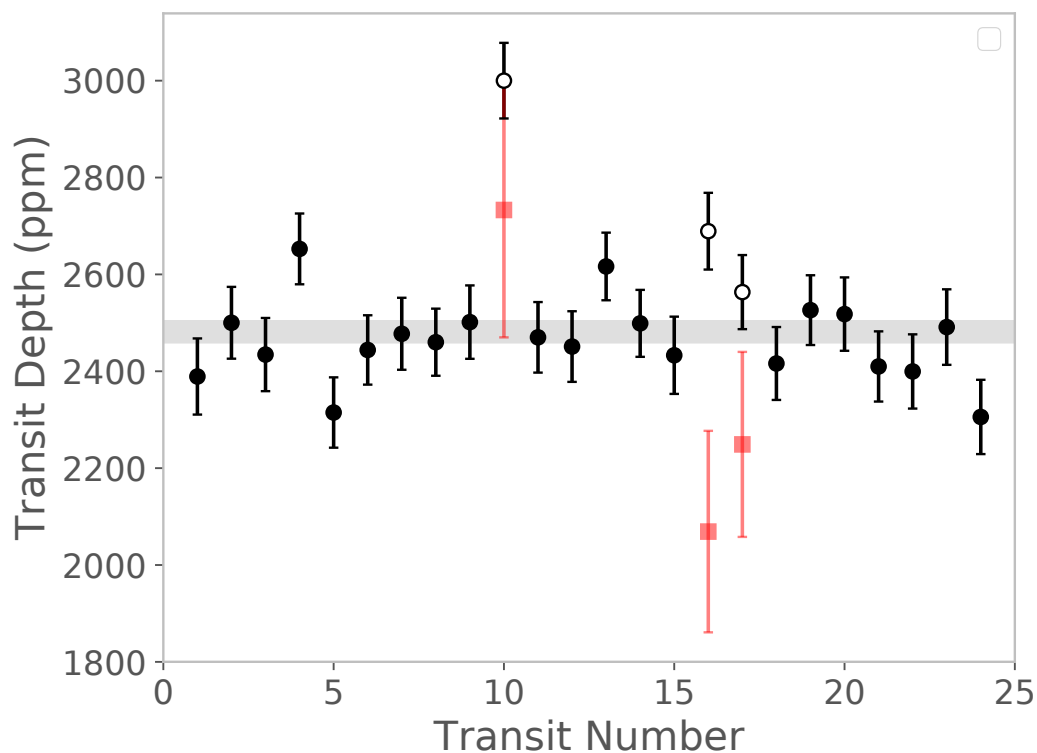


Figure 5.3: Transit depth measurements for each individual transit of Kepler-79d observed at short cadence. The grey region marks the 1σ limits on the transit depth from our joint fit to the *Kepler* and *HST* data. Black empty circles mark the transits that were significantly affected by correlated noise and red squares show their transit depth measurements obtained using Gaussian Process modelling.

light curve and variability analysis. The remaining 21 *Kepler* transit depths do not display any significant epoch to epoch variability (reduced χ^2 value of 1.25, Figure 5.3). This stands in contrast to the large epoch to epoch variability observed in the measured *Kepler* transit depths of Kepler-51b and d, which Libby-Roberts et al. (2020) attribute to stellar activity. This lack of variability is in good agreement with the lack of detectable photometric variability for Kepler-79 ($< 0.2\%$) and the absence of any obvious spot crossing events in the *Kepler* light curves.

For the three transits with significant correlated noise, we used Gaussian Processes (GP) modeling to obtain improved estimates of their transit depths and corresponding uncertainties. We fixed the orbital parameters and limb darkening coefficients to the best-fit global values as before and allowed R_p/R_* to vary as a free parameter in the fit. We do not include a quadratic function of time to detrend the data, as the GP is

able to fit these trends as part of its noise model. We adopted a squared exponential kernel:

$$C_{ij} = h^2 \exp\left[-\frac{(t_i - t_j)^2}{2\eta^2}\right] + \sigma^2 \delta_{ij} \quad (5.3)$$

where C_{ij} are elements of the covariance matrix, t_i is the time of the i th observation, δ_{ij} is the Kronecker delta function, h is the amplitude of the covariance, η is the correlation timescale, and σ is an additional white noise component. We show the resulting transit depth estimates from these fits using red squares in Figure 5.3. As expected, the increased uncertainties obtained using GP reflect the presence of significant correlated noise in the data for these three transits. As a check, we also fit two randomly selected transits with low levels of red noise (1 and 5) using GP and confirm that their transit depths are consistent within 1σ and their uncertainties increase only by 10–20% relative to the values we obtained with a simple quadratic baseline fit. The 21 transits depths combined with the depths of these three transits with significant red noise (obtained using GP) do not display significant variability either (slightly higher reduced χ^2 of 1.35).

We find that the transit depths for the two *HST* visits (visit 1: 2283 ± 58 ppm, visit 2: 2465 ± 56 ppm) differ by 2.3σ . This difference is commensurate with expectations from *HST* white light curves (similar differences observed in previous studies, e.g. Mansfield et al., 2018; Wakeford et al., 2018), which often suffer from residual time-correlated noise and therefore may have modestly underestimated uncertainties when fit assuming white Gaussian noise. This increase in uncertainties is also corroborated by analyses that use Gaussian Processes instead of parametric models to fit for the systematic noise in *HST* light curves (e.g. Evans et al., 2018; Gibson et al., 2012; Mikal-Evans et al., 2019). We find that the difference in the transit depths between the two *HST* visits is comparable in magnitude to the difference between the averaged *HST* and *Kepler* transit depths, further reinforcing our conclusion that our data appear to be consistent with a flat line.

Transit Timing Variation Fits

Our transit timing dataset includes the *Kepler* data analyzed by Jontof-Hutter et al. (2014), who performed dynamical fits to the first 16 quarters of *Kepler* data using all short cadence data available. To this dataset, we add the few Q 17 transits catalogued from long cadence data by Rowe & Thompson (2015), and the two transit times measured from WFC3. The timing uncertainty on the first *HST* visit was 1.31

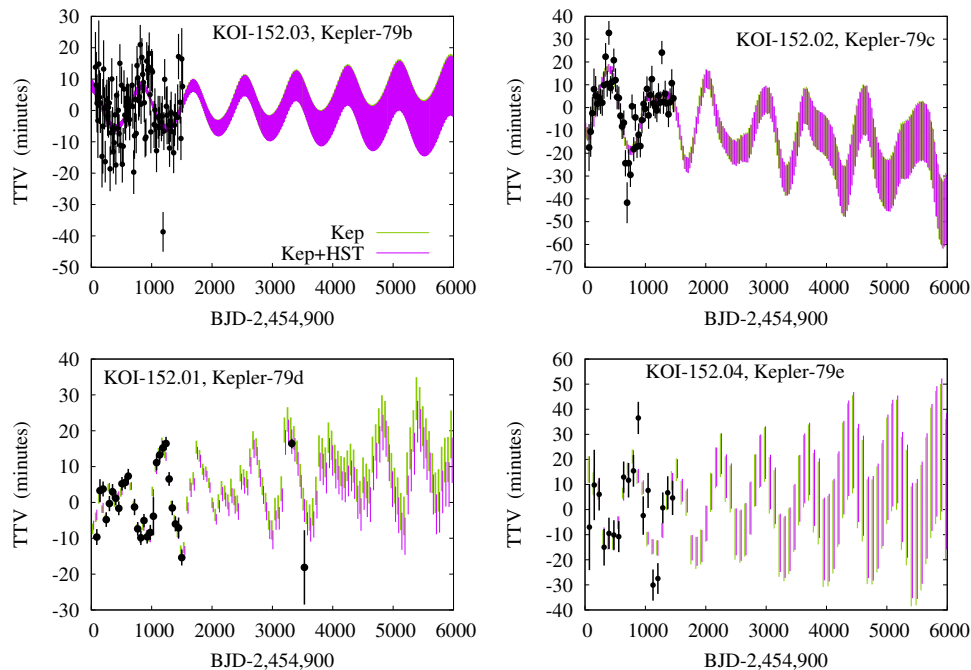


Figure 5.4: Observed and simulated deviations of transit times from a linear fit to the observed *Kepler* data. The colored bands mark the standard deviation of 1000 simulated transit times from the posterior sampling models, with green marking the solutions following *Kepler* only, and magenta marking the dataset including the *HST* times.

minutes. During the second visit, data gaps during both ingress and egress reduced the precision on the transit timing, leaving an uncertainty of 10.4 minutes.

Our TTV models assumed coplanarity, and included five free parameters per planet: orbital period P , phase-at-epoch T_0 , planet-star mass ratio M_p/M_* , and the eccentricity vector components $e \sin \omega$ and $e \cos \omega$. Coplanarity is a reasonable assumption as mutual inclinations have little effect on transit times unless the mutual inclinations reach relatively large angles (Nesvorný & Vokrouhlický, 2014), which is very unlikely for a multi-planet system where all planets transit the host star (*Kepler* multi-planet systems are nearly coplanar; Fabrycky et al., 2014). For orbital period, phase-at-epoch, and the planet-star mass ratio, we adopted a uniform prior. The planet-star mass ratio was also assumed to be positive definite as some of the posterior sampling reaches zero mass. No other limits are placed on these three parameters although in practice the orbital period and transit epoch are known so precisely that the samples never deviate from the best-fit value by more than a few minutes. For the eccentricity vector components $e \sin \omega$ and $e \cos \omega$, we assumed

a Gaussian prior centered at zero with a standard deviation of 0.1. This Gaussian prior for eccentricity is motivated by the fact that high eccentricity solutions, which can often fit the data as well as the low eccentricity models, are unlikely or unstable for closely-packed multi-planet systems (e.g. Jontof-Hutter, 2019; Jontof-Hutter et al., 2015, 2016). To sample the posteriors of these parameters, we used a Differential Evolution Markov Chain Monte Carlo algorithm (Jontof-Hutter et al., 2015, 2016; Ter Braak, 2006), beginning the chains close to the best-fit model found by Jontof-Hutter et al. (2014).

We perform a TTV model fit to just the *Kepler* data as well as the full set of *Kepler* + *HST* data and compare the effect of adding the *HST* data. Figure 5.4 shows the observed and simulated TTVs for these data. The mid-transit time of the first visit with WFC is very close to the value predicted following the *Kepler* data, while the mid-transit time of the second visit with the larger uncertainty is earlier than expected at the $\sim 1.5\sigma$ level. The agreement between the predicted and observed transit time of the first *HST* visit bolsters the mass measurements of the *Kepler* only dataset, and confirms the low density of Kepler-79 d. The earlier time for the second visit, causes the TTV model to favor a slightly shorter orbital period for Kepler-79 d, although well within the uncertainty following the *Kepler* dataset alone. The effect is a systematic revision of predicted transit times to occur several minutes earlier for the next few years. For the other planets, the *HST* data has a smaller effect on the predicted transit times.

Table 5.2 shows the parameter estimates from these fits. Although our mass estimates from a fit to the *Kepler* data alone agree with the masses from Jontof-Hutter et al. (2014) to better than 1σ , they are consistently lower and possess smaller uncertainties than the previously published values. This is because the previous study utilized Levenberg-Marquardt χ^2 minimization and estimated parameter values and uncertainties from a union of solutions found by this technique. This led to different median values for the planet masses and overestimated uncertainties. The results presented in this work are more appropriately derived from MCMC sampling of the posterior. Since the updated TTV values for Kepler-79d’s period, eccentricity, and argument of periastron values are slightly different from those assumed in our light curve fitting (we used values from Jontof-Hutter et al., 2014, see § 5.3), we refit our combined *Kepler* and *HST* light curves by placing TTV-derived Gaussian priors and accounting for covariances for these parameters. Results from this fit are in good agreement with the reported parameter estimates in § 5.4 (differences $\lesssim 1\sigma$). We

Table 5.2: Transit time variations fit results

Properties	Kepler-79b	Kepler-79c	Kepler-79d	Kepler-79e
Mass Ratio (M_p/M_*) (<i>Kepler</i> + <i>HST</i>)	$1.84^{+1.00}_{-0.62} \times 10^{-5}$	$1.09^{+0.32}_{-0.27} \times 10^{-5}$	$1.30^{+0.24}_{-0.21} \times 10^{-5}$	$9.39^{+1.77}_{-1.68} \times 10^{-6}$
Mass/ M_\oplus ^a (<i>Kepler</i> + <i>HST</i>)	$7.6^{+3.8}_{-2.6}$	$4.6^{+1.3}_{-1.1}$	$5.3^{+0.9}_{-0.9}$	$3.8^{+0.7}_{-0.6}$
Mass/ M_\oplus ^a (<i>Kepler</i> only)	$7.6^{+4.2}_{-2.7}$	$4.6^{+1.4}_{-1.1}$	$5.3^{+1.0}_{-0.8}$	$3.9^{+0.7}_{-0.7}$
Radius/ R_\oplus ^b	3.51 ± 0.10	3.76 ± 0.11	7.15 ± 0.20	3.53 ± 0.16
Density ^c (g/cc)	$0.97^{+0.49}_{-0.33}$	$0.48^{+0.14}_{-0.12}$	$0.08^{+0.02}_{-0.02}$	$0.48^{+0.09}_{-0.10}$
Period (days)	$13.48451^{+0.00010}_{-0.00008}$	$27.4026^{+0.0004}_{-0.0003}$	$52.0897^{+0.0006}_{-0.0005}$	$81.0665^{+0.0007}_{-0.0006}$
$e \sin \omega$	$-0.0007^{+0.0038}_{-0.0033}$	$-0.026^{+0.012}_{-0.014}$	$0.044^{+0.015}_{-0.016}$	$0.015^{+0.013}_{-0.014}$
$e \cos \omega$	$-0.022^{+0.007}_{-0.010}$	$-0.028^{+0.011}_{-0.014}$	$0.014^{+0.024}_{-0.025}$	$0.007^{+0.018}_{-0.020}$
e^d	$0.022^{+0.010}_{-0.007}$	$0.038^{+0.019}_{-0.014}$	$0.051^{+0.016}_{-0.016}$	$0.025^{+0.013}_{-0.011}$
ω^d (degrees)	182^{+10}_{-9}	223^{+12}_{-12}	71^{+33}_{-25}	59^{+66}_{-57}
T_0 (BJD - 2,454,900)	784.3061 ± 0.0009	806.4771 ± 0.0014	821.0104 ± 0.0008	802.1269 ± 0.0019

Notes.

^aPlanet masses calculated using stellar mass $M_* = 1.244^{+0.027}_{-0.042} M_\odot$ from Fulton & Petigura (2018). Mass estimates from *Kepler* data alone are shown purely for comparison with estimates obtained from the combination of *Kepler* and *HST* data.

^b R_p/R_* values for all planets except Kepler-79d are taken from Jontof-Hutter et al. (2014) and the updated value of $R_* = 1.316^{+0.038}_{-0.037} R_\odot$ from Fulton & Petigura (2018) is used to calculate planetary radii.

^cMass estimates from the combination of *Kepler* and *HST* data are used.

^d e and ω are calculated using posteriors of $e \sin \omega$ and $e \cos \omega$.

also use this fit’s results to estimate the stellar mass (e.g. Winn et al., 2010) using the *Gaia* stellar radius value and find that it is consistent with stellar mass value reported in Fulton & Petigura (2018).

The addition of the new *HST* data has a relatively minor effect on the best-fit TTV masses and corresponding uncertainties. This is because the *Kepler* dataset already sampled many frequencies (near resonances as well as synodic chopping) in the TTVs with a high signal-to-noise ratio (SNR). This breaks the mass-eccentricity and eccentricity-eccentricity degeneracies for the Kepler-79 system (Jontof-Hutter, 2019), reducing the value of additional transit timing measurements at later epochs. Nonetheless, we find that the revision of the planetary masses to lower values, in particular for Kepler-79d, encourages continued interest in this planetary system and further cements Kepler-79d’s status as a super-puff.

Transmission Spectrum and Atmospheric Modeling

HST WFC3 Spectrum

The transmission spectrum for Kepler-79d in the *HST* WFC3 bandpass is shown in Figure 5.5, with the corresponding R_p/R_* values tabulated in Table 5.3. There is good agreement between the spectra obtained from the two visits in all but two bandpasses. Transit depths measurements from the two visits in the $1.12 - 1.15 \mu\text{m}$ and $1.48 - 1.51 \mu\text{m}$ wavelength bands show a larger scatter. Spectroscopic light curves for both visits are shown for comparison in Figure 5.6. The transmission spectrum from the second visit has a smaller scatter in the spectroscopic transit depths and is more commensurate with a flat line than the spectrum from the first visit.

Table 5.4 lists the values of Bayesian evidence for the fiducial constant and linear models as well as some physically plausible models that represent limiting cases for Kepler-79d’s atmosphere. We calculate the Bayes factor \mathcal{B} (ratio of evidence) for a particular model by comparing its evidence with that of the constant transit depth model. We find that the HST data provide moderate evidence (\mathcal{B} of 16.9) in favor of the constant model relative to the model with a linear trend in the WFC3 transmission spectrum. We quantify the statistical significance of the rise in transit depth between $1.1\mu\text{m}$ and $1.2\mu\text{m}$ as well as the dip around $1.45\mu\text{m}$ by comparing the evidence for the constant transit depth model with a squared exponential GP model. The GP model provides us with a non-parametric way that is independent of any forward model for fitting the shape of the transmission spectrum. With a \mathcal{B}

Table 5.3: Spectroscopic light curve fit results

Wavelength (μm)	R_p/R_*	$\pm 1\sigma$	Transit Depth (ppm)	$\pm 1\sigma$ (ppm)
1.120-1.150	0.04588	0.00154	2105	141
1.150-1.180	0.04820	0.00122	2323	118
1.180-1.210	0.05067	0.00129	2567	131
1.210-1.240	0.05214	0.00129	2719	135
1.240-1.270	0.05039	0.00117	2539	118
1.270-1.300	0.04989	0.00120	2489	120
1.300-1.330	0.04962	0.00129	2462	128
1.330-1.360	0.04930	0.00117	2430	115
1.360-1.390	0.04882	0.00103	2383	101
1.390-1.420	0.04976	0.00108	2476	108
1.420-1.450	0.04661	0.00124	2172	116
1.450-1.480	0.04696	0.00126	2206	118
1.480-1.510	0.04588	0.00148	2105	136
1.510-1.540	0.04966	0.00137	2466	136
1.540-1.570	0.04659	0.00165	2170	154
1.570-1.600	0.05048	0.00146	2548	147
1.600-1.630	0.04535	0.00177	2057	161
1.630-1.660	0.04951	0.00150	2452	149

Table 5.4: *HST* model evidence

Model	\log_e (Evidence)	Bayes factor (\mathcal{B})
Constant	124.6	–
Linear	121.8	1:16.9
150 \times solar (fixed T)	116.8	1:2578
1000 \times solar (fixed T)	121.6	1:19.9
Metal free (fixed T)	122.5	1:8
Metal free	123.6	1:2.9

of 3.1 in favor of the GP model, the structure in the spectrum is only marginally significant.

We next investigate a range of physically motivated models in order to determine which of these models are ruled out by our data. Given Kepler-79b’s low density, it is reasonable to consider very low metallicity atmospheric compositions. We therefore compare the data with forward models that only includes collision induced absorption (CIA) and Rayleigh scattering contributions from hydrogen and helium (see also Libby-Roberts et al., 2020). We use the Planetary Atmospheric Transmission for Observer Noobs (PLATON) atmospheric modeling and retrieval suite (Zhang

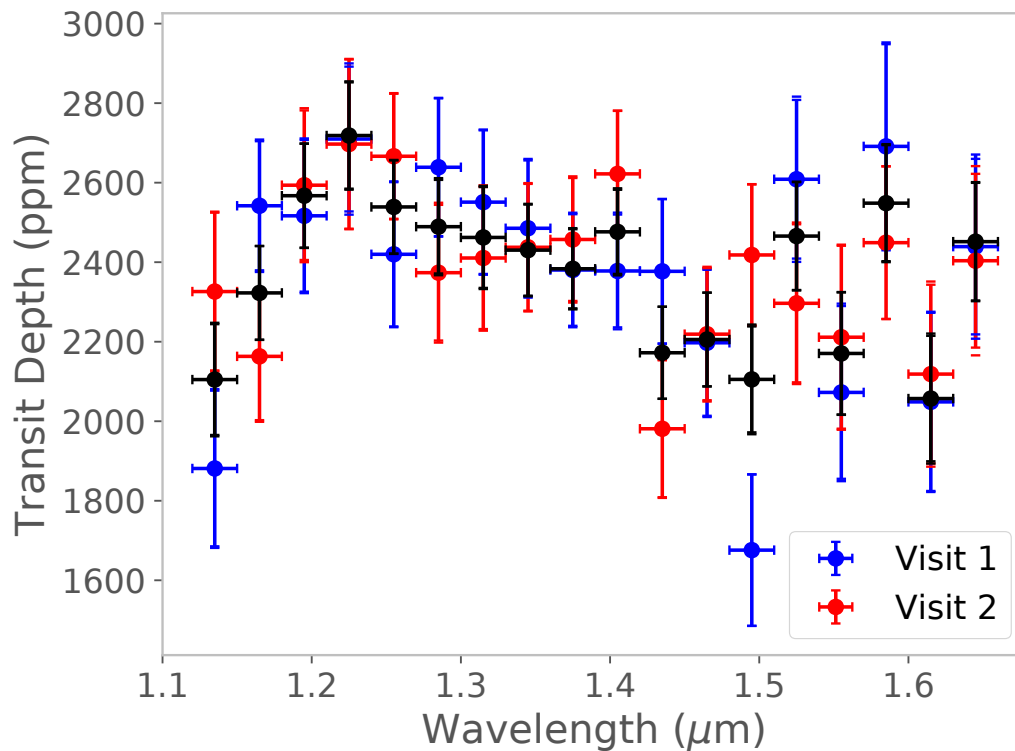


Figure 5.5: The transmission spectrum of Kepler-79d measured during 2 visits with the *HST* WFC3 instrument. Black points show the spectrum obtained from a joint fit of the two visits. There is good agreement between the two visits except in two bandpasses centered at 1.135 and 1.495 μm , which show a larger scatter in the measured transit depths.

et al., 2019, 2020) to compare the data and models in a retrieval framework. For all of our retrievals with PLATON, we place Gaussian priors on planet mass and stellar radius. For the metal-free atmosphere scenario, we initially allow both the planet’s radius (at a pressure of 1 bar) and the atmosphere’s isothermal temperature to vary. We find that the temperature is poorly constrained and its posterior covers the entire prior range (200 – 700 K), with a marginal preference for lower temperatures. Fixing the temperature to 630 K and fitting only for the planet radius only results in a slight decrease in the model evidence, as expected from the weak constraints on temperature in the previous fit. The constant transit depth model is moderately favored (\mathcal{B} of 2.9 – 8) over either of these models.

In principle, this planet’s low measured density implies a strict upper limit of 150 \times solar on its bulk metallicity and consequently its atmospheric metallicity (assuming the metals and envelope are homogeneously mixed throughout; Lopez & Fortney,

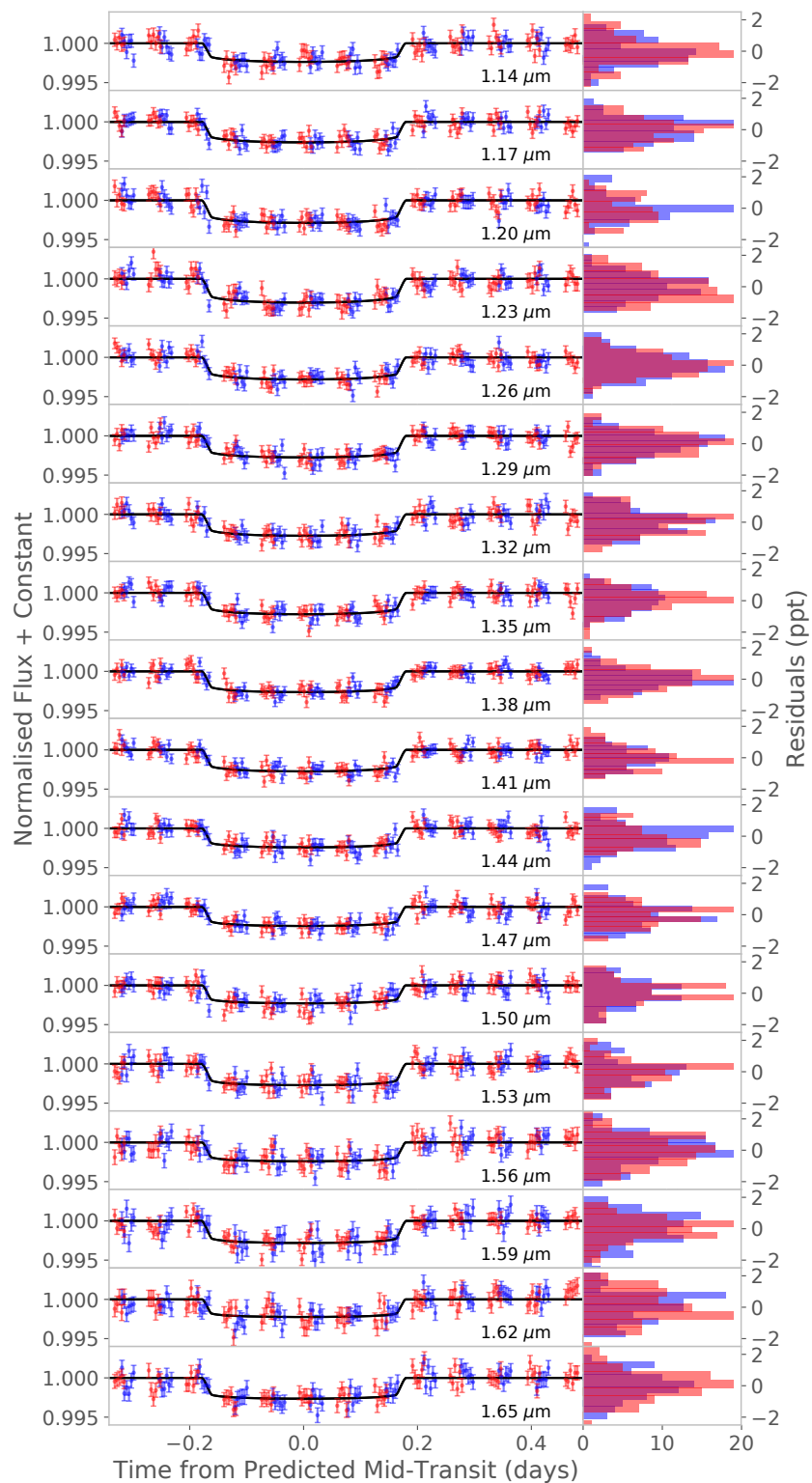


Figure 5.6: Spectroscopic light curves as well as the best-fit transit models for the 2 *HST* visits (visit 1 in blue and visit 2 in red) and a histogram of the residuals (in parts per thousand).

2014; Thorngren & Fortney, 2019)¹. However, this upper limit can be relaxed to values as high as 350× solar if high-altitude hazes shift the photospheric pressure to $\sim 10\mu\text{m}$ bar or 1000× solar if tidal heating (e.g. from obliquity tides, Millholland, 2019) augments the internal heat flux of the planet. Both the presence of hazes at low pressures and the increase in internal heat flux reduce the envelope to core mass ratio required to match the planet’s mass and radius, thereby increasing the upper limit of the planet’s bulk and atmospheric metallicity. We therefore also consider two higher metallicity atmosphere models, where we fix the metallicity to either 150× or 1000× solar metallicity. As before, we fix the atmospheric temperature to 630 K. We also assume a solar C/O ratio = 0.53, include Rayleigh scattering from gas, and exclude clouds and any other sources of scattering. The only quantity that we vary is then the planet’s radius. The constant transit depth model is strongly favored over either the 150× and 1000× solar models with \mathcal{B} of 2578 and 19.9, respectively.

Fitting the WFC3 spectrum and Kepler WLC depth

The relative values of the *Kepler* white light curve depth and the WFC3 transmission spectrum give us important information about Kepler-79d’s atmosphere, especially if scattering from aerosols dominates the absorption cross-section. Kepler-79d is the first super-puff for which we can make such a comparison, as the optical transit depths for the Kepler-51 planets are strongly biased by stellar activity (Libby-Roberts et al., 2020). Table 5.5 lists the Bayesian evidence and the Bayes factor \mathcal{B} relative to the constant transit depth model, where we have updated our fits to include both the *Kepler* and *HST* data. Figure 5.7 shows Kepler-79d’s transmission spectrum as well as the best-fit retrieved models for the different atmospheric scenarios listed in Table 5.5 and discussed below. We find that even with the addition of the *Kepler* transit depth, the transmission spectrum prefers a constant transit depth model. Although the transit depths in the two bands differ by 100 ppm, this difference is only marginally significant (2.2σ) and therefore has a negligible influence on \mathcal{B} for the linear model.

The addition of the *Kepler* depth has a larger influence on \mathcal{B} for the metal poor model. The *Kepler* depth provides a much stronger constraint on the Rayleigh scattering contribution of the hydrogen-helium atmosphere, which depends directly

¹Although we provide updated mass and radius measurements in this work, we expect that these updates will not significantly affect the bulk metallicity estimate reported in in Lopez & Fortney (2014).

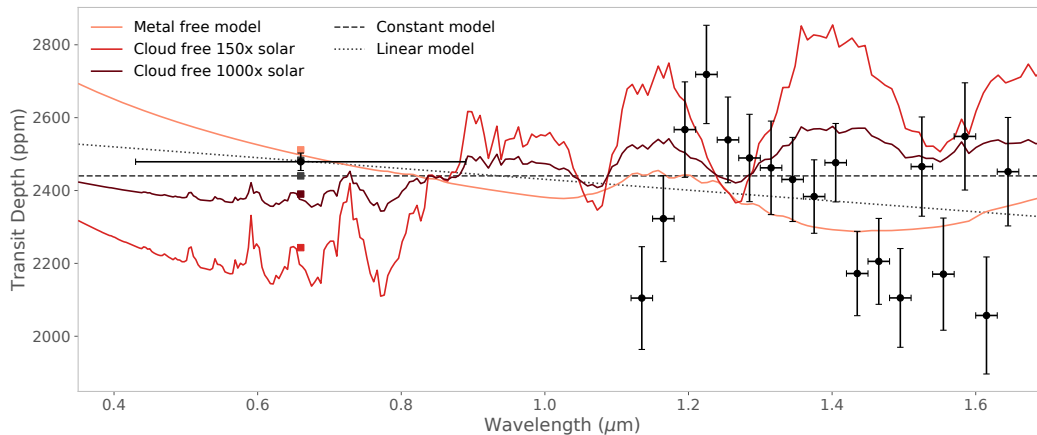


Figure 5.7: The transmission spectrum of Kepler-79d measured with *Kepler* and *HST* WFC3. The best-fit cloud free models with metal poor composition, 150 \times solar metallicity, and 1000 \times solar metallicity are plotted along with the best-fit constant and linear models. The data are consistent with a constant transit depth model. The Bayesian evidence and the Bayes factor for these models are reported in Table 5.5.

Table 5.5: *Kepler* + *HST* model evidence

Model	\log_e (Evidence)	Bayes factor (\mathcal{B})
Constant	131.8	–
Linear	128.9	1:16.7
150 \times solar (fixed T)	113.7	1 : 6.9×10^7
1000 \times solar (fixed T)	124.7	1:1157
Metal free (fixed T)	124.4	1:1622
Metal free	129.6	1:8.8

on the planet’s scale height ($d R_p/d \ln \lambda = -4H$ in the Rayleigh regime where H is the scale height). This leads to a strong preference for models with low atmospheric temperatures (< 364 K at 2σ confidence) as the scale height for the zero-albedo full heat redistribution equilibrium temperature of 630 K is much too large to fit the relative difference between the *Kepler* and *HST* transit depths. Fixing the temperature to 630 K leads to a significant increase in the preferred planet mass ($7.1 \pm 0.7 M_\oplus$), an increase that is driven by the need for a smaller scale height to match the transmission spectrum. The Gaussian prior we placed on the planet mass penalizes the model evidence for this increase and leads to a significant increase in \mathcal{B} . A metal free atmosphere with a plausible temperature of ~ 600 K at a slant optical depth of unity (at ~ 0.1 bar) is therefore ruled out by the data.

Although significantly cooler metal poor models provide an improved match to the data, a reduction of the temperature at this pressure by a factor of two is very unlikely: it would require highly inefficient heat redistribution and/or a very high albedo (comparable to that of the icy moons). Both theoretical and observation constraints favor efficient circulation and small day-night temperature gradients for planets cooler than 1000 K (Cowan & Agol, 2011; Garhart et al., 2020; Komacek & Showman, 2016; Perez-Becker & Showman, 2013). For planets with volatile-rich envelopes, the most plausible way to increase the albedo is to introduce an optically thick reflective cloud layer at low pressures. Not only are most clouds not expected to have such a high albedo, the presence of such a cloud layer would be inconsistent with the assumption of a very low atmospheric metallicity itself as metals are needed to form clouds. We therefore regard the metal poor model as a highly improbable explanation for the measured transmission spectrum.

The constant model is strongly favored over either of the cloud-free high atmospheric metallicity ($150\times$ and $1000\times$ solar) models when we include the Kepler depth. We conclude that there is no evidence for any of the expected absorption or scattering features in the combined *Kepler* and *HST* data. This suggests that Kepler-79d must host a high-altitude cloud or haze layer that effectively mutes the signature of atmospheric absorption. The lack of a detectable scattering slope in the *Kepler* and WFC3 bandpasses can be used to place a lower limit on the particle size distribution for this scattering haze. Rather than fitting a parameterized cloud model, we instead investigate whether microphysical models of photochemical hazes can match our observations. Although these same microphysical models can also be used to study condensate cloud formation, Gao & Zhang (2020) found that photochemical hazes dominate the scattering opacity for planets with temperatures similar to that of Kepler-79d.

CARMA Photochemical Haze Models

In this section we investigate whether a physically motivated photochemical haze model can match the observed transmission spectrum. We use a modified and simplified version of the Community Aerosol and Radiation Model for Atmospheres (CARMA) to study the formation and distribution of hazes in Kepler-79d's atmosphere. CARMA is a 1D bin-scheme aerosol model that can account for microphysical processes such as nucleation, growth by condensation and coagulation, evaporation, and transport. The aerosol continuity equation is discretized over

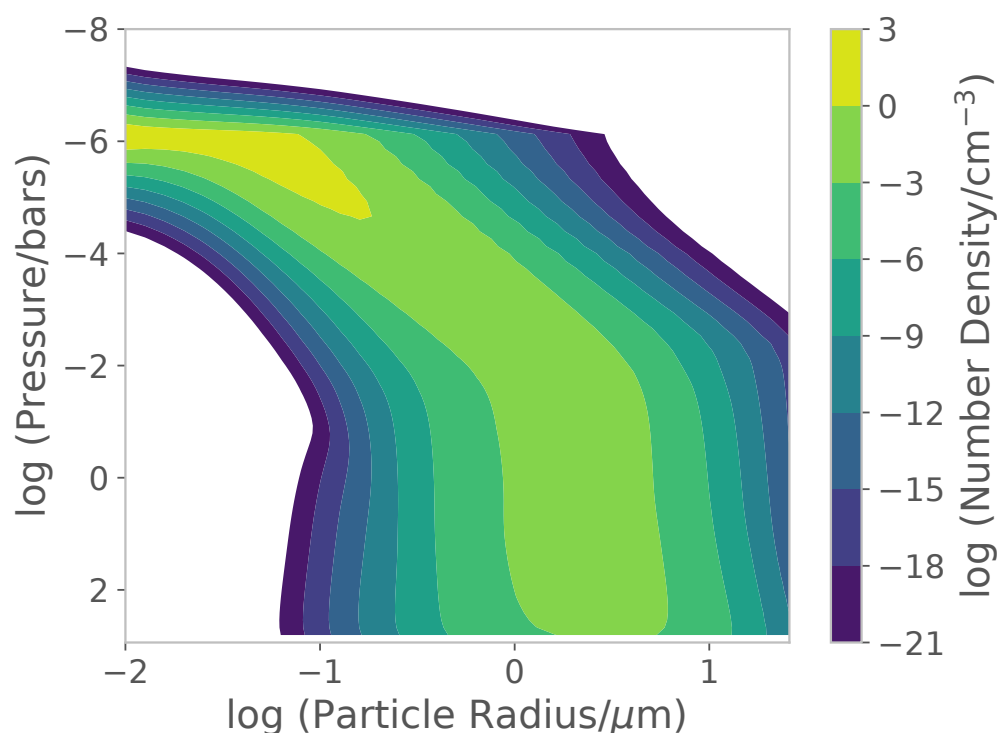


Figure 5.8: Number density of haze particles of different radii at different pressure levels in the atmosphere for $M_{\text{core}} = 5M_{\oplus}$, $T_{\text{int}} = 75 \text{ K}$, $K_{zz} = 10^7 \text{ cm}^2 \text{ s}^{-1}$, and atmospheric mass fraction of 18%. Haze formation at low pressures and transport due to outflowing wind, vertical mixing, and sedimentation leads to an abundance of sub-micron sized particles at low pressures ($\sim 1 - 10 \mu\text{bar}$).

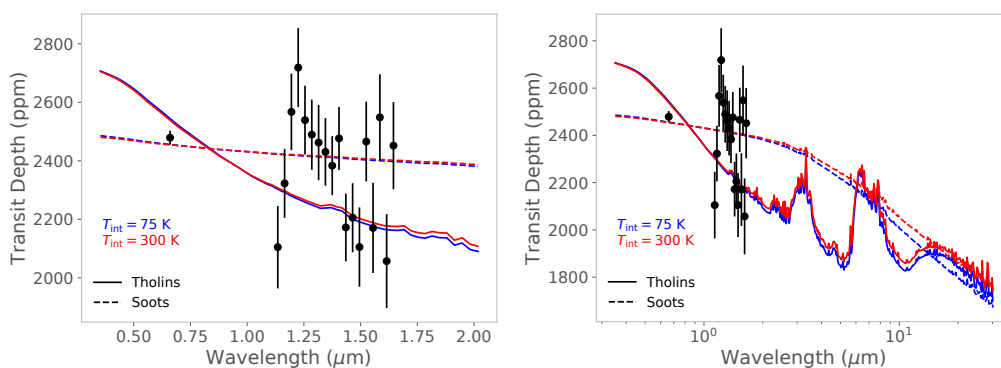


Figure 5.9: Forward CARMA models of the transmission spectrum of Kepler-79d for different optical properties of the aerosols (soots and tholins) and T_{int} values. In the left panel, we compare the models with the transmission spectra. The right panel shows the predicted transmission spectrum out to $30 \mu\text{m}$.

particle radius bins and mass exchange due to microphysical processes is allowed between these bins. For a more detailed description of CARMA, we direct the reader to Gao et al. (2018) and Adams et al. (2019). Our modified and simplified CARMA model is fully described in Gao & Zhang (2020) and we briefly mention key features here for completeness.

Haze ‘seed’ particles are generated at the pressure level where methane is photolyzed (typically centered around $\sim \mu\text{bar}$) with a production rate equal to the methane photolysis rate multiplied by an efficiency factor of 0.1. These seed particles are transported through the atmosphere and allowed to grow by coagulation. Particle transport usually includes sedimentation under the effect of gravity and turbulent vertical mixing. One additional important transport mechanism that is relevant to super-puffs is entrainment by the outflowing hydrodynamic wind that is responsible for mass loss. We take the outward flux due to this wind into account in our model and simplify other aspects of the model in order to keep it computationally tractable. The eddy diffusion coefficient (K_{zz}), which parameterizes vertical mixing, is assumed to be constant ($= 10^7 \text{ cm}^2 \text{ s}^{-1}$) throughout the atmosphere. The value of K_{zz} is not well constrained by current observational data sets for transiting exoplanets, and a plausible range of values inferred from general circulation models can span many orders of magnitude (e.g. Charnay et al., 2015; Moses et al., 2011; Parmentier et al., 2013; Zhang & Showman, 2018a,b). Following these works, we varied the value of this parameter between 10^6 and $10^8 \text{ cm}^2 \text{ s}^{-1}$ and found that it had a negligible impact on our results, in agreement with Gao & Zhang (2020). We additionally adopt a simple but adequate atmosphere model that incorporates both a convective and a radiative layer and uses the ideal gas law and hydrostatic equilibrium to obtain the atmospheric temperature-pressure (TP) profile (Gao & Zhang, 2020, similar to previous models, e.g. Owen & Wu, 2017).

The equilibrium temperature (T_{eq}) of the planet is set to 630 K and we assume a core mass of $5 M_{\oplus}$. For the internal heat flux of the planet, we choose values of $T_{\text{int}} = 75 \text{ K}$ and 300 K (where $F_{\text{int}} = \sigma_{\text{SB}} T_{\text{int}}^4$). The former value reflects the expected residual heat of formation for a $\sim 1 \text{ Gyr}$ old planet with a mass equal to that of Kepler-79 d (Lopez & Fortney, 2014). The latter value corresponds to the expected internal heat flux from dissipation due to obliquity tides (Millholland, 2019, optimistic case, calculated using their Equation 11). We only include hydrogen, helium, water, and methane (the primary constituents of a solar composition atmosphere at $\sim 600 \text{ K}$) in our models. All other species are not expected to contribute significantly either to

the number density or the opacity in the optical and near infrared (Burrows, 2014; Lodders & Fegley, 2002). Since the optical properties of the hazes are unknown, we consider two distinct end cases: scattering hazes (‘tholins,’ refractive index taken from Khare et al., 1984) and absorbing hazes (‘soots,’ Lavvas & Koskinen, 2017; Morley et al., 2015).

We find that the atmospheric mass fraction needed to fit the observed planet radius decreases when a high-altitude haze is present. The best-fit atmospheric mass fractions for $T_{\text{int}} = 75$ K for soots and tholins are 17% and 18%, respectively. These values are roughly half of the previous estimate, which used 20 mbar for the photospheric pressure (Lopez & Fortney, 2014). Models containing soots require a slightly lower atmospheric mass fraction, as soot particles absorb more strongly than tholins. For $T_{\text{int}} = 300$ K, Millholland (2019) found that an atmospheric mass fraction of $\sim 10\%$ could match the planetary radius. However, with haze formation, this value falls precipitously to $\sim 0.6\%$, which is akin to the typical atmospheric mass fraction for super-Earths in the *Kepler* sample (e.g. Chiang & Laughlin, 2013; Lopez & Fortney, 2014; Owen & Wu, 2017; Wolfgang & Lopez, 2015). This raises the intriguing possibility that some super-puffs might simply be super-Earths with unusually high internal heat fluxes and a high-altitude haze. However, whether such planets can manage to retain their atmospheres remains to be seen; we discuss this topic in more detail in § 5.4.

Figure 5.8 shows the number density of haze particles for a representative CARMA model and Figure 5.9 shows the resulting transmission spectra for Kepler-79d. Figure 5.8 indicates that a large number of sub-micron particles are present at pressures of $1 - 10 \mu\text{bar}$, resulting in a transmission spectrum that is dominated by haze opacity. However, our predictions for the corresponding shape of the transmission spectrum can vary significantly depending on what we assume for the optical properties of the haze. We find that the soot models fit the data as well as our fiducial constant model ($\Delta \text{BIC} \sim 1$ in favor of the soot models); our results are comparable in this case regardless of the value we assume for T_{int} (Figure 5.9). Tholins provide a slightly worse fit ($\Delta \text{BIC} = 28$ and 32 in favor of the constant model for $T_{\text{int}} = 300$ K and 75 K, respectively). This suggests that that the prospective hazes in Kepler-79d’s atmosphere are more absorbing at these wavelengths than their Titan counterparts. For Kepler-79d, CARMA provides a physically motivated forward model that is able to match the planet’s transmission spectrum. It also offers predictions for the transmission spectrum at longer wavelengths that can be tested by

facilities such as the *James Webb Space Telescope (JWST)* (Figure 5.9, right panel) in the future.

Stellar Activity

In this section, we investigate whether or not stellar activity might alter the shape of Kepler-79d’s observed transmission spectrum at a level that would affect our interpretation of these data. Kepler 79 is a $1.3_{-0.4}^{+1.0}$ Gyrs old quiescent late-F type star with a line-of-sight rotational velocity ($v \sin i$) of $14 \pm 1 \text{ km s}^{-1}$ (Fulton & Petigura, 2018; Petigura et al., 2017c). This corresponds to a rotation period $P \leq 4.8$ days, which is typical for main sequence *Kepler* stars with effective temperatures within 2σ of Kepler-79 (i.e. stars with T_{eff} in the range $6389 \pm 120 \text{ K}$; McQuillan et al., 2014). We examined median normalized *Kepler* light curves and found that this star’s peak-to-peak variability is $< 0.2\%$, which is typical for F stars in the *Kepler* sample ($0.13_{-0.06}^{+0.23}\%$; McQuillan et al., 2014; Rackham et al., 2019). Such a low variability amplitude would cause the measured transit depth to vary by less than 5 ppm from one epoch to the next in the *Kepler* band; this is much smaller than the measurement errors for individual *Kepler* transit depths. We see no evidence for any spot crossings in the *Kepler* (and WFC3) transits of Kepler-79d, which has the deepest and best signal-to-noise ratio amongst the four planets. For the other three planets, which have significantly shallower transits, the signal-to-noise ratio for individual transits is too low to provide useful constraints on spot or faculae crossings. We find no evidence for epoch-to-epoch variability in the measured *Kepler* transit depths for Kepler-79d (see § 5.4), in good agreement with the lack of detectable photometric variability and the apparent absence of any spot or faculae occultations.

Although we can place a tight upper limit on Kepler-79’s photometric variability, unocculted spots and faculae that are nearly uniformly distributed in longitude may still introduce a wavelength dependent bias in the transit depths while maintaining a near-constant stellar flux. Spots could remain unocculted if they occur at a specific range of latitudes (similar to the Sun) that the transiting planet does not traverse; this is plausible for the case where the planet’s orbit is well-aligned with the star’s spin axis, but unlikely for planets with nearly pole-on orbits. Although the 100 ppm offset between the measured *Kepler* and *HST* transit depths for Kepler-79d is only marginally significant (2.2σ ; see § 5.4 & 5.4), we can nonetheless use it to place limits on the spot properties of Kepler-79. Regardless of whether or not this

offset is produced by unocculted spots, it gives us a useful metric for what might be considered a significant effect of the star spots on the transmission spectrum of Kepler-79d.

We estimate the fractional area of the star that must be covered by spots (spot coverage fraction ε) for a range of spot temperatures in order to reproduce the ~ 100 ppm offset between the *Kepler* and *HST* depths. To do this, we follow the procedure outlined in Evans et al. (2018) and fit our transmission spectrum assuming that the planet has the same underlying transit depth D in this wavelength range ($0.4 - 1.7\mu\text{m}$), which is then altered by the spots in a wavelength dependent manner to produce the observed depth $D_{\text{obs},\lambda}$:

$$D_{\text{obs},\lambda} = \frac{D}{1 - \varepsilon(1 - F_{\text{spot},\lambda}/F_{*,\lambda})} = \frac{D}{1 - \varepsilon\alpha} \quad (5.4)$$

where $F_{\text{spot},\lambda}$ and $F_{*,\lambda}$ are the stellar intensity profiles (in this case, BT-NextGen stellar models; Allard et al., 2012) for the temperatures corresponding to the spots and the homogeneous stellar surface, respectively, and α is the resulting spot contrast. We fix the stellar surface's temperature to 6389 K and consider spot temperatures that decrease in increments of 500 K up to a temperature difference of 2500 K (i.e. minimum spot temperature of 3889 K). As the spot temperature decreases, the best-fit value of D decreases from 2267 ppm to 2108 ppm and the best-fit ε decreases from 30% (for $T_{\text{spot}} = 5889$ K) to $\sim 15\%$ (for $T_{\text{spot}} \lesssim 4889$ K).

We next ask whether such values for ε are compatible with our upper limit on the observed photometric variability of Kepler-79 in the *Kepler* bandpass. Unfortunately, the predicted photometric variability is degenerate with the assumed spot properties including temperature and size. Nonetheless, for random distribution of spots in longitude, we can expect the variability amplitude to scale as $\alpha\Omega\sqrt{n}$, where Ω is the solid angle of a spot and n is the number of spots (Rackham et al., 2019). To pin this relationship to an absolute value of the variability amplitude, we use the *Kepler* variability amplitude determined by Rackham et al. (2019) for a specific spot temperature and size. For a spot temperature of ~ 4290 K (based on scaling from spot temperatures for stars in the spectral range G1–M3), spot size of 2° (covering 100 ppm of the entire stellar surface; based on observations of large spot groups on the Sun), and $\varepsilon = 15\%$ (required by our fits to produce a 100 ppm offset between the *Kepler* and *HST* bandpasses), Kepler-79 should display variability in the *Kepler* bandpass with an amplitude of $1.8_{-0.6}^{+0.8}\%$. This value is an order of magnitude

larger than the upper limit of $< 0.2\%$ that is inferred from *Kepler* observations of Kepler-79.

Keeping the spot size the same and varying only the spot temperature (and consequently α), we find that an order of magnitude decrease in variability amplitude requires a spot temperature of ~ 6239 K (150 K cooler than the stellar photosphere) and an implausibly large $\varepsilon = 82\%$. This value of ε is large enough that it would significantly affect the spectral characterization of Kepler-79. Conversely, for a fixed spot temperature of ~ 4389 K and fixed $\varepsilon = 15\%$, the spots' Ω would need to be roughly two orders of magnitude smaller (corresponding to ~ 1 ppm of the stellar surface) to be consistent with our upper limit on the observed variability amplitude. The reduction in Ω is roughly two orders of magnitude rather than one because reducing Ω while keeping ε fixed also leads to an increase in the spot number n , which acts to offset the effect of reducing Ω on the variability amplitude. A spot covering 1 ppm of the stellar surface would be comparable in size to a single granule on the surface of Kepler-79 (using scaling relationships from Freytag et al., 1997; Trampedach et al., 2013; Tremblay et al., 2013). We might expect that spots on Kepler-79 would be smaller than those on the Sun, as it rotates faster and has a thinner outer convective zone (spot area $\propto \omega^{-1} (\rho_b/\rho_t)$, where ω is the rotational frequency, and ρ_b and ρ_t are the densities at the base and the top of the outer convective zone; Giampapa & Rosner, 1984; Schmitt & Rosner, 1983), but spots this small are close to the physically plausible limit for Kepler-79, and therefore seem unlikely in practice. Even if they are present with a coverage fraction ε of 15%, corresponding to the maximum coverage fraction consistent with the observed *Kepler* variability amplitude, these spots would only produce a 100 ppm (2.2σ) offset between the measured *Kepler* and *HST* transit depths.

In the end, we find no evidence to suggest that stellar activity has appreciably altered the measured shape of Kepler-79b's transmission spectrum. Furthermore, allowing for the potential presence of spots does not lead to a material change in our picture of Kepler-79d's atmosphere. If spots are present, they might marginally influence our inferences regarding the haze particle size distribution by changing the slope of the spectrum, but they cannot render the existence of haze particles unnecessary. These haze particles are required to explain the featureless WFC3 spectrum (§ 5.4) and their presence at low pressures is also needed to reconcile Kepler-79b's predicted mass loss rate with its atmospheric lifetime (§ 5.4). Future observations at longer infrared wavelengths with *JWST* will be even less sensitive to the potential presence

of spots and will place much tighter constraints on the underlying particle size distribution in Kepler-79d’s atmosphere.

Implications of Mass Loss for Puffy Planets

The extended atmospheres and low surface gravities of super-puffs make them vulnerable to catastrophic mass loss. The question of how their inferred mass loss histories can be reconciled with their present-day ages is a matter of considerable debate. One promising idea put forward by Wang & Dai (2019) and Gao & Zhang (2020) is that the measured radii of super-puffs are inflated by the presence of dust particles lofted by the atmospheric outflow ($\tau \sim 1$ at tens of μbar , see Figure 5.8). If these planets are systematically smaller and denser than their observed radii would seem to suggest, it would significantly reduce the estimated mass loss rates. Here, we investigate whether or not this mechanism suffices to explain the observed properties of low-density planets from the *Kepler* survey. We select a sample of systems from the TTV catalogue of Hadden & Lithwick (2017) that have robust mass determinations (robust flag = 1) and updated stellar parameters from Gaia (Fulton & Petigura, 2018). Since TTV fits constrain the planet to star mass ratios, we update the corresponding planet masses using the new stellar masses from Gaia². We then select the subsample of planets with masses $< 100 M_{\oplus}$ and bulk density $< 1 \text{ g cm}^{-3}$. These limits are generous enough to ensure that we do not exclude any potential super-puffs from this sample. Table 5.6 shows some key properties for the planets in our sample.

We calculate the expected mass loss rate, \dot{M} , for each of these planets using the isothermal Parker wind model (Parker, 1958)³:

$$\dot{M} = 4\pi r_s^2 c_s \rho_p \exp(3/2 - 2r_s/R_p) \quad (5.5)$$

where $c_s = \sqrt{k_B T_{\text{eq}}/\mu}$ is the isothermal sound speed, k_B is the Boltzmann constant, and μ is the mean molecular weight of the atmosphere (fixed to 2.2 here), respectively. ρ_p is the atmospheric density at the measured planet radius R_p , and we calculate it by assuming that R_p corresponds to a pressure of 10 mbar or 10

²Fulton & Petigura (2018) note that the uncertainties on these stellar masses are likely to be underestimated as they are obtained by fitting isochrones. Nonetheless, the updated estimates are likely to be more accurate than the previously published values for these systems and we therefore adopt them in this study.

³We find that the photoevaporation mass loss rate is smaller than the Parker wind mass loss rate for part of our sample that is vulnerable to catastrophic mass loss. The handful of planets for which photoevaporation dominates are quite massive (10s of M_{\oplus}) and the mass loss rate is too small to be significant.

Table 5.6: Planet properties for our ‘Puffy’ planets sample

Name	Mass ^a (M_{\oplus})	Radius ^b (R_{\oplus})	Density (g/cc)	Semimajor Axis ^b (AU)	Incident Stellar Flux ^b (F_{\oplus})	Age ^b (Gyrs)	$\log_{10}(\text{AtmosphericLifetime/Gyrs})$
Kepler-9 b	43.2 ^{+1.3} _{-1.2}	8.1 ± 0.2	0.45 ^{+0.04} _{-0.03}	0.1418 ± 0.0012	47.2 ± 3.2	1.8 ^{+1.5} _{-1.2}	2.9 ^{+0.3} _{-0.6}
Kepler-9 c	29.7 ^{+0.6} _{-0.8}	8.1 ± 0.2	0.31 ^{+0.03} _{-0.02}	0.2266 ± 0.0019	18.5 ± 1.2	1.8 ^{+1.5} _{-1.2}	2.9 ^{+0.3} _{-0.6}
Kepler-11 e	7.3 ^{+1.1} _{-1.1}	4.0 ± 0.1	0.61 ^{+0.11} _{-0.10}	0.1964 ± 0.0022	30.3 ± 2.1	6.5 ^{+1.6} _{-1.8}	2.6 ^{+0.2} _{-0.2}
Kepler-11 f	1.9 ^{+0.3} _{-0.4}	2.8 ± 0.2	0.46 ^{+0.17} _{-0.13}	0.2526 ± 0.0029	18.3 ± 1.3	6.5 ^{+1.8} _{-1.8}	-0.6 ^{+2.1} _{-1.8}
Kepler-18 d	14.8 ^{+2.7} _{-4.0}	5.1 ± 0.1	0.60 ^{+0.13} _{-0.12}	0.1177 ± 0.0010	46.5 ± 3.2	2.0 ^{+1.8} _{-1.7}	2.1 ^{+0.4} _{-1.0}
Kepler-33 d	4.3 ^{+2.0} _{-2.0}	4.5 ± 0.1	0.25 ^{+0.12} _{-0.12}	0.1626 ± 0.0022	109.8 ± 8.3	4.8 ^{+1.4} _{-0.6}	-0.5 ^{+3.3} _{-3.2}
Kepler-33 e	6.1 ^{+1.1} _{-1.0}	3.5 ± 0.1	0.79 ^{+0.17} _{-0.15}	0.2092 ± 0.0028	66.4 ± 5.1	4.8 ^{+1.4} _{-0.6}	2.1 ^{+0.3} _{-0.2}
Kepler-36 c	7.7 ^{+0.3} _{-0.2}	4.0 ± 0.1	0.68 ^{+0.08} _{-0.07}	0.1269 ± 0.0009	190.3 ± 12.7	7.4 ^{+0.5} _{-0.5}	2.0 ^{+0.1} _{-0.1}
Kepler-33 f	10.6 ^{+1.6} _{-1.5}	3.9 ± 0.1	0.95 ^{+0.18} _{-0.16}	0.2480 ± 0.0033	47.2 ± 3.6	4.8 ^{+1.4} _{-0.6}	3.1 ^{+0.2} _{-0.2}
Kepler-51 b ^c	3.5 ^{+1.8} _{-1.5}	6.9 ± 0.1	0.06 ^{+0.03} _{-0.03}	0.2423 ± 0.0013	10.7 ± 0.8	0.5 ^{+0.3} _{-0.2}	-0.8 ^{+2.4} _{-2.9}
Kepler-51 c ^c	4.2 ^{+0.5} _{-0.5}	9.0 ± 2.8	0.03 ^{+0.06} _{-0.07}	0.3702 ± 0.0020	4.6 ± 0.3	0.5 ^{+0.3} _{-0.2}	0.8 ^{+0.7} _{-0.8}
Kepler-51 d ^c	5.4 ^{+1.1} _{-0.9}	9.5 ± 0.2	0.03 ^{+0.07} _{-0.07}	0.4907 ± 0.0026	2.6 ± 0.2	0.5 ^{+0.3} _{-0.2}	1.4 ^{+0.7} _{-0.7}
Kepler-79 d ^d	5.3 ^{+0.9} _{-0.9}	7.2 ± 0.2	0.08 ^{+0.01} _{-0.01}	0.2937 ± 0.0027	30.0 ± 2.1	1.3 ^{+1.0} _{-0.4}	0.4 ^{+1.3} _{-0.3}
Kepler-79 e ^d	3.8 ^{+0.7} _{-0.6}	3.5 ± 0.2	0.48 ^{+0.06} _{-0.30}	0.3945 ± 0.0037	16.6 ± 1.2	1.3 ^{+1.0} _{-0.4}	1.5 ^{+0.4} _{-0.4}
Kepler-89 c	8.8 ^{+3.0} _{-2.0}	3.9 ± 0.1	0.84 ^{+0.30} _{-0.23}	0.0986 ± 0.0008	252.2 ± 15.9	3.5 ^{+0.6} _{-0.6}	1.5 ^{+0.6} _{-0.4}
Kepler-89 d	62.1 ^{+10.3} _{-10.8}	10.1 ± 1.6	0.33 ^{+0.24} _{-0.13}	0.1640 ± 0.0013	91.2 ± 5.8	3.5 ^{+0.6} _{-0.6}	3.4 ^{+0.3} _{-0.3}
Kepler-177 b	5.0 ^{+0.8} _{-0.8}	4.5 ± 0.4	0.30 ^{+0.11} _{-0.08}	0.2110 ± 0.0018	38.1 ± 3.5	11.7 ^{+1.1} _{-1.0}	2.4 ^{+0.2} _{-0.2}
Kepler-177 c	12.2 ^{+2.4} _{-2.3}	9.3 ± 0.4	0.08 ^{+0.02} _{-0.02}	0.2566 ± 0.0022	25.8 ± 2.3	11.7 ^{+1.1} _{-1.0}	3.0 ^{+0.2} _{-0.2}
Kepler-223 b	3.7 ^{+1.8} _{-2.0}	2.8 ± 0.2	0.88 ^{+0.34} _{-0.48}	0.0752 ± 0.0008	414.4 ± 57.1	8.9 ^{+1.1} _{-1.0}	-2.6 ^{+3.5} _{-3.6}
Kepler-223 c	12.1 ^{+2.6} _{-2.7}	4.3 ± 0.8	0.79 ^{+0.69} _{-0.34}	0.0912 ± 0.0009	281.3 ± 38.2	8.9 ^{+1.1} _{-1.0}	2.4 ^{+0.4} _{-0.4}
Kepler-223 d	5.9 ^{+1.9} _{-1.8}	5.9 ± 0.8	0.15 ^{+0.10} _{-0.06}	0.1196 ± 0.0012	163.8 ± 22.4	8.9 ^{+1.1} _{-1.0}	-0.6 ^{+2.5} _{-2.1}
Kepler-359 c	2.7 ^{+1.9} _{-1.4}	4.1 ± 0.5	0.21 ^{+0.19} _{-0.11}	0.2744 ± 0.0033	8.1 ± 1.3	6.3 ^{+4.2} _{-4.0}	1.7 ^{+7.1} _{-4.9}
Kepler-359 d	2.7 ^{+1.8} _{-1.3}	4.6 ± 0.9	0.15 ^{+0.19} _{-0.09}	0.3329 ± 0.0040	5.5 ± 0.9	6.3 ^{+4.2} _{-4.0}	1.4 ^{+7.3} _{-4.7}

Notes.

^aMass estimates are obtained by using mass ratio posteriors from Hadden & Lithwick (2017) unless otherwise specified and stellar mass estimates from Fulton & Petigura (2018).

^bValues from Fulton & Petigura (2018). The only parameter for which asymmetric error bars are important is stellar age.

^cMass ratio posteriors, planetary radii, and stellar age from Libby-Roberts et al. (2020).

^dMass ratio posteriors and radius estimate from this study.

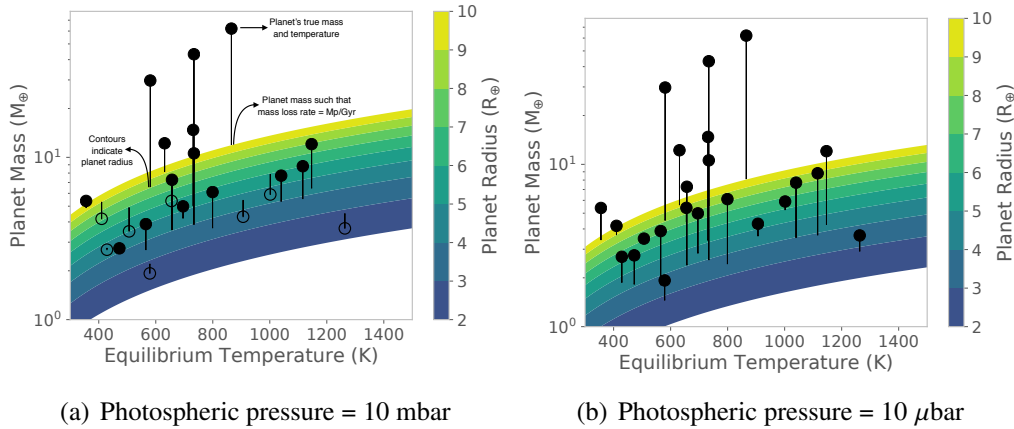


Figure 5.10: Planet mass vs equilibrium temperature. The contours correspond to planetary radii for which Parker wind mass loss rates would be equal to $M_p \text{ Gyr}^{-1}$. Planets with a mass loss rate smaller (larger) than this value are plotted with filled (empty) circles. Vertical lines originating from the scatter points terminate at the planet mass value for which the mass loss rate would be $M_p \text{ Gyr}^{-1}$ (keeping the planet radius and equilibrium temperature constant). Kepler-79d is plotted at 630 K and $5.3 M_\oplus$ and changes from being an open to a filled circle when the photospheric pressure is changed.

μ bar (Figure 5.10). The usage of T_{eq} as the local temperature here is acceptable for this pressure range. The sonic radius $r_s = GM_p/2c_s^2$, where M_p is the planet mass and G is the gravitational constant. For a range of planet masses and equilibrium temperatures, we calculate the planet radii that would yield a mass loss rate of $M_p \text{ Gyr}^{-1}$. Although a planet's envelope mass is more relevant than the total mass for mass loss estimates, the envelope mass should roughly scale with the total mass⁴. Planets in our sample are overplotted with filled ($\dot{M} < M_p \text{ Gyr}^{-1}$) and empty ($\dot{M} > M_p \text{ Gyr}^{-1}$) circles. For each planet's radius and equilibrium temperature, we calculate the mass, $M_{\text{perpetual}}$, it would need to possess for \dot{M} to be equal to $M_p \text{ Gyr}^{-1}$. The values of $M_{\text{perpetual}}$ are the end points of vertical lines connected to the filled and empty circles. The length of these lines is an indicator of how much larger or smaller the planets' mass loss rates are relative to $M_p \text{ Gyr}^{-1}$ and therefore becomes a proxy for the atmospheric lifetimes. Figure 5.10 shows that moving the transit radius to lower pressures can significantly increase the inferred atmospheric lifetimes, resolving the apparent tension between the predicted mass loss rates and reported ages for these objects.

⁴We performed the same analysis for a mass loss rate of $0.1M_p \text{ Gyr}^{-1}$ ($M_{\text{env}} \sim 0.1M_p$ is representative of puffy planets, e.g. Lopez & Fortney, 2014) and found no qualitative differences in our inferences.

To estimate planet specific impact of mass loss, we calculate the atmospheric lifetime for each planet. First, we calculate the expected envelope mass fraction from the tables of Lopez & Fortney (2014) for a given planet mass, radius, stellar insolation, and age. Instead of assuming that the photosphere lies at 20 mbar as Lopez & Fortney (2014) do, we set the measured radius to correspond to a pressure of 10 μ bar and calculate the 20 mbar radius by using the planetary isothermal scale height. This leads to a significantly lower envelope mass fraction estimate as our 20 mbar radius is smaller than the observed planetary radius. Lopez & Fortney (2014) only provide tables for envelope mass fractions between 0.01% and 20%. For planets that require an envelope mass fraction higher than 20% or lower than 0.01% to match their mass and radius, we set it to these bounding limits instead. In addition, for any planet mass or age value that lies beyond the grid limits in Lopez & Fortney (2014), we set it to nearest value that is present in their tables.

The mass loss rate for each planet is calculated using both Parker wind and photoevaporation models and we then use the dominant mechanism to estimate the atmospheric lifetime. Mass loss due to photoevaporation is calculated using the standard energy limited prescription (e.g. Salz et al., 2016b; Watson et al., 1981):

$$\dot{M} = \frac{\epsilon \pi F_{\text{XUV}} R_{\text{XUV}}^3}{GM} \quad (5.6)$$

where F_{XUV} is the high energy flux received from the star (taken from Ribas et al., 2005⁵), R_{XUV} is the typical radius at which this flux is absorbed (radius corresponding to pressure of 10 nbar, estimated using the planet’s isothermal scale height), G is the gravitational constant, M is the planet’s mass, and $\epsilon = 0.1$ is an ‘efficiency’ parameter that encapsulates the complicated process of conversion of photon energy to kinetic and thermal energy of the wind. We obtain posteriors for the atmospheric lifetime by using posterior distributions for all the relevant input parameters (shown in Table 5.6) except the atmospheric mass fraction. Calculating the atmospheric mass fraction for all our posterior samples would impose a large computational overhead. Using a smaller sample size, we find that for the majority of planets in our sample, the 84th percentile and the 16th percentile value for the atmospheric mass fraction differ only by a factor of 2. This factor is more than an order of magnitude

⁵Although the relationship provided by Ribas et al. (2005) is applicable only to G stars, in the absence of such information for other stellar types, we use it for all the stars in our sample. The fact that we use the planet’s semimajor axis to estimate F_{XUV} does compensate for differences in spectra of different stellar types to a certain extent. For example, for later type stars, the bolometric luminosity at a given semimajor axis is lower but the fraction of energy emitted in the XUV is higher compared to G stars.

only for the planets for which we cannot place tight meaningful constraints on the atmospheric lifetime due to imprecise planetary properties.

Figure 5.11 shows how the median atmospheric lifetime of our sample compares with the planetary (stellar) ages. A majority of the planets that have atmospheric lifetimes longer than their ages are most susceptible to photoevaporative mass loss. In contrast, Parker winds drive the envelope loss for all the low density planets that have atmospheric lifetime shorter than their ages. It is worth noting that the uncertainty on the atmospheric lifetime (not shown for clarity) for most planets is so large that they are $< 1\sigma$ away from the atmospheric lifetime and age equality. We therefore caution the reader to not use this plot to draw inferences regarding any trends in atmospheric lifetime with host star age or planet density. This plot simply shows that the median atmospheric lifetimes for all but a handful of these planets are larger than their present-day ages. The calculated atmospheric lifetimes and the corresponding 1σ uncertainties are listed in Table 5.6.

Within this parameter space, Kepler-51 b, Kepler-223 b and d, Kepler-33 d, and Kepler-11 f stand out as some of the shortest-lived puffy planets. For Kepler-51 b, we find that using the updated mass values from Libby-Roberts et al. (2020) increases the median atmospheric lifetime by almost 3 orders of magnitude for just a 50% increase in median planet mass. This is a result of the exponential sensitivity of Parker wind mass loss rate to planet mass. Similarly, Kepler-11 f's low atmospheric lifetime is a consequence of the fact that it is the lowest mass puffy planet in our sample. The continued cooling and contraction of Kepler-51 b (which likely still possesses its heat of formation) as it ages would also reduce the inferred mass loss rate at later times (see Libby-Roberts et al., 2020). Interestingly, Kepler-223 and Kepler-33 have inflated stellar radii and are evolving off the main sequence (in fact it is their evolution off the main sequence that allows us to measure their ages much more precisely than for typical main sequence stars). Their planets therefore may have recently started losing significant mass in response to the increasing luminosity of their host stars. The planets' current mass loss rates are likely to be significantly larger than during the main sequence phase of the host stars. Hence, the incompatibility between their atmospheric lifetimes and age does not necessarily pose a contradiction. For planets with very high mass loss rates (such as Kepler-51 b), the outflowing wind may loft hazes to pressures as low as 10 – 100 nbar (Gao & Zhang, 2020), increasing their apparent size and the corresponding atmospheric lifetime by 2 – 3 orders of magnitude relative to the 10 μ bar case.

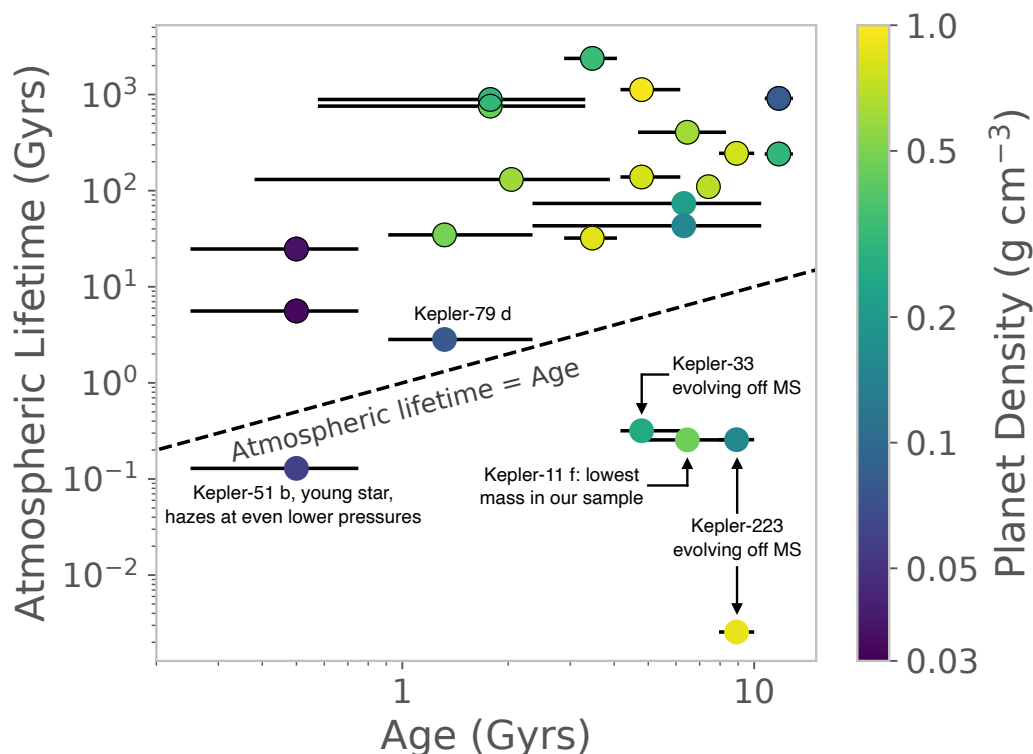


Figure 5.11: Atmospheric lifetime versus planet (stellar) age obtained from Fulton & Petigura (2018). Atmospheric lifetime is calculated by dividing the envelope mass fraction inferred from Lopez & Fortney (2014) with the mass loss rate from either photoevaporation or Parker wind (whichever one is larger, photoevaporation dominated planets circled with black outline). Due to large uncertainties in planetary properties, the uncertainties on the atmospheric lifetime (not shown) are large enough that most planets lie $< 1\sigma$ away from the atmospheric lifetime = age dashed line.

Another physical explanation that has recently been used to explain the large radii of super-puffs without invoking large envelope mass fraction is tidal heating (Millholland, 2019). Here, we briefly comment on the consequences of this model for the atmospheric lifetime of super-puffs, with a particular emphasis on the case of Kepler-79d. Supplementing the internal luminosity of the planet with tidal heating leads to a significant decrease in envelope mass fraction (e.g., a factor of 3 decrease for Kepler-79d for a haze free atmosphere; Millholland, 2019) without necessarily affecting the atmospheric mass loss rate significantly. Atmospheres of tidally-heated super-puffs that are haze-free or have a haze at 10 mbar are then even more vulnerable to envelope loss than super-puffs without tidal heating. For an atmospheric haze at 10 μ bar, our CARMA models indicate that the envelope mass fraction for a

tidally heated Kepler-79d ($T_{\text{int}} = 300$ K) is nearly 30 times lower than that for the model without tidal heating ($T_{\text{int}} = 75$ K). This order of magnitude decrease in the envelope mass fraction almost nullifies the advantage of placing hazes at $10\mu\text{bar}$ to reconcile mass loss history with atmospheric lifetime. This suggests that tidal heating may not play a key role in the super-puff story, especially for longer period super-puffs such as Kepler-79d. Instead, tidal heating is likely to be more important for the population of low-density planets with close-in orbits (e.g. $P \lesssim 30$ days) and moderate eccentricities, as shown in Millholland et al. (2020). It is worth noting that our analysis only provides a weak and indirect constraint on models with tidal heating. Nevertheless, it could be a valuable and independent semi-observational test for such models in the future.

It has previously been suggested that the high inferred mass loss rates for super-puffs might stem from incorrect mass loss rate prescriptions or incorrect values for planet mass or temperature (Cubillos et al., 2017). We note two caveats in the mass loss prescriptions we use in this work. Firstly, we assume an isothermal Parker wind structure for the outflow driven by the bolometric flux of the star and this gives us an upper limit on the mass loss rate. If the outflow cools as it propagates outwards, the mass loss rate would be lower. Secondly, the exact mass loss rate is sensitive to the assumed atmospheric structure. Mass loss models often assume an inner adiabat with adiabatic index of $7/5$ that either extends to the photosphere (Gao & Zhang, 2020) or transitions to an isothermal layer or an wind-launching surface (Wang & Dai, 2018). Such structure maximizes the rate of mass loss as the atmospheric mass is outwardly concentrated (Lee et al., 2018). At formation, a more realistic adiabatic index for super-puffs is ~ 1.2 which gives rise to inwardly concentrated mass profile (Lee & Chiang, 2016; Lee et al., 2014). Self-consistent treatment with the evolving inner adiabat for super-puffs is yet to be conducted. Notwithstanding these limitations, we note that atmospheric mass loss models have been relatively successful to date in matching the measured mass loss rates for transiting gas giant planets (e.g. Odert et al., 2019; Salz et al., 2016a, 2018) as well as the bimodality in the radius distribution of the sub-Neptune-sized planets in the *Kepler* sample (Fulton et al., 2017; Lopez & Fortney, 2013; Owen & Wu, 2017), making it unlikely that our mass loss rates are incorrect by many orders of magnitude.

Similarly, it would require an implausibly large reduction in the planetary temperature (corresponding to albedos as high as those of the icy moons in the solar system; see also Cubillos et al., 2017) to reconcile the predicted mass loss rates with plan-

etary ages. Mass estimates, on the other hand, can be quite uncertain for many of these planets (the median fractional uncertainty in planet mass for our sample is 21%) and the mass loss rate is quite sensitive to the assumed value (Equation 5.5). It is evident from Table 5.6 that planets with uncertain masses have a 1σ range in atmospheric lifetime that spans many orders of magnitude. Therefore, until the masses of these planets are more precisely determined⁶, we cannot dismiss outright the possibility that uncertainties in planet mass might also contribute to the apparently short atmospheric lifetimes of some super-puffs.

5.5 Future Directions and Conclusions

In this work, we present new observational constraints on the properties of Kepler-79d, a quintessential super-puff. Our revised planet mass further cements its status as a low density planet. The availability of *Kepler* and *HST* data as well as the relatively low activity level of the host star allows us to constrain the atmospheric scattering signature across optical and infrared wavelengths. We find that the transmission spectrum does not contain any statistically significant absorption signatures and is consistent with a flat line. Our data rule out both metal-enriched cloud free models and metal-poor models with only collision-induced absorption and Rayleigh scattering from hydrogen and helium. We therefore conclude that Kepler-79d most likely hosts a high-altitude haze. We use CARMA models that incorporate haze entrainment by an outflowing wind to show that the resultant transmission spectrum provides a reasonable fit to the data. The shift of the slant photosphere to lower pressures reduces the amount of primordial gas required to match the planet’s bulk density and lengthens the atmospheric lifetime by decreasing the mass loss rate. We also show that this effect of reducing the photospheric pressure significantly affects our mass loss inferences for low density planets in the *Kepler* sample and tends to reconcile planetary ages with their current primordial envelope content.

Super-puffs are an enigmatic and exciting sub-population of the *Kepler* planets. Their minuscule bulk densities pose difficult challenges for planet formation theories and atmospheric evolution models. It remains to be seen whether they are ringed planets (Piro & Vissapragada, 2020), typical super-Earths with large internal heat fluxes (Millholland, 2019), or planets with large primordial atmospheric content (e.g. Lee & Chiang, 2016; Lopez & Fortney, 2014). Hazes seem likely to be a

⁶With the advent of the *Gaia* era, the planet mass uncertainties are dominated by the uncertainties in the mass ratios obtained from TTV fits rather than the uncertainties in stellar masses. The only exceptions to this in our sample are Kepler-9 (fractional stellar mass uncertainty twice that of mass ratio’s) and Kepler-36 (fractional stellar mass and mass ratio uncertainties comparable).

part of the super-puff story, as they may simultaneously explain their transmission spectra (Libby-Roberts et al., 2020) and the mass loss history (Gao & Zhang, 2020; Wang & Dai, 2019). High-altitude hazes also have the advantage of offering a more universal explanation for the properties of super-puff atmospheres compared to the other hypotheses. Follow up studies are critical for making further inferences but the dimness of the *Kepler* super-puff hosts has hitherto limited our ability to do so. This is likely to change with the advent of the *JWST* era with its increased sensitivity and access to a broad and optimal wavelength range for targeting super-puff atmospheres. *JWST* observations will provide data that are truly diagnostic and powerful at distinguishing between different models. The discovery of super-puffs around bright nearby host stars will also provide us with significantly more favorable targets for atmospheric characterization (e.g. Santerne et al., 2019).

Chapter 6

CONCLUSIONS

In this thesis, I have shown how dust plays a fundamental role in planet formation and evolution processes that span a timescale of billions of years. Planets are thought to form by first assembling rocky/icy cores that form from the dust in protoplanetary disks. In Chapter 2, I demonstrated that the emerging paradigm of pebble accretion for giant planet core formation is fully compatible with the observed correlation between cold giant planets and inner super-Earths. Dust transport in protoplanetary disks is central to the emergence of this theoretical compatibility.

Going forward, there is a need to study the formation of close-in super-Earths within the outer giant planet's orbit more carefully. Our study simply shows that the mass needed to form super-Earths in the inner disk is available. The timescale over which this dust mass is converted into planetesimals and eventually super-Earths needs to be investigated. This will shed some light on when during the evolution of the disk super-Earths emerge. Another promising avenue to explore further is the effect of changing the stellar type on the ability of super-Earths and giant planets to form and co-exist. Since the efficiency with which a growing core accretes pebbles is sensitive to the stellar mass and temperature structure of the disk, a comparison of the dust budget of disks with dust mass required to form giant planet cores and super-Earths can shed light on the dependence of their occurrence rate on stellar type.

Dust also controls the rate at which growing planets can accrete gas as it strongly influences the gas' cooling rate. In Chapter 3, I again elicited the role of dust transport in creating regions with disparate environments for gas accretion. In particular, rapid radial drift of dust grains at intermediate distances lead to a region with low dust-to-gas ratio between $\sim 1 - 10$ au. These large variations in the ability of cores to accrete gas might explain why giant planet occurrence peaks at intermediate distances and why close-in super-Earth cores do not undergo runaway gas accretion.

The results of this study need to be extended to account for possible variation in the underlying core mass distribution of super-Earths and giant planets. The combination of the location dependence of the core mass distribution and gas accretion rates

will be critical for determining the root cause behind the occurrence rate profile of giant planets and for predicting super-Earth and sub-Neptune occurrence rates beyond the water snowline. An additional complication that should be addressed in future work is the effect of pressure bumps (induced by embedded planets or by some other phenomena) on the conclusions of this study. Since disk substructures appear to be universal, it is important to understand how they affect the global evolution of the disk's dust-to-gas ratio and consequently the gas accretion rates of planetary cores. Finally, a deeper understanding of dust dynamics and accretion while accounting for the 3D gas flows around an embedded planet is sorely needed. Theoretical and observational advancements suggest the presence of a meridional flow that brings small dust grains from high above the disk midplane to a planet's Hill sphere and circumplanetary disk. The subsequent evolution and accretion of dust onto the planet remain poorly understood. The discovery of actively accreting planets in the PDS 70 system provides us with an opportunity to observe the evolution of accreted dust in infalling gas and compare it with theoretical models.

The simultaneous accretion of dust and gas is expected to influence planetary envelope composition. Since the accretion rate of dust is dependent on the planet's environment, measurements of envelope composition can be useful tracers for formation history. Neptune-class planets are most likely to display their formation history in this way because they stop growing in the process of becoming a gas giant. In Chapter 4, I study one such promising warm-Neptune, HAT-P-11b. I constructed and analyzed its transmission spectrum over a wide wavelength range to find that its envelope metal content is strikingly low. Its low metallicity is testament to the diversity of atmospheric compositions and originations of Neptunes.

Further progress on relating atmospheric metallicity to formation history requires both observational and theoretical advances. Observationally, we need significantly better precisions for the measured atmospheric metallicity to pin down the formation histories. In addition, it would be useful to base the metallicity constraints on more than one atmospheric molecule to obtain more reliable estimates of the composition. Both of these objectives will be realized with data from *JWST*. Theoretically, there is a need to further establish links between envelope metallicity and formation conditions for Neptunes. The local solid surface density influences the bulk and atmospheric metallicities as well as the metallicity profile as a function of planetary radius. A broad parameter study that relates formation conditions to planetary metallicity would therefore be useful. Moreover, there is a need to study the thermal

and compositional evolution of planets with compositional gradients. Recent studies suggest that convective mixing can progressively homogenize the envelope outside-in. It is therefore important to evaluate mixing's impact on our ability to relate formation history and envelope composition.

Finally, dust in the form of aerosols is nearly ubiquitous in planetary atmospheres, where it affects the temperature structure and the spectral features of the atmosphere. In Chapter 5, we argue that there is compelling evidence for the presence of aerosols in the atmosphere of super-puff Kepler-79d. As an archetypal super-puff, Kepler-79d has a very low bulk density. Instead of observing large atmospheric absorption features as we might expect, we observe a featureless spectrum that is best fit by a straight line. In addition, the low surface gravity of Kepler-79d would suggest that it would lose its envelope age but it manages to retain it. To solve this riddle, we test the hypothesis that the actual mass loss rate is lower because of a lower pressure at the photosphere of the planet. We find that aerosols that get entrained in the planetary outflow can easily get transported to low pressures and reconcile the mass loss rate with Kepler-79d's age. Moreover, this holds true for the larger population of super-puffs.

One key question that needs to be answered is what might be driving these super-puff outflows. Although the outflows only require a small fraction of the incident bolometric flux to be converted into heat, it is unclear how this happens in practice. Photoevaporation due to heating and ionization of hydrogen and helium that drives outflows on close-in planets is not a viable mechanism for super-puffs as they orbit their stars at greater distances. Here again, dust in the outflow might hold the key if electrons knocked out from dust particles by high energy photons are heating the ambient gas and driving the outflow. Observational confirmation of the presence of aerosols is also necessary to establish this widely held theoretical picture of super-puff atmospheres and for testing whether planetary rings or high internal heat flux are responsible for their low bulk densities. The extended scale heights of super-puffs also make them ideal laboratories for studying aerosol properties. *JWST* is set to observe two super-puffs and obtain their spectra across the entire near-infrared spectral range ($0.6 - 5\mu\text{m}$) in Cycle 1. These observations will prove revolutionary for the study of super-puffs and planetary aerosols at large. They will shed an unprecedented light on aerosol size distribution and composition in an exoplanetary atmosphere for the first time.

Bibliography

- Ackerman, A. S., & Marley, M. S. 2001, *The Astrophysical Journal*, 556, 872
- Adams, D., Gao, P., de Pater, I., & Morley, C. V. 2019, *The Astrophysical Journal*, 874, 61
- Adcroft, A., Campin, J.-M., Hill, C., et al. 2004, *Monthly Weather Review*, 132, 2845
- Agol, E., Luger, R., & Foreman-Mackey, D. 2020, *The Astronomical Journal*, 159, 123
- Akimkin, V., Vorobyov, E., Pavlyuchenkov, Y., & Stoyanovskaya, O. 2020, *Monthly Notices of the Royal Astronomical Society*, 499, 5578
- Alam, M. K., Nikolov, N., López-Morales, M., et al. 2018, *The Astronomical Journal*, 156, 298
- Alexander, D. R., & Ferguson, J. W. 1994a, *International Astronomical Union Colloquium*, 146, 149
- . 1994b, *The Astrophysical Journal*, 437, 879
- Alibert, Y., Venturini, J., Helled, R., et al. 2018, *Nature Astronomy*, 2, 873
- Allard, F., Homeier, D., & Freytag, B. 2012, *Philosophical Transactions of the Royal Society of London Series A*, 370, 2765
- Allart, R., Bourrier, V., Lovis, C., et al. 2018, *Science*, eaat5879
- Andrews, S. M. 2015, *Publications of the Astronomical Society of the Pacific*, 127, 961
- Andrews, S. M., Rosenfeld, K. A., Kraus, A. L., & Wilner, D. J. 2013, *The Astrophysical Journal*, 771, 129
- Andrews, S. M., Huang, J., Pérez, L. M., et al. 2018, *The Astrophysical Journal*, 869, L41
- Ansdell, M., Williams, J. P., van der Marel, N., et al. 2016, *The Astrophysical Journal*, 828, 46
- Asplund, M., Grevesse, N., Sauval, A. J., & Scott, P. 2009, *Annual Review of Astronomy and Astrophysics*, 47, 481
- Astropy Collaboration, Robitaille, T. P., Tollerud, E. J., et al. 2013, *Astronomy & Astrophysics*, 558, A33
- Astropy Collaboration, Price-Whelan, A. M., Sipőcz, B. M., et al. 2018, *The Astronomical Journal*, 156, 123

- Ataiee, S., Baruteau, C., Alibert, Y., & Benz, W. 2018, *Astronomy & Astrophysics*, 615, A110
- Bakos, G. Á., Torres, G., Pál, A., et al. 2010, *Astrophysical Journal*, 710, 1724
- Banzatti, A., Pinilla, P., Ricci, L., et al. 2015, *The Astrophysical Journal Letters*, 815, L15
- Barbato, D., Sozzetti, A., Desidera, S., et al. 2018, *Astronomy & Astrophysics*, 615, A175
- Baron, F., Lafrenière, D., Artigau, É., et al. 2019, *The Astronomical Journal*, 158, 187
- Batalha, N. M., Rowe, J. F., Bryson, S. T., et al. 2013, *The Astrophysical Journals*, 204, 24
- Batygin, K., & Brown, M. E. 2010, *The Astrophysical Journal*, 716, 1323
- Bell, K. R., & Lin, D. N. C. 1994, *The Astrophysical Journal*, 427, 987
- Benítez-Llambay, P., Masset, F., Koenigsberger, G., & Szulágyi, J. 2015, *Nature*, 520, 63
- Benneke, B., & Seager, S. 2012, *The Astrophysical Journal*, 753, 100
- . 2013, *The Astrophysical Journal*, 778, 153
- Benneke, B., Knutson, H. A., Lothringer, J., et al. 2019a, *Nature Astronomy*, 3, 813
- Benneke, B., Wong, I., Piaulet, C., et al. 2019b, *The Astrophysical Journal Letters*, 887, L14
- Berta, Z. K., Charbonneau, D., Désert, J.-M., et al. 2012, *The Astrophysical Journal*, 747, 35
- Béthune, W., & Rafikov, R. R. 2019, *Monthly Notices of the Royal Astronomical Society*, 488, 2365
- Birnstiel, T., Andrews, S. M., Pinilla, P., & Kama, M. 2015, *The Astrophysical Journal Letters*, 813, L14
- Birnstiel, T., Dullemond, C. P., & Brauer, F. 2010, *Astronomy & Astrophysics*, 513, A79
- Birnstiel, T., Klahr, H., & Ercolano, B. 2012, *Astronomy & Astrophysics*, 539, A148
- Birnstiel, T., Ormel, C. W., & Dullemond, C. P. 2011, *Astronomy & Astrophysics*, 525, 1

- Birnstiel, T., Dullemond, C. P., Zhu, Z., et al. 2018, *The Astrophysical Journal*, 869, L45
- Bitsch, B., Izidoro, A., Johansen, A., et al. 2019, *Astronomy & Astrophysics*, 88
- Bitsch, B., Johansen, A., Lambrechts, M., & Morbidelli, A. 2015, *Astronomy & Astrophysics*, 575, 28
- Bitsch, B., Morbidelli, A., Johansen, A., et al. 2018, *Astronomy & Astrophysics*, 612, A30
- Blum, J., & Wurm, G. 2008, *Annual Review of Astronomy and Astrophysics*, 46, 21
- Borucki, W. J., Koch, D., Basri, G., et al. 2010, *Science*, 327, 977
- Boss, A. P. 1997, *Science*, 276, 1836
- Bouchy, F., Mayor, M., Lovis, C., et al. 2009, *Astronomy & Astrophysics*, 496, 527
- Bourrier, V., Lecavelier des Etangs, A., Ehrenreich, D., et al. 2018, *Astronomy & Astrophysics*, 620, A147
- Bowler, B. P., & Nielsen, E. L. 2018, *Occurrence Rates from Direct Imaging Surveys*, ed. H. J. Deeg & J. A. Belmonte (Cham: Springer International Publishing), 1967–1983
- Bradley, L., Sipocz, B., Robitaille, T., et al. 2018, *Astropy/Photutils: V0.5*
- Brauer, F., Dullemond, P., & Henning, T. 2008, *Astronomy & Astrophysics*, 480, 859
- Brogi, M., Line, M., Bean, J., Désert, J.-M., & Schwarz, H. 2017, *The Astrophysical Journal*, 839, L2
- Brouwers, M. G., Vazan, A., & Ormel, C. W. 2018, *Astronomy & Astrophysics*, 611, A65
- Bryan, M. L., Knutson, H. A., Lee, E. J., et al. 2019, *The Astronomical Journal*, 157, 52
- Buchhave, L. A., Latham, D. W., Johansen, A., et al. 2012, *Nature*, 486, 375
- Burrows, A. S. 2014, *Proceedings of the National Academy of Sciences*, 111, 12601
- Carrera, D., Gorti, U., Johansen, A., & Davies, M. B. 2017, *The Astrophysical Journal*, 839, 16
- Chabrier, G., Mazevet, S., & Soubiran, F. 2019, *The Astrophysical Journal*, 872, 51
- Chachan, Y., Knutson, H. A., Gao, P., et al. 2019, *The Astronomical Journal*, 158, 244

- Chachan, Y., Jontof-Hutter, D., Knutson, H. A., et al. 2020, *The Astronomical Journal*, 160, 201
- Charnay, B., Meadows, V., & Leconte, J. 2015, *The Astrophysical Journal*, 813, 15
- Chen, H., & Rogers, L. A. 2016, *The Astrophysical Journal*, 831, 180
- Chen, Y.-X., Li, Y.-P., Li, H., & Lin, D. N. C. 2020, *The Astrophysical Journal*, 896, 135
- Chiang, E., & Laughlin, G. 2013, *Monthly Notices of the Royal Astronomical Society*, 431, 3444
- Chiang, E., & Youdin, A. 2010, *Annual Review of Earth and Planetary Sciences*, 38, 493
- Chiang, E. I., & Goldreich, P. 1997, *The Astrophysical Journal*, 490, 368
- Choi, J., Dotter, A., Conroy, C., et al. 2016, *The Astrophysical Journal*, 823, 102
- Ciardi, D. R., Beichman, C. A., Horch, E. P., & Howell, S. B. 2015, *The Astrophysical Journal*, 805, 16
- Cieza, L. A., Casassus, S., Tobin, J., et al. 2016, *Nature*, 535, 258
- Cimerman, N. P., Kuiper, R., & Ormel, C. W. 2017, *Monthly Notices of the Royal Astronomical Society*, 471, 4662
- Claret, A., & Bloemen, S. 2011, *Astronomy & Astrophysics*, 529, A75
- Colaprete, A., Toon, O. B., & Magalhães, J. A. 1999, *Journal of Geophysical Research: Planets*, 104, 9043
- Cowan, N. B., & Agol, E. 2011, *The Astrophysical Journal*, 729, 54
- Cresswell, P., & Nelson, R. P. 2006, *Astronomy & Astrophysics*, 450, 833
- Crossfield, I. J. M., & Kreidberg, L. 2017, *The Astronomical Journal*, 154, 261
- Cubillos, P., Erkaev, N. V., Juvan, I., et al. 2017, *Monthly Notices of the Royal Astronomical Society*, 466, 1868
- Cumming, A., Butler, R. P., Marcy, G. W., et al. 2008, *Publications of the Astronomical Society of the Pacific*, 120, 531
- Cutri, R. M., Skrutskie, M. F., van Dyk, S., et al. 2003, *VizieR Online Data Catalog*, II/246
- Cutri, R. M., Wright, E. L., Conrow, T., et al. 2014, *VizieR Online Data Catalog*, II/328

- Da Rio, N., Robberto, M., Hillenbrand, L. A., Henning, T., & Stassun, K. G. 2012, *The Astrophysical Journal*, 748, 14
- Dai, F., Winn, J. N., Schlaufman, K., et al. 2020, *The Astronomical Journal*, 159, 247
- Dalba, P. A., Fulton, B., Isaacson, H., Kane, S. R., & Howard, A. W. 2020, *The Astronomical Journal*, 160, 149
- Dalba, P. A., & Muirhead, P. S. 2016, *The Astrophysical Journal Letters*, 826, L7
- Dalba, P. A., & Tamburo, P. 2019, *The Astrophysical Journal Letters*, 873, L17
- Dalba, P. A., Kane, S. R., Li, Z., et al. 2021, arXiv e-prints, arXiv:2107.06901
- Dalba, P. A., Kane, S. R., Isaacson, H., et al. 2021, *The Astronomical Journal*, 161, 103
- D'Alessio, P., Calvet, N., & Hartmann, L. 2001, *The Astrophysical Journal*, 553, 321
- D'Alessio, P., Canto, J., Calvet, N., & Lizano, S. 1998, *The Astrophysical Journal*, 500, 411
- Dawson, R. I., & Johnson, J. A. 2018, *Annual Review of Astronomy and Astrophysics*, 56, 175
- Dawson, R. I., Lee, E. J., & Chiang, E. 2016, *The Astrophysical Journal*, 822, 54
- Deming, D., Sada, P. V., Jackson, B., et al. 2011, *The Astrophysical Journal*, 740, 33
- Deming, D., Wilkins, A., McCullough, P., et al. 2013, *The Astrophysical Journal*, 774, 95
- Deming, D., Knutson, H., Kammer, J., et al. 2015, *The Astrophysical Journal*, 805, 132
- Dotter, A. 2016, *The Astrophysical Journals*, 222, 8
- Doyle, L. R., Carter, J. A., Fabrycky, D. C., et al. 2011, *Science*, 333, 1602
- Draine, B. T. 2003, *The Astrophysical Journal*, 598, 1026
- . 2006, *The Astrophysical Journal*, 636, 1114
- Draine, B. T., & Lee, H. M. 1984, *The Astrophysical Journal*, 285, 89
- Dressing, C. D., & Charbonneau, D. 2015, *The Astrophysical Journal*, 807, 45
- Drażkowska, J., & Alibert, Y. 2017, *Astronomy & Astrophysics*, 608, 92

- Drażkowska, J., Alibert, Y., & Moore, B. 2016, *Astronomy & Astrophysics*, 594, 105
- Drażkowska, J., Li, S., Birnstiel, T., Stammler, S. M., & Li, H. 2019, *The Astrophysical Journal*, 885, 91
- Drażkowska, J., Stammler, S. M., & Birnstiel, T. 2021, *Astronomy & Astrophysics*, 647, 1
- Drażkowska, J., & Szulágyi, J. 2018, *The Astrophysical Journal*, 866, 142
- Dubber, S. C., Mortier, A., Rice, K., et al. 2019, *Monthly Notices of the Royal Astronomical Society*, 490, 5103
- Dubrulle, B., Morfill, G., & Sterzik, M. 1995, *Icarus*, 114, 237
- Dunham, M. M., Stutz, A. M., Allen, L. E., et al. 2014, in *Protostars and Planets VI*, ed. H. Beuther, R. S. Klessen, C. P. Dullemond, & T. Henning, 195
- Eastman, J., Gaudi, B. S., & Agol, E. 2013, *Publications of the Astronomical Society of the Pacific*, 125, 83
- Eastman, J., Siverd, R., & Gaudi, B. S. 2010, *Publications of the Astronomical Society of the Pacific*, 122, 935
- Eastman, J. D., Rodriguez, J. E., Agol, E., et al. 2019, arXiv e-prints, arXiv:1907.09480
- Elias, T., Haefelin, M., Drobniski, P., et al. 2009, *Atmospheric Research*, 92, 443
- Espinoza, N., & Jordán, A. 2015, *Monthly Notices of the Royal Astronomical Society*, 450, 1879
- Estrada, P. R., & Cuzzi, J. N. 2015, in *AAS/Division for Planetary Sciences Meeting Abstracts*, Vol. 47, *AAS/Division for Planetary Sciences Meeting Abstracts #47*, 507.02
- Estrada, P. R., Cuzzi, J. N., & Morgan, D. A. 2016, *The Astrophysical Journal*, 818, 200
- Evans, T. M., Sing, D. K., Wakeford, H. R., et al. 2016, *The Astrophysical Journal Letters*, 822, L4
- Evans, T. M., Sing, D. K., Kataria, T., et al. 2017, *Nature*, 548, 58
- Evans, T. M., Sing, D. K., Goyal, J. M., et al. 2018, *The Astronomical Journal*, 156, 283
- Fabrycky, D. C., Lissauer, J. J., Ragozzine, D., et al. 2014, *The Astrophysical Journal*, 790, 146

- Fernandes, R. B., Mulders, G. D., Pascucci, I., Mordasini, C., & Emsenhuber, A. 2019, *The Astrophysical Journal*, 874, 81
- Fischer, W. J., Megeath, S. T., Furlan, E., et al. 2017, *The Astrophysical Journal*, 840, 69
- Flaherty, K. M., Hughes, A. M., Rosenfeld, K. A., et al. 2015, *The Astrophysical Journal*, 813, 99
- Flaherty, K. M., Hughes, A. M., Teague, R., et al. 2018, *The Astrophysical Journal*, 856, 117
- Flaherty, K. M., Hughes, A. M., Rose, S. C., et al. 2017, *The Astrophysical Journal*, 843, 150
- Fletcher, L., Orton, G., Teanby, N., Irwin, P., & Bjoraker, G. 2009, *Icarus*, 199, 351
- Foreman-Mackey, D. 2018, *Research Notes of the American Astronomical Society*, 2, 31
- Foreman-Mackey, D., Agol, E., Ambikasaran, S., & Angus, R. 2017, *The Astronomical Journal*, 154, 220
- Foreman-Mackey, D., Hogg, D. W., Lang, D., & Goodman, J. 2013, *Publications of the Astronomical Society of the Pacific*, 125, 306
- Foreman-Mackey, D., Morton, T. D., Hogg, D. W., Agol, E., & Schölkopf, B. 2016, *The Astronomical Journal*, 152, 206
- Foreman-Mackey, D., Luger, R., Agol, E., et al. 2021, arXiv e-prints, arXiv:2105.01994
- Fossati, L., Erkaev, N. V., Lammer, H., et al. 2017, *Astronomy & Astrophysics*, 598, A90
- Fraine, J., Deming, D., Benneke, B., et al. 2014, *Nature*, 513, 556
- Freedman, R. S., Lustig-Yaeger, J., Fortney, J. J., et al. 2014, *ApJSS*, 214
- Fressin, F., Torres, G., Charbonneau, D., et al. 2013, *The Astrophysical Journal*, 766, 81
- Freytag, B., Holweger, H., Steffen, M., & Ludwig, H. G. 1997, in *Science with the VLT Interferometer*, ed. F. Paresce, 316
- Fromang, S., & Nelson, R. P. 2009, *Astronomy & Astrophysics*, 496, 597
- Fu, G., Deming, D., Knutson, H., et al. 2017, *The Astrophysical Journal Letters*, 847, L22
- Fulton, B. J., & Petigura, E. A. 2018, *The Astronomical Journal*, 156, 264

- Fulton, B. J., Petigura, E. A., Howard, A. W., et al. 2017, *The Astronomical Journal*, 154, 109
- Fulton, B. J., Rosenthal, L. J., Hirsch, L. A., et al. 2021, arXiv e-prints, arXiv:2105.11584
- Fung, J., Artymowicz, P., & Wu, Y. 2015, *The Astrophysical Journal*, 811, 101
- Fung, J., & Lee, E. J. 2018, *The Astrophysical Journal*, 859, 126
- Fung, J., Zhu, Z., & Chiang, E. 2019, *The Astrophysical Journal*, 887, 152
- Gaia Collaboration, Brown, A. G. A., Vallenari, A., et al. 2018, *Astronomy & Astrophysics*, 616, A1
- . 2021, *Astronomy & Astrophysics*, 649, A1
- Gao, P., & Benneke, B. 2018, *The Astrophysical Journal*, Volume 863, Issue 2, article id. 165, 23 pp. (2018)., 863
- Gao, P., Marley, M. S., & Ackerman, A. S. 2018, *The Astrophysical Journal*, 855, 86
- Gao, P., & Zhang, X. 2020, *The Astrophysical Journal*, 890, 93
- Gao, P., Fan, S., Wong, M. L., et al. 2017, *Icarus*, 287, 116
- Garcia, A. J. L., & Gonzalez, J.-F. 2020, *Monthly Notices of the Royal Astronomical Society*, 493, 1788
- Garhart, E., Deming, D., Mandell, A., et al. 2020, *The Astronomical Journal*, 159, 137
- Giampapa, M. S., & Rosner, R. 1984, *The Astrophysical Journal Letters*, 286, L19
- Gibson, N. P., Aigrain, S., Roberts, S., et al. 2012, *Monthly Notices of the Royal Astronomical Society*, 419, 2683
- Gibson, S. R., Howard, A. W., Marcy, G. W., et al. 2016, in *Society of Photo-Optical Instrumentation Engineers (SPIE) Conference Series*, Vol. 9908, *Ground-based and Airborne Instrumentation for Astronomy VI*, ed. C. J. Evans, L. Simard, & H. Takami, 990870
- Gordon, I., Rothman, L., Hill, C., et al. 2017, *Journal of Quantitative Spectroscopy and Radiative Transfer*, 203, 3
- Gundlach, B., & Blum, J. 2015, *The Astrophysical Journal*, 798
- Gundlach, B., Schmidt, K. P., Kreuzig, C., et al. 2018, *Monthly Notices of the Royal Astronomical Society*, 479, 1273
- Hadden, S., & Lithwick, Y. 2017, *The Astronomical Journal*, 154, 5

- Hallatt, T., & Lee, E. J. 2022, *The Astrophysical Journal*, 924, 9
- Hartmann, L., Herczeg, G., & Calvet, N. 2016, *Annual Review of Astronomy and Astrophysics*, 54, 135
- Hayashi, C. 1981, *Progress of Theoretical Physics Supplement*, 70, 35
- He, C., Hörst, S. M., Lewis, N. K., et al. 2018a, *The Astrophysical Journal Letters*, 856, L3
- . 2018b, *The Astronomical Journal*, 156, 38
- Helled, R., & Guillot, T. 2018, in *Handbook of Exoplanets* (Cham: Springer International Publishing), 167–185
- Helling, C. 2018, *Ann. Rev. Earth Planet. Sci*
- Hendler, N., Pascucci, I., Pinilla, P., et al. 2020, *The Astrophysical Journal*, 895, 126
- Heng, K. 2018, *Research Notes of the AAS*, 2, 128
- Henning, T., & Stognienko, R. 1996, *Astronomy & Astrophysics*, 311, 303
- Herman, M. K., Zhu, W., & Wu, Y. 2019, *The Astronomical Journal*, 157, 248
- Hirano, T., Narita, N., Shporer, A., et al. 2011, *PASJ*, 63, 531
- Hori, Y., & Ikoma, M. 2011, *Monthly Notices of the Royal Astronomical Society*, 416, 1419
- Hörst, S. M., He, C., Lewis, N. K., et al. 2018, *Nature Astronomy*, 2, 303
- Howard, A. W., & Fulton, B. J. 2016, *Publications of the Astronomical Society of the Pacific*, 128, 114401
- Howard, A. W., Johnson, J. A., Marcy, G. W., et al. 2010a, *The Astrophysical Journal*, 721, 1467
- Howard, A. W., Marcy, G. W., Johnson, J. A., et al. 2010b, *Science*, 330, 653
- Howard, A. W., Marcy, G. W., Bryson, S. T., et al. 2012, *ApJSS*, 201, 15
- Huber, K. F., Czesla, S., & Schmitt, J. H. M. M. 2017, *Astronomy & Astrophysics*, 597, 113
- Husser, T. O., Wende-von Berg, S., Dreizler, S., et al. 2013, *Astronomy & Astrophysics*, 553, A6
- Ikoma, M., & Hori, Y. 2012, *The Astrophysical Journal*, 753, 66
- Ikoma, M., Nakazawa, K., & Emori, H. 2000, *The Astrophysical Journal*, 537, 1013

- Inamdar, N. K., & Schlichting, H. E. 2015, *Monthly Notices of the Royal Astronomical Society*, 448, 1751
- Isaacson, H., & Fischer, D. 2010, *The Astrophysical Journal*, 725, 875
- Izidoro, A., Morbidelli, A., Raymond, S. N., Hersant, F., & Pierens, A. 2015, *Astronomy & Astrophysics*, 582, A99
- James, E., Toon, O., & Schubert, G. 1997, *Icarus*, 129, 147
- Jenkins, J. M., Caldwell, D. A., Chandrasekaran, H., et al. 2010, *The Astrophysical Journal Letters*, 713, L87
- Johansen, A., & Bitsch, B. 2019, *Astronomy & Astrophysics*, 631, A70
- Johansen, A., Ida, S., & Brasser, R. 2019, *Astronomy & Astrophysics*, 622, A202
- Johansen, A., & Lambrechts, M. 2017, *Annual Review of Earth and Planetary Sciences*, 45, 359
- Johansen, A., Mac Low, M.-M., Lacerda, P., & Bizzarro, M. 2015, *Science Advances*, 1, 1500109
- Johansen, A., Oishi, J. S., Low, M.-M. M., et al. 2007, *Nature*, 448, 1022
- Johnson, A., Zawadowicz, M., Lance, S., & Cziczo, D. 2018, *American Astronomical Society, DPS meeting #50*, id.220.03, 50
- Johnson, A. V., Schneiderman, T. M., Bauer, A. J. R., & Cziczo, D. J. 2017, *American Geophysical Union, Fall Meeting 2017*, abstract #P43E-2938
- Jontof-Hutter, D. 2019, *Annual Review of Earth and Planetary Sciences*, 47, 141
- Jontof-Hutter, D., Lissauer, J. J., Rowe, J. F., & Fabrycky, D. C. 2014, *The Astrophysical Journal*, 785, 15
- Jontof-Hutter, D., Rowe, J. F., Lissauer, J. J., Fabrycky, D. C., & Ford, E. B. 2015, *Nature*, 522, 321
- Jontof-Hutter, D., Ford, E. B., Rowe, J. F., et al. 2016, *The Astrophysical Journal*, 820, 39
- Kammer, J. A., Knutson, H. A., Line, M. R., et al. 2015, *The Astrophysical Journal*, Volume 810, Issue 2, article id. 118, 16 pp. (2015)., 810
- Kanodia, S., Wolfgang, A., Stefansson, G. K., Ning, B., & Mahadevan, S. 2019, *The Astrophysical Journal*, 882, 38
- Karkoschka, E., & Tomasko, M. G. 2011, *Icarus*, 211, 780

- Kataria, T., Showman, A. P., Fortney, J. J., Marley, M. S., & Freedman, R. S. 2014, *The Astrophysical Journal*, Volume 785, Issue 2, article id. 92, 11 pp. (2014)., 785
- Kataria, T., Sing, D. K., Lewis, N. K., et al. 2016, *The Astrophysical Journal*, Volume 821, Issue 1, article id. 9, 16 pp. (2016)., 821
- Kawahara, H., & Masuda, K. 2019, *The Astronomical Journal*, 157, 218
- Kawashima, Y., & Ikoma, M. 2018, *The Astrophysical Journal*, 853, 7
- . 2019, *The Astrophysical Journal*, 877, 109
- Kempton, E. M. R., Bean, J. L., & Parmentier, V. 2017, *The Astrophysical Journal Letters*, Volume 845, Issue 2, article id. L20, 6 pp. (2017)., 845
- Khare, B., Sagan, C., Arakawa, E., et al. 1984, *Icarus*, 60, 127
- Kimura, H., Wada, K., Kobayashi, H., et al. 2020, *Monthly Notices of the Royal Astronomical Society*, 1813, 1801
- Kipping, D. M., Torres, G., Henze, C., et al. 2016, *The Astrophysical Journal*, 820, 112
- Kitzmann, D., & Heng, K. 2018, *Monthly Notices of the Royal Astronomical Society*, 475, 94
- Knutson, H. A., Benneke, B., Deming, D., & Homeier, D. 2014a, *Nature*, 505, 66
- Knutson, H. A., Howard, A. W., & Isaacson, H. 2010, *The Astrophysical Journal*, 720, 1569
- Knutson, H. A., Lewis, N., Fortney, J. J., et al. 2012, *The Astrophysical Journal*, 754, 22
- Knutson, H. A., Dragomir, D., Kreidberg, L., et al. 2014b, *The Astrophysical Journal*, 794, 155
- Komacek, T. D., & Showman, A. P. 2016, *The Astrophysical Journal*, 821, 16
- Kraus, A. L., Ireland, M. J., Hillenbrand, L. A., & Martinache, F. 2012, *The Astrophysical Journal*, 745, 19
- Kreidberg, L. 2015, *Publications of the Astronomical Society of the Pacific*, 127, 1161
- Kreidberg, L., Line, M. R., Thorngren, D., Morley, C. V., & Stevenson, K. B. 2018, *The Astrophysical Journal Letters*, 858, L6
- Kreidberg, L., Bean, J. L., Désert, J.-M., et al. 2014a, *The Astrophysical Journal Letters*, 793, L27

- . 2014b, *Nature*, 505, 69
- Kreidberg, L., Line, M. R., Bean, J. L., et al. 2015, *The Astrophysical Journal*, 814, 66
- Kretke, K. A., & Lin, D. N. C. 2007, *The Astrophysical Journal Letters*, 664, L55
- Krumholz, M. R., Klein, R. I., & McKee, C. F. 2012, *The Astrophysical Journal*, 754, 71
- Kuntschner, H., Bushouse, H., Kümmel, M., & Walsh, J. R. 2009, WFC3 SMOV proposal 11552: Calibration of the G102 grism, Space Telescope WFC Instrument Science Report
- Kuntschner, H., Bushouse, H., Kümmel, M., & Walsh, J. R. 2009, ST-ECF Instrument Science Report WFC3-2009-17, 29 pages
- Kuntschner, H., Kümmel, M., Walsh, J. R., & Bushouse, H. 2011, Revised Flux Calibration of the WFC3 G102 and G141 grisms, Space Telescope WFC Instrument Science Report
- Kurokawa, H., & Tanigawa, T. 2018, *Monthly Notices of the Royal Astronomical Society*, 479, 635
- Kurucz, R. L. 1979, *The Astrophysical Journals*, 40, 1
- Lambrechts, M., & Johansen, A. 2012, *Astronomy & Astrophysics*, 544
- . 2014, *Astronomy & Astrophysics*, 572, A107
- Lambrechts, M., Johansen, A., & Morbidelli, A. 2014, *Astronomy & Astrophysics*, 572, A35
- Lambrechts, M., & Lega, E. 2017, *Astronomy & Astrophysics*, 606, A146
- Lambrechts, M., Morbidelli, A., Jacobson, S. A., et al. 2019, *Astronomy & Astrophysics*, 83, 1
- Laor, A., & Draine, B. T. 1993, *The Astrophysical Journal*, 402, 441
- Lavvas, P., & Koskinen, T. 2017, *The Astrophysical Journal*, 847, 32
- Lebreuilly, U., Commerçon, B., & Laibe, G. 2020, *Astronomy & Astrophysics*, 641, A112
- Lebreuilly, U., Hennebelle, P., Colman, T., et al. 2021, arXiv e-prints, arXiv:2107.08491
- Lee, E. J. 2019, *The Astrophysical Journal*, 878, 36
- Lee, E. J., & Chiang, E. 2015, *The Astrophysical Journal*, 811, 41

- . 2016, *The Astrophysical Journal*, 817, 90
- Lee, E. J., Chiang, E., & Ormel, C. W. 2014, *The Astrophysical Journal*, 797, 95
- Lee, E. J., & Connors, N. J. 2020, arXiv e-prints, arXiv:2008.01105
- Lee, G. K. H., Blečić, J., & Helling, C. 2018, *Astronomy & Astrophysics*, 614, A126
- Lee, Y.-N., Charnoz, S., & Hennebelle, P. 2021, *Astronomy & Astrophysics*, 648, A101
- Lenz, C. T., Klahr, H., Birnstiel, T., Kretke, K., & Stammler, S. 2020, *Astronomy & Astrophysics*, 640, A61
- Lewis, N. K., Showman, A. P., Fortney, J. J., et al. 2010, *The Astrophysical Journal*, Volume 720, Issue 1, pp. 344-356 (2010)., 720, 344
- Lewis, N. K., Knutson, H. A., Showman, A. P., et al. 2013, *The Astrophysical Journal*, 766
- Li, H., Lubow, S. H., Li, S., & Lin, D. N. C. 2009, *The Astrophysical Journal Letters*, 690, L52
- Libby-Roberts, J. E., Berta-Thompson, Z. K., Désert, J.-M., et al. 2020, *The Astronomical Journal*, 159, 57
- Lightkurve Collaboration, Cardoso, J. V. d. M., Hedges, C., et al. 2018, *Lightkurve: Kepler and TESS time series analysis in Python*, *Astrophysics Source Code Library*
- Lin, J. W., Lee, E. J., & Chiang, E. 2018, *Monthly Notices of the Royal Astronomical Society*, 480, 4338
- Lindegren, L., Klioner, S. A., Hernández, J., et al. 2021, *Astronomy & Astrophysics*, 649, A2
- Liu, B., & Ormel, C. W. 2018, *Astronomy & Astrophysics*, 615, A138
- Lodders, K. 1999, *The Astrophysical Journal*, 519, 793
- Lodders, K., & Fegley, B. 2002, *Icarus*, 155, 393
- Long, F., Pinilla, P., Herczeg, G. J., et al. 2018, *The Astrophysical Journal*, 869, 17
- Long, F., Herczeg, G. J., Harsono, D., et al. 2019, *The Astrophysical Journal*, 882, 49
- Lopez, E. D., & Fortney, J. J. 2013, *The Astrophysical Journal*, 776, 2
- Lopez, E. D., & Fortney, J. J. 2014, *The Astrophysical Journal*, 792, 1

- Lothringer, J. D., Benneke, B., Crossfield, I. J. M., et al. 2018, *The Astronomical Journal*, 155, 66
- Luger, R., Agol, E., Foreman-Mackey, D., et al. 2019, *The Astronomical Journal*, 157, 64
- Lynden-Bell, D., & Pringle, J. E. 1974, *Monthly Notices of the Royal Astronomical Society*, 168, 603
- M-R Kempton, E., Lupu, R., Owusu-Asare, A., Slough, P., & Cale, B. 2017, *Publications of the Astronomical Society of the Pacific*, 129, 044402
- Ma, Q., & Ghosh, S. K. 2021, arXiv e-prints, arXiv:2106.00972
- Madhusudhan, N. 2012, *The Astrophysical Journal*, 758
- Madhusudhan, N., & Seager, S. 2011, *The Astrophysical Journal*, 729
- Mamajek, E. E. 2009, in *American Institute of Physics Conference Series*, Vol. 1158, *Exoplanets and Disks: Their Formation and Diversity*, ed. T. Usuda, M. Tamura, & M. Ishii, 3–10
- Mankovich, C. R., & Fuller, J. 2021, *Nature Astronomy*, 5, 1103
- Mansfield, M., Bean, J. L., Oklopčić, A., et al. 2018, *The Astrophysical Journal Letters*, 868, L34
- Marley, M. S., & McKay, C. P. 1999, *Icarus*, 138, 268
- Masuda, K. 2014, *The Astrophysical Journal*, 783, 53
- Masuda, K., Winn, J. N., & Kawahara, H. 2020, *The Astronomical Journal*, 159, 38
- Mathis, J. S., Rumpl, W., & Nordsieck, K. H. 1977, *The Astrophysical Journal*, 217, 425
- Mayor, M., Marmier, M., Lovis, C., et al. 2011, arXiv e-prints, arXiv:1109.2497
- McCullough, P., & MacKenty, J. 2012, *Considerations for using Spatial Scans with WFC3*, *Space Telescope WFC Instrument Science Report*
- McCullough, P. R., Crouzet, N., Deming, D., & Madhusudhan, N. 2014, *The Astrophysical Journal*, 791, 55
- McQuillan, A., Mazeh, T., & Aigrain, S. 2014, *The Astrophysical Journals*, 211, 24
- Mikal-Evans, T., Sing, D. K., Goyal, J. M., et al. 2019, *Monthly Notices of the Royal Astronomical Society*, 488, 2222
- Millholland, S. 2019, *The Astrophysical Journal*, 886, 72

- Millholland, S., Petigura, E., & Batygin, K. 2020, *The Astrophysical Journal*, 897, 7
- Mills, S. M., Fabrycky, D. C., Migaszewski, C., et al. 2016, *Nature*, 533, 509
- Mills, S. M., Howard, A. W., Weiss, L. M., et al. 2019, *The Astronomical Journal*, 157, 145
- Miyake, K., & Nakagawa, Y. 1993, *Icarus*, 106, 20
- Mizuno, H. 1980, *Progress of Theoretical Physics*, 64, 544
- Moe, M., & Di Stefano, R. 2017, *The Astrophysical Journals*, 230, 15
- Morbidelli, A., Lambrechts, M., Jacobson, S., & Bitsch, B. 2015, *Icarus*, 258, 418
- Morbidelli, A., & Nesvorný, D. 2012, *Astronomy & Astrophysics*, 546, A18
- Morbidelli, A., Tsiganis, K., Crida, A., Levison, H. F., & Gomes, R. 2007, *The Astronomical Journal*, 134, 1790
- Mordasini, C. 2018, in *Handbook of Exoplanets* (Cham: Springer International Publishing), 2425–2474
- Morley, C. V., Fortney, J. J., Marley, M. S., et al. 2012, *The Astrophysical Journal*, Volume 756, Issue 2, article id. 172, 17 pp. (2012)., 756
- Morley, C. V., Fortney, J. J., Marley, M. S., et al. 2015, *The Astrophysical Journal*, 815, 110
- Morley, C. V., Knutson, H., Line, M., et al. 2017, *The Astronomical Journal*, 153, 86
- Morris, B. M., Hebb, L., Davenport, J. R. A., Rohn, G., & Hawley, S. L. 2017a, *The Astrophysical Journal*, 846, 99
- Morris, B. M., Hawley, S. L., Hebb, L., et al. 2017b, *The Astrophysical Journal*, 848, 58
- Morton, T. D., & Swift, J. 2014, *The Astrophysical Journal*, 791, 10
- Moses, J. I., Visscher, C., Fortney, J. J., et al. 2011, *The Astrophysical Journal*, 737, 15
- Moses, J. I., Line, M. R., Visscher, C., et al. 2013, *The Astrophysical Journal*, 777, 34
- Mulders, G. D., & Dominik, C. 2012, *Astronomy & Astrophysics*, 539, 9
- Murgas, F., Chen, G., Pallé, E., Nortmann, L., & Nowak, G. 2019, *Astronomy & Astrophysics*, 622, A172

- Musiolik, G., & Wurm, G. 2019, *The Astrophysical Journal*, 873, 58
- Nesvorný, D., & Vokrouhlický, D. 2014, *The Astrophysical Journal*, 790, 58
- Nielsen, E. L., De Rosa, R. J., Macintosh, B., et al. 2019, *The Astronomical Journal*, 158, 13
- Nikolov, N., Sing, D. K., Pont, F., et al. 2014, *Monthly Notices of the Royal Astronomical Society*, 437, 46
- Nikolov, N., Sing, D. K., Burrows, A. S., et al. 2015, *Monthly Notices of the Royal Astronomical Society*, 447, 463
- Nikolov, N., Sing, D. K., Fortney, J. J., et al. 2018a, *Nature*, 557, 526
- Nikolov, N., Sing, D. K., Goyal, J., et al. 2018b, *Monthly Notices of the Royal Astronomical Society*, 474, 1705
- Ning, B., Wolfgang, A., & Ghosh, S. 2018, *The Astrophysical Journal*, 869, 5
- Oberg, K. I., & Bergin, E. A. 2021, *Physics Reports*, 893, 1
- Oberg, K. I., Murray-Clay, R., & Bergin, E. A. 2011, *The Astrophysical Journal Letters*, 743, L16
- Odert, P., Erkaev, N. V., Kislyakova, K. G., et al. 2019, arXiv e-prints, arXiv:1903.10772
- Offner, S. S. R., & McKee, C. F. 2011, *The Astrophysical Journal*, 736, 53
- Ofir, A., Dreizler, S., Zechmeister, M., & Husser, T.-O. 2014, *Astronomy & Astrophysics*, 561, A103
- Ormel, C. W. 2017, in *Astrophysics and Space Science Library*, Vol. 445, *Formation, Evolution, and Dynamics of Young Solar Systems*, ed. M. Pessah & O. Gressel, 197
- Ormel, C. W., & Cuzzi, J. N. 2007, *Astronomy & Astrophysics*, 466, 413
- Ormel, C. W., & Klahr, H. H. 2010, *Astronomy & Astrophysics*, 520
- Ormel, C. W., & Liu, B. 2018, *Astronomy & Astrophysics*, 615, A178
- Ormel, C. W., Liu, B., & Schoonenberg, D. 2017, *Astronomy & Astrophysics*, 604, A1
- Ormel, C. W., Shi, J.-M., & Kuiper, R. 2015, *Monthly Notices of the Royal Astronomical Society*, 447, 3512
- Orosz, J. A., Welsh, W. F., Haghighipour, N., et al. 2019, *The Astronomical Journal*, 157, 174

- Owen, J. E., & Wu, Y. 2016, *The Astrophysical Journal*, 817, 107
- . 2017, *The Astrophysical Journal*, 847, 29
- Paardekooper, S. J., Baruteau, C., Crida, A., & Kley, W. 2010, *Monthly Notices of the Royal Astronomical Society*, 401, 1950
- Parker, E. N. 1958, *The Astrophysical Journal*, 128, 664
- Parmentier, V., Showman, A. P., & Lian, Y. 2013, *Astronomy & Astrophysics*, 558, A91
- Parviainen, H., & Aigrain, S. 2015, *Monthly Notices of the Royal Astronomical Society*, 453, 3821
- Paxton, B., Bildsten, L., Dotter, A., et al. 2011, *The Astrophysical Journals*, 192, 3
- Paxton, B., Cantiello, M., Arras, P., et al. 2013, *The Astrophysical Journals*, 208, 4
- Paxton, B., Marchant, P., Schwab, J., et al. 2015, *The Astrophysical Journals*, 220, 15
- Perez-Becker, D., & Showman, A. P. 2013, *The Astrophysical Journal*, 776, 134
- Petigura, E. A. 2015, PhD thesis, University of California, Berkeley
- Petigura, E. A., Sinukoff, E., Lopez, E. D., et al. 2017a, *The Astronomical Journal*, 153, 142
- Petigura, E. A., Howard, A. W., Marcy, G. W., et al. 2017b, *The Astronomical Journal*, 154, 107
- . 2017c, *The Astronomical Journal*, 154, 107
- Petigura, E. A., Marcy, G. W., Winn, J. N., et al. 2018, *The Astronomical Journal*, 155, 89
- Pinhas, A., & Madhusudhan, N. 2017, *Monthly Notices of the Royal Astronomical Society*, 471, 4355
- Pinilla, P., Birnstiel, T., Ricci, L., et al. 2012, *Astronomy & Astrophysics*, 538, A114
- Pinilla, P., Klarmann, L., Birnstiel, T., et al. 2016, *Astronomy & Astrophysics*, 585, A35
- Pinilla, P., Pohl, A., Stammler, S. M., et al. 2017, *The Astrophysical Journal*, 845, 68
- Pinnick, R. G., Hoihjelle, D. L., Fernandez, G., et al. 1978, *Journal of the Atmospheric Sciences*, 35, 2020

- Pinte, C., Dent, W. R. F., Menard, F., et al. 2016, *The Astrophysical Journal*, 816, 25
- Piro, A. L., & Vissapragada, S. 2020, *The Astronomical Journal*, 159, 131
- Piso, A. M. A., & Youdin, A. N. 2014, *The Astrophysical Journal*, 786, 21
- Piso, A.-M. A., Youdin, A. N., Murray-Clay, R. A., et al. 2015, *The Astrophysical Journal*, 800, 82
- Pollack, J. B., Hubickyj, O., Bodenheimer, P. H., et al. 1996, *Icarus*, 124, 62
- Pont, F., Knutson, H., Gilliland, R. L., Moutou, C., & Charbonneau, D. 2008, *Mon. Not. R. Astron. Soc.*, 385, 109
- Pont, F., Zucker, S., & Queloz, D. 2006, *Monthly Notices of the Royal Astronomical Society*, 373, 231
- Poppe, T., Blum, J., & Henning, T. 2000, *The Astrophysical Journal*, 533, 454
- Powell, D., Murray-Clay, R., Pérez, L. M., Schlichting, H. E., & Rosenthal, M. 2019, *The Astrophysical Journal*, 878, 116
- Powell, D., Zhang, X., Gao, P., & Parmentier, V. 2018, *The Astrophysical Journal*, 860, 18
- Pu, B., & Valencia, D. 2017, *The Astrophysical Journal*, 846, 47
- Pudritz, R. E., Cridland, A. J., & Alessi, M. 2018, *Connecting Planetary Composition with Formation*
- Rackham, B. V., Apai, D., & Giampapa, M. S. 2018, *The Astrophysical Journal*, 853, 122
- Rackham, B. V., Apai, D., & Giampapa, M. S. 2019, *The Astronomical Journal*, 157, 96
- Rafikov, R. R. 2002, *The Astrophysical Journal*, 572, 566
- Ribas, I., Guinan, E. F., Güdel, M., & Audard, M. 2005, *The Astrophysical Journal*, 622, 680
- Ricker, G. R., Winn, J. N., Vanderspek, R., et al. 2015, *Journal of Astronomical Telescopes, Instruments, and Systems*, 1, 014003
- Rogers, J. G., & Owen, J. E. 2020, arxiv:2007.11006
- Rogers, L. A. 2015, *The Astrophysical Journal*, 801, 41
- Rosenthal, L. J., Fulton, B. J., Hirsch, L. A., et al. 2021, *The Astrophysical Journals*, 255, 8

- Rosenthal, M. M., & Murray-Clay, R. A. 2018, *The Astrophysical Journal*, 864, 66
- Rowan, D., Meschiari, S., Laughlin, G., et al. 2016, *The Astrophysical Journal*, 817, 104
- Rowe, J. F., & Thompson, S. E. 2015, arXiv e-prints, arXiv:1504.00707
- Salvatier, J., Wiecki, T. V., & Fonnesbeck, C. 2016, *PeerJ Computer Science*, 2, e55
- Salz, M., Czesla, S., Schneider, P. C., & Schmitt, J. H. M. M. 2016a, *Astronomy & Astrophysics*, 586, A75
- Salz, M., Schneider, P. C., Czesla, S., & Schmitt, J. H. M. M. 2016b, *Astronomy & Astrophysics*, 585, L2
- Salz, M., Czesla, S., Schneider, P. C., et al. 2018, *Astronomy & Astrophysics*, 620, A97
- Sanchis-Ojeda, R., & Winn, J. N. 2011, *The Astrophysical Journal*, 743, 61
- Santerne, A., Malavolta, L., Kosiarek, M. R., et al. 2019, ArXiv e-prints, 1911.07355
- Savvidou, S., Bitsch, B., & Lambrechts, M. 2020, *Astronomy & Astrophysics*, 640, 63
- Schib, O., Mordasini, C., Wenger, N., Marleau, G. D., & Helled, R. 2021, *Astronomy & Astrophysics*, 645, A43
- Schlafly, E. F., & Finkbeiner, D. P. 2011, *The Astrophysical Journal*, 737, 103
- Schlecker, M., Mordasini, C., Emsenhuber, A., et al. 2020, *Astronomy & Astrophysics*, 1
- Schmitt, J. H. M. M., & Rosner, R. 1983, *The Astrophysical Journal*, 265, 901
- Segura-Cox, D. M., Schmiedeke, A., Pineda, J. E., et al. 2020, *Nature*, 586, 228
- Shakura, N. I., & Sunyaev, R. A. 1973, *Astronomy & Astrophysics*, 24, 337
- Shen, X., Sun, J., Zhang, X., et al. 2015, *Atmospheric Environment*, 120, 307
- Showman, A. P., Cho, J. Y.-K., & Menou, K. 2009, *The Astrophysical Journal*, 699, 564
- Simon, J. B., Armitage, P. J., Li, R., & Youdin, A. N. 2016, *The Astrophysical Journal*, 822, 55
- Sing, D. K. 2010, *Astronomy and Astrophysics*, 510, A21
- Sing, D. K., Vidal-Madjar, A., Desert, J. M., des Etangs, A. L., & Ballester, G. 2008, *The Astrophysical Journal*, Volume 686, Issue 1, pp. 658-666 (2008)., 686, 658

- Sing, D. K., Pont, F., Aigrain, S., et al. 2011, *Mon. Not. R. Astron. Soc.*, 416, 1443
- Sing, D. K., Wakeford, H. R., Showman, A. P., et al. 2015, *Monthly Notices of the Royal Astronomical Society*, 446, 2428
- Sing, D. K., Fortney, J. J., Nikolov, N., et al. 2016, *Nature*, 529, 59
- Sing, D. K., Lavvas, P., Ballester, G. E., et al. 2019, *The Astronomical Journal*, 158, 91
- Smith, J. C., Stumpe, M. C., Van Cleve, J. E., et al. 2012, *Publications of the Astronomical Society of the Pacific*, 124, 1000
- Southworth, J. 2011, *Monthly Notices of the Royal Astronomical Society*, 417, 2166
- Sromovsky, L., Fry, P., & Kim, J. 2011, *Icarus*, 215, 292
- Steinpilz, T., Teiser, J., & Wurm, G. 2019, *The Astrophysical Journal*, 874, 60
- Stevenson, D. J. 1982a, *Planet. Space Sci.*, 30, 755
- . 1982b, *Ann. Rev. Earth Planet. Sci.*, 10, 257
- Stevenson, K. B., Désert, J.-M., Line, M. R., et al. 2014, *Science*, 346, 838
- Strassmeier, K. G., Granzer, T., Weber, M., et al. 2004, *Astronomische Nachrichten*, 325, 527
- Stumpe, M. C., Smith, J. C., Van Cleve, J. E., et al. 2012, *Publications of the Astronomical Society of the Pacific*, 124, 985
- Takeuchi, T., & Lin, D. N. C. 2005, *The Astrophysical Journal*, 623, 482
- Tayar, J., Claytor, Z. R., Huber, D., & van Saders, J. 2020, *arXiv e-prints*, arXiv:2012.07957
- Tennyson, J., Yurchenko, S., Tennyson, J., & Yurchenko, S. N. 2018, *Atoms*, 6, 26
- Ter Braak, C. J. F. 2006, *Statistics and Computing*, 16, 239
- Testi, L., Natta, A., Shepherd, D. S., & Wilner, D. J. 2003, *Astronomy & Astrophysics*, 403, 323
- Thorngren, D., & Fortney, J. J. 2019, *The Astrophysical Journal*, 874, L31
- Thorngren, D. P., & Fortney, J. J. 2018, *arXiv: 1811.11859*
- Thorngren, D. P., Fortney, J. J., Murray-Clay, R. A., & Lopez, E. D. 2016, *The Astrophysical Journal*, 831, 64
- Tobin, J. J., Sheehan, P. D., Megeath, S. T., et al. 2020, *The Astrophysical Journal*, 890, 130

- Toon, O., McKay, C., Griffith, C., & Turco, R. 1992, *Icarus*, 95, 24
- Toon, O. B., Turco, R. P., Hamill, P., Kiang, C. S., & Whitten, R. C. 1979, *Journal of the Atmospheric Sciences*, 36, 718
- Trampedach, R., Asplund, M., Collet, R., Nordlund, Å., & Stein, R. F. 2013, *The Astrophysical Journal*, 769, 18
- Tremblay, P. E., Ludwig, H. G., Freytag, B., Steffen, M., & Caffau, E. 2013, *Astronomy & Astrophysics*, 557, A7
- Tsiaras, A., Waldmann, I. P., Rocchetto, M., et al. 2016, *The Astrophysical Journal*, 832, 202
- Tsiaras, A., Waldmann, I. P., Zingales, T., et al. 2018, *The Astronomical Journal*, 155, 156
- Turner, N. J., Fromang, S., Gammie, C., et al. 2014, in *Protostars and Planets VI* (University of Arizona Press), 411
- Tychoniec, Ł., Manara, C. F., Rosotti, G. P., et al. 2020, *Astronomy & Astrophysics*, 640, A19
- Uehara, S., Kawahara, H., Masuda, K., Yamada, S., & Aizawa, M. 2016, *The Astrophysical Journal*, 822, 2
- van de Hulst, H. C. 1957, *Light Scattering by Small Particles* (John Wiley & Sons)
- Venturini, J., Alibert, Y., & Benz, W. 2016, *Astronomy & Astrophysics*, 596, 90
- Venturini, J., Alibert, Y., Benz, W., & Ikoma, M. 2015, *Astronomy & Astrophysics*, 576, A114
- Venturini, J., Guilera, O. M., Ronco, M. P., & Mordasini, C. 2020, *Astronomy & Astrophysics*
- Vissapragada, S., Jontof-Hutter, D., Shporer, A., et al. 2020, *The Astronomical Journal*, 159, 108
- Visscher, C. 2012, *The Astrophysical Journal*, 757
- Visser, R. G., & Ormel, C. W. 2016, *Astronomy & Astrophysics*, 586, A66
- Vogt, S. S., Allen, S. L., Bigelow, B. C., et al. 1994, in *Proc. SPIE, Vol. 2198, Instrumentation in Astronomy VIII*, ed. D. L. Crawford & E. R. Craine, 362
- Wada, K., Tanaka, H., Okuzumi, S., et al. 2013, *Astronomy & Astrophysics*, 559, A62
- Wahl, S. M., Hubbard, W. B., Militzer, B., et al. 2017, *Geophysical Research Letters*, 44, 4649

- Wakeford, H. R., & Sing, D. K. 2015, *Astronomy & Astrophysics*, 573
- Wakeford, H. R., Wilson, T. J., Stevenson, K. B., & Lewis, N. K. 2019, *Research Notes of the AAS*, 3, 7
- Wakeford, H. R., Sing, D. K., Kataria, T., et al. 2017a, *Science*, 356, 628
- Wakeford, H. R., Stevenson, K. B., Lewis, N. K., et al. 2017b, *The Astrophysical Journal Letters*, 835
- Wakeford, H. R., Sing, D. K., Deming, D., et al. 2018, *The Astronomical Journal*, 155, 29
- Wang, J., Fischer, D. A., Barclay, T., et al. 2015, *The Astrophysical Journal*, 815, 127
- Wang, L., & Dai, F. 2018, *The Astrophysical Journal*, 860, 175
- Wang, L., & Dai, F. 2019, *The Astrophysical Journal*, 873, L1
- Warren, S. G., & Brandt, R. E. 2008, *JGRA*, 113
- Watson, A. J., Donahue, T. M., & Walker, J. C. G. 1981, *Icarus*, 48, 150
- Weidenschilling, S. 1977, *Monthly Notices of the Royal Astronomical Society*, 57
- Welsh, W. F., Orosz, J. A., Carter, J. A., et al. 2012, *Nature*, 481, 475
- Wilkins, A. N., Deming, D., Madhusudhan, N., et al. 2014, *The Astrophysical Journal*, 783, 113
- Williams, J. P., & Cieza, L. A. 2011, *Annual Review of Astronomy and Astrophysics*, 49, 67
- Winn, J. N. 2018, *Planet Occurrence: Doppler and Transit Surveys*, ed. H. J. Deeg & J. A. Belmonte (Cham: Springer International Publishing), 1–18
- Winn, J. N., Johnson, J. A., Howard, A. W., et al. 2010, *The Astrophysical Journal Letters*, 723, L223
- Wittenmyer, R. A., Butler, R. P., Tinney, C. G., et al. 2016, *The Astrophysical Journal*, 819, 28
- Wittenmyer, R. A., Wang, S., Horner, J., et al. 2020, *Monthly Notices of the Royal Astronomical Society*, 492, 377
- Woitke, P., Helling, C., Hunter, G. H., et al. 2018, *Astronomy & Astrophysics*, 614, A1
- Wolfgang, A., & Lopez, E. 2015, *The Astrophysical Journal*, 806, 183

- Wong, I., Knutson, H. A., Kataria, T., et al. 2016, *The Astrophysical Journal*, 823, 122
- Wong, I., Benneke, B., Gao, P., et al. 2020, *The Astronomical Journal*, 159, 234
- Wong, M. H., Mahaffy, P. R., Atreya, S. K., Niemann, H. B., & Owen, T. C. 2004, *Icarus*, 171, 153
- Wright, J. T., Marcy, G. W., Butler, R. P., & Vogt, S. S. 2004, *The Astrophysical Journals*, 152, 261
- Wu, Y. 2019, *The Astrophysical Journal*, 874, 91
- Xie, J.-W. 2014, *The Astrophysical Journals*, 210, 25
- Yee, S. W., Petigura, E. A., & von Braun, K. 2017, *The Astrophysical Journal*, 836, 77
- Yee, S. W., Petigura, E. A., Fulton, B. J., et al. 2018, *The Astronomical Journal*, 155, 255
- Youdin, A. N., & Goodman, J. 2005, *The Astrophysical Journal*, 620, 459
- Zeng, L., Jacobsen, S. B., Sasselov, D. D., et al. 2019, *Proceedings of the National Academy of Sciences*, 116, 9723
- Zhang, M., Chachan, Y., Kempton, E. M.-R., & Knutson, H. A. 2019, *Publications of the Astronomical Society of the Pacific*, 131, 034501
- Zhang, M., Chachan, Y., Kempton, E. M.-R., Knutson, H. A., & Chang, W. H. 2020, *The Astrophysical Journal*, 899, 27
- Zhang, M., Knutson, H. A., Kataria, T., et al. 2018a, *The Astronomical Journal*, 155, 83
- Zhang, X., & Showman, A. P. 2018a, *The Astrophysical Journal*, 866, 1
- . 2018b, *The Astrophysical Journal*, 866, 2
- Zhang, Z., Zhou, Y., Rackham, B. V., & Apai, D. 2018b, *The Astronomical Journal*, 156, 178
- Zhou, Y., Apai, D., Lew, B. W. P., & Schneider, G. 2017, *The Astronomical Journal*, 153, 243
- Zhu, W., & Wu, Y. 2018, *The Astronomical Journal*, 156, 92
- Zhu, Z., Stone, J. M., Rafikov, R. R., & Bai, X.-n. 2014, *The Astrophysical Journal*, 785, 122

Appendix A

PEBBLE ACCRETION EFFICIENCY

The pebble flux threshold determined by Lambrechts et al. (2019) for super-Earth formation is applicable for a solar mass star. To obtain the integrated pebble flux threshold for super-Earth formation around a less massive star, we need to determine the stellar mass dependence of the pebble accretion efficiency. The pebble accretion efficiency is equal to the pebble accretion rate divided by the radial pebble flux at the growing planet's location. Depending on whether the pebble scale height is smaller or larger than the Hill radius of the planet (2D or 3D regime), this efficiency ϵ is given by:

$$\epsilon_{2D/3D} = \frac{\dot{M}_{2D/3D}}{2\pi r v_r \Sigma_d} \quad (\text{A.1})$$

where $\dot{M}_{3D} = f_{3D} \dot{M}_{2D}$ when $f_{3D} < 1$ (see Equations 2.4-2.6). In the expression for the radial pebble flux, r is the radial distance from the star, Σ_d is the surface density of pebbles (equal to Σ_1 in our two-population model), and $v_r = 2\eta r \Omega_K \text{St}$ is the radial drift velocity of the pebbles. Here, $\eta = -0.5 \text{ d} \ln P / \text{d} \ln r (H_g/r)^2$ is a measure of the deviation of gas' orbital velocity from the Keplerian velocity. Following through, we obtain the following expressions for pebble accretion efficiency in the 2D and 3D regimes:

$$\epsilon_{2D} = \left(\frac{10}{3}\right)^{2/3} \frac{1}{2\pi} \frac{q^{2/3}}{\eta \text{St}^{1/3}} \approx 0.36 \frac{q^{2/3}}{\eta \text{St}^{1/3}} \quad (\text{A.2})$$

$$\epsilon_{3D} = \left(\frac{5}{6}\right) \frac{1}{\sqrt{2\pi}} \frac{q r}{\eta H_d} \approx 0.33 \frac{q}{\eta h_d}. \quad (\text{A.3})$$

Here, $q = M_p/M_*$ is the mass ratio of the growing planet and $h_d = H_d/r$. The numerical coefficients and the physical dependencies we obtain match those given in Table 2 of Ormel & Liu (2018) (listed under Morbidelli et al., 2015 and Lambrechts & Johansen, 2014, which matches our prescription). The numerical coefficients are in reasonable agreement with the values determined from 3D simulations in Ormel & Liu (2018) (our ϵ_{2D} is 50% higher and ϵ_{3D} is 15% lower, most of the seeds in our models accrete in the 3D so ϵ_{3D} is the relevant value). Our expression for ϵ_{3D} is larger by a factor of 10/3 compared to the value obtained by Lambrechts et al. (2019).

Super-Earths form in the inner disk and accrete in the 3D regime in Lambrechts et al. (2019), where the pebble accretion efficiency $\epsilon_{3D} \propto 1/M_*$. Therefore, accounting for the higher pebble accretion efficiency (factor of 10/3), the lower stellar mass ($0.75 M_\odot$) in our models, and 50% mass loss due to sublimation of water ice from pebbles, the threshold for super-Earth formation by pebble accretion is roughly $190 \times 3/10 \times 0.75/0.5 \sim 86 M_\oplus$. We note that this is the integrated pebble flux that must reach the inner disk after the super-Earth seeds have formed. This threshold therefore does not include the pebble mass required to form the seeds in the first place. We have also ignored the stellar mass dependence of other quantities in the expression, most notably the disk aspect ratio and the Stokes number of pebbles in the inner disk.

Appendix B

DISK FRACTION AND FORMATION THRESHOLD

Of the 425 disks targeted by ALMA in Tobin et al. (2020), 45 disks lie above the $M_{\text{iso}} = 15 M_{\oplus}$ threshold. However, this sample is likely to contain both massive and low mass stars that will bias our estimate of f_{disk} . Restricting the observational sample of protostars to a range of masses is notoriously difficult as protostellar masses are highly uncertain for Class 0 and I sources (e.g., Dunham et al., 2014; Fischer et al., 2017). Instead, we correct for contamination from massive and low mass stars using the measured initial mass function (IMF) for the Orion nebula. In order to do so, we need to know how well the ALMA sample captures the IMF, including the threshold stellar mass below which we miss most protostellar objects. Given the wide range ($10^{-2} - 10^3 L_{\odot}$) of protostellar luminosities exhibited by the sources in Tobin et al. (2020), it is likely that we are only missing protostars that reach $\lesssim 0.1 - 0.2 M_{\odot}$ at the end of accretion (e.g., Hartmann et al., 2016; Offner & McKee, 2011). Adopting the IMF from Da Rio et al. (2012) along with the modification suggested by Krumholz et al. (2012) to account for stars more massive than $2 M_{\odot}$, we find that these stars constitute $\sim 20\%$ of the stellar population.

Therefore, assuming that the ALMA survey likely samples only the top 80% of the IMF, stars more massive than $1.4 M_{\odot}$ should comprise approximately 12.5% of our sample (53 sources). We expect a substantial fraction of disks above our formation threshold to be hosted by these massive stars. However, nearly $\sim 50\%$ of massive stars have a companion within $\log P = 5$ (Moe & Di Stefano, 2017), which are associated with lower disk masses and/or lifetimes (Kraus et al., 2012). This means that at most half of the massive stellar population should host massive disks in our survey sample. We must also correct for contamination from M stars that lie above the luminosity threshold. We assume that disks around M stars are likely to have lower masses¹, and we therefore do not expect a substantial number of these disks to lie above our formation threshold. Using the assumption adopted earlier that we only miss the bottom 20% of the IMF, we would expect

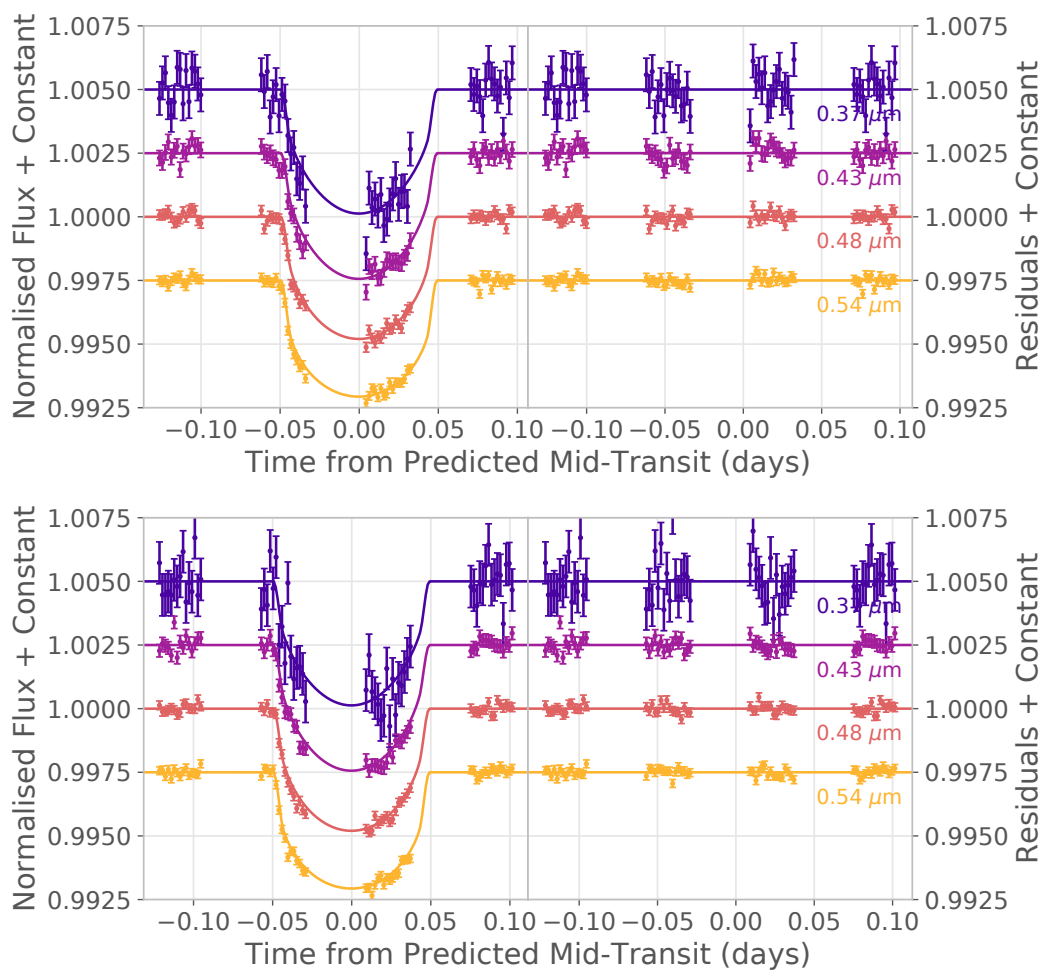
¹This is at least well supported by observations of Class II disks (e.g., Andrews et al., 2013; Ansdell et al., 2016). For Class 0 and I disks, Tobin et al. (2020) observe a weak correlation between disk mass and protostellar luminosity ($M_{\text{dust}} \propto L_{\text{bol}}^{0.31 \pm 0.05}$ for non-multiple sources, see their Figure 8), where the latter serves as a relatively poor tracer of stellar mass.

half the stars in our sample to be $< 0.5 M_{\odot}$ (212 sources). Finally, we expect $\sim 20\%$ of the remaining FGK stars (32 out of the remaining 160) to have close-in companions ($\lesssim 50$ au, Moe & Di Stefano, 2017) that we cannot detect², and we must therefore remove these from the denominator. Performing all these steps, we find $f_{\text{disk}} = (45 - 53/2)/(425 - 53 - 212 - 32) \approx 14\%$.

²Although Tobin et al. (2020) indicate whether a set of sources are part of a multiple system or not, they can only resolve companions separated by $\gtrsim 40$ au. Using the position coordinates, *Gaia* distances to the sources, and disk radii provided in Tobin et al. (2020), we find that there is likely only a single pair of bona fide binary stars in their sample with separation < 50 au.

Appendix C

HST SPECTROSCOPIC LIGHT CURVES FOR HAT-P-11B

Figure C.1: *HST* STIS G430L wavelength dependent light curves for visits 1 and 2.

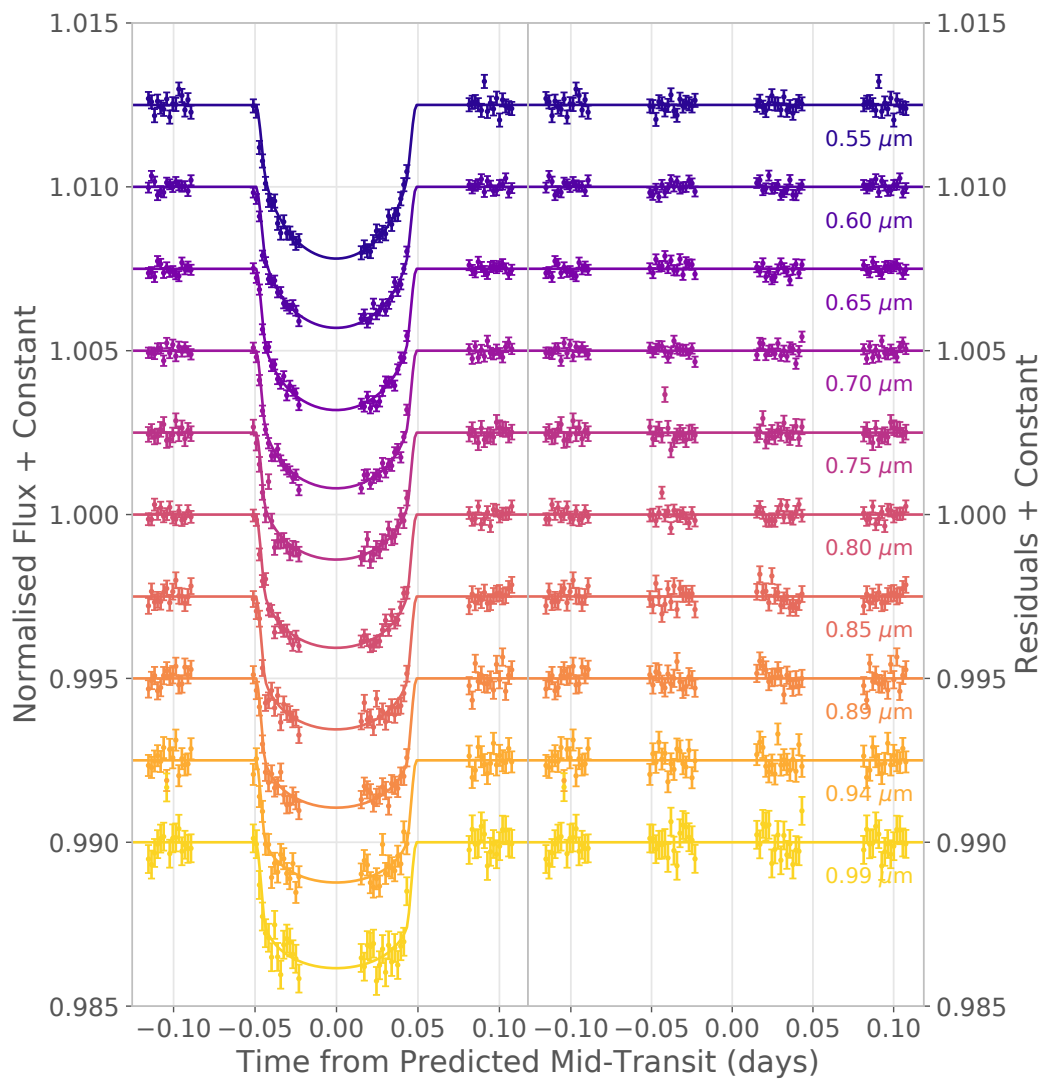


Figure C.2: *HST* STIS G750L wavelength dependent light-curves.

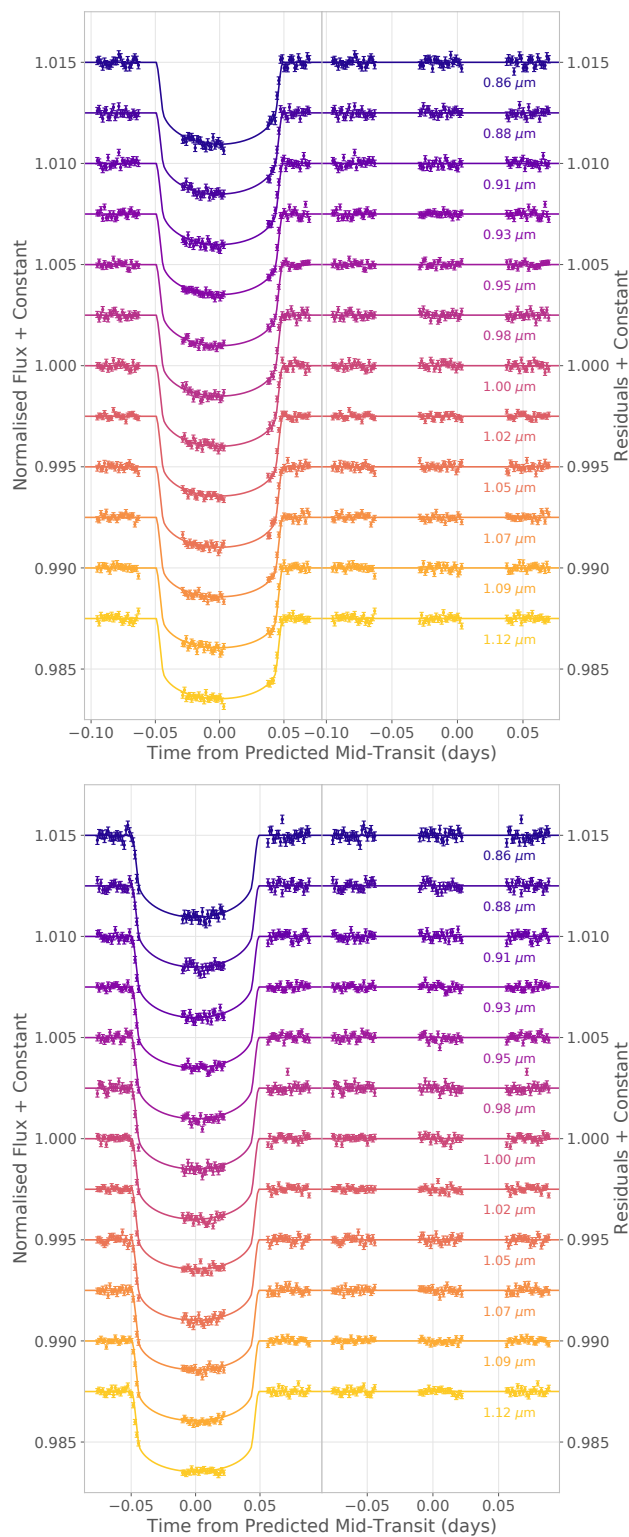


Figure C.3: *HST* WFC3 G102 wavelength dependent light curves for visits 1 and 2.

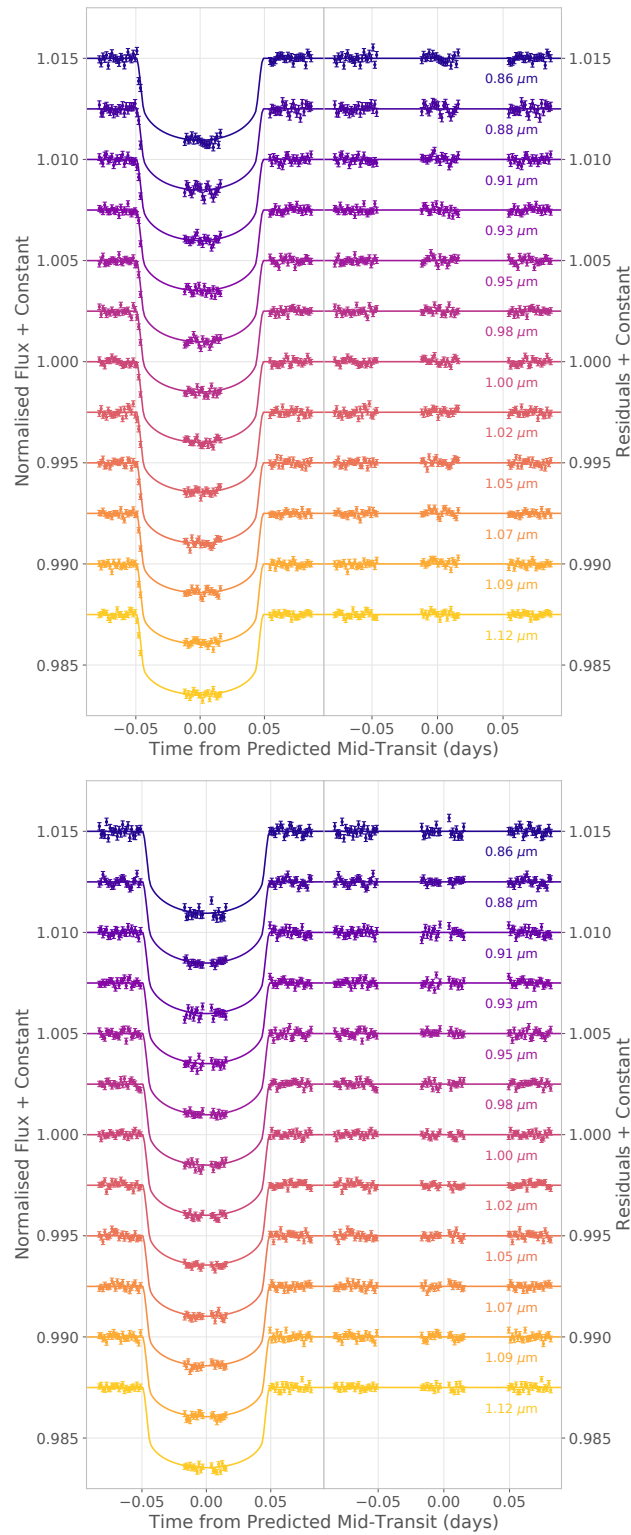


Figure C.4: *HST* WFC3 G102 wavelength dependent light curves for visits 3 and 4.

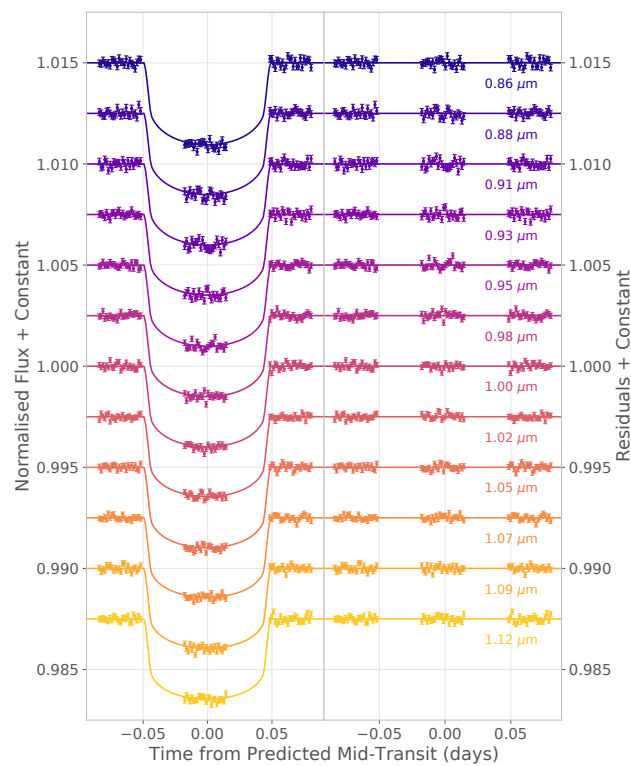


Figure C.5: *HST* WFC3 G102 wavelength dependent light curves for visit 5.

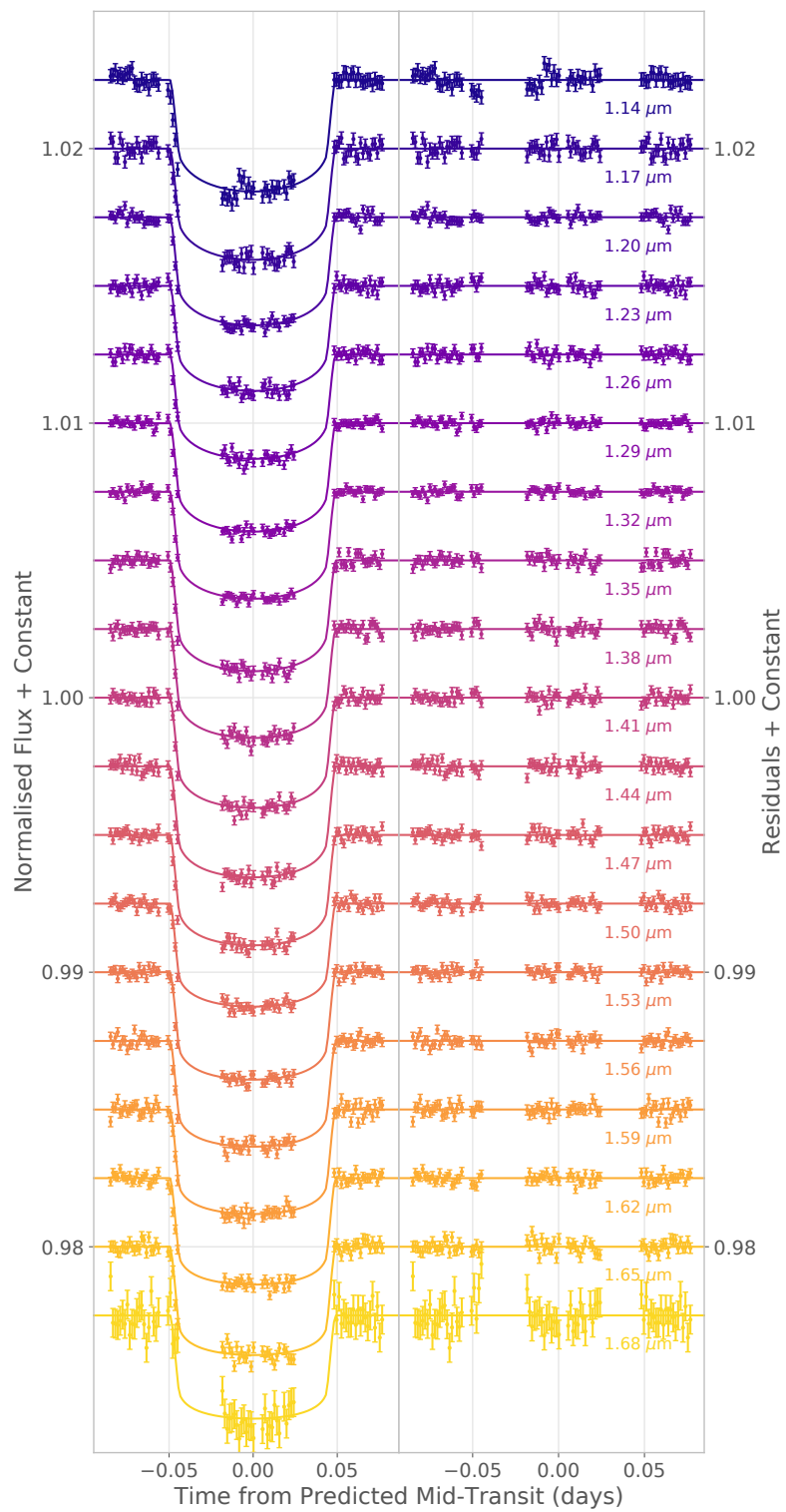


Figure C.6: *HST* WFC3 G141 wavelength dependent light curves.